Repetitive bubble injection for control of turbulent boundary layers

Hyun Jin Park

Laboratory for Flow Control,
Division of Energy and Environmental Systems
Graduate School of Engineering
Hokkaido University

Supervised by
Prof. Dr. Yuichi Murai

21th January 2016

Repetitive bubble injection for control of turbulent boundary layers

Thesis for Ph.D. (Engineering) at Hokkaido University
Submitted at 25th December 2015

Published and distributed by:
Laboratory for Flow Control
Division of Energy and Environmental Systems
Graduate School of Engineering
Hokkaido University
Kita-ku, N 11 N 8, Sapporo 060-8628
Japan

Advisory Committee
Prof. Dr. (Eng.) Yuichi Murai, Hokkaido University, Chair/Chief examiner
Prof. Dr. (Eng.) Nobuyuki Oshima, Hokkaido University, Co-examiner
Prof. Dr. (Eng.) Masao Watanabe, Hokkaido University, Co-examiner
Prof. Dr. (Eng.) TeknD Koji Fukagata, Keio University, Co-examiner
Assoc. Prof. Dr. (Eng.) Yuji Tasaka, Hokkaido University, Co-examiner

Acknowledgment

This research works were carried out at the Laboratory for Flow Control in Hokkaido University, and supported by the Fundamental Research Developing Association for Shipbuilding and Offshore (REDAS) and the Grant-in-Aid for Japan Society for the Promotion of Science (JSPS) Research Fellow No. 15J00147. The author of this thesis would like to express their appreciation for these supports.

At first, I would like to express my grateful thanks to my supervisor Prof. Dr. Yuichi Murai. He suggested to me returning to the laboratory when I worked as a research engineer in LG electronics for a military service in Korea, and have given many interesting ideas to me during a doctoral course in Hokkaido University. And also he has provided environment for studying freely on what I want to know. Thanks to his committed supports, I could concentrate my study.

I would like to thank Assoc. Prof. Dr. Yuji Tasaka. He has given me pointed advices and comments on my study. I think that many interesting researches included in this thesis are not possible to complete without his supports.

I would like to thank Technician Mr. Toshiyuki Sampo. He has supported for my study by his excellent technique. He always made excellent experimental facilities better than my design.

I would like to thank Assist. Prof. Dr. Yoshihiko Oishi in Muroran Institute of Technology for giving me chances to discuss many things. Thanks to the discussions, abundant discussions are written in this thesis.

And also I would like to thank Tokyo Gas Co. Ltd. and Hiroshima University for supporting experimental facilities.

Finally, I would like to express grateful thanks to all of my friends and family which have prayed for me. Especially, I could not have been able to through this period of my life without prays of mother in Korea and father in the heaven. Thank you.

25th December 2015.

Hyun Jin Park

Sapporo in Japan

Contents

1 Introduction

1.1 Reviews of previous studies

1.1.1 Techniques for turbulent boundary layer control

Structures for turbulent boundary layer control found at creatures in the nature have been respected in a long time to improve a lift force or reduce a friction drag (Bushnell, 1991), and many techniques have been developed by imitating the structures. Techniques achieving larger lift at airplanes, for example, a vortex generator (Lin et al., 1994), a circulation control wing (Englar and Huson, 1984), a synthetic jet (Glezer and Amitay, 2002) and a plasma actuator (Roupassov et al., 2009), are developed. In water or hydrodynamic applications, the drag reduction techniques are also developed to reduce the friction drag, for example, using riblet (Walsh, 1983), compliant surface (Hahn et al., 2002), super-hydrophobic surface (Fukagata et al., 2006), deformation wall (Endo et al., 2000), spanwise oscillation of wall (Baron and Quadrio, 1996) and Lorentz force (Berger, 2000), and injecting polymers (den Toonder et al., 1997), surfactant (Ohlendorf et al., 1986) and bubbles (McCormick and Bhattacharyya, 1973). These drag reduction techniques are classified as passive, active and additive controls as shown in **Table 1.1**. Comparing the passive and active control techniques, they have both merits and demerits. The passive control techniques do not require energy for actuator but cannot control the drag reduction rate. On the contrary, the active control techniques requires the energy but is possible to control the drag reduction rate. As common characteristics, the passive and active control techniques can reduce only the frictional drag on their installation area. And almost of them, types of installation at the wall surface, have to maintain clean surface to demonstrate their ability. Comparing with these techniques, the additive control techniques have advantages; one is wide effective area because they consistently modify the boundary layer by traveling with a main flow, and another is controllability of drag reduction rate by control of injection amount. In this thesis, we focus on a turbulent boundary layer control using injecting bubbles. The bubbly drag reduction is suitable for external flow because it has no damage on environments comparing with other additives. Therefore, it is expected to promote the energy efficiency of low speed huge vessels by reducing the frictional drag that occupies 80% of total drag acting on the vessels.

1.1.2 Turbulent boundary layer control by bubble injection

Bubbly flows have been studied in a long time by many researchers because bubbles injected into liquid–phase flows affect heat, mass and momentum transfers of the flows. Characteristics of

bubbly flows change dependency on the direction of buoyancy relative to the main flow direction. Especially vertical bubbly flows are targeted for the study in almost cases because of industrial demands for boilers and heat exchangers (Hibiki and Ishii, 2002). Bubbles are deformed and fragmented by shear of the flow, and coalesced by their surface tension when they contact with each other. Moreover, mutual interactions of the bubbles exist in the bubbly flows, e.g. bubble–bubble interaction (Kamp et al., 2001; Kitagawa et al., 2004) and bubble–flow structure (Brücker, 1999; Fujiwara et al., 2004). To understand bubbles' behaviors, we have to solve multi-scale problem called in the bubbly flows (e.g., Sugiyama et al., 2001), which ranges from the thickness of gas–liquid interface to the length scale of a bulk system. Therefore, we do not understand yet completely their behaviors and their effect on the bubbly flows despite many researches for the bubbles have been performed. On the other hand, horizontal bubbly flows have received less attention than the vertical bubbly flows because they are unsuitable for the industrial demands and more complex flows, multi-dimensionalized irresistibly by buoyancy of bubbles which acts on dispersed the bubbles perpendicularly to the mainstream, than vertical flows. Bubbles concentrated neat the upper wall of a horizontal system by buoyancy disturbs heat exchanges between liquid–phase and the wall, and contributes hardly to mass transfer in the systems. However, the bubbles injected into a horizontal flow can modify and control efficiently a turbulent boundary layer formed beneath a horizontal flat wall because the congregated bubbles near the wall.

How do bubbles behave within the boundary layer near a wall and how do these bubbles modify the boundary layer? These questions are critical issues on the boundary layer control using bubbles. First of all, we review previous researches for behaviors of bubbles in a flow. For considering simply the behaviors, we classify them by number of bubbles; a case of a single bubble and a case of more than two bubbles. In the case of a single bubble, behavior of the bubble changes mainly according to Weber number and Reynolds number of the bubble (Bhaga and Weber, 1981; Ryskin and Leal, 1984). Even in the simplest case that a single bubble is rising up in still liquid–phase by its buoyancy, its rising velocity, shape and moving line are dependency on its size. In the case of more than two bubbles, the behavior becomes more complex. Sometimes the bubbles approach to each other by the mutual interactions and make a bubble cluster. Floating bubbles in still liquid–phase are arranged horizontally or vertically by the bubble–bubble interaction (Kitagawa et al., 2004; Takagi and Matsumoto, 2011). In some cases of horizontal bubbly flows, small bubbles are congregated at ejection region between two streamwise vortices and form bubble chains arranged in the streamwise direction (Nierhaus et al., 2007; Harleman et al., 2011). And Murai (2014) reported several types of bubble cluster according to void fraction in the horizontal bubbly flows and Reynolds number defined by a height of channel. Furthermore, using simulations for turbulent bubbly Taylor–Couette flows, Chouippe et al. (2014) showed that bubbles are congregated near the inner wall or quasi-uniformly dispersed in the whole region according to

interactions among three factors, which are Reynolds number of the Taylor–Couette flows, size of bubbles and their buoyancy. Summarizing these researches, the behaviors are affected by several parameters associated the flows.

Next, we review previous researches for effects of bubbles in boundary layer on a flow. The effects are classified into two categories, static effects and dynamic effects. The static effects usually caused by relatively small bubbles comparing with thickness of boundary layers are characterized by modifications of fluid properties such as decreased average density and increased effective viscosity (Einstein, 1906; Rust and Manga, 2002; Murai et al., 2008). The dynamic effects are induced by modification of vertical flow structures, such as streamwise vortices, in turbulent boundary layers by fragmentation and deformation of bubbles. Reynolds shear stress that dominates skin frictional drag in the turbulent flows is reduced by injected bubbles, because the bubbles reduce turbulent energy and modify the components of velocity fluctuations (Meng and Uhlman, 1989; Kawamura and Kodama, 2002; Xu et al., 2002; Kitagawa et al., 2005). Considering not only bubbles but also air film, we can consider separation effects by the air film. The air film separates liquid–phase of the flows and the solid wall by locating between them, and interrupts the momentum transfer from the flows to the wall (Fukuda et al., 2000; Mäkiharju et al., 2013). Murai (2014) summarized effects by bubble injection on the flow and its conduciveness on the drag reduction at his review paper and made a map of main effect of bubbles according into a flow speed and a bubble size. However, unfortunately this transition map is not perfect because the effect and its conduciveness are influenced by other factors such as void fraction (Ceccio, 2010), wall roughness (van den Berg et al., 2007) and entrance distance from a bubble injector (Murai et al., 2006; Hara et al., 2011).

1.2 Problems on bubbly drag reduction and its solution on the thesis

Frictional drag reduction by bubble injection has been researched in over 40 years. Recently, some researchers performed experiments using real ships (Kodama et al., 2008; Kumagi et al., 2015) and some shipbuilding companies have tried to adopt it to operating ships (Mizokami et al., 2013; Jang et al., 2014). In spite of these, it is not actively engaged now in the industrial fields. According to a review paper (Ceccio, 2010), clout of bubbles to the boundary layer is determined generally by void fraction in the layer. For example, high void fractions which reach 40% can reduce frictional drag approximately 80% (Madavan et al., 1984) but too much low void fractions cannot reduce the drag. Summarizing these, we obtain a tendency indicated as a black solid line in **Figure 1.1**. In a case of drag reduction by traditional bubble injection, we have to inject void fraction more than critical void fraction ($\alpha_{\mathrm{critical}}$) into the boundary layer to obtain positive drag reduction rates. Therefore maintaining high void fractions is required to get good controllability of the boundary

layer. Unfortunately, a lot of energy for injecting bubbles into the boundary layer is required to maintain high void fractions and sometimes it is too much high cost comparing with benefits achieved from the boundary layer control (Kodama et al., 2008; Murai 2014). It is one of reasons why the boundary layer control by bubble injection is not adopted yet in the industrial fields. Another reason is a low reproducibility of the control (Ceccio, 2010). The bubbles change perpetually their behaviors and do not reach at a stable condition when they are traveling in the boundary layer because of the mutual interactions. As a result, if initial conditions determined when bubbles are injected into a flow are set as the same, results obtained by experiments are changed according to experimental facility.

In this thesis, repetitive bubble injection (RBI) is examined to solve these problems. This RBI is designed to use air resource efficiently to maintain high void fractions locally and avoid low void fractions which have bad controllability of the boundary layer. To explain concept of RBI, schematic diagrams of bubble distribution injected by traditional bubble injection and RBI are shown in **Figure 1.2**. Assuming that **Figure 1.2**(a) and (b) indicate bubbles with a lower and a higher void fractions than $\alpha_{\mathrm{critical}}$, drag reduction rate will be negative in the case of (a) and positive in the case of (b), respectively. **Figure 1.2**(c) shows a case of RBI, where bubble swarms generated by RBI have the same void fraction in the case of (b) and void fraction averaged in temporal domain is the same as that in the case of (a). Here, we can classify void fraction in the case of RBI as the void fraction on bubble swarms and the time-averaged void fraction, and they are designated by local void fraction (α_{RBI}) and mean void fraction (α_{mean}), respectively. Assuming drag reduction rate only depends on local void fraction and the high void fraction is maintained in the whole region on the bubble swarms, drag reduction rate will be located on a black dashed line in **Figure 1.1**. As a result, although a mean void fraction is low, a positive drag reduction rate is maintained by RBI. Furthermore, it is expected that conditions of the bubbles injected by the RBI are maintained statistically at the same phase of the injection period because the RBI generates artificially periodic voidage wave with high fluctuations. The clout to the boundary layer may be more strongly exerted by the high fluctuations of the void fraction because of a non-linear relationship between the clout and the void fraction (Oishi et al., 2009). If the clout promoted by the high fluctuations caused by RBI, drag reduction rate with RBI becomes higher than values on the black dashed line in **Figure 1.1**. Consequently, the RBI has potentials to enhance efficiency of the boundary layer control and reproducibility of phenomena. In this thesis, the RBI is performed in horizontal channel flows and at model ship experiments. Considering many previous research articles associated to our questions mentioned in the **Subsection 1.1.2**, evaluation of bubbly flows requires multiple investigations for several parameters associated the flows and effects of bubbles on the flows. Therefore, we estimate variable information for bubble swarms generated by the RBI in turbulent flows such as behaviors of bubble swarms and their effects on wall friction and the

flow. Also, for the investigation, measurement methodologies for the boundary layer on bubbly flows are introduced, developed and used complexly at the experiments.

1.3 Research purpose in each chapter

This theses consists of seven chapters, which are introduction of the study, five individual researches and conclusion of the study, respectively. Each chapter which introduces the researches has an individual introduction and an individual conclusion. Purpose of the research in each chapter are described as follows.

For the first step, in the **Chapter 2**, we estimate behaviors of bubbles traveling beneath a bottom plate of the model ship. RBI is designed for using a clustering of bubbles traveling in a turbulent boundary layer and a non-linearity between void fraction and wall friction. Unfortunately these two phenomena cannot be assured in external flows because the previous experiments associated with these two phenomena performed at turbulent flows with closed system (Nierhaus et al., 2007; Oishi et al., 2009; Harleman et al., 2011; Chouippe et al., 2014; Murai et al., 2014). The closed system may play important role on creation of the voidage wave. Therefore, evaluation of this in an open flow system is required and we perform model ship experiments for investigating behaviors of bubbles traveling beneath the ship bottom. It is expected that these bubbles are in relatively similar conditions as that of real ships comparing with the laboratory model experiments.

In the **Chapter 3**, an interaction between the bubble swarm and vortical structures in a turbulent boundary layer is estimated at a turbulent channel flow by a visualization with flakes particles and two different color laser sheets. Bubbles injected into the turbulent boundary layer affect streamwise vortices located in the same layer and modify wall friction (Lu et al., 2005). It is expected that a similar effect on the streamwise vortices occurs when the bubble swarm is passing through the channel. Estimation using visualized structures allows deepen understanding about effects on the turbulent boundary layer caused by RBI.

In the **Chapter 4**, effects on the turbulent boundary layer caused by RBI are investigated by several experimental instruments, which are a shear sensor mounted at the upper wall and two ultrasonic velocity profilers (UVP), at the horizontal rectangular channel employed in the **Chapter 3**. Experimental results are evaluated by statistical analysis to ensure reproducibility of the effects caused by RBI. By summarizing and comparing experimental results, e.g. modified wall sear stress, velocity vector fields in liquid–phase and vortical structures, it is expected that we can grasp mechanism of drag reduction caused by RBI.

Variation of void fraction in the whole region of a system such as channels and ship bottoms is required to control parameters of RBI for effective use. In the industrial fields, it is hard to get the variation in the whole region by measurements considering high cost for the measurements.

Therefore, we have to predict spatial and temporal variation of void fraction in the whole region of the system using measurement data obtained from few places. In the **Chapter 5**, we try to establish a simple model for transition of the voidage wave. To establish it, the transition in turbulent channel flows is evaluated using statistical analysis.

To use the prediction method of the transition, mentioned in the **Chapter 5**, at a ship, measurement instrument which endures physical damage by strong shear of a flow beneath the ship bottom is required for measurements in a real situation. Therefore, in the **Chapter 6**, ultrasonic echography with a high durability is developed for adopting at ships by processing echo signal obtained from UVP. UVP is suitable for measuring velocity profile of flows in real situations, such as river, because of its simplicity of installation and high durability (Takeda, 2012). By measuring bubbles using the echo signal, it is expected that we can monitor voidage wave and velocity profile in liquid–phase, simultaneously, beneath the ship bottom using a single ultrasonic measurement setup.

Finally, in the **Chapter 7**, we review contents in each chapter and summarizes conclusions of this thesis.

• Nomenclature and units

$\alpha_{critical}$ critical coefficient, dimensionless

α_{mean} mean void fraction, dimensionless

α_{RBI} local void fraction on bubble swarms generated by repetitive bubble injection, dimensionless

• References

Baron A. and Quadrio M., 1996. Turbulent drag reduction by spanwise wall oscillations, *Appl. Sci. Res.* **55**, 311–326.

van den Berg T.H., van Gils D.P.M., Lathrop D.P. and Lohse D., 2007. Bubbly turbulent drag reduction is a boundary layer effect, *Phys. Rev. Lett.* **98**, 084501.

Berger T.W., Kim J., Lee C. and Lim J., 2000. Turbulent boundary layer control utilizing the Lorentz force, *Phys. Fluids* **12**, 631–649.

Bhaga D. and Weber M.E., 1981. Bubbles in viscous liquids: shapes, wakes and velocities, *J. Fluid Mech.* **105**, 61–85.

Brücker C., 1999. Structure and dynamics of the wake of bubbles and its relevance for bubble interaction, *Phys. Fluids* **11**, 1781–1796.

Bushnell D.M., 1991. Drag reduction in nature, *Annu. Rev. Fluid Mech.* **23**, 65–79.

Ceccio S.L., 2010. Frictional drag reduction of external flow with bubble and gas injection, *Annu. Rev. Fluid Mech.* **42**, 183–203.

Chouippe A., Climent E., Legendre D. and Gabillet C., 2014. Numerical simulation of bubble dispersion in turbulent Taylor–Couette flow, *Phys. Fluids* **26**, 043304.

Einstein A., 1906. Eine neue bestimmung der moleküldimensionen, *Ann. Phys.* **324**, 289–306.

Endo T., Kasagi N. and Suzuki Y., 2000. Feedback control of wall turbulence with wall deformation, *Int. J. Heat and Fluid Flow* **21**, 568–575.

Englar R.J. and Huson G., 1984. Development of advanced circulation control wing high-lift airfoils, *J. Aircraft* **21**, 476–483.

Fujiwara A., Danmoto Y., Hishida K. and Maeda M., 2004. Bubble deformation and flow structure measured by double shadow images and PIV/LIF, *Exp. Fluids* **36**, 157–165.

Fukagata K., Kasagi N. and Koumoutsakos P., 2006. A theoretical prediction of friction drag reduction in turbulent flow by superhydrophobic surfaces, *Phys. Fluids* **18**, 051703.

Fukuda K., Tokunaga J., Nobunaga T., Nakatani T. and Iwasaki T., 2000. Frictional drag reduction with air lubricant over a super-water-repellent surface, *J. Mar. Sci. Technol.* **5**, 123–130.

Glezer A. and Amitay M., 2002. Synthetic jets, *Annu. Rev. Fluid Mech.* **34**, 503–529.

Hahn S., Je J. and Choi H., 2002. Direct numerical simulation of turbulent channel flow with permeable walls, *J. Fluid Mech.* **450**, 259–285.

Hara K., Suzuki T. and Yamamoto F., 2011. Image analysis applied to study on frictional drag reduction by electrolytic microbubbles in a turbulent channel flow, *Exp. Fluids* **50**, 715–727.

Harleman M.J.W., Delfos R., Terwisga T.J.C.V. and Westerweel J., 2011. Dispersion of bubbles in fully developed channel flow, *J. Phys.: Conf. Ser.* **318**, 052007.

Hibiki T. and Ishii M., 2002. Interfacial area concentration of bubbly flow systems, *Chem. Eng. Sci.* **57**, 3967–3977.

Jang J., Choi S.H., Ahn S., Kim B. and Seo J.S., 2014. Experimental investigation of frictional resistance reduction with air layer on the hull bottom of a ship. *Int. J. Nav. Archit. Ocean Eng.* **6**, 363–379.

Kamp A.M., Chesters A.K. and Colin C., 2001. Bubble coalescence in turbulent flows: a mechanistic model for turbulence-induced coalescence applied to microgravity bubbly pipe flow, *Int. J. Multiphase Flow* **27**, 1363–1396.

Kawamura T. and Kodama Y., 2002. Numerical simulation method to resolve interaction between bubbles and turbulence, *Int. J. Heat Fluid Flow* **26**, 627–638.

Kitagawa A., Sugiyama K. and Murai Y., 2004. Experimental detection of bubble-bubble interactions in a wall-sliding bubble swarm, *Int. J. Multiphase Flow* **30**, 1213–1234.

Kitagawa A., Hishida K. and Kodama Y., 2005. Flow structure of microbubble-laden turbulent channel flow measured by PIV combined with the shadow image technique, *Exp. Fluids* **38**, 466–475.

Kodama Y., Hinatsu M., Hori T., Kawashima H., Takeshi H., Makino M., Ohnawa M., Sanada Y., Murai Y. and Ohta S., 2008. A full-Scale air lubrication experiment using a large cement carrier for energy saving (Result and analysis). *Jpn. Soc. Naval Architects Ocean Eng.*, 163–166, (in Japanese).

Kumagai I., Takahashi Y. and Murai Y., 2015. A new power-saving device for air bubble generation using a hydrofoil for reducing ship drag: theory, experiments, and applications to ships, *Ocean Eng.* **95**, 183–194.

Lin J.C., Robinson S.K., McGhee R.J. and Valarezo W.O., 1994. Separation control on high-lift airfoils via micro-vortex generators, *J. Aircraft* **31**, 1317–1323.

Lu J., Fernandez A. and Tryggvason G., 2005. The effect of bubbles on the wall drag in a turbulent channel flow, *Phys. Fluids* **17**, 095102.

Madavan N.K., Deutsch S. and Merkle C.L., 1984. Reduction of turbulent skin friction by microbubbles, *Phys. Fluids* **27**, 356–363.

Mäkiharju S.A., Elbing B.R., Wiggins A., Schinasi S., Vanden-Broeck J.-M., Perlin M., Dowling D.R. and Ceccio S.L., 2013. On the scaling of air entrainment from a ventilated partial cavity, *J. Fluid Mech.* **732**, 47–76.

McCormick M.E. and Bhattacharyya R., 1973. Drag reduction of a submersible hull by electrolysis, *Nav. Eng. J.* **85**, 11–16.

Meng J.C.S. and Uhlman Jr. J.S., 1989. Microbubble formulation and splitting in a turbulent boundary layer for turbulence reduction. in: advances in fluid dynamics. *Springer*; New York, 168–217.

Mizokami S., Kawakado M., Kawano M., Hasegawa T. and Hirakawa I., 2013. Implementation of ship energy-saving operations with Mitsubishi air lubrication system, *MHI. Technical Review* **50**, 44–49.

Murai Y., Oishi Y., Takeda Y. and Yamamoto F., 2006. Turbulent shear stress profiles in a bubbly channel flow assessed by particle tracking velocimetry, *Exp. Fluids* **41**, 343–352.

Murai Y., Oiwa H. and Takeda Y., 2008. Frictional drag reduction in bubbly Couette-Taylor flow, *Phys. Fluids* **20**, 034101.

Murai Y., 2014. Frictional drag reduction by bubble injection, *Exp. Fluids* **55**, 1733.

Nierhaus T., Vanden Abeele D. and Deconinck H., 2007. Direct numerical simulation of bubbly flow in the turbulent boundary layer of a horizontal parallel plate electrochemical reactor, *Int. J. Heat Fluid Flow* **28**, 542–551.

Ohlendorf D., Interthal W. and Hoffman H., 1986. Surfaetant systems for drag reduction: physico-chemical properties and rheological behavior, *Rheol. Acta* **25**, 468–486.

Oishi Y., Murai Y., Tasaka Y. and Takeda Y., 2009. Frictional drag reduction by wavy advection of deformation bubbles, *J. Phys.: Conf. Ser.* **147**, 012020.

Roupassov D.V., Nikipelv A.A, Nudnova M.M. and Starikovskii A.Y., 2009. Flow separation control by plasma actuator with nanosecond pulsed-periodic discharge, *AIAA J.* **47**, 168–185.

Rust A.C. and Manga, M., 2002. Effects of bubble deformation on the viscosity of dilute suspensions. *J. Non-Newtonian Fluid Mech.* **104**, 53–63.

Ryskin G. and Leal L.G., 1984. Numerical solution of free-boundary problems in fluid mechanics. Part 2. Buoyancy-driven motion of a gas bubble through a quiescent liquid, *J. Fluid Mech.* **148**, 19–35.

Sugiyama K., Takagi S. and Matsumoto Y., 2001. Multi-scale analysis of bubbly flow, *Comput. Methods Appl. Mech. Eng.* **191**, 689–704.

Takagi S. and Matsumoto Y., 2011. Surfactant effects on bubble motion and bubbly flows, *Annu. Rev. Fluid Mech.* **43**, 615–636.

Takeda Y. (Ed.), 2012. Ultrasonic Doppler velocity profiler for fluid flow, *Springer*; Japan.

den Toonder J.M.J., Hulsen M.A., Kuiken G.D.C. and Nieuwstadt F.T.M, 1997. Drag reduction by polymer additives in a turbulent pipe flow: numerical and laboratory experiments, *J. Fluid Mech.* **337**, 193–231.

Walsh M.J., 1983. Riblets as a viscous drag reduction technique, *AIAA J.* **21**, 485–486.

Xu J., Maxey M.R. and Karniadakis G.E.M., 2002. Numerical simulation of turbulent drag reduction using micro-bubbles, *J. Fluid Mech.* **468**, 271–281.

- **Tables**

Table 1.1 Classification of drag reduction techniques.

Passive controls	*Active controls*	*Additive controls*
Riblet	Deformation wall	Polymer injection
Compliant surface	Wall oscillation	Surfactant injection
Super-hydrophobic surface	Lorentz force	Bubble injection

- **Figures**

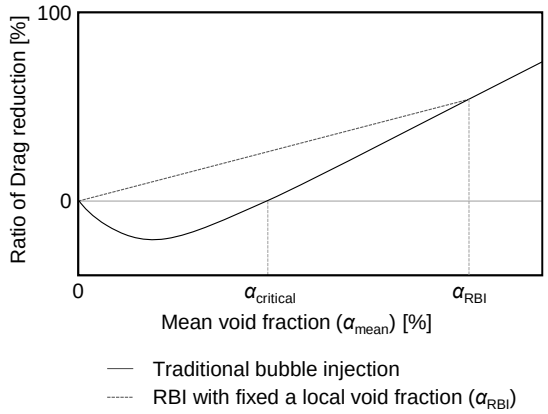

Figure 1.1 Schematic representations of drag reduction by bubble injection parameterized in terms of mean void fraction, where a gray solid line indicates values with no drag reduction, $\alpha_{\mathrm{critical}}$ is the critical void fraction required to obtain drag reduction with traditional bubble injection and RBI is designed based on the traditional bubble injection with a void fraction α_{RBI}.

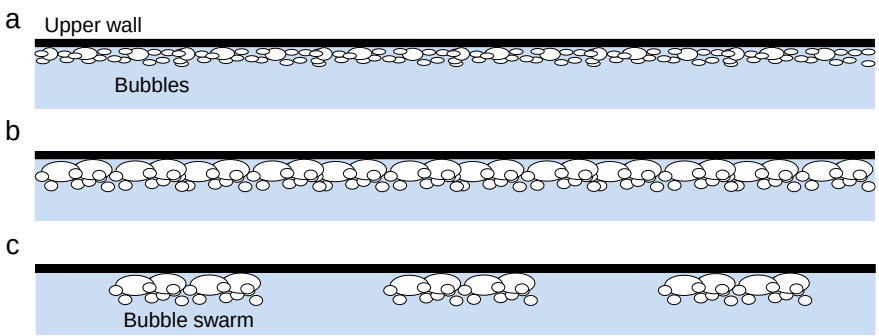

Figure 1.2 Schematic diagrams of bubble distribution injected by traditional injection and RBI; (a) traditional injection with a low void fraction, (b) traditional injection with a high void fraction and (c) RBI, where bubble swarms generated by RBI maintain the same void fraction in the case of (b) and void fraction averaged in temporal domain is also the same as that in the case of (a).

2 Behaviors of bubbles traveling in a turbulent boundary layer on a flat plate

- **Preface**

We propose repetitive bubble injection, which was suggested in the **Chapter 1** to promote efficient drag reduction based on the premise that bubbles traveling in a turbulent boundary layer generate bubble clusters, i.e., a voidage wave. Almost all previous reports mentioning about the bubble clusters or voidage wave describe experiments performed in closed systems. Because the closed system may play a significant role in creating the voidage waves, we cannot be assured of the existence of voidage waves in external flows. Therefore, in this chapter, we describe model ship experiments to investigate the behavior of bubbles passing underneath the hull of a ship an open system.

2.1 Introduction

Bubbly drag reduction (BDR) is a technique for reducing frictional drag by injecting bubbles in turbulent boundary layers. It has received attention as a means to decrease fuel consumption of low-speed vessels such as container ships. In academic fields, the drag reduction rate in channel flow and assessed on a real ship were reported as 80% (Madavan et al., 1984) and 10% (Kumagai et al., 2015), respectively. BDR has been adopted recently in ship design by Mitsubishi Heavy Industries (Mizokami et al., 2013); Samsung Heavy Industries is also reviewing this technique (Jang et al., 2014). Although the technique is in the optimization stage preparation for commercial use, the BDR mechanism and the behavior of bubbles skimming along a ship's hull remain unclear for two reasons. One is that it is hard to perceive how bubbles advect beneath the ship from results of laboratory model experiments, because the order of the Reynolds number in real situations is much larger than that of laboratory model experiments. The other is that the BDR mechanism and performance change depending on experimental facilities and parameters. According to a review by Ceccio (2010), even if the void fraction in experimental flows is fixed at the same value, the performance is not maintained in other experiments using different experimental facilities. Murai (2014) has reviewed much of the previous BDR researches performed over the last 40 years and, in a chart, summarized the mechanisms, which were classified by bubble sizes and main flow velocity.

In a study to understand BDR mechanisms underpinning the performance improvements, Oishi et al. (2009) discovered that bubbles injected into the turbulent boundary layer in channel flow naturally generated a voidage wave which induces fluctuations in wall shear stress. They concluded that the voidage wave possibly enhances BDR through a non-linear relationship between these fluctuations and the wave. Moreover, Murai (2014) confirmed that the bubbles traveling in turbulent channel flows form clusters, although their shapes change in the channel flow depending on the existing experimental conditions, such as void fraction and Reynolds number. The cluster creates a locally high void fraction. Specifically, the sparseness and denseness of voids are generated by the clusters in the channel flow. The inference is that the voidage wave grows as the individual bubbles cluster together. Nevertheless, these two reports did not demonstrate conclusively that voidage waves exist in general situations, because their conclusions were based on experiments performed in turbulent channel flows in a closed system that may have played a significant role in the creation of the voidage wave. Therefore, the evaluation of this aspect is required in an open flow system. Experiments on a model ship were performed to investigate the behavior of bubbles passing over its hull. With the laboratory experiments, the bubbles are assumed to be in relatively similar conditions as experienced around real ships, and hence aid our understanding of the relationship between bubble behavior and BDR.

2.2 Experimental method

2.2.1 Experimental facility

To analyze the formation of voidage waves and BDR performance, experiments using a model ship were designed to incorporate an ultrasonic bubble measurement system. The experiments were performed at a towing tank facility in Hiroshima University. **Table 2.1** lists various system parameter settings of the experimental facility. Temperature, density (ρ_l), viscosity (ν), surface tension (σ), and speed of sound (c) of water in the towing tank are 29.8°C, 996 kg/m^3, 8.47×10^{-7} m^2/s, 71.2×10^{-3} N/m and 1507 m/s, respectively. Schematic diagrams of the model ship are shown in **Figure 2.1**. The model ship made of transparent acrylic resin is 4000 mm in overall length (L), 600 mm in width (W), and 500 mm in height (H). The x, y, and z coordinates are defined respectively as the streamwise distance from the leading edge, vertical position from the bottom plate, and spanwise position from the center of the ship. To avoid influences of the wave generated by the prow, two side walls reaching 20 mm up from the bottom plate are installed as seen in **Figure 2.1**(c). To simulate a boundary layer on a flat plate, the ship hull is shaped as a flat plate and the leading edge of the plate and the two side walls were beveled with 45° angles. Bubbles are introduced into the boundary layer using an air injector 0.7 m from the leading edge. Air is introduced into a buffer chamber of total volume 5.0×10^{-3} m^3 by a compressor and an air flow control system, and subsequently injected into the boundary layer through an injection plate having 42 holes of 5 mm diameter (see **Figure 2.1**(d)). A servo valve in the system is controlled automatically by a PC to supply air with a stable constant flow rate (see **Figure 2.2**). Shear stress sensors and ultrasonic transducers, installed at three points, 1.1 m, 2.3 m and 3.5 m from the edge and labeled according to locations as front, middle, and rear, respectively. From experience, the same type of sensor is used as in a previous study (Kodama et al., 2000) to estimate the wall shear stress with bubbly two-phase flows. Signals from both the shear sensors and air-flow control system and the velocity of the towing train are recorded by a data logger (see **Figure 2.2**). The air-flow control system is a smaller design of Takeuchi and Kagawa's system (2013). To detect and characterize bubbles, an ultrasonic transducer is mounted inside the bottom wall with a silt angle of θ = 8° to the vertical direction and located at approximately 28 mm away from the shear sensor. On the ship's hull, the distance between the shear sensor and the ultrasonic pulse emitted from the transducer is 25 mm. A cavity on the front space of the transducer is filled with refractive index matching material to prevent ultrasonic echoes from the bottom plate (see **Figure 2.1**(e)). Each transducer is connected in parallel with a pulse generator and another data logger of higher sampling frequency. The data logger records electrical signals with a maximum temporal resolution of 100 MHz, and is employed to obtain the instantaneous ultrasonic echo distribution without averaging. These instruments are for echography to analyze bubble shape in the vertical direction.

Shear stress sensors and data loggers are synchronized by a trigger in the measurement system (see **Figure 2.2**). **Table 2.2** lists the parameter settings for the instrument. Shear stress measurements were performed in 7.00 s because the towing train maintains the maximum setting speed in approximately 7.00 s. The data logger records the echo four times for 330 ms, when the shear sensor is operating because of memory capacity constraints. Also, two cameras are installed in the model ship to visualize bubbles passing underneath the hull. One is mounted above the hull and the other is underneath the leading edge in the water (see **Figure 2.1**(b)).

2.2.2 Boundary layer characteristics of the model ship

Figure 2.3(a) shows that the wall shear stress (τ_s) in single-phase flows rises with towing speeds (U_{main}); the same trend was reported in a previous study using a flat plate towed in a tank (Mori et al., 2009). To confirm the characteristics of the boundary layer at the measurement points, the relationships between friction coefficient and Re_x. These dimensionless number are defined as

$$Re_x = \frac{xU_{main}}{\nu} \qquad \textbf{Equation 2.1}$$

and

$$C_f = \frac{2\tau_s}{\rho_l U_{main}^{\ 2}}, \qquad \textbf{Equation 2.2}$$

and plotted for the model ship as shown in **Figure 2.3**(b). Each line in the figure plots the Blasius friction law for laminar flows and the empirical friction coefficient for turbulent flows reported by Schlichting (1979). The corresponding formula for the curves are respectively,

$$C_f = \frac{1.328}{\sqrt{Re_x}} \qquad \textbf{Equation 2.3}$$

and

$$\frac{e^{\frac{0.558}{\sqrt{C_f}}}}{C_f} = Re_x . \qquad \textbf{Equation 2.4}$$

The plots confirm that flows in the boundary layer of the model ship are turbulent when $Re_x > 2.0\times10^6$.

2.2.3 Experimental conditions

For the experimental conditions (listed in **Table 2.3**), a range of U_{main} between 2.00–3.00 m/s is prescribed to maintain a turbulent boundary layer at all measurement regions; also, the air-flow rate (Q_{g}) is regulated for six settings in the range 0.42×10^{-3}–2.5×10^{-3} m^3/s. The void fraction in the turbulent boundary layer is determined from

$$\alpha_\delta = \frac{Q_{\mathrm{g}}}{Q_{\mathrm{l}}+Q_{\mathrm{g}}} \approx \frac{Q_{\mathrm{g}}}{W\int_0^{\delta_x} u_y dy} \approx \frac{Q_{\mathrm{g}}}{W\int_0^{\delta_x} U_{\mathrm{main}}\left(\frac{y}{\delta_x}\right)^{\frac{1}{7}} dy}, \qquad \textbf{Equation 2.5}$$

where it is assumed that the velocity distribution (u_y) in the turbulent boundary layer is not modified by the presence of bubbles. Although U_{main} and Q_{g} are fixed, α_δ decreases in the downstream regions because the boundary layer thickness (δ_x), defined as

$$\delta_x = 0.37x^{\frac{4}{5}}\left(\frac{\nu}{U_{\mathrm{main}}}\right)^{\frac{1}{5}} \qquad \textbf{Equation 2.6}$$

becomes large as x increases.

2.3 Results and discussions

2.3.1 Conditions of bubble migration beneath the ship bottom

To begin, from optical visualizations, we shall confirm the behaviors of the bubbles passing underneath the hull. **Figure 2.4** shows snapshot of the bubbles taken by the camera located near the middle region, $x \approx 2.1$ m. The bubbles become smaller with faster U_{main}, because shear in the turbulent boundary layer becomes stronger. Also, when the air-flow rate, i.e., void fraction, is larger, bubbles coalesce and become larger. Finally, almost the entire area under the ship's hull is covered with large bubbles. To estimate the characteristics of these bubbles, we analyzed them statistically focusing on specific characteristics of single bubbles.

2.3.1.1 Statistical conditions of the bubbles

Figure 2.5 shows the averaged advection velocity (u_{b}) of the bubbles obtained from the images taken by the camera mounted above the hull, where error bars indicate standard deviations. The values of u_{b} take almost half the values of U_{mian} for all experimental conditions; this trend was found in previous research in a study involving a real ship (Johansen el al., 2010). The reason is because the bubbles are located near the wall. From **Equation 2.5**, u_{b} takes a low streamwise

velocity near the wall region. As a result, the bubbles decelerate because of this low velocity in the liquid–phase. At each condition, u_b maintains its value in the middle and at the rear regions, suggesting that bubbly flow beneath the hull is fully developed until reaching the middle region.

The bubbles with high Q_g become films of air which cannot maintain a circular shape. The behavior of these bubbles is hard to estimate because of their wide extent in images and ill-defined shape. Therefore, we estimated statistically the conditions of bubbles with $Q_g \approx 0.42\times10^{-3}$ m^3/s at $x \approx 3.3$ m by focusing on small bubbles having relatively circular shapes and being in the most developed flow in the three measurement regions. As shown in **Figure 2.6**, images of these small bubbles were binarized, and their coordinates for the center of mass and equivalent diameters (d_e) were calculated from these binary images. **Figure 2.7** shows the variation in the probability distributions of d_e; very small bubbles, $d_e < 1.0$ mm, were neglected because these bubbles are indistinguishable from noises generated from binarization during image processing. Statistically the bubbles were confirmed to become smaller in size as U_{main} increases. The justification is two-fold. One is that shear stress in the boundary layer is strengthened as U_{main} increases because bubbles with shear stress in the liquid–phase are fragmented. The other is that void fraction decreases, such as α_δ. Under the experimental conditions, Q_g is fixed although U_{main} increases. In **Figure 2.4**, we find bubble clusters composed of smaller bubbles locating close together. For confirmation, the estimated distances between the centers of two bubbles located at the closest distance are calculated; the results are summarized in **Figure 2.8**. Gray lines in the figure indicate the distance between bubbles when they are realigned to have the same distance; distributions of the distances are located on the left-hand side of the gray lines. Also the directions to the center of the closest bubble are calculated and summarized in **Figure 2.9**. These methods were introduced by Kitagawa et al. (2004) to estimate a structure for the bubble cluster. Considering the bubble sizes shown in **Figure 2.7**, the closest distance distributions mean that almost all bubbles have neighboring bubbles located very close by or in contact. Consequently, it is confirmed that the bubbles make clusters comprising more than two bubbles. A numerical simulation performed by Nierhaus et al. (2007) showed that tiny bubbles in a turbulent boundary layer tend to cluster along the coherent structures in the layer. Harleman et al. (2011) explained that these tiny bubbles are captured by ejections between two streamwise vortices and arranged on low-speed streaks. In the present experiments, although they are arranged closely and make a cluster, the direction that bubbles are arranged is not restricted because bubble sizes are much larger than the width of the streamwise vortices in the turbulent boundary layer. Considering that the width of low-speed streaks is 100 times the friction length (l_τ) (Smith and Metzler, 1983; Zacksenhouse et al., 2001) and assuming that the width of streamwise vortices is the same as the width of low-speed streaks, streaks and vortices in turbulent boundary layers are strongly coupled in a process termed a self-sustaining cycle (Hamilton et al., 1995). Here, l_τ is defined as

$$l_\tau = \frac{\nu\sqrt{\rho}}{\sqrt{\tau_s}} \,. \qquad \textbf{Equation 2.7}$$

The width of streamwise vortices in the rear region is approximately 0.7–1.0 mm when U_{main} is in the range 2.00–3.00 m/s. Hence, d_{e} beneath the hull is approximately 3–4 times longer than the width of the streamwise vortices and the bubbles lie on several streamwise vortices. As a result, the bubbles are not captured by the ejection of streamwise vortices. Recently, Murai (2014) reported that a variety of shapes for bubble clusters exists in turbulent channel flows, a depending on void fraction and Reynolds number. Therefore, although the shapes of clusters are basically maintained in these experiments, it is possible that the shape changes when experimental conditions are changed.

2.3.1.2 Deformation of a single bubble

We focus next on the behavior of a single bubble that is not a member of a bubble cluster. When a bubble is subject to an external force, such as shear stress in the turbulent boundary layer, the bubble resonates in a manner dependent on the external force and its surface tension. The resonance frequency (f_n) of the bubble is given by

$$f_n = \frac{1}{2\pi}\sqrt{\frac{8n(n+1)(n-1)(n+2)\sigma}{\left((n+1)\rho_{\mathrm{l}} + n\rho_{\mathrm{g}}\right)d_{\mathrm{e}}^{\,3}}} \approx \frac{1}{\pi}\sqrt{\frac{2n(n-1)(n+2)\sigma}{\rho_{\mathrm{l}} d_{\mathrm{e}}^{\,3}}} \qquad \textbf{Equation 2.8}$$

where n and ρ_{g} are the shape mode number and bubble density, respectively (Lamb, 1932). **Figure 2.10** shows diagrams of various mode shapes for a resonating bubble. A fluid with small bubbles has viscoelastic characteristics derived by the elastic force acting on the bubbles, i.e., surface tension. In this situation, the effective viscosity should be considered (Frankel and Acrivos, 1970; Rust and Manga, 2002). If bubbles passing underneath the hull resonate by shear stress of the fluid in the turbulent boundary layer, the bubbles modify the viscosity of the fluid. To estimate the resonances of bubbles, we analyzed two bubbles of different sizes, $d_{\mathrm{e}} \approx 2.6$ mm and 4.6 mm, under experimental conditions of $U_{\mathrm{main}} = 3.00$ m/s and $Q_{\mathrm{g}} \approx 0.42\times10^{-3}$ m^3/s. The bubbles were taken near the rear region, $x \approx 3.3$ m. These sizes were the more prevalent and relatively larger size given the conditions (see **Figure 2.8**). When the shape of the bubble is stretched under shearing, large and small alterations in shape produce different effects on the viscosity (Tasaka et al., 2015). These effects are possible to estimate using the two different bubble sizes because they have different amounts of deformation arising from the different ratios between surface tension and shear. **Figure 2.11** shows temporal variations of each bubble deformation. For the large bubble, capillary waves are observed suggesting that a thin liquid film exists above it. First, as shown in **Figure 2.12**, the

angular variation in radius ($r(\theta_b)$) of the bubble as a function of angle (θ_b) is obtained from **Figure 2.11**, for the wave-number analysis of the shape deformation. Here $r(\theta_b)$ and θ_b are based on the center of mass obtained from the bubble image and the streamwise direction, respectively. Second, $r(\theta_b)$ at each time step is analyzed using Fourier analysis and the averaged amplitudes of the vibration for the bubble radius of each mode n are taken and shown in **Figure 2.13**; here the amplitude is normalized using a half of d_e and the error bars are standard deviations. The smaller bubble ($d_e \approx 2.6$ mm) has only one dominant mode, $n = 2$. In contrast, the larger bubble has two dominant modes, $n = 2$ and 3. Finally, we investigated the frequency of vibration for the dominant modes on each bubble using the two-dimensional Fourier transform for θ_b and time. If the surface of the bubbles vibrates at frequency f_n for the dominant modes, then a single external force, i.e., the shear is mainly involved. The f_n for each n are summarized in **Table 2.4** and results of the Fourier transform analysis are presented in **Figure 2.14**. In the figure, the resolution of the frequency is 31.25 Hz. For the smaller bubble ($d_e \approx 2.6$ mm), a single peak occurs at 62.50 Hz in $n = 2$. Although the resolution is low, this frequency has too large a gap to f_n, 81 Hz at $n = 2$. Furthermore, for the large bubble, peaks in the frequency at the dominant modes cover a wide band in the frequency from 31.25–62.50 Hz. This suggests that the shape of bubbles is not altered by a single external force, but by several external forces such as forces from vortices in the turbulent boundary layer.

2.3.1.3 Naturally generated voidage wave

In the previous **Subsubsection 2.3.1.1**, the existence of a cluster of bubbles is predicted from a statistical analysis. If the cluster is generated according to a specific rule, the clusters are arranged regularly in space and time, and a certain frequency is observed in the voidage wave. At first, to confirm the existence of the bubble cluster visually, we take line scan images of snapshots taken by the underwater camera at $x \approx 3.7$ m (see **Figure 2.15**). **Figure 2.16** gives typical examples of these images with $U_{main} = 3.00$ m/s and several Q_g. Bubble clusters with lateral waves can be seen in these sample images. To check whether a rule exists, voidage waves obtained from the images are Fourier analyzed with the results summarized in **Figure 2.17**, where values of the linear spectra are normalized by the maximum brightness of the line scan images. For $Q_g \approx 1.67\times10^{-3}$ m^3/s and 2.50×10^{-3} m^3/s, peak frequencies exist in the range 3 Hz < f_{void} < 8 Hz with specific tendencies. One is that they are shifted to higher frequencies when U_{main} increases. If the cluster maintains the same spatial structures regardless of U_{main}, the peak frequencies shift proportionately to higher frequencies. The results of the frequency analysis show that the shift in the peaks obeys this assumption. Another tendency is that the peaks are shifted to lower frequencies when Q_g increases. Fi one assumes that the cluster combines with other clusters because of an excessive void fraction, it becomes a spatially large cluster a resulting in lower frequencies. Even if a peak does not appear

in a frequency analysis, the cluster exists (see **Figure 2.16**(a) and **Figure 2.17**(h)), implying that the cluster is randomly generated and passing beneath the ship's hull in these conditions.

Two possible reasons are suggested for the appearance of these peaks. One is that the clusters are generated naturally and grow into a regular spatial structure when the bubbles are transported by the turbulent boundary layer. The other is that flow instabilities occur when air passes through the holes of the injector (e.g. Plateau–Rayleigh instability and instability of a jet in crossflow (Bagheri et al., 2009)). To assess the validity of these assumptions, air is injected with an artificial fluctuation generated by repetitive bubble injection (RBI); see in **Figure 2.18**. the fluctuation is controlled by the flow controller (see **Figure 2.2**). If the peak frequencies are mainly governed by the instabilities occurring at the injector, the peaks are expected to be modified by this artificial fluctuation. The base experimental conditions are selected (U_{main} = 3.00 m/s and $Q_{\mathrm{g}} \approx 1.67\times10^{-3}$ m^3/s), where the peak frequency stands out in the frequency analysis, and the RBI frequency (f_{RBI}) is fixed at 2 Hz and 4 Hz. The results of the subsequent frequency analysis of these RBI experiments are shown in **Figure 2.19**. For f_{RBI} = 2 Hz, several peaks appear in the linear spectrum. The largest peak is at $f_{\mathrm{void}} \approx 2$ Hz whereas other peaks appear at integer multiple frequencies of this peak frequency. In contrast, only one peak appears at $f_{\mathrm{void}} \approx 8$ Hz for f_{RBI} = 4 Hz. Without RBI, the peak of the linear spectrum is at $f_{\mathrm{void}} \approx 7$ Hz. When the higher artificial frequency f_{RBI} is used during air injection, the voidage wave with RBI is not mainly dominated by f_{RBI} although the peak is shifted to integer multiple frequencies of f_{RBI}. Therefore, with this consideration, voidage wave without RBI occurs by naturally, generated by bubble clusters.

2.3.2 Effects on shear stress by bubble injection

In this subsection, we discuss the effects of bubble injection on wall shear stress with U_{main} fixed at 3.00 m/s, the fastest setting for these experiments, to attain the largest wall shear stress. Assuming that the drag reduction rate (*DR*) using bubble injection is the same regardless of U_{main} for the void fraction, estimating *DR* at the fastest U_{main} is easier because the shear stress modified by the bubble injection takes its largest value. **Figure 2.20** shows *DR* at each measurement point with U_{main} = 3.00 m/s. The *DR* is determined from

$$DR = \frac{\tau_{\mathrm{s}} - \tau}{\tau_{\mathrm{s}}}, \qquad \textbf{Equation 2.9}$$

where τ_{s} and τ are the respective values of the shear stress in the single-phase flow and in an experimental condition. In the front region, *DR* is negative except for the lowest α_δ and friction increases rapidly with increasing α_δ. Contrariwise, in the middle and in the rear regions, low void fractions, α_δ < 2.0%, do not affect *DR* as much but high void fractions, α_δ > 2.0%, reduce the wall friction and *DR* is enhanced through the increase in α_δ. The trends for *DR* in the middle and in the

rear regions correspond with results of a previous reports (Ceccio, 2010). However, the trend for the *DR* at the front region is different than for the others. The assumption is that strong wall friction is caused by the air jet at the injector and the area near the injector, i.e. the front region, is significantly affected. Therefore, the BDR on a vessel in actual use should be analyzed using not only the local shear stress but also averaged shear stress over the whole area of the vessel's hull.

2.3.3 Relationship between shear stress and liquid film above traveling bubbles

In the **Subsubsection 2.3.1.2**., we confirmed the presence of a liquid film existing above a bubble. In this subsection, a relationship between the liquid film and the shear stress is assessed from ultrasonic echograms. **Figure 2.21**(a) shows a sample of raw distribution of the echo amplitude against each pulse emission in a bubbly flows with α_δ ~ 0.7% measured in the middle region. Electrical noise exists within 10.00 μs after ultrasonic pulse emission, t_f < 10.00 μs. To attenuate the noise and avoid the disturbing echo from the bubbles, the transducer was located at distance *h* away from the hull, *y* = 0 (see **Figure 2.1**(e)). Basically, ultrasound cannot pass through the bubbles and is reflected at the gas–liquid interface because of a large difference between the acoustic impedances of air and water. The echo from the bubbles appears around at t_f ~ 20.00 μs. By comparing the echo distributions in single-phase flows and bubbly flows, it is possible to detect the upper surface of the bubble and the surfaces are indicated in **Figure 2.21**(b). Here, black plots represent the echo from bubbles determined as the first peak in each ultrasonic emissions, and a gray line indicates interface of the bottom plate. The bubble size in the streamwise direction, converted using Taylor's hypothesis regarding frozen turbulence, and the thickness of the liquid film between the hull and bubbles are calculated from

$$x' = -tu_b \qquad \textbf{Equation 2.10}$$

and

$$y = t_f c \cos\theta - h, \qquad \textbf{Equation 2.11}$$

respectively; here, the respective spatial resolution is determined from

$$\Delta x' = \frac{u_b}{f_r} \approx 0.5\text{mm} \qquad \textbf{Equation 2.12}$$

and

$$\Delta y = \frac{c}{2 f_s} \approx 15\,\mu\text{m}\,. \qquad \textbf{Equation 2.13}$$

Figure 2.22 shows the detailed shapes of upper surface on advective bubbles, which are converted from **Figure 2.21**(b). Large bubbles, cf. x' ~ 30 mm or x' ~ 70 mm, have flat upper surfaces because of the upper wall and its buoyancy. Moreover, the heads of the large bubbles are raised by a lifting force, caused by their higher advection velocities than the streamwise velocity of the ambient water flow near the wall. According to the shape and lifting force, thin liquid films are generated above the advective large bubbles. In contrast, smaller bubbles, cf. x' > 120 mm, do not have thin films and maintain quasi-spherical shapes because of their surface tension. The shapes and their behaviors obtained from the echograms correspond with optical visualization results reported from a previous study (Oishi and Murai, 2014).

With the explanation of the existence of liquid films above the bubbles, the thickness of the liquid film is a particularly important factor for BDR and frictional shear stress is reduced when a thin liquid film exists (Tisné et al., 2003). **Figure 2.23** shows the averaged thickness of the liquid film and projection void fraction ($\alpha_{\text{proj.}}$), where the averaged thickness is defined by the averaged depth of the upper surface of bubbles and $\alpha_{\text{proj.}}$ is determined by bubble detected time over the total measurement duration. At the front region, the thickness is about 2 times thicker than that in other regions (see **Figure 2.23**(a)). Bubbles injected vertically from the holes in the injector float because of their buoyancy and approach the bottom wall. The thicker film at the front region indicates bubbles rising towards the hull. The liquid film thickness is not affected by Q_g and only depends on distance from the injector in these experiments. In considering these floating bubbles and *DR* at the front region, the supposition is that they affect adversely on *DR*. The $\alpha_{\text{proj.}}$ at each measurement points signifies that bubbles do not reach an equilibrium state for the model ship (see **Figure 2.23**(b)). Bubbles introduced from the injector float and disperse in the spanwise direction until reaching the middle region. Hence the liquid film thickness and $\alpha_{\text{proj.}}$ obtained at the middle region are thinner and higher than that at other regions. The $\alpha_{\text{proj.}}$ at the middle region correspond with the occupation rate of bubbles estimated from photographs, such as **Figure 2.4**. Although film thickness remains unchanged in between middle and rear regions, $\alpha_{\text{proj.}}$ decreases in this region. To maintain the total volume fraction of bubbles in all regions, the thickness of bubbles has to be larger downstream from the middle region thorough the coalescence of bubbles.

2.4 Conclusions

We investigated the behavior of bubbles injected into a turbulent boundary layer using a 4 m long model ship and evaluated BDR of its hull from these bubbles. Bubble characteristics, such as the

distributions for advection velocity, size, spatial and temporal location, void fraction, thickness of liquid film above the bubbles, and wall shear friction are obtained at three points, front, middle and rear regions of the hull using optical visualizations, echography, and shear sensors.

Initially, we observed the behavior of bubbles passing beneath the ship's hull using optical visualizations. By statistical analysis of visualized bubble images, we confirmed that the bubbles form bubble clusters with lateral wave and their advection velocity is approximately 0.5 times slower than the main flow speed (U_{main}). The clusters generate a naturally induced voidage wave by traveling with a spatially and temporally regular structure, and so the voidage wave has a tendency whereby its frequency become higher with increasing U_{main} and decreasing void fraction. Furthermore, we focused on the shape deformation of a single bubble that had not coalesced into bubble cluster, as well as a mode number (n) analysis of the shape deformation. Each bubble has dominant shape modes. Although the dominant mode is basically $n = 2$, a higher mode ($n > 2$) starts to appear when the bubble size becomes larger. The frequency of the dominant mode does not correspond with the theoretical resonance frequency and sometimes several frequencies coexist in the mode. This indicates that bubbles are deformed by several external forces. In other words, bubbles are affected by not only shear stress in the boundary layer but also vortices in the layer.

Next, the relationship between the liquid film thickness and BDR, which is hard to visualize, was investigated using echography and shear sensor data. Near the bubble injector, injected bubbles exist at a small distance from the hull of the ship, at approximately 2.0 mm, and shear stress increases slightly with bubble injection. In contrast, further downstream from the injector, the bubbles are located around 1.0 mm from the hull and BDR occurs. The distance between hull and bubbles depends on the advection distance of bubbles. When bubbles approach the hull surface, the area of the wall covered with bubbles expands. However, when bubbles slide close enough to the hull surface, the bubble-covered area shrinks because the bubbles coalesce even if the distance between the hull surface and bubbles remains significantly unchanged inside the boundary layer.

• Nomenclature and units

C_f	frictional coefficient, dimensionless
c	speed of sound, m/s
d_e	equivalent diameter of bubble, m
f_n	resonant repetition of bubbles at each shape mode, Hz
f_r	pulse repetition frequency for ultrasonic emission, Hz
f_s	sampling frequency of data logger, Hz
f_{void}	frequency of voidage wave, Hz
H	height of the model ship, m
L	length of the model ship, m
l_τ	friction length, m
n	shape mode of a bubble, dimensionless
Q_g	injected gas flow rate, m^3/s
Q_l	liquid flow rate in the boundary layer, m^3/s
Re_x	Reynolds number on flat plate, dimensionless
t	time, s
t_f	time of flight of ultrasonic pulse, s
U_{main}	main flow velocity (equivalent to towing speed), m/s
u_b	averaged advection velocity of bubbles, m/s
u_y	averaged streamwise velocity at each depth, m/s
W	width of the model ship, m
x, y, z	x, y, z coordinates on the model ship, m
x'	length from the measurement point, m
$\alpha_{proj.}$	projection void fraction, dimensionless
α_δ	void fraction in the boundary layer, dimensionless
$\Delta x', \Delta y$	spatial resolutions of ultrasonic measurement, m
δ_x	thickness of the boundary layer, m
θ	angle of ultrasonic beam direction, degree
ν	viscosity of water, m^2/s
ρ_g	density of air, kg/m^3
ρ_l	density of water, kg/m^3
σ	surface tension, N/m
τ	wall shear stress, Pa
τ_s	averaged wall shear stress in single-phase flow, Pa

• References

Bagheri S., Schlatter P., Schmid P.J. and Henningson D.S., 2009. Global stability of a jet in crossflow, *J. Fluid Mech.* **624**, 33–44.

Ceccio S.L., 2010. Frictional drag reduction of external flow with bubble and gas injection, *Annu. Rev. Fluid Mech.* **42**, 183–203.

Frankel N.A. and Acrivos A., 1970. The constitutive equation for a dilute emulsion, *J. Fluid Mech.* **44**, 65–78.

Hamilton J.M., Kim, J. and Waleffe F., 1995. Regeneration mechanisms of near-wall turbulence structures, *J. Fluid Mech.* **287**, 317–348.

Harleman M.J.W., Delfos R., Terwisga T.J.C.V. and Westerweel J., 2011. Dispersion of bubbles in fully developed channel flow, *J. Phys.: Conf. Ser.* **318**, 052007.

Jang J., Choi S.H., Ahn S., Kim B. and Seo J.S., 2014. Experimental investigation of frictional resistance reduction with air layer on the hull bottom of a ship, *Int. J. Nav. Archit. Ocean Eng.* **6**, 363–379.

Johansen J., Castro A.M. and Carrica P., 2010. Full-scale two-phase flow measurements on Athena research vessel, *Int. J. Multiphase Flow* **36**, 720–737.

Kitagawa A., Sugiyama K. and Murai Y., 2004. Experimental detection of bubble-bubble interactions in a wall-sliding bubble swarm, *Int. J. Multiphase Flow* **30**, 1213–1234.

Kodama Y., Kakugawa A., Takahashi T. and Kawashima H., 2000. Experimental study on microbubbles and their applicability to ships for skin friction reduction, *Int. J. Heat and Fluid Flow* **21**, 582–588.

Kumagai I., Takahashi Y. and Murai Y., 2015. A new power-saving device for air bubble generation using a hydrofoil for reducing ship drag: theory, experiments, and applications to ships, *Ocean Eng.* **95**, 183–194.

Lamb H., 1932. Hydrodynamics, 6th edition, *Cambridge University Press*.

Madavan N.K., Deutsch S. and Merkle C.L., 1984. Reduction of turbulent skin friction by microbubbles, *Phys. Fluids* **27**, 356–363.

Mizokami S., Kawakado M., Kawano M., Hasegawa T. and Hirakawa I., 2013. Implementation of ship energy-saving operations with Mitsubishi air lubrication system, *MHI. Technical Review* **50**, 44–49.

Mori K., Imanishi, H., Tsuji Y., Hattori T., Matsubara M. and Mochizuki S., 2009. Direct total skin-friction measurement of a flat plate in zero-pressure-gradient boundary layers, *Fluid Dyn. Res.* **41**, 021406.

Murai Y., 2014. Frictional drag reduction by bubble injection, *Exp. Fluids* **55**, 1733.

Nierhaus T., Vanden Abeele D. and Deconinck H., 2007. Direct numerical simulation of bubbly flow in the turbulent boundary layer of a horizontal parallel plate electrochemical reactor, *Int. J. Heat Fluid Flow* **28**, 542–551.

Oishi Y., Murai Y., Tasaka Y. and Takeda Y., 2009. Frictional drag reduction by wavy advection of deformation bubbles, *J. Phys.: Conf. Ser.* **147**, 012020.

Oishi Y. and Murai Y., 2014. Horizontal turbulent channel flow interacted by a single large bubble, *Exp. Therm. Fluid Sci.* **55**, 128–139.

Rust A.C. and Manga M., 2002. Effects of bubble deformation on the viscosity dilute suspensions. *J. Non-Newton. Fluid Mech.* **104**, 53–63.

Schlichting H., 1979. Boundary–layer theory, 7th edition, McGraw-Hill Higher Education.

Smith C.R. and Metzler S.P., 1983. The characteristics of low-speed streaks in the near-wall region of a turbulent boundary layer, *J. Fluid Mech.* **129**, 27–54.

Takeuchi T. and Kagawa T., 2013. Applicability of frequency response test for stability evaluation of gas pressure regulator. *Trans. Soc. Instrum. Control Eng.*, 747–754, (in Japanese).

Tasaka Y., Kimura T. and Murai Y., 2015. Estimating the effective viscosity of bubble suspensions in oscillatory shear flows by means of ultrasonic spinning rheometry, *Exp. Fluids* **56**, 1867.

Tisné P., Aloui F. and Doubliez L., 2003. Analysis of wall shear stress in wet foam flows using the electrochemical method, *Int. J. Multiphase Flow* **29**, 841–854.

Zacksenhouse M., Abramovich G. and Hetsroni G., 2001. Automatic spatial characterization of low-speed streaks from thermal images, *Exp. Fluids* **31**, 229–239.

• Tables

Table 2.1 Parameters of the water tank, towing train, and model ship.

Towing tank		
Length	80	m
Depth	3.5	m
Width	8	m
Towing train		
Acceleration	±0.1	m/s^2
Maximum speed	3.00	m/s
Period of constant traveling velocity at maximum speed	≥ 7	s
Model ship		
Material	Acrylic resin	
Length (*L*)	4000	mm
Height (*H*)	500	mm
Width (*W*)	600	mm
Weight (unloaded)	149.2	kg
Draft (unloaded)	68	mm

Table 2.2 Parameters of the measuring instruments.

Shear stress sensor		
Measurement area	25π	$(mm)^2$
Temporal resolution	20	Hz
Range of shear stress	±250	Pa
Ultrasonic pulse generator and ultrasonic transducer		
Ultrasonic frequency	4	MHz
Number of cycle	4	-
Pulse repetition frequency (f_r)	3.2	kHz
Voltage for ultrasonic emission	150	V
Ultrasonic beam diameter	5	mm
Divergence half-angle	2.2	deg.
Data logger for echography		
Sampling frequency (f_s)	50	MHz
Range of voltage	±2	V
Resolution of voltage	4	mV
Recording time	330	ms
Number of recording trial in an experiment	4	-
Camera above the ship		
Frame rate	500	fps
Resolution	0.08	mm/pixel
Recording time	0.6	s
Underwater camera		
Frame rate	120	fps

Table 2.3 Experimental conditions with bubble injection

Controlled Parameters		
Towing speed	2.00–3.00	m/s
Air flow rate	0.42×10^{-3}–2.5×10^{-3}	m^3/s
At the injector		
Reynolds number (Re_x)	1.6×10^6–2.5×10^6	-
Thickness of the boundary layer (δ_x)	5.8–8.2	mm
Void fraction in the boundary layer (α_δ)	1.9–16.1	%
At the front region		
Reynolds number (Re_x)	2.6×10^6–3.9×10^6	-
Thickness of the boundary layer (δ_x)	8.6–12.2	mm
Void fraction in the boundary layer (α_δ)	1.4–11.2	%
At the middle region		
Reynolds number (Re_x)	5.4×10^6–8.1×10^6	-
Thickness of the boundary layer (δ_x)	16.3–23.2	mm
Void fraction in the boundary layer (α_δ)	6.2–18.9	%
At the rear region		
Reynolds number (Re_x)	8.2×10^6–1.2×10^7	-
Thickness of the boundary layer (δ_x)	23.5–33.5	mm
Void fraction in the boundary layer (α_δ)	0.5–4.4	%

Table 2.4 Theoretical natural frequencies on various shape modes.

	$n = 2$	$n = 3$	$n = 4$	$n = 5$	$n = 6$	$n = 7$	$n = 8$
$d_e \approx 2.6$ mm	81 Hz	157 Hz	243 Hz	339 Hz	444 Hz	557 Hz	678 Hz
$d_e \approx 4.6$ mm	34 Hz	67 Hz	103 Hz	144 Hz	189 Hz	237 Hz	288 Hz

- **Figures**

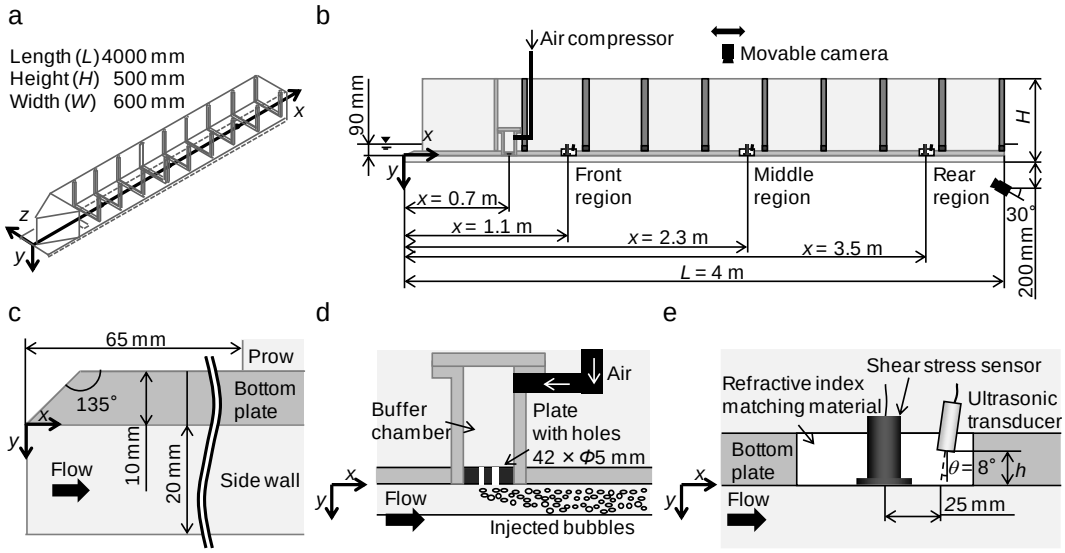

Figure 2.1 Schematic diagram of the experimental facility; (a) top view of the model ship, (b) side view of the model ship, (c) detail of leading edge, (d) detail of air injector and (e) detail of measurement instrument.

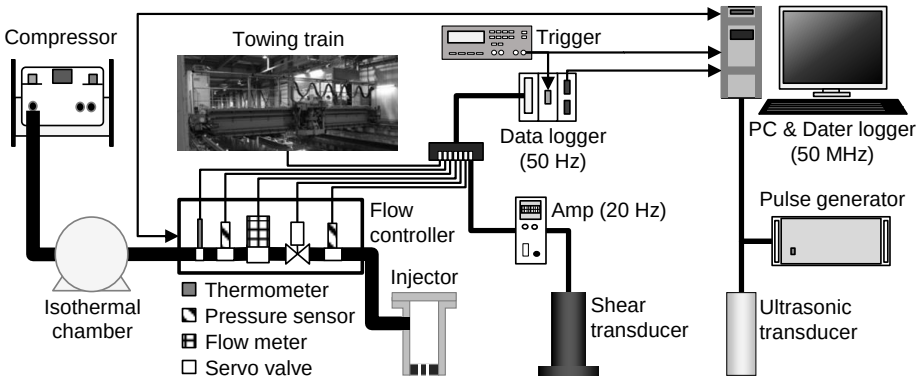

Figure 2.2 Schematic diagram of the measurement system.

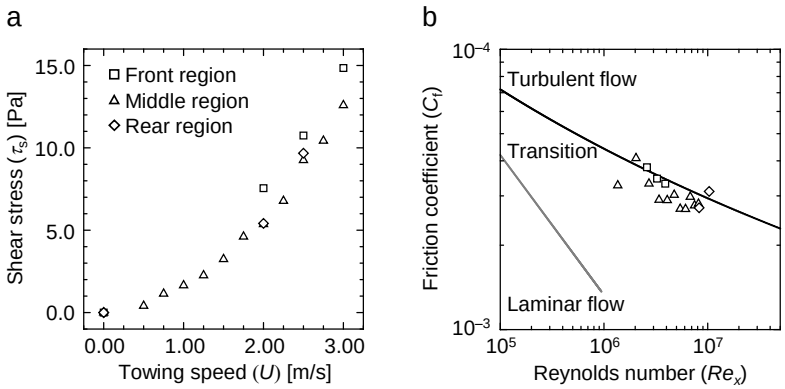

Figure 2.3 Results from shear stress sensor in single-phase flows for the model ship; (a) wall shear stress and (b) friction coefficient.

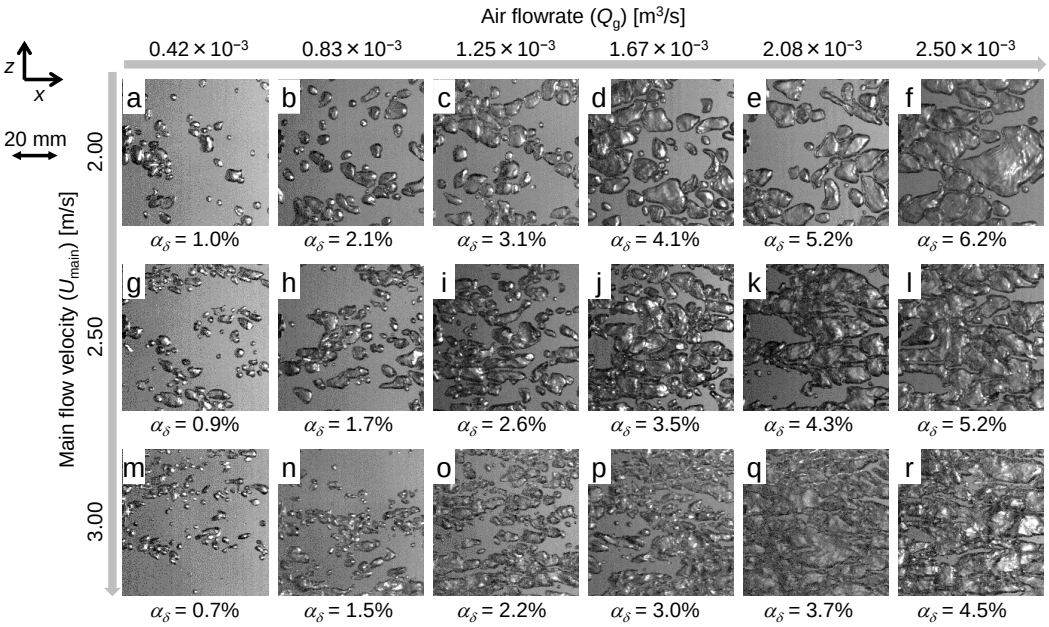

Figure 2.4 Snap shots of advective bubbles near the middle region, $x \approx 2.1$ m, where α_δ is the void fraction in the boundary layer.

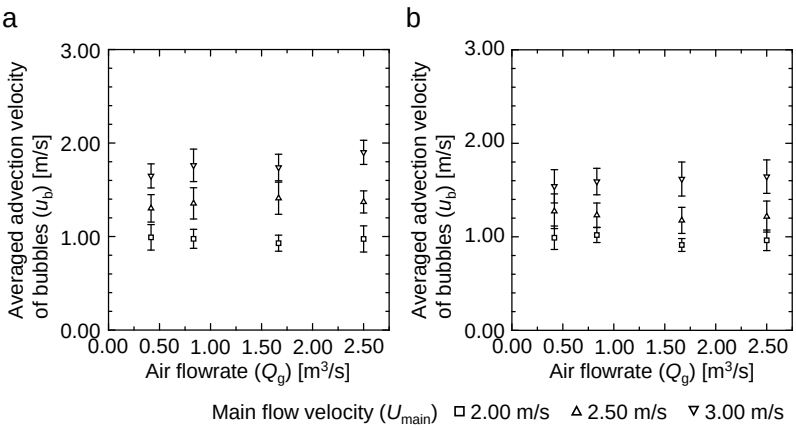

Figure 2.5 Averaged advection velocity of bubbles, where error bars indicate standard deviations; (a) $x \approx 2.1$ m and (b) 3.3 m.

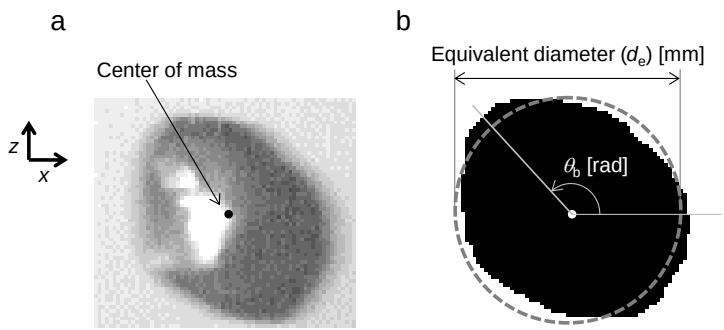

Figure 2.6 Definition of equivalent diameter (d_e) and phase (θ_b) of a bubble; (a) raw image and (b) binary image, where the gray dashed line indicates equivalent area of the bubble.

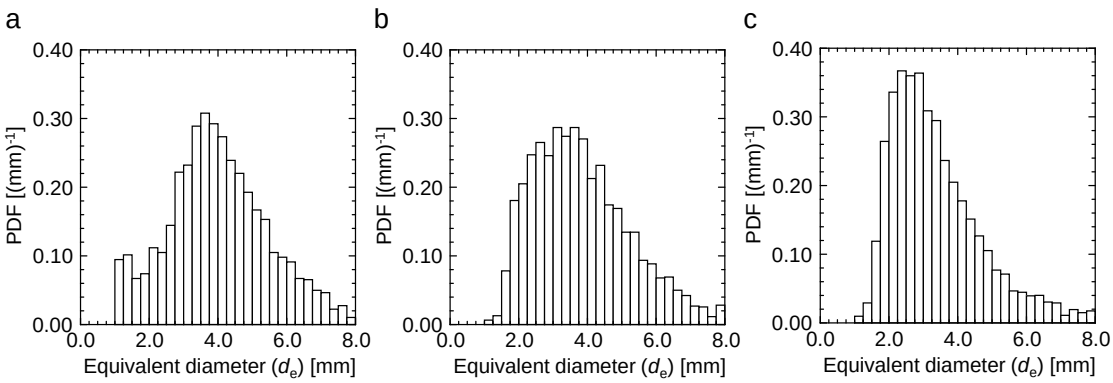

Figure 2.7 Probability density distributions of equivalent diameters of bubbles with $Q_g \approx 0.42\times10^{-3}$ m^3/s at $x \approx 3.3$ m, where small bubbles, $d_e < 1.0$ mm, are neglected; (a) $U_{main} = 2.00$ m/s, (b) 2.50 m/s and (c) 3.00 m/s.

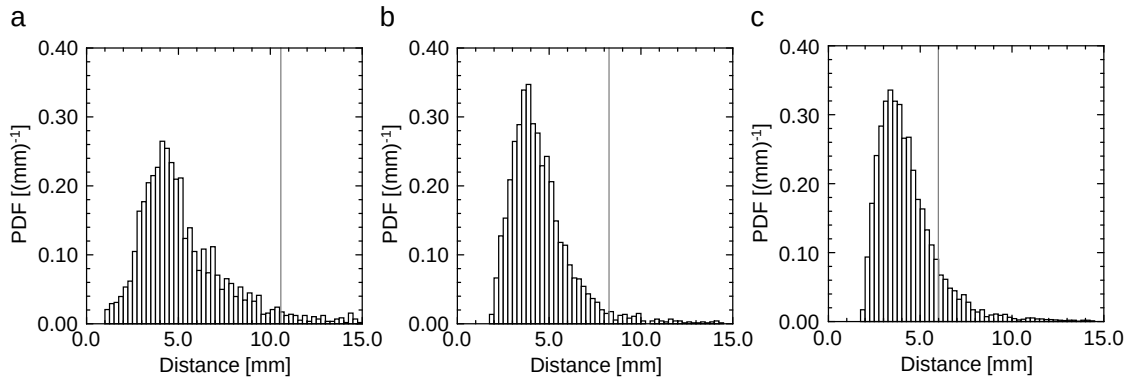

Figure 2.8 Probability density distribution of distance to the closest bubble with $Q_g \approx 0.42\times10^{-3}$ m^3/s at $x \approx 3.3$ m, where small bubbles, $d_e < 1.0$ mm, are neglected and the gray vertical lines indicate the distance between bubbles when they are normalized to have the same distance; (a) $U_{main} = 2.00$ m/s, (b) 2.50 m/s and (c) 3.00 m/s.

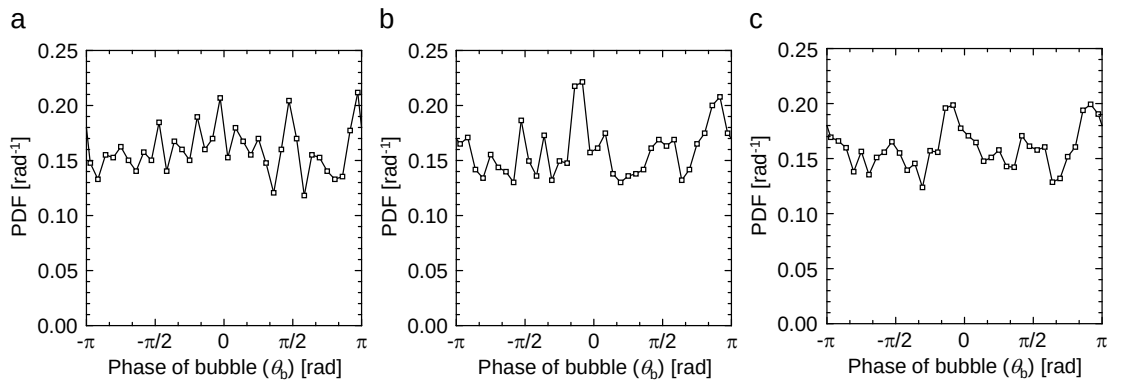

Figure 2.9 Probability density distribution of direction of the closest bubble with $Q_g \approx 0.42\times10^{-3}$ m^3/s at $x \approx 3.3$ m, where small bubbles, $d_e < 1.0$ mm, are neglected; (a) $U_{main} = 2.00$ m/s, (b) 2.50 m/s and (c) 3.00 m/s.

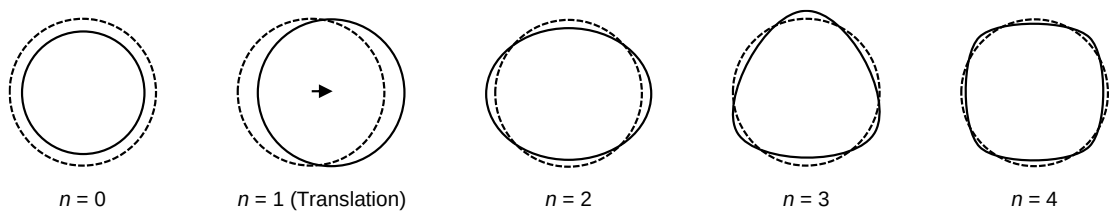

Figure 2.10 Shape of bubbles and mode number (n).

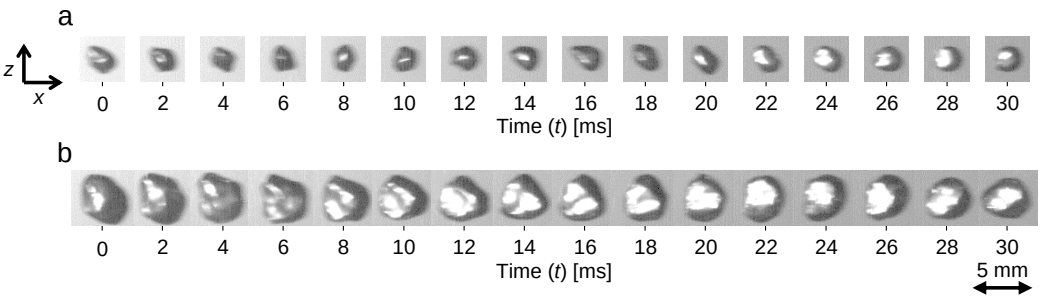

Figure 2.11 Temporal variation of bubble deformation near the rear region, $x \approx 3.3$ m, with U_{main} = 3.00 m/s and $Q_g \approx 0.42\times10^{-3}$ m^3/s; (a) $d_e \approx 2.6$ mm and (b) 4.6 mm.

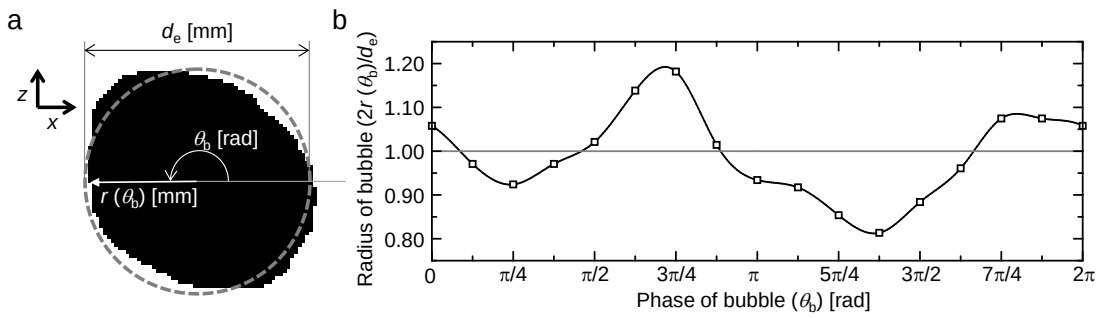

Figure 2.12 Definition of radius on the bubble; (a) binary image of the bubble shown in **Figure 2.11**(b) at t = 0 ms and (b) variation of the radius sampling at each π/8 rad, where the gray dashed and solid lines indicate equivalent area of the bubble and half of an equivalent diameter of the bubble, respectively, and the black line is a spline curve of the variation.

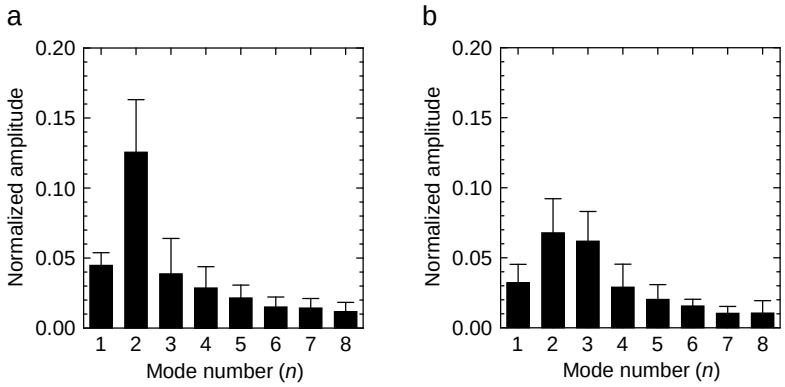

Figure 2.13 Averaged amplitude of the vibration on the bubble's radius shown in **Figure 2.11** at each mode number, where the amplitude is normalized by a half of d_e and error bars are standard deviations; (a) $d_e \approx 2.6$ mm and (b) 4.6 mm.

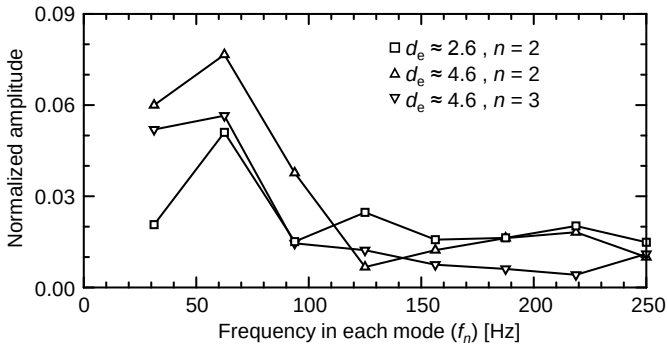

Figure 2.14 Frequency of the vibration on a bubble's radius at dominant shape modes, where the amplitude is normalized by half of the d_e.

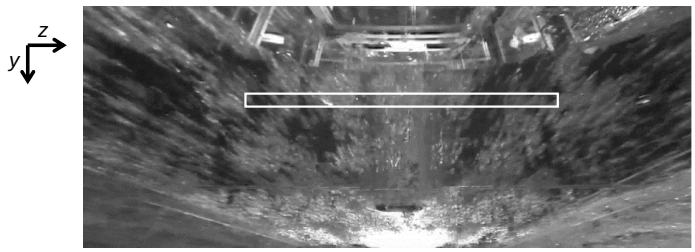

Figure 2.15 Snapshot of picture taken by the underwater camera, where the framed area is located at $x \approx 3.7$ m and used to make line scan images, e.g., **Figure 2.16**.

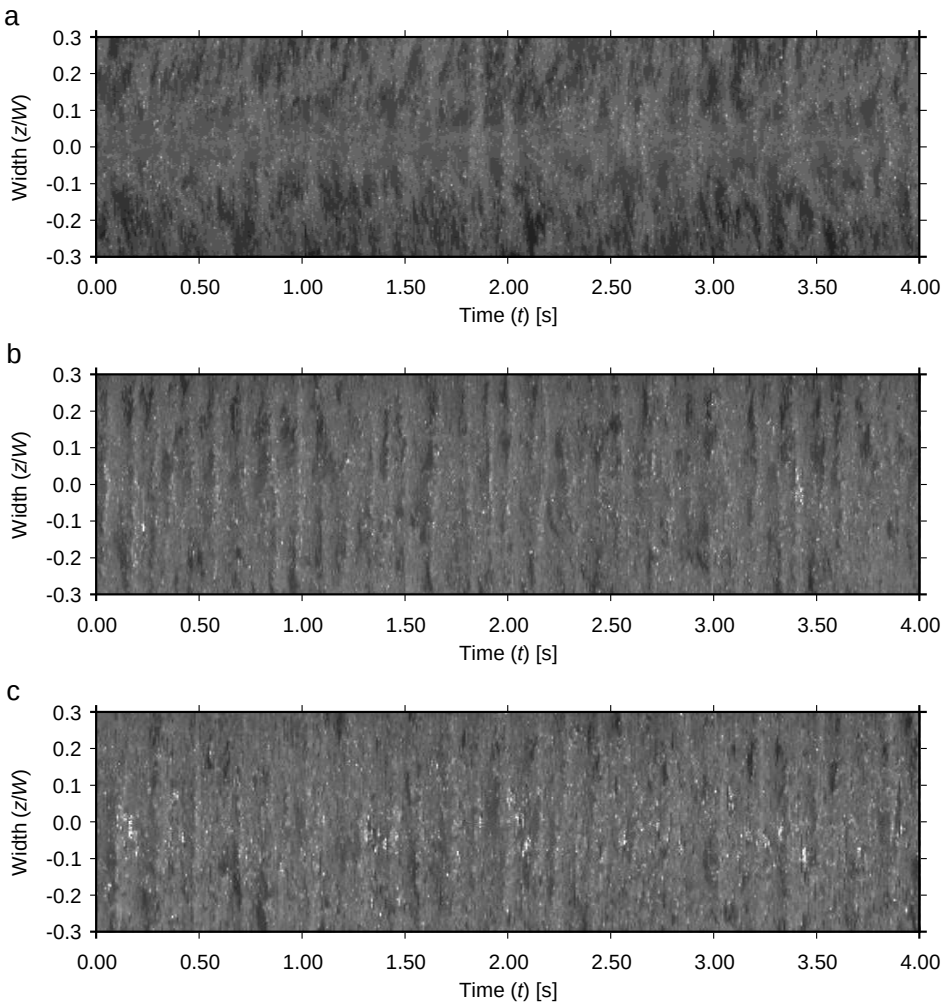

Figure 2.16 Sampling of line scan images taken at $x \approx 3.7$ m, where experimental conditions of the sample image are $U_{\mathrm{main}} = 3.00$ m/s; (a) $Q_{\mathrm{g}} \approx 0.83\times10^{-3}$ m^3/s, (b) 1.67×10^{-3} m^3/s and (c) 2.50×10^{-3} m^3/s.

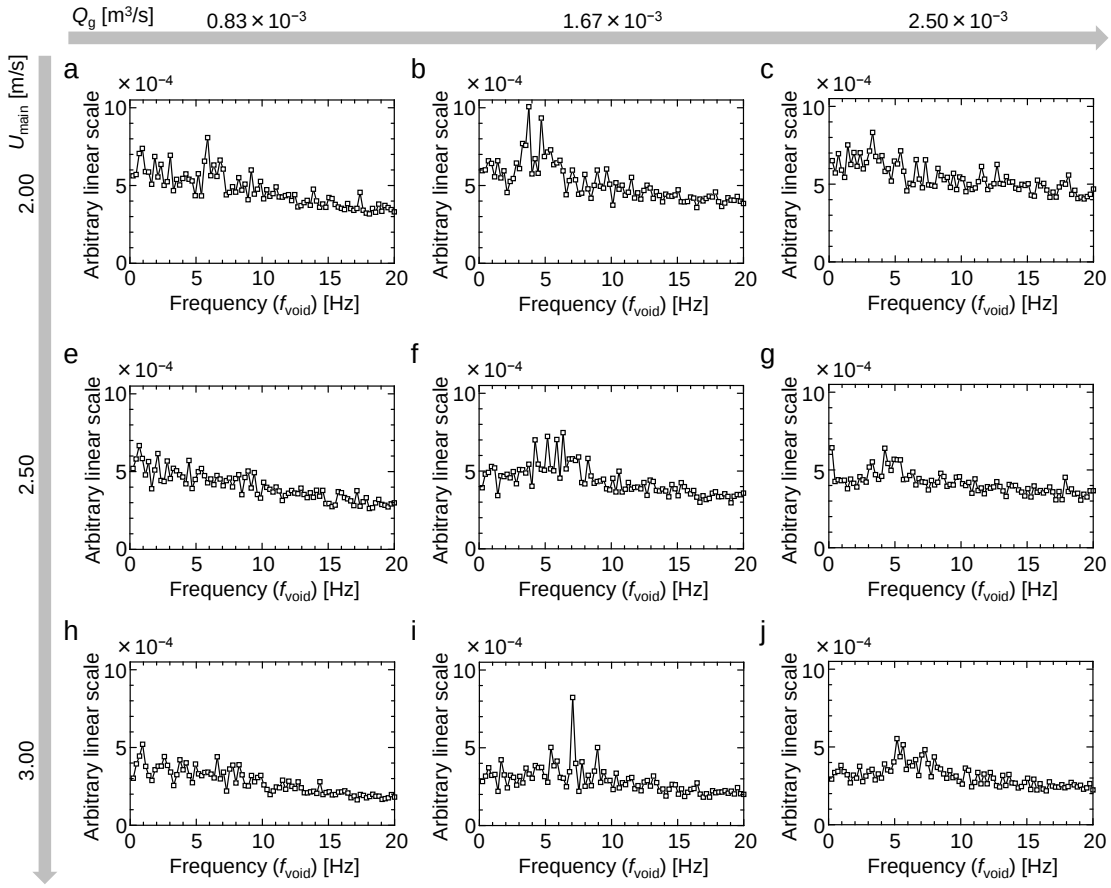

Figure 2.17 Linear spectra of voidage wave naturally generated underneath a ship's hull, where the spectra is obtained from line scan images (e.g., **Figure 2.16**) and values of the spectra are normalized by the maximum brightness of the line scan images.

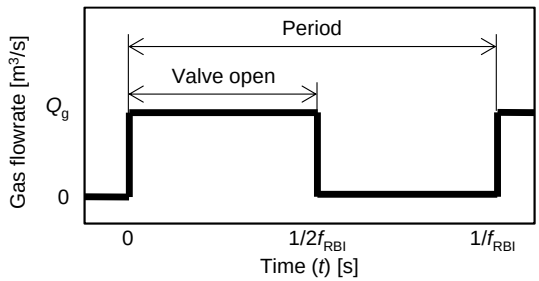

Figure 2.18 Repetitive bubble injection (RBI), where f_{RBI} is the frequency of valve control.

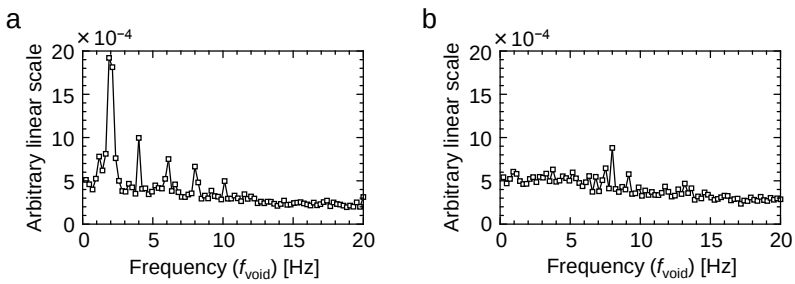

Figure 2.19 Linear spectra of voidage wave with artificial fluctuation by RBI with U_{main} = 3.00 m/s and $Q_g \approx 1.67\times10^{-3}$ m^3/s, where values of the spectra are normalized by the maximum brightness of the line scan images; (a) f_{RBI} = 2 Hz and (b) 4 Hz.

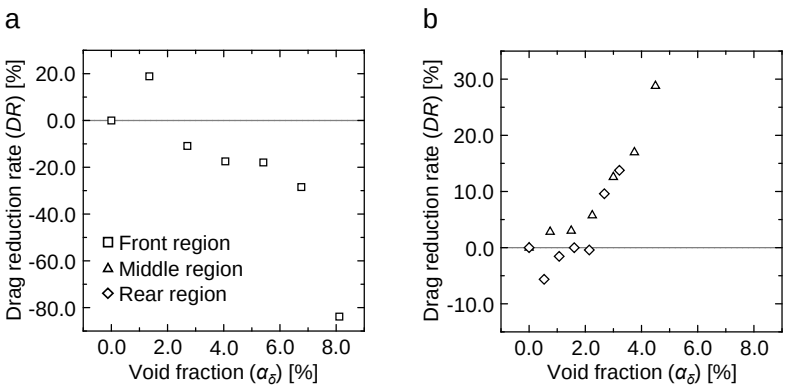

Figure 2.20 Bubbly drag reduction (BDR) measured in 7 s with U_{main} = 3.00 m/s; (a) front region, and (b) middle and rear regions.

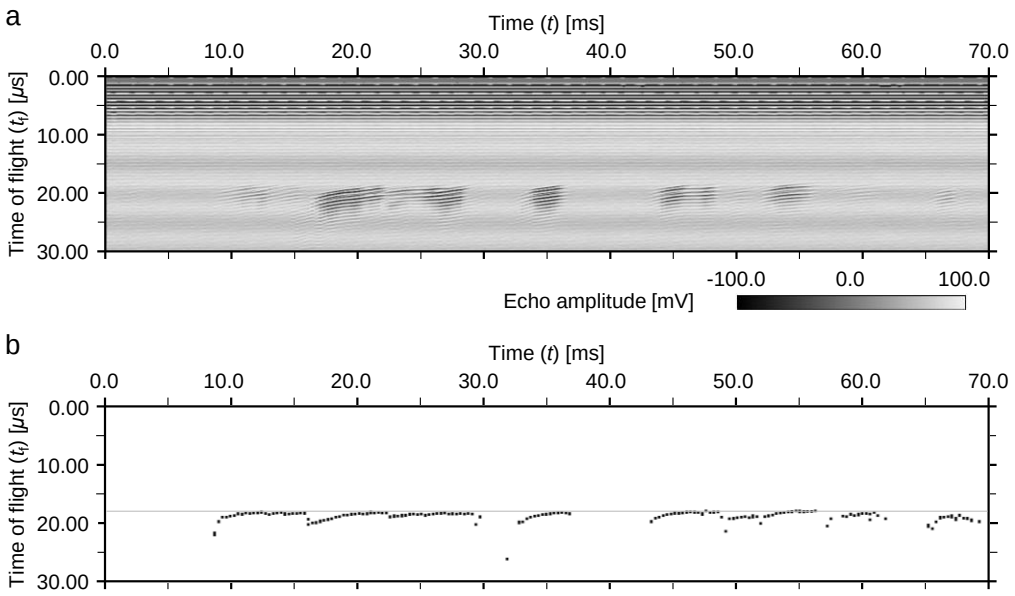

Figure 2.21 Typical ultrasonic echogram; (a) raw echo amplitude and (b) detected upper surface of bubbles (black dots), where the gray line indicates the liquid–solid interface at the ship's hull.

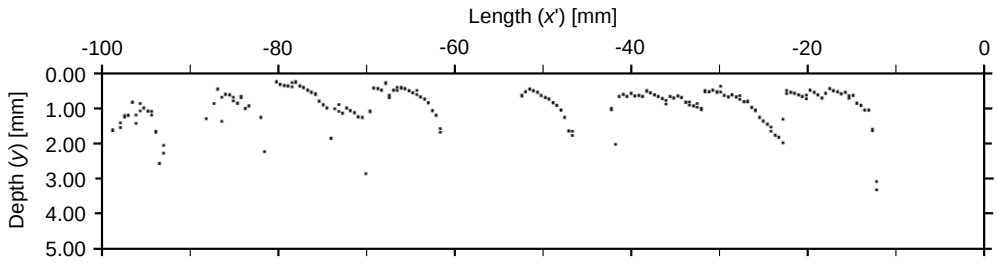

Figure 2.22 Shapes of a bubble's upper surface converted from **Figure 2.21**(b).

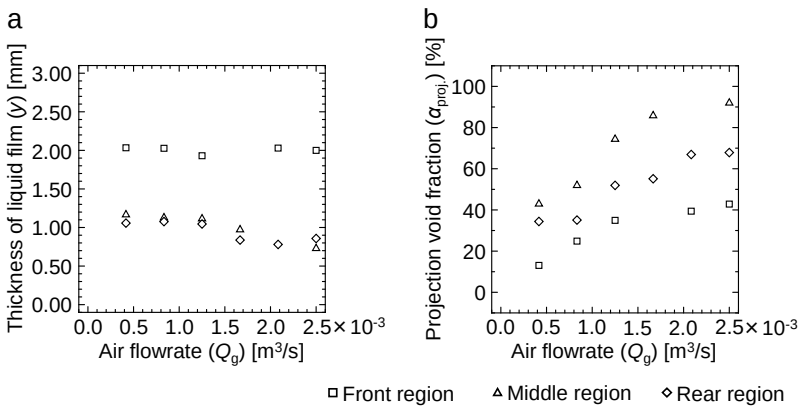

Figure 2.23 Statistics of the advective bubbles with U_{main} = 3.00 m/s obtained from ultrasonic echograms; (a) averaged thickness of liquid films above the bubbles and (b) projection void fraction.

3 Vortical structures swept by a bubble swarm in turbulent boundary layers

• Preface

Streamwise vortices in a turbulent boundary layer are stretched by a shear in the layer and finally burst. The bursting event is one of reasons for wall friction. Therefore, if repetitive bubble injection mentioned in the **Chapter 1** reduces frictional drag efficiently, bubble swarms injected into the layer by the injection affect some effects to the streamwise vortices. In this chapter, we suggest a novel visualization method for detecting vortical structures using means of two-color laser-sheet illumination of the wall turbulence with a dilute suspension of flakes. And using this method, interactions between the vortical flow structures and the bubble swarm.

3.1 Introduction

Bubbly two-phase flows still pose various questions despite a long history of study. Conventional theoretical modeling has limitations in precisely reproducing the complex effects of deformation, coalescence and fragmentation of bubbles on the behavior of two-phase flow. This is the so-called multi-scale problem of bubbly flow (e.g., Sugiyama et al., 2001), which ranges from the thickness of a gas–liquid interface, via the bubble size, to the length scale of a bulk system. This nature of bubbly flow accompanied by a broad spectrum in the flow structure always brings us difficulties in prediction and control, especially for bubbly two-phase turbulent boundary layer. In this chapter, the present research has focused on finding local instantaneous phenomena in the wall boundary layer associated with bubbles, expecting that the solution will lead to breakthrough technologies in chemical, biological, thermal, and fluid engineering.

Most engineering processes utilizing bubbly flows have a solid wall as a boundary of the system. In the case of a vertical system, intensive works have been reported for vertical bubbly pipe flows because of industrial demands for boilers and heat exchangers (Hibiki and Ishii, 2002). Two-phase flow patterns in pipes affect the heat transfer and pressure loss characteristics (Deckwer, 1980; Heijnen and Riet, 1984; Joshi et al., 2002). The same flows in very small geometry have totally different characteristics, which has opened a new field of research on microscopic thermo-chemical devices (Qu and Mudawar, 2003; Kandlikar, 2004). A significant promotion of heat transfer by the injection of microbubbles about the thermal boundary layer was reported by Kitagawa and Murai (2013). Their experiment showed that bubbles work as a thermal transporter in turbulence while the bubbles themselves are thermal insulators in the region without turbulence.

Horizontal configurations of bubbly flow have received less attention than vertical systems in engineering fields since it is unsuitable for stable heat and mass transfers. In a horizontal main stream, buoyancy acts on dispersed bubbles perpendicularly to the stream so that the flow field is multi-dimensionalized irresistibly. In a boundary layer formed beneath a horizontal flat wall, bubbles congregate near the wall to persistently affect the inner-layer structure of the wall turbulence. Synchronically, turbulent shear stress and resultant eddies affect the spatial and size distributions of bubbles. Bubbly flow structure in the equilibrium states of such mutual interaction can hardly be predicted theoretically if we are unaware of what happens to the local two-phase turbulence. Accordingly, a well-schemed experimentation is desired to achieve a graphical understanding of bubble–vortex two-way interaction, which will contribute to all applications of heat, mass and momentum transfer using bubbles in horizontal flow configurations.

Objective in this chapter also has strong relevance to the frictional drag reduction by injection of bubbles, i.e. decrease in turbulent momentum transfer of a solid wall. Since the paper of McCormick and Bhattacharyya (1973) for ship drag reduction, horizontal bubbly flow close to a wall has been investigated by many institutes over 40 years and it concluded that the use of such

flow is feasibly practical although the underlying physics are still unsolved comprehensively (Ceccio, 2010). Drag reduction using bubbles is classified roughly into two types by bubble size. In the first case, drag reduction is achieved with bubbles that are sufficiently smaller than the thickness of the boundary layer (Kato et al., 1999), which is often called microbubble drag reduction. In the second case, air films are formed to occupy the wall surface and thus separate turbulent flow from the wall (Latorre, 1997; Fukuda et al., 2000). These two methods have different mechanisms of drag reduction. Coherent structures of quasi-streamwise vortices, which are generated in the wall boundary layers, are the targets of fluid dynamic curiosity because they have a strong relation with the wall frictional drag (Robinson, 1991; Kravchenko et al., 1993). Iwasaki et al. (2001) simulated numerically such streamwise vortices affected by presence of deformable bubbles, and Lu et al. (2005) found with their simulation that soft deformation of bubbles leads to a significant drag reduction as the streamwise vortices around them are suppressed. Additionally, alternation of streamwise vortices due to mixing of microbubbles was ascertained by the experiments in the last decade (Hassan et al, 2005; Zhen and Hassan, 2006). Oishi et al. (2007) found that microbubbles of micron size shorten the streamwise vortices and incline them in the spanwise direction even though their volume fraction is less than 1%. Between the two approaches of microbubbles and air films, the role of intermediate-sized bubbles has not yet been clarified. The intermediate-sized bubbles, named here, range from 1 mm to 100 mm in characteristic length scale, which is comparable with or larger than typical thickness of turbulent boundary layer in engineering such as for ships. The number of intermediate-sized bubbles increases naturally during the migration of various sized bubbles downstream owing to coalescence of small bubbles and fragmentation of large bubbles in turbulent shear flow. Thus, from both aspects of engineering and science, we are facing a strong need for fundamental knowledge on turbulence–bubble interaction in the whole range of bubble sizes.

Some researchers have constructed an experimental facility to investigate the local and transient reactions of a boundary layer given an injection of bubbles. One of the representative results obtained by the group is that relatively small bubbles produce a negative turbulent shear stress component that correlates to fluctuation of the local void fraction (Murai et al., 2006). Another finding, for relatively large bubbles, is that an air film works properly when the bubbles are longer than five times the boundary layer thickness in the streamwise direction (Murai et al., 2007). In other words, shorter bubbles behave as neutral additives in drag reduction. Further interesting results were obtained by Oishi et al. (2009), who showed the waveform of the local skin friction when the void fraction has a naturally provided fluctuation and found that the average drag reduction is promoted by amplifying the fluctuation in the local void fraction. This phenomenon is hypothetically explained by the non-linear relationship and the time lag between drag reduction ratio and the local void fraction. On one hand, we already know that there is a contribution of a

single large bubble passing the wall intermittently to the drag reduction. Oishi and Murai (2014) measured the turbulent shear stress field modified by such a single bubble passage in the vicinity of wall. On the other hand, intermittent passage of bubbles' ensemble would produce the similar effect. If the scenario is successfully executed in a flow with bubble swarm generated by air injection, it means that the passing bubble swarm modifies vortical structures more effectively, which are the source of turbulent momentum transfer, i.e. turbulent shear stress. It is because that size of bubbles injected into the turbulent boundary layer using air compressor is in *O*(mm) and these bubbles is hard to change fluid properties, such as an effective viscosity and a density (in the **Chapter 2**). Following to the methodology of artificial pulsation in void fraction, we investigate how turbulent flow structures (vortical structures) are altered by a bubble swarm using an originally developed visualization technique so that enhancement mechanism of the drag reduction by means of repetitive bubble injections is understood.

3.2 Experimental setup

A schematic diagram of the experimental facility is shown in **Figure 3.1**. The test section is a horizontal rectangular channel made of transparent acrylic resin. The test section is 40 mm in height ($H = 2h$), 160 mm in width (W) and 6000 mm in length. Test fluid is 10 cSt silicone oil at 28 ºC; density (ρ) of the oil is 932 kg/m^3, kinematic viscosity (ν) is 7.7×10^{-6} m^2/s, and surface tension (σ) is 19.9×10^{-3} N/m. Using the oil avoids effects of contamination on bubble interfaces and allows large deformation of the bubbles even for turbulent flows with relatively low Reynolds numbers because the surface tension of the oil is lower than that of water. The silicone oil circulates in the channel, and bubbles are mixed through honeycombed holes of a bubble injector mounted on the upper wall of the channel at $x/H = 43.75$ from the channel inlet, where the boundary layer is in a turbulent condition. Here, x, y, and z directions are defined to be the streamwise, vertical and spanwise directions. The origin of the coordinate system corresponds to the channel inlet, upper plate and nearside wall of the channel. Measurement equipment is installed in a test section located a distance $25H$ from the injector to investigate the development of bubbly flows. The bubbles are removed at the end of the channel by swirling the fluid in a bubble removal tank before the fluid is returned to the inlet of the channel. The Reynolds number (Re) is defined as

$$Re = \frac{Uh}{\nu} = \frac{Q_l}{2W\nu} \qquad \textbf{Equation 3.1}$$

and fixed at 2200, where U and Q_l are respectively the cross-sectional mean velocity and volumetric flow rate of the test fluid. According to the variation of the friction coefficient (C_f) against Re obtained in the experimental facility (see **Figure 3.2**), there is a transition regime from

laminar to turbulent flows at $800 \leq Re \leq 1200$. Therefore it is assumed that the flows at $Re = 2200$ at which the experiments in the chapter were performed are fully turbulent. The bubble injector is connected with an electric valve so that an arbitrary fluctuation in the gas flow rate can be realized with a function generator. Using this valve system makes it possible to control the duration of bubble injection (t_{in}) and the void fraction during the injection of bubbles (α) defined as

$$\alpha = \frac{Q_g}{Q_g + Q_l}, \qquad \textbf{Equation 3.2}$$

where Q_g is the gas flow rate for the bubble injection. In this chapter, α and t_{in} are fixed at 1.5×10^{-2} and 0.5 s, respectively. Under these conditions, the swarm of bubbles introduced by a single injection contains variously sized bubbles from sub-millimeter-sized bubbles to air films. **Figure 3.3** shows snapshot pictures of a bubble swarm. Large air films are observed at the front of the swarm and the bubble size decreases toward the tail of the swarm.

For flow visualization, tiny aluminum flakes were used as laser scattering platelets. A microscope image of the flakes is shown in **Figure 3.4**(a). The platelets have size of about 10–30 μm and act as glistening flat scales. These flakes allow us to visualize the structure of coherent streamwise vortices generated by the wall friction with the help of features of the anisotropic light reflection principle (Cenwell et al., 1978). The flakes align into a direction of the principal strain and the heterogeneous optical reflection is occurred by the distortion in fluid flows (see **Figure 3.4**(b)). That is, the use of aluminum flakes allows us to visualize the distortion field in shear-induced turbulence. Hence, visualization using flakes expresses the distortion field as has been demonstrated by numerical simulation for infinitesimal platelets (Goto et al., 2011). Pearl powders, mica and Kalliroscope flakes (Kwangjai et al., 1981; Abcha et al., 2008) have a similar function, but aluminum flakes provide much higher reflectivity. Low concentrations of aluminum flakes can thus be used to maintain transparency of the fluid that is required for visualization of the flow structures in layers slightly away from the top wall. The flakes do not trace high-frequency fluctuations due to turbulent eddies because of their much higher density relative to the test fluid (2.9 times as high as that of the test fluid). Therefore, the visualized flow patterns mainly display the coherent structure in the boundary layer.

Figure 3.5 is a schematic diagram of the optical setup for visualizing streamwise vortices near the wall using green and blue laser sheets and the aluminum flakes. The wavelengths of the lasers are $\lambda_G = 531$ and $\lambda_B = 473$ nm. The thickness of the laser sheets is less than 3 mm. The laser sheets are placed 5, 10 or 15 mm from the upper wall corresponding to $y^+ \approx 50$, 100 and 150 in wall units. y^+ is defined as

$$y^{+} = \frac{yu_{\tau}}{\nu} = \frac{y\sqrt{\tau_{s}}}{\nu\sqrt{\rho}}, \qquad \textbf{Equation 3.3}$$

where y, u_τ and τ_s are respectively the distance from the upper wall, the friction velocity and the shear stress at the upper wall in single-phase flows obtained from a shear sensor before doing this experiment. As parallel light sheets are projected from each side to the streamwise vortices (in **Figure 3.5**), light scatters toward the camera (upward in the figure) in the region that has oblique streamlines for the vortex arrangement. **Figure 3.6** shows the estimated arrangement of streamwise vortices in the boundary layer of the channel flow in the y–z cross section, and **Figure 3.7** indicates the corresponding pattern of light scattered from the flakes against the incident layer sheets. If there are ideal, quasi-circular vortices like in **Figure 3.6**(a), the vortices would be represented by a pattern of pairs of stripes of two colors in the image as shown in **Figure 3.6**(b). According to a previous study on the boundary layer, however, vortices in actual flows are distorted as in **Figure 3.7**(a) (Sheng et al., 2009). In this case, the streamwise vortices reflect either green or blue laser light toward the camera in a much wider area than that for the quasi circular vortices because of their distorted shape (in **Figure 3.7**(b)). This visualizing method using lasers of two different colors makes it possible to observe the vortices more clearly, because a pair of streamwise vortices is expressed as a pair of colored stripes in any case. The image of the flow structure was acquired using a high-speed digital video camera with a depth of field of 15 mm, frame rate of 4000 fps, image size of 512×512 pixels, and corresponding spatial resolution of 0.166 mm/pixel.

3.3 Image processing

Figure 3.8(a) is a sample of an original acquired image, which corresponds to an area defined by $67.68 \le x/H \le 69.82$ in the streamwise direction and $0.27 \le z/W \le 0.73$ in the spanwise direction of the channel. The images display only the central part of the channel to exclude the side-wall effects. The flakes are identifiable as green or blue dot patterns in this picture. The reflection of light by the flakes under two-color illumination generates a stripe pattern in the image, which represents the structure of the longitudinal turbulent vortices in the channel. Because the density of the aluminum flakes is 2.9 times that of the silicone oil, the flakes do not trace the high-frequency fluctuations of the flow, and thus, the individual small dots corresponding to the flakes in the image is meaningless in this case. To highlight the stripe patterns representing the longitudinal vortices, low-pass filtering was applied to the image. The filtering was implemented based on the combination of two-dimensional Fourier transform and the inverse transform of snapshot images with giving the threshold on the wavenumber in the both directions, where the threshold is 460 m^{-1}. **Figure 3.8**(b) shows the result of low-pass filtering of the image shown in 8 (a) as a sample of the filtering, where

spatial fluctuations larger than 460 m^{-1} are eliminated from the original image. This filtering allows the image to focus on the structure of turbulence. It is worth noting that there is a preferential concentration of heavy particles in turbulence. For instance, it is well known that heavy particles naturally accumulate in the region where the second invariant of the velocity gradient tensor takes a negative value. This trend results in a high concentration of aluminum flakes in the low-speed streak region in the wall boundary layer of the channel flow. However, the preferential concentration does not affect the image patterns in the results of visualization when two-color illumination is implemented. We only use the distribution of the dominant color to grasp the flow structure while the influence of the biased concentration is cancelled out by the binarization of the color image patterns. To distinguish streamwise vortices from other flow structures in the low-pass filtered images, each color component, green or blue, in the image is binarized. Thin lines expressing the streamwise vortex are drawn at the boundary where one color changes to another color, according to the optical configuration shown in **Figure 3.6** and **Figure 3.7**, because streamwise vortices are in pairs generated by a positive and a negative vorticity in the streamwise direction. Hence, it is assumed that unpaired stripes are not streamwise vortices and are ignored in the analysis of streamwise vortices. **Figure 3.8**(c) is a sample of the streamwise vortices detected from 8 (b) using this process. Green lines express the boundary where the color changes from blue to green and blue lines express the boundary where the color changes from green to blue.

The layer beneath the bubble swarm is focused on for the bubbly flows. A bubble's shape in the swarm is identified by thin vague lines, illuminated by the diffusing light of flakes, in **Figure 3.9**(a) because of the sufficient depth of field of the camera. The present low-pass filter works well to remove a bubble's edge, with remaining stripe patterns representing the streamwise vortices under the bubbles (see **Figure 3.9**(b)). Hence, it is possible to analyze the flow structures obtained from the original image without the influence of noise due to a bubble's edge and the shape of bubbles (see **Figure 3.9**(c)).

3.4 Results and discussions

3.4.1 Vortical structure of the turbulent boundary layer visualized under single-phase conditions

As fundamental information about the turbulent flow structures, the advection velocity was measured by particle image velocimetry of low-pass-filtered images. By the filtering we can investigate the vertical structures, not the individual particles. **Figure 3.10** shows the advection velocity of structures ($u_{\mathrm{structure}}$); (a) near the upper wall, $y^+ \approx 50$, (b) in a layer that is slightly deeper, $y^+ \approx 100$, and (c) in a layer deeper still (hereafter referred to as the deepest layer), $y^+ \approx 150$, where

y^+ is determined by the friction velocity of the single-phase condition (u_τ) and kinematic viscosity of the test fluid (ν). The structures in the deeper layers flow faster than those in the shallower layers. Assuming that the structures move with a local stream velocity, the results shown in **Figure 3.8** are reasonable. The advection velocity does not change so much with time.

Examples of low-pass-filtered images obtained under single-phase flow conditions for different layers are shown in **Figure 3.11**. There are a number of patterns composed of two green and blue stripes in the streamwise direction representing the structure of the streamwise vortices near the wall (**Figure 3.11**(a), $y^+ \approx 50$). These vortices become shorter and incline in the slightly deeper layer, $y^+ \approx 100$, as shown in **Figure 3.11**(b), and become more homogeneous in the deepest layer, $y^+ \approx 150$, as shown in **Figure 3.11**(c), where stripe patterns in the streamwise direction mostly disappear. **Figure 3.12** shows the linear spectra of color patterns expressed by brightness fluctuations of green and blue components in the spanwise direction, for the low-pass-filtered images of the three layers. As expressed by the gray lines, the spatial averaging of 512 the linear spectra obtained from single images shown in **Figure 3.11** has large scatter and seems discontinuous. This is because the streamwise vortices take modifications by turbulence events, namely sweep and ejection due to bursting. To extract meaningful spatial information of the vortices, we made further temporal averaging of the spatially averaged linear spectra for 4000 sequential images corresponding to a period of 1 s with assuming that the flows are statistically equivalent. The spectra depicted by black lines show the results of time averaging, and the averaging removes scattering and smoothes the spectra. In the near-wall layer (**Figure 3.12**(a)), the spectrum has a local maximal that corresponds to the wavenumber of flow structures, $k_{gap} = 82\ \mathrm{m}^{-1}$, in the channel spanwise direction (z axis). The spectrum has a monotonically decreasing trend in the deeper layers (**Figure 3.11**(b) and (c)) that indicates that organized structures of the turbulence disappear as the distance from the wall increases. In general turbulent boundary layers, organized vortex structures creating Reynolds shear stress exist in the buffer layer, $5 < y^+ < 70$ (Ganapathisubramani et al., 2003). If ideal streamwise vortices exist in the turbulent boundary layer like in **Figure 3.6**(a), then the corresponding spanwise distance between two streamwise vortices, $1/k_{gap}l_\tau$, is 125, where l_τ is friction length in the single-phase flow and defined as

$$l_\tau = \frac{\nu}{u_\tau}. \qquad \textbf{Equation 3.4}$$

It was assumed that the spacing of streaks is twice the spacing of streamwise vortices because there are low-speed streaks for ejection flow between two streamwise vortices, and streaks and vortices in turbulent boundary layers interact in what is called a self-sustaining cycle (Hamilton et al., 1995). The result corresponds with the distance between low-speed streaks reported in previous studies (Smith and Metzler, 1983; Zacksenhouse et al., 2001). This means that the shape of the streamwise

vortex is not circular but distorted like that in **Figure 3.7**(a). It is confirmed that the present visualization method can visualize streamwise vortices that are generated by low-speed streaks at the upper wall of the channel.-

To characterize the longitudinal vortices, the streamwise vortex determined in **Figure 3.8**(c) is substituted with an equivalent straight line calculated using the least-squares method, and the angle of the streamwise vortex is thus obtained as the angle of the equivalent line relative to the streamwise direction. **Figure 3.13** shows the length (l_{major}) and angle (θ) of each streamwise vortex near the upper wall determined from 4000 sequential images. Individual plots in the figure express information of individual streamwise vortices; there are more than 600,000 plots in the figure. The tilting angle of the vortex has a symmetric distribution relative to the streamwise direction and a strong vortex that has longer length tends to match the streamwise direction. This result is consistent with previous results (Oishi et al., 2007). The applicability of the present technique to the visualization of longitudinal vortices is thus confirmed.

To characterize the probability that a longitudinal vortex has a certain length and angle, the time-averaged existing probability density of each condition in the single-phase flow is calculated for the three layers as shown in **Figure 3.13**, where the total count indicated in the figures is the average number of vortices distinguished in one frame. Near the upper wall, there are many streamwise vortices directed in the streamwise direction and these have a wide length distribution beyond $l_{\mathrm{major}}/l_{\tau}$ = 170 (**Figure 3.14**(a)). The total count decreases with increasing y^{+}, and the probability distribution becomes more isotropic with increasing y^{+} (**Figure 3.14**(b) and (c)); i.e., extent of the distributions in l_{major} narrows at small angles. At large angles, the shape of the distribution does not change so much. In the buffer layer, the longitudinal vortices along the streamwise direction coexist with quasi-isotropic shorter vortices. The organized components then decrease with increasing y^{+} beyond the boundary between the buffer layer and logarithmic layer because streamwise vortices transform to arch-shaped vortical structures in the logarithmic layer (Zhou et al., 2010). Heads of arch-shaped vortical structures are visualized in **Figure 3.11**(c) by one-color stripes in the spanwise direction. There are always two peaks at almost the same position in these distributions. The highest peaks are at an angle of 0 degrees and have length 27 times l_{τ}. The second peaks are located at angles of ±67 degrees and have length 14 times l_{τ}.

3.4.2 Behavior of bubbles in swarms

Figure 3.3 shows that a bubble swarm comprises bubbles of various sizes as the result of fragmentation and coalescence. Generally, a bubble in a flow interacts with other bubbles (Kamp et al., 2001) and flow structures (Fujiwara et al., 2004). We also expect mutual interactions between bubbles and streamwise vortices in the turbulent boundary layer that we observed in the last **Subsection 3.4.1**. However, in the present case, the leading air film of the bubble swarm occupies

most of the upper surface of the channel. Where do the streamwise vortices escape to against invasion of the air film? What are the interactions between the vortices and the bubbles of variable size in the swarm? The vortical structures beneath the bubble swarm and the bubbles are investigated in this subsection. Additional visualization tells us the shape and advection velocity of the bubbles and flake visualization elucidates the vortical structure affected by the bubbles.

Figure 3.15 shows the phase-averaged height of the bubble swarm measured by ultrasonic echography under the same experimental conditions as used for the flake visualization, where the phase averaging is based on more than 150 bubble swarms. Error bars in the figure represent the standard deviation of the height. In the two-phase conditions, the layer near the upper wall considered for the single-phase condition is occupied by bubbles. Although the phase-averaged height of the swarm in this experiment is less than the distance between the upper wall and the layer near the upper wall defined as $y^+ \approx 50$ for the single-phase condition, considerable deviation of the height affects the visualization of the layer. Therefore, the incident light is hardly scattered by interfaces of these bubbles and we cannot obtain images of vortices while maintaining sufficient quality. Therefore the flow structures under the bubble swarm layers ($y^+ \leq 100$ for the single-phase condition) are observed.

Since the incident laser light sheets have considerable thickness, outlines of bubbles that exist in the upper layer overlap with images of longitudinal vortices. Bubble shapes detected from the images are shown in **Figure 3.16**. The figure is a line-scanned image of bubble shapes extracted from sequential images taken over 2 s. Injections of the bubble swarms into the channel are controlled with an electric valve and the figure corresponds to a single shot of bubble injection. In the swarm, larger bubbles lead at the front and smaller bubbles trail at the tail. **Figure 3.17** shows advection velocities of bubbles (u_{bubble}) calculated for bubbles in a central area of the channel, $0.41 < z/W < 0.59$, which should include more than two streamwise vortices considering the vortex size determined under the single-phase condition. Gray dots in the figure represent the velocities of individual bubbles in the area at the scanning line. Black dots are their average in 0.05-s intervals and error bars are the standard deviations of the velocity and time. Some large bubbles at the front of the swarm have higher advection velocity than smaller bubbles. At the middle of the swarm around 1.3 s in the figure, there is variety of bubble sizes and large deviations in the corresponding advection velocities. This middle part corresponds to transition of the bubble size, owing to fragmentation and coalescence, mainly from larger to smaller size. Large bubbles that have higher advection speed follow the leading air film and smaller bubbles that have lower advection speed are released to the tail of the swarm. At the rear of the swarm, only small bubbles remain and some of them populate bubble columns in the streamwise direction. The advection velocity of the streamwise vortices in the near-wall layer in single-phase flow is almost 10 times u_τ (see **Figure 3.10**) and is lower than the advection velocity of the leading air film. It is supposed that the

streamwise vortices near the upper wall are pushed aside or destroyed by the air film. After passing the air film, if the vortices are not destroyed by the air film and advection velocities of the vortices near the upper wall and with the swarm are maintained for the conservation of momentum, bubbles in the swarm are advected with bubble–vortex interaction because, except for the large bubbles in the front of the swarm, advection velocities of the streamwise vortices near the upper wall and bubbles are almost the same.

3.4.3 Vortical structure beneath the swarms

As mentioned in the previous **Subsection 3.4.2**, the bubble swarm led by large air films sweeps away liquid-phase fluid at the top boundary where longitudinal vortices were shown to exist in the **Subsection 3.4.1**. In this subsection, the whereabouts of vortical structures swept away by the bubbles are investigated using the present visualization technique. To avoid irregular light scattering on the bubble surface, the laser sheet is located in the lower layers beneath the bubble swarm, $y^+ \approx 100$. **Figure 3.18** shows low-pass-filtered snapshot images taken at $y^+ = 100$ for eight specific moments during the passing of a bubble swarm; (a) $t = 0$, the flow can be assumed as a single-phase flow like that in **Figure 3.10**(b), (b) $t = 0.24$ s, just before the swarm reaches the measurement area, (c) $t = 0.30$ s, arrival of the leading air film of the front of the swarm, (d) $t = 0.41$ s, after the large air films have passed, (e) $t = 0.64$ s, arrival of the middle part of the bubble swarm where smaller bubbles are released by fragmentation, (f) $t = 0.76$ s, departure of the middle part ; (g) $t = 1.00$ s, arrival of the tail of the swarm, and (h) $t = 1.50$ s, after the bubble swarm has passed. White lines in the images indicate outlines of bubbles obtained from the original image. There are complex color patterns presented in the images. This indicates that there are vortical structures below the bubbles. To characterize these structures, their advection velocities are determined employing the same procedure summarized in the **Subsection 3.4.1**. **Figure 3.19** shows the advection velocities obtained at $y^+ = 100$, where the dashed line represents the averaged advection velocity of the vortical structures obtained under the single-phase condition at $y^+ = 100$. Before the bubble swarm reaches the measurement area, $t < 0.24$ s, the velocities are the same as for the single-phase condition. However, the velocities are affected by passing bubbles when the bubble swarm passes the test section. The velocity decreases by a maximum of 14%. Relating to the structure of the experimental channel, the result defies common sense because the mean velocity of the main flow should increase when bubbles are injected into the limited cross-sectional area of a closed channel. It is supposed that the observed phenomenon is caused by bubble–streamwise vortex interactions. Although the averaged advection velocity of bubbles in the horizontal channel flow is equal to or lower than the velocity of the main flow, the air films at the front of the bubble swarm move faster than the flow structure near the wall. Therefore, streamwise vortices in the buffer layer are destroyed or pushed below the bubble swarm by the air films. Here,

it is assumed that the streamwise vortices dive under the action of the large air films because vortices are not destroyed immediately by contact with a free interface so as to maintain their momentum (Willmarth et al., 1988; Bernal and Kwon, 1989). The diving streamwise vortices, which have lower advection velocity in the buffer layer than structures in the deeper layer, exist under the bubble layer and push the existing structures into a deeper layer. Hence, the measured velocities of structures under the swarm of bubbles are lower than those before the passing of the swarm and have values between velocity of structure near the upper wall and velocity of structure in a slightly deeper layer with single-phase flow while the bubble swarm passes. At the rear of the swarm, around t = 1.35 s, the advection velocities of vortical structures return to the original velocities. Small bubbles are released from large air films by fragmentation and seem to be arranged along the streamwise direction as columns (see **Figure 3.17**(h)). Considering the number of columns in the spanwise direction and the linear spectrum for the single-phase flow shown in **Figure 3.12**(a), it is supposed that the small bubbles are captured between two vortices because of the balance between buoyancy acting on the bubbles and drag due to the streamwise vortices. A similar pattern has already been reported from numerical simulation: small bubbles in a turbulent boundary layer are ejected between two streamwise vortices (Harleman et al., 2011). There are two possibilities for the origin of these streamwise vortices. The first is that the streamwise vortices that have dived beneath the leading air films maintain their structure until the bubble swarm has passed. The second is that the original structures dissipate and the structures are reproduced by skin friction on the upper wall because of the negligibly small influence of small bubbles on the flow structures.

To evaluate the description of streamwise vortices being brought beneath the bubble swarm, quantitative information of vortical structures (i.e., length and tilting angle of the vortices) in the visualized image shown in **Figure 3.18** are extracted employing the same procedure introduced in the **Subsection 3.4.1**. **Figure 3.20** shows the instantaneous probability density distribution of the streamwise vortex at each time corresponding to the snapshot images shown in **Figure 3.18**. The probability density distributions are calculated using 200 frames of the snapshot image that correspond to a period of 0.05 s. Before the bubble swarm reaches the measurement area (see **Figure 3.20**(a) and (b)), the distributions take a shape similar to those for the single-phase flow shown in **Figure 3.14**(b). Under the large air films (see **Figure 3.20**(c)), the distribution has a characteristic observed in the near-wall layer of single-phase flow shown in **Figure 3.14**(b); i.e., the distribution is extended around the zero angle corresponding to the streamwise vortices. This indicates that the streamwise vortices are brought beneath the large air films by the invasion of the large air films as we expected. This characteristic is maintained at least until $t \approx 0.64$ s as indicated in **Figure 3.20**(d) and (e). Around that time, large bubbles fragment into smaller bubbles, and larger bubbles follow the leading air films and smaller bubbles withdraw from the swarm. At the next time step (**Figure 3.20**(f)), the typical shape of the probability density distribution tends to

disappear and the distribution is restored to the original shape under the single-phase condition as in **Figure 3.14**(b) at the rear of the swarm (**Figure 3.20**(h)) via an intermediate state (**Figure 3.20**(g)). As shown in **Figure 3.18**(h), very small bubbles remain in the flow at the tail of swarm. These bubbles, however, do not affect the vertical structure in the visualized layer because of small bubble size and low local void fraction.

3.5 Conclusions

We investigated transformations of vortical structures in turbulent boundary layers of a horizontal channel flow during passage of a bubble swarm. The swarm is regarded as a single shot of a void wave, which is introduced into the flow by a short duration of air injection. To quantitatively visualize vortical structures, a novel visualization technique was established using aluminum flakes and two laser sheets of different colors that are projected in opposite directions. The technique characterized the structure of a buffer layer and a logarithmic layer in the boundary layer of single-phase flows in terms of advection velocity, spacing in the spanwise direction between two structures, and streamwise length and angle, without measuring the fluid flow velocity. The results of visualizations for the single-phase condition are consistent with knowledge of boundary layers; i.e., existence of longitudinal vortices in the buffer layer, their decay in the wall-normal direction, and the wavenumber of vortices. Injected bubble swarms consist of larger bubbles at the front (leading air films) and smaller bubbles at the tail. The leading air films have higher advection speed than the smaller bubbles, and fragmentation of the films into smaller bubbles provides fluctuations of the local void fraction even inside the swarm. Since the advection speed of the leading air films is also higher than that of the longitudinal vortices existing around the same height with the films, the longitudinal vortices in the boundary layer are swept away from the layer by the film. The present visualization clarified that the swept vortices do not disappear but survive on the backside (i.e., the opposite side of the wall) of the films during the passage. The vortices then retake their original positions near the wall with repositioning of the bubbles aligned along the vortices at the tail of the swarm.

• Nomenclature and units

C_f	friction coefficient, dimensionless
H	height of the channel, m
h	half height of the channel, m
k_{gap}	wavenumber of coherent structures, m^{-1}
l_{major}	length of streamwise vortex, m
l_τ	friction length, m
Re	Reynolds number, dimensionless
t	time, s
t_{in}	duration of bubble injection, s
U	cross-sectional mean velocity of the test fluid, m/s
u_{bubble}	advection velocity of bubble, m/s
$u_{structure}$	advection velocity of coherent structures, m/s
u_τ	friction velocity, m/s
W	width of the channel, m
x, y, z	x, y, z coordinates in the channel, dimensionless
y^+	wall units, dimensionless
α	void fraction during the injection of bubbles, dimensionless
θ	angle of streamwise vortex relative to the streamwise direction, degree
λ_B	wavelength of blue laser, m
λ_G	wavelength of green laser, m
ν	kinematic viscosity of the test fluid, m^2/s
ρ	density of the test fluid, kg/m^3
σ	surface tension of the test fluid, N/m
τ_s	shear stress at the upper wall, Pa

• References

Abcha N., Latrache N., Dumouchel F. and Mutabazi I., 2008. Qualitative relation between reflected light intensity by Kalliroscope flakes and velocity field in the Couette–Taylor flow system, *Exp. Fluids* **45**, 85–94.

Bernal L.P. and Kwon J.T., 1989. Vortex ring dynamics at a free surface, *Phys. Fluids A* **3**, 449–451.

Ceccio S.L., 2010. Frictional drag reduction of external flow with bubble and gas injection, *Annu. Rev. Fluid Mech.* **42**, 183–203.

Cenwell B.J., Coles D. and Dimotakis P., 1978. Structure and entrainment in the plane of symmetry of a turbulent spot, *J. of Fluid Mech.* **87**, 641–672.

Dean R.B., 1978. Reynolds number dependence of skin friction and other bulk flow variables in two-dimensional rectangular duct flow, *Trans. ASME J. Fluids Eng.* **100**, 215–223.

Deckwer W.D., 1980. On the mechanism of heat transfer in bubble column reactors, *Chem. Eng. Sci.* **35**, 1341–1346.

Fujiwara A., Danmoto Y., Hishida K. and Maeda M., 2004. Bubble deformation and flow structure measured by double shadow images and PIV/LIF, *Exp. Fluids* **36**, 157–165.

Fukuda K., Tokunaga J., Nobunaga T., Nakatani T. and Iwasaki T., 2000. Frictional drag reduction with air lubricant over a super-water-repellent surface, *J. Mar. Sci. Technol.* **5**, 123–130.

Ganapathisubramani B., Longmire E.K. and Marusic I., 2003. Characteristics of vortex packets in turbulent boundary layers, *J. Fluid Mech.* **478**, 35–46.

Goto S., Kida S. and Fujiwara S., 2011. Flow visualization using reflective flakes, *J. Fluid Mech.* **683**, 417–429.

Hamilton J.M., Kim, J. and Waleffe F., 1995. Regeneration mechanisms of near-wall turbulence structures, *J. Fluid Mech.* **287**, 317–348.

Harleman M.J.W., Delfos R., Terwisga T.J.C.V. and Westerweel J., 2011. Dispersion of bubbles in fully developed channel flow, *J. Phys.: Conf. Ser.* **318**, 052007.

Hassan Y.A., Gutierrez-Torresb C.C. and Jimenez-Bernalb J.A., 2005. Temporal correlation modification by microbubbles injection in a channel flow, Int. Commun, *Heat Mass Transf.* **32**, 1009–1015.

Heijnen J.J. and Riet K.V., 1984. Mass transfer, mixing and heat transfer phenomena in low viscosity bubble column reactors, *Chem. Eng. J.* **28**, B21–B42.

Hibiki T. and Ishii M., 2002. Interfacial area concentration of bubbly flow systems, *Chem. Eng. Sci.* **57**, 3967–3977.

Iwasaki T., Nishimura K., Tanaka M. and Hagiwara Y., 2001. Direct numerical simulation of turbulent Couette flow with immiscible droplets, *Int. J. Heat Fluid Flow* **22**, 332–342.

Joshi J.B., Vitankar V.S., Kulkarni A.A., Dhotre M.T. and Ekambara K., 2002. Coherent flow structures in bubble column reactors, *Chem. Eng. Sci.* **57**, 3157–3183.

Kamp A.M., Chesters A.K. and Colin C., 2001. Bubble coalescence in turbulent flows: a mechanistic model for turbulence-induced coalescence applied to microgravity bubbly pipe flow, *Int. J. Multiphase Flow* **27**, 1363–1396.

Kandlikar S.G., 2004. Heat transfer mechanisms during flow boiling in microchannels, *ASME J. Heat Transf.* **126**, 8–16.

Kato H., Iwashina T., Miyanaga M. and Yamaguhi H., 1999. Effect of microbubbles on the structure of turbulence in a turbulent boundary layer, *J. Mar. Sci. Technol.* **4**, 155–162.

Kitagawa A. and Murai Y., 2013. Natural convection heat transfer from a vertical heated plate in water with microbubble injection, *Chem. Eng. Sci.* **99**, 215–224.

Kravchenko A.G., Choi H. and Moin P., 1993. On the relation of near-wall streamwise vortices to wall skin friction in turbulent boundary layers, *Phys. Fluids A* **5**, 3307–3309.

Kwangjai P., Gerald L. and Russel J.D., 1981. Determination of transition in Couette flow in finite geometries, *Phys. Rev. Lett.* ***74***, 1448–1450.

Latorre R., 1997. Ship hull drag reduction using bottom air injection, *Ocean Eng.* **24**, 161–175.

Lu J., Fernandez A. and Tryggvason G., 2005. The effect of bubbles on the wall drag in a turbulent channel flow, *Phys. Fluids* **17**, 095102.

McCormick M.E. and Bhattacharyya R., 1973. Drag reduction of a submersible hull by electrolysis, *Nav. Eng. J.* **85**, 11–16.

Murai Y., Oishi Y., Takeda Y. and Yamamoto F., 2006. Turbulent shear stress profiles in a bubbly channel flow assessed by particle tracking velocimetry, *Exp. Fluids* **41**, 343–352.

Murai Y., Fukuda H., Oishi Y., Kodama Y. and Yamamoto F., 2007. Skin friction reduction by large air bubbles in a horizontal channel flow, *Int. J. Multiphase Flow* **33**, 147–163.

Oishi Y., Murai Y., Tasaka Y. and Takeda Y., 2007. Motion of microbubbles relative to streamwise vortices in the wall turbulence, *Int. Conf. Multiphase Flow* **6**, 535.

Oishi Y., Murai Y., Tasaka Y. and Takeda Y., 2009. Frictional drag reduction by wavy advection of deformation bubbles, *J. Phys.: Conf. Ser.* **147**, 012020.

Oishi Y. and Murai Y., 2014. Horizontal turbulent channel flow interacted by a single large bubble, *Exp. Therm. Fluid Sci.* **55**, 128–139.

Qu W. and Mudawar I., 2003. Flow boiling heat transfer in two-phase micro-channel heat sinks – I. Experimental investigation and assessment of correlation methods, *Int. J. Heat Mass Transf.* **46**, 2755–2771.

Robinson S.K., 1991. Coherent motions in the turbulent boundary layer, *Annu. Rev. Fluid Mech.* **23**, 601–639.

Sheng J., Malkiel E. and Katz J., 2009. Buffer layer structures associated with extreme wall stress events in a smooth wall turbulent boundary layer, *J. Fluid Mech.* **633**, 17–60.

Smith C.R. and Metzler S.P., 1983. The characteristics of low-speed streaks in the near-wall region of a turbulent boundary layer, *J. Fluid Mech.* **129**, 27–54.

Sugiyama K., Takagi S. and Matsumoto Y., 2001. Multi-scale analysis of bubbly flow, *Comput. Methods Appl. Mech. Eng.* **191**, 689–704.

Willmarth W.W., Tryggvason G., Hirsa A. and Yu D., 1988. Vortex pair generation and interaction with a free surface, *Phys. Fluids A* **2**, 170–172.

Zacksenhouse M., Abramovich G. and Hetsroni G., 2001. Automatic spatial characterization of low-speed streaks from thermal images, *Exp. Fluids* **31**, 229–239.

Zhen L. and Hassan Y.A., 2006. Wavelet autocorrelation identification of the turbulent flow multi-scales for drag reduction process in microbubbly flows, *Chem. Eng. Sci.* **61**, 7107–7114.

Zhou Z., Wang Z. and Fan J., 2010. Direct numerical simulation of the transitional boundary-layer flow induced by an isolated hemispherical roughness element, *Comput. Methods Appl. Mech. Eng.* **199**, 1573–1582.

- **Figures**

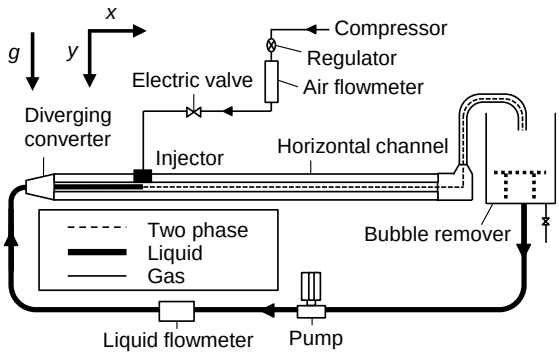

Figure 3.1 Schematic diagram of the experimental facility.

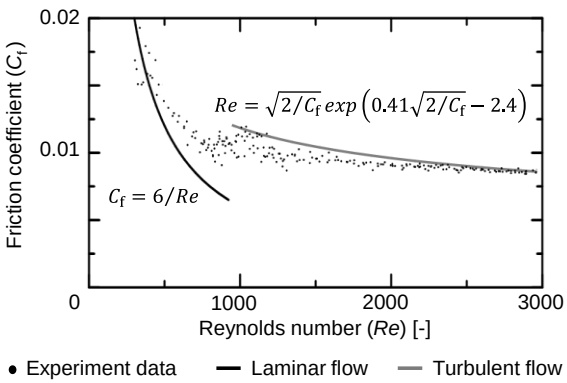

Figure 3.2 Relation between the friction coefficient and Reynolds number under single-phase conditions for the present experimental channel, where solid lines are the theoretical friction coefficient for laminar flows and semi-empirical friction coefficient for turbulent flows (Dean, 1978) and dots are the experimental data for the present facility.

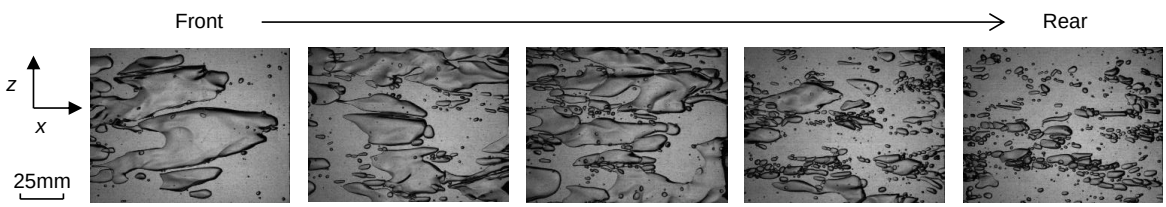

Figure 3.3 Snapshot pictures of a bubble swarm.

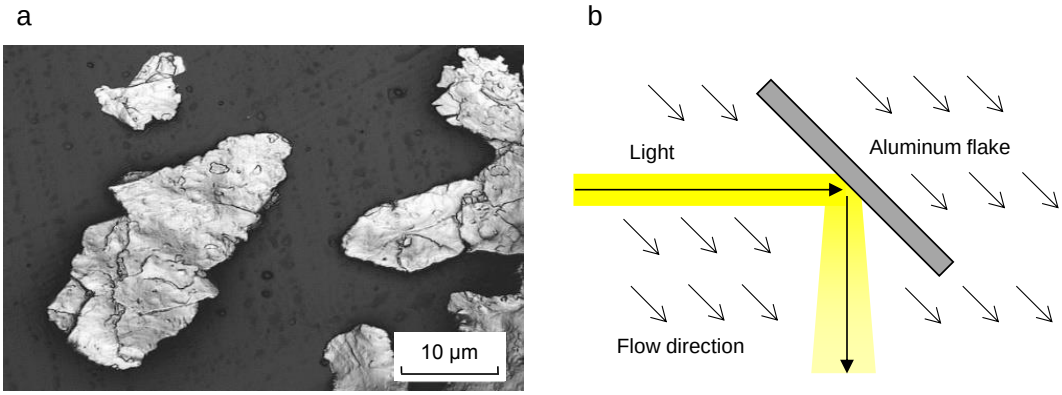

Figure 3.4 Characteristics of aluminum flakes; (a) microscopic image and (b) schematic diagram of light reflection.

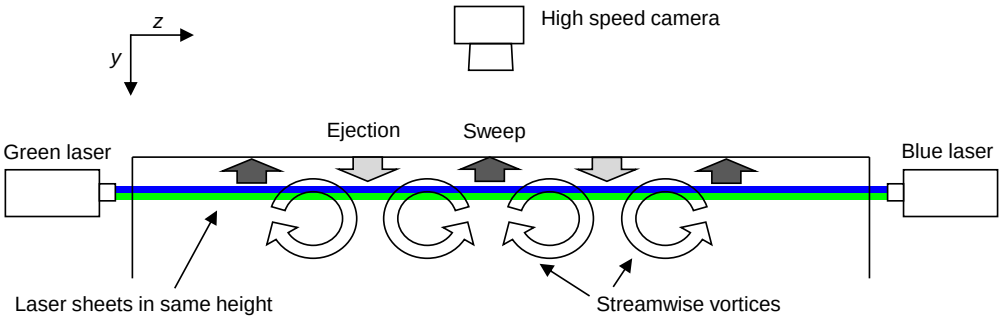

Figure 3.5 Schematic diagram of the visualization setup for streamwise vortices using two laser sheets and aluminum flakes.

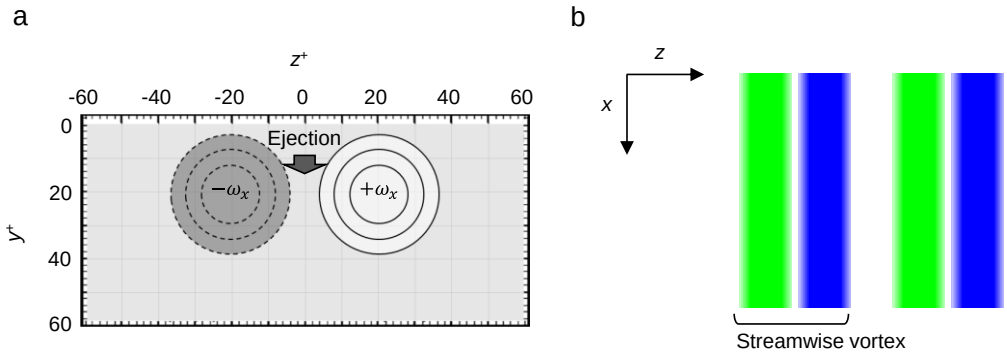

Figure 3.6 Ideal quasi-circular vortices; (a) contour of the vorticity component corresponding to a pair of vortices and (b) estimated color stripe patterns from the upper view of the test section corresponding to the estimated vortex arrangement.

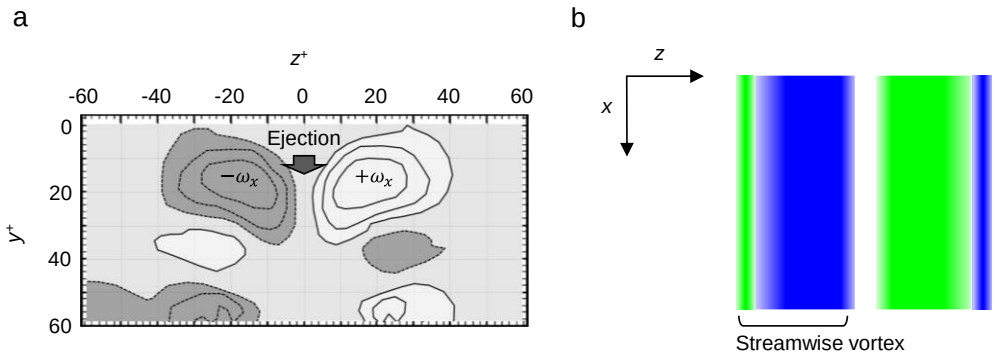

Figure 3.7 Distorted vortices obtained in a previous study for the channel flow; (a) contour of the vorticity component corresponding to a pair of vortices (Sheng et al., 2009) and (b) estimated color stripe patterns from the upper view of the test section corresponding to the estimated vortex arrangement.

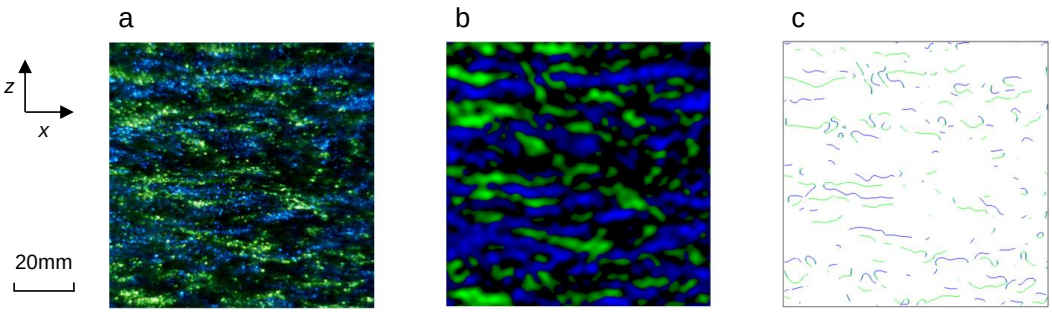

Figure 3.8 Sample of images taken in the near-wall layer, $y^+ \approx 50$, in a single-phase flow; (a) original image, (b) low-pass filtered image and (c) detected streamwise vortices.

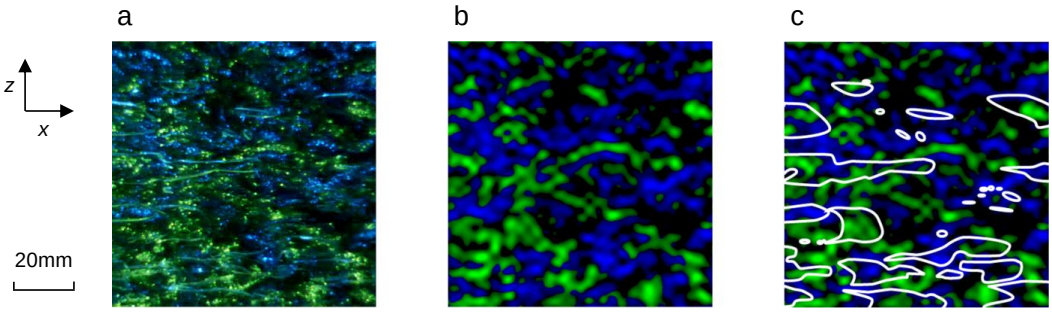

Figure 3.9 Sample of images taken beneath the bubble swarm, $y^+ \approx 100$; (a) original image, (b) low-pass filtered image and (c) flow structures with bubbles, where white lines are outlines of bubbles obtained from the original image.

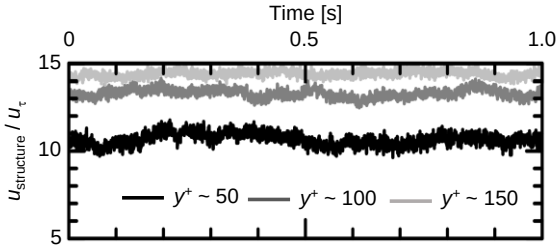

Figure 3.10 Averaged advection velocity of flow structures in the single-phase flow.

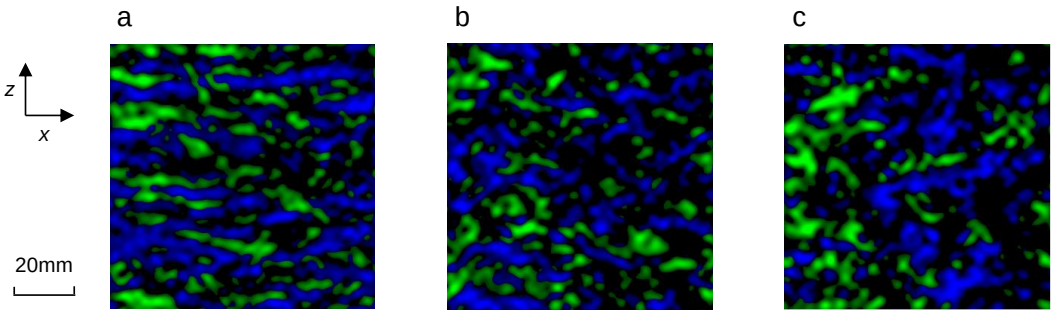

Figure 3.11 Low-pass-filtered image of visualized flow structures obtained at different heights under the single-phase condition; (a) near the upper wall ($y^+ \approx 50$), (b) slightly deeper layer ($y^+ \approx 100$) and (c) deepest layer ($y^+ \approx 150$).

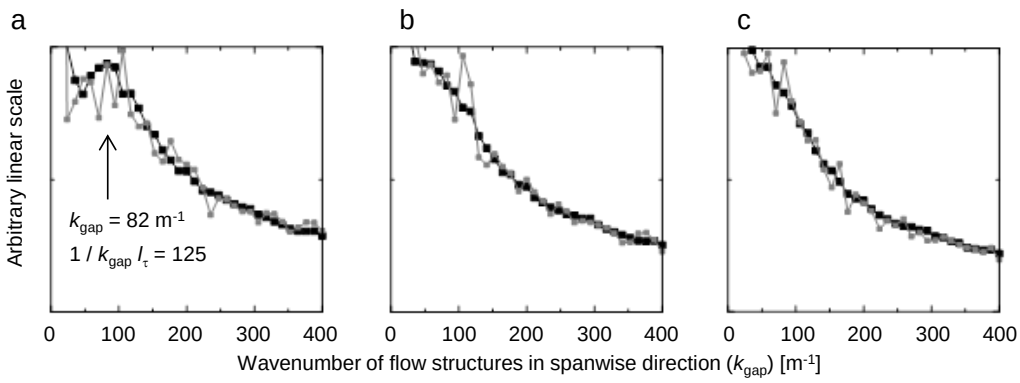

Figure 3.12 Wavenumber spectra of the low-pass filtered image of flow structures in the spanwise direction, z; (a) near the upper wall ($y^+ \approx 50$), (b) slightly deeper layer ($y^+ \approx 100$) and (c) deepest layer ($y^+ \approx 150$), where the gray line is for the snapshot image shown in Figure 3.11 and the black line is the spectrum averaged over 4000 sequential images.

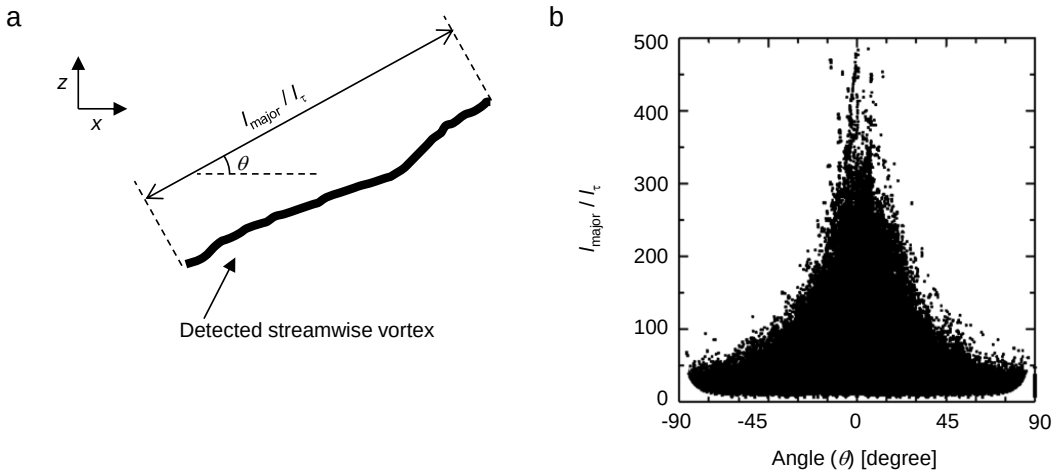

Figure 3.13 Length and angle elements of streamwise vortices near the upper wall; (a) definition of length and angle of the streamwise vortex and (b) scattergram of streamwise vortices.

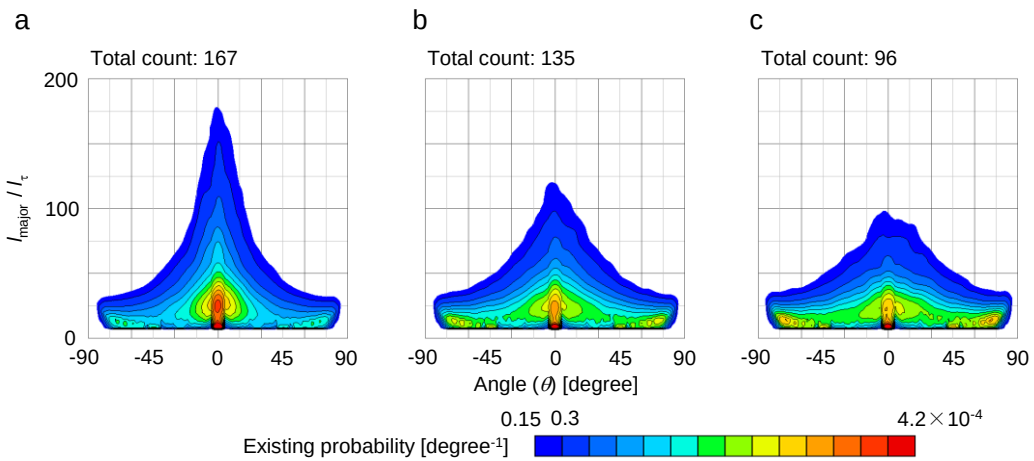

Figure 3.14 Probability density distribution of streamwise vortices in single-phase flow; (a) near the upper wall ($y^+ \approx 50$), (b) slightly deeper layer ($y^+ \approx 100$) and (c) deepest layer ($y^+ \approx 150$).

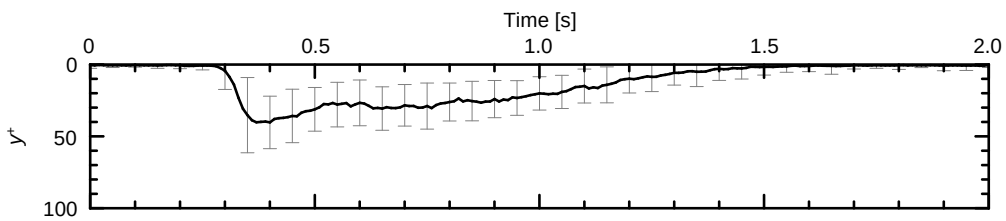

Figure 3.15 Phase-averaged height of the bubble swarm corresponding to that for the flake visualizations at the center of the channel, z/W = 0.5, where error bars represent the standard deviation of the bubble's height.

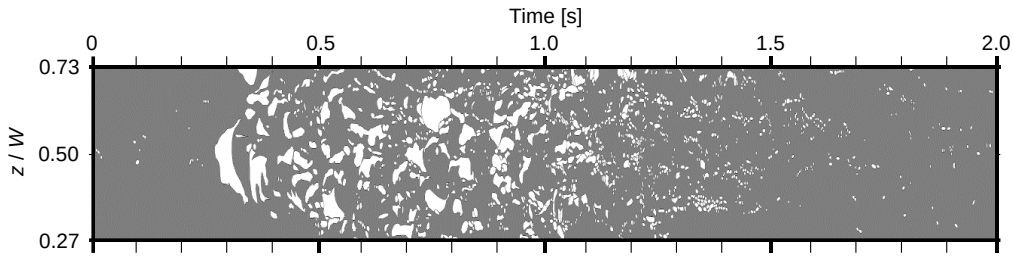

Figure 3.16 Line-scanned image of a bubble swarm, where the white area represents bubbles.

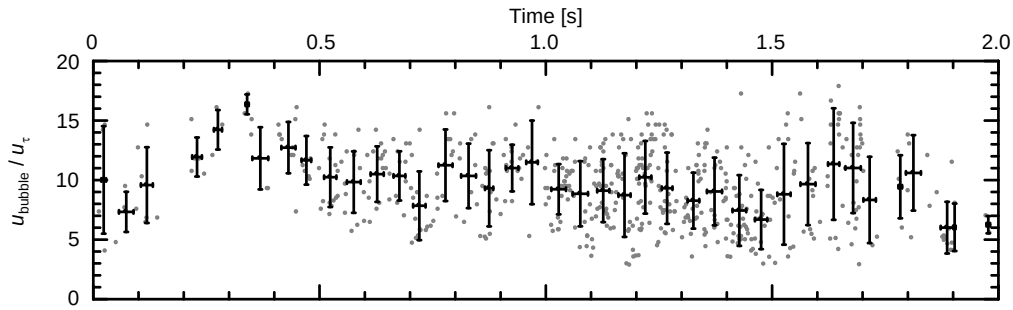

Figure 3.17 Advection velocities of bubbles in the central area of visualized images; gray and black dots respectively represent the velocity of individual bubbles and their average in 0.05 s intervals, where error bars represent the standard deviations of the velocity and time.

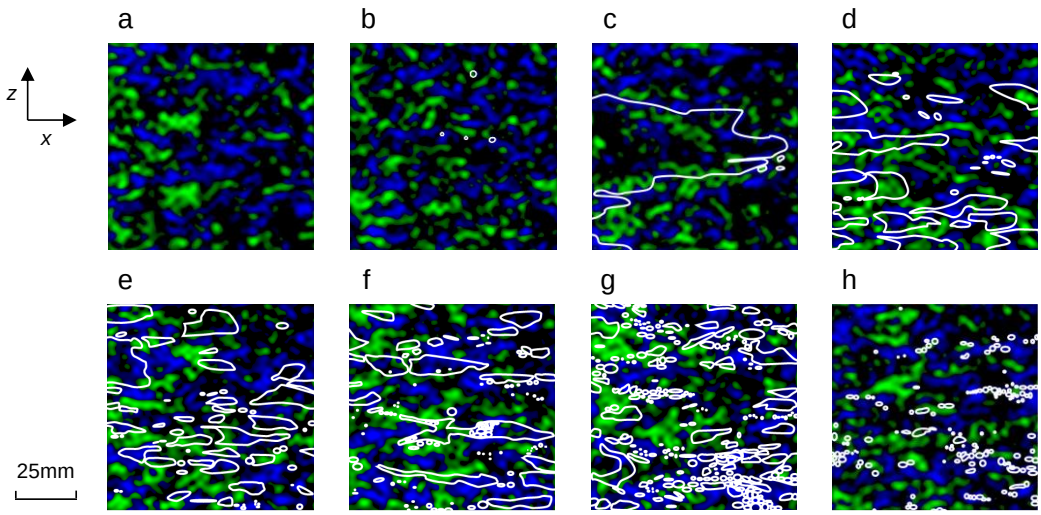

Figure 3.18 Snapshot images of vortical flow structure under the bubble swarm taken at $y^+ = 100$ for each time step; (a) $t = 0$ s, (b) 0.24 s, (c) 0.30 s, (d) 0.41 s, (e) 0.64 s, (f) 0.76 s, (g) 1.00 s and (h) 1.50 s, where white lines indicate the outlines of bubbles.

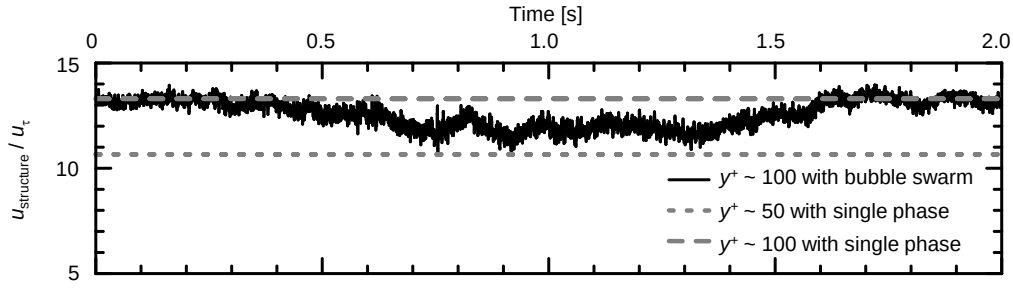

Figure 3.19 Averaged velocity of flow structures for each condition, where dashed lines are spatio-temporally averaged.

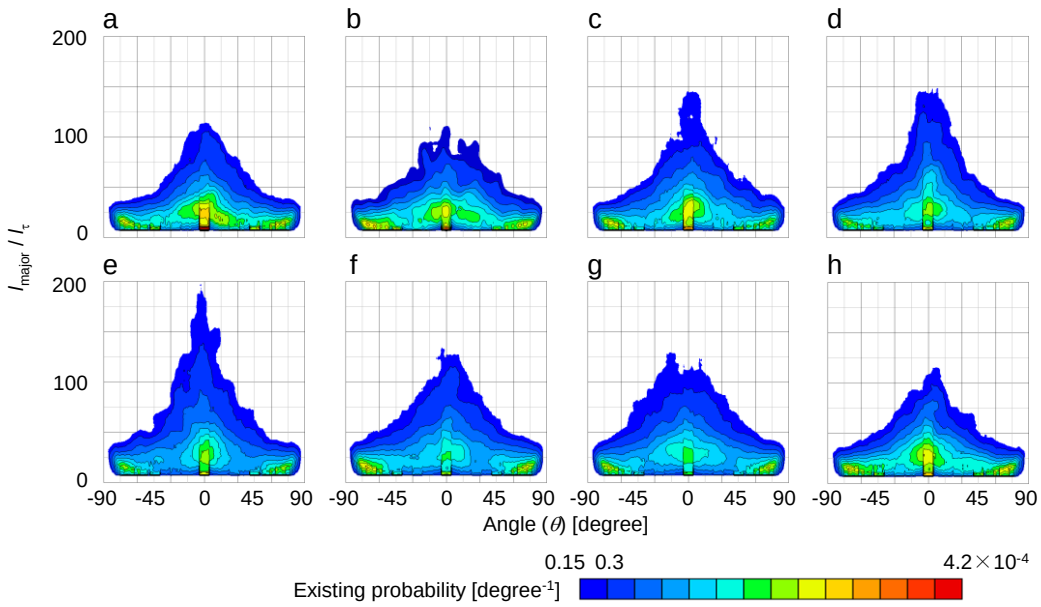

Figure 3.20 Probability density distribution of streamwise vortices under the bubble layer obtained at $y^+ = 100$ for each time step; (a) $t = 0$, (b) 0.24 s, (c) 0.30 s, (d) 0.41 s, (e) 0.64 s, (f) 0.76 s, (g) 1.00 s and (h) 1.50 s.

4 Drag reduction promoted by repetitive bubble injection in turbulent channel flows

• Preface

Reasons for recession of commercialization of bubbly drag reduction are mainly a low efficiency and a low reproducibility. To solve these problems, repetitive bubble injection (RBI) is suggested in the **Chapter 1**. In this chapter, RBI is adopted horizontal channel flows, and its performance and effects on the flows are statistically evaluated using several measurement instruments installed in the channel. At the first, the reproducibility of bubble swarms generated by RBI is estimated. And then, we estimate how much drag reduction is promoted by repetitive bubble injection comparing with continuous bubble injection, i.e. traditional injection. Finally, we estimate effects of the bubble swarms on the flows, and grasp mechanism of drag reduction with RBI by summarizing experimental results of this chapter and the **Chapter 3**.

4.1 Introduction

Turbulent boundary layer control by injection of bubbles into the boundary layer is expected to enhance the energy efficiency of vessels by reducing the frictional drag that constitutes nearly 80% of the total drag acting on large class vessels. This is also attractive to engineers because it offers installation simplicity and is pollution-free. This technique has been studied in a number of institutes to clarify the drag reduction mechanism and to enable practical use on actual vessels since McCormick and Bhattacharyya (1973) first introduced the technique. Some studies indicate the importance of modifications to the vortical flow structures in turbulent boundary layers caused by the fragmentation and deformation of bubbles; these structures create Reynolds shear stress that dominates the skin friction drag in turbulent flows (Meng and Uhlman, 1989; Kawamura and Kodama, 2002; Xu et al., 2002; Kitagawa et al., 2005; Jacob et al., 2010). As a practical demonstration, Kodama et al. (2005; 2008) evaluated the performance of this technique on a real vessel, a cement carrier named the Pacific Seagull, and a net power saving of approximately 5%, calculated based on the fuel consumption and the energy consumption required to inject bubbles, was reported. Other groups experimenting on the same vessel also reported that the maximum average drag reduction reached approximately 11% in their experiments (Hoang et al., 2009). These experimental results using a real vessel posed two problems, which must be addressed for practical applications: (i) high energy consumption occurs when injecting bubbles at the bottom of deep draft ships against hydrostatic pressure; (ii) only a small bulk drag reduction effect is obtained, whereas sufficient local drag reduction can be realized. Adoption of huge vessels with shallow draft can avoid the first problem but restricts general use of the technique for various other types of vessel. In fact, to cause relatively low or negative drag reduction effects, researchers have indicated that two-phase flow structures in the case of low void fractions (i.e., the volume fraction of the bubbles) should be studied (Kato et al., 1999; van den Berg et al., 2007). Fatter bubbles that are comparable in size to the boundary layer thickness also increase the wall shear stress (Murai et al., 2007). **Figure 4.1** summarizes these known facts schematically. **Figure 4.1**(a) represents the existence of a critical void fraction, α_c, at which the wall shear stress becomes smaller than the original value without the bubbles. The value at which α_c appears depends on the Reynolds, Froude, and Weber numbers. Typically, α_c has a value of more than 0.1 in the case of low Reynolds number turbulent flows, and tends to infinity for laminar boundary layers containing spherical bubbles. **Figure 4.1**(b) illustrates the bubble size (D_b) dependency: microbubbles and air films achieve drag reduction by different mechanisms (Elbing et al., 2008), but very often intermediate-sized bubbles conversely increase the wall shear stress. The bubble-to-liquid interactions of these intermediate bubbles were measured by Oishi and Murai (2014), and their results indicate that inclusion of such fat bubbles should be avoided to obtain stable drag reduction performance. Also, the size of the bubbles generated by the most commonly used types of bubble generators, such as blowers, changes with

the void fraction. The bubbles are naturally small in size at low void fractions and become larger with increasing void fraction. This means that conventional bubble generators cannot control the bubble size and the void fraction independently, which means that the drag reduction performance could not be maximized using these generators.

A novel bubble injection control method is proposed to improve the efficiency of drag reduction produced by bubble injection and enables the historically accumulated knowledge of the parametric dependency to be applied effectively. The method involves control of repetitive bubble injection (RBI). This control is realized by simple open-close iteration of a valve for the bubble supply, but provides complex variability in the bubbly two-phase turbulent boundary layers to lead to new phenomenological discussions. This RBI scheme is expected to produce (i) concentration of the air resource to increase the local void fraction so that the system avoids a drag-increasing regime at low void fractions, (ii) reduction of the air volume flow rate required to introduce bubbles at deep locations where the hydrostatic pressure is high, and (iii) repetitive renewal of the vortical flow structures that develop inside the turbulent boundary layers. The first and second expectations are obvious, as the author mentioned in the previous paragraph. A previous work on flow visualization in the **Chapter 3** indicated that the RBI system provides reproducible bubble swarms in the downstream region with leading air films that insulate the vortical structures present in the turbulent boundary layer from the wall. Interestingly, we found that the most of the vortical structures survive underneath the bubble swarms and their capability to create frictional drag on the wall, as in the single-phase condition, may be restored after the passage of the leading air films, although with a considerable delay. This series of visualizations has indicated to us that the renewal time of the vortical flow structures promotes drag reduction as a third effect of RBI, and this effect can be added to the previously mentioned purposes of RBI.

The RBI method that is adopted in this chapter injects bubble swarms with locally high void fractions into a turbulent boundary layer at controlled intervals. Even if the mean void fraction is set to be low, these bubble swarms produce strong void fraction fluctuations within the boundary layer to maintain the two-way interaction between the bubbles and the liquid flows. As it will be shown later in this chapter, individual bubble swarms are always led by local air films that refresh the turbulent boundary layer that is developing spatially in the streamwise direction. In this chapter, a new series of experimental data is reported and the data were obtained by multiple diagnoses, including the ultrasound Doppler method, which leads to an in-depth discussion of the improved performance of RBI-based drag reduction. As a platform for these investigations, a turbulent channel flow at relatively low Reynolds numbers, where $Re \approx 10^3$, is employed. In this regime, bubbly drag reduction hardly occurs in the case of continuous bubble injection (Oishi and Murai, 2014), and, contrastingly, the effects of RBI can be clearly distinguished. Since viscous modification by bubbles remains significant in this low Reynolds number turbulent flow regime,

we can discuss the reason why the drag reduction is promoted by RBI, based on comparing the wall shear stress and the Reynolds shear stress profiles.

4.2 Experimental setup

4.2.1 Setup and measurement equipment

A schematic diagram of the experimental apparatus is shown in **Figure 4.2**. The test section is a horizontal rectangular channel made from transparent acrylic resin, and is 40 mm high (H = 2h), 160 mm wide (W) and 6000 mm long. Silicone oil (KF-96-10cs, Shin-Etsu Chemical Co., Ltd.) is used rather than water as the working fluid to ensure the reproducibility of the experimental results by avoiding any uncontrollable influences of contamination of the bubble interfaces by tracer particles and other impurities, because the oil is a non-polar liquid. The kinematic viscosity (ν), density (ρ_0) and the surface tension of the silicone oil at 25°C are 10×10^{-6} m^2/s, 930 kg/m^3 and 20.1 mN/m, respectively. Spherical polyolefin fine powders called FLO BEADS (CL-2507, Sumitomo Seika Chemical Co., Ltd.) are adopted as tracer particles to measure the velocity vector fields. The average diameter of these particles (D_p) is 180 μm and the particle density (ρ_p) is 920 kg/m^3. Concerning the traceability in turbulence, relaxation time of the particles in the liquid phase (t_p) is estimated to be 0.27 ms as defined by

$$t_p = \frac{(2\rho_p + \rho_0)D_p^{\,2}}{36\nu\rho_0}. \qquad \textbf{Equation 4.1}$$

In the case of fully developed turbulent flow at the maximum bulk velocity at U_{bulk} = 2.0 m/s, Stokes number (St) of the particle, $St = t_p/t_\eta$, being estimated from the equivalent Kolmogorov time scale (t_η) is smaller than 0.07, thus sufficiently smaller than unity. A bubble injector plate, which has a single open slit with 10 mm in the streamwise side and 120 mm in the spanwise length, is mounted on the upper wall of the channel without step at x/H = 43.75 from the channel inlet, where the x, y, and z coordinates are defined as the streamwise distance from the channel inlet, the vertical downward coordinate from the upper wall and the spanwise location from the center between two side walls of the channel, respectively. The injector is connected to an electromagnetic valve so that the arbitrary temporal fluctuation in the gas flow rate is produced by a function generator. Bubble size is naturally determined by the balance between air flow rate and shear of the liquid flow at the outlet of the gas supplying slit. The balance changes also with operation scheme of the repetitive bubble injection which is explained in the next **Subsection 4.2.2**. Bubbles that reach the end of the channel are removed from the oil in a swirling tank set at the channel outlet before re-entering into

a pump. Equipment to be used for the various measurements is located more than 20*H* away from the bubble injector to investigate the downstream development of bubbly flows.

Two 4 MHz ultrasonic transducers are attached to the bottom wall of the channel 25*H* away from the injector to act as ultrasonic velocity profilers (UVPs) and measure the internal flow structures. The distance between the two transducers is 0.25*H* in the streamwise direction and the transducers are set at different angles, ±8° from the vertical axis, while maintaining line symmetry. The active diameter of the transducer used to generate the ultrasonic beam is 5 mm and the divergence half-angle of the beam is 2.2°. In this set-up, UVP detects local instantaneous velocity of liquid phase along the measurement line at the spatial resolution of 5 mm in the diameter and 0.5 mm in the beam direction. The resolution is insufficient to detect velocity fluctuation smaller than the Kolmogorov length scale, $\eta \approx 0.20$ mm, in the channel flows. However, the turbulence larger than the resolution is correctly measured in a non-invasive way. Furthermore, local instantaneous variation of the gas-liquid interface is also captured by the same set-up of UVP so that two-phase flow structure is visualized quantitatively as a function of time. The ultrasonic beams generated by the two transducers cross near the upper wall of the channel, and thus the interactions between bubbles that are migrating close to the upper wall and the liquid flow structure are investigated. From the instantaneous velocity vector information obtained in the crossed area, which is obtained by the two synchronized UVPs, turbulence characteristics such as the Reynolds shear stress profiles are evaluated in a similar manner to the system used by Taishi et al. (2002) for turbulent pipe flows. Ultrasonic absorbing boards are attached to both the upper and lower walls of the channel around the measurement line of the UVPs to eliminate multiple reflections from ultrasonic waves that would otherwise remain around the measurement section. The absorbing board is set to be a part of the channel wall such that it would not affect the local boundary layer structures. To estimate the wall friction, a shear transducer, which measures the local wall shear force directly, is mounted 21.25*H* away from the injector on the upper wall. Similar sensors were used to investigate the wall shear stress of bubbly flows in several previous studies (Guin et al., 1996; Kodama et al., 2000; Moriguchi and Kato, 2002).

All of these measurement instruments are synchronized in the present set-up, so that we can simultaneously capture data for multiple different physical quantities to evaluate the internal frictional drag reduction mechanism enabled by RBI. The measurement conditions are summarized in **Table 4.1**. In the table, the spatial resolution of 0.5 mm means a velocity profiling resolution in ultrasound beam direction, which is determined by a half wavelength of ultrasonic pulse, $cC/2f_u$, where c, C and f_u are the speed of sound in the liquid, the cycle number of waves constituting the ultrasonic pulse, and the ultrasonic frequency, respectively. Since the velocity profile obtained from a single shot of ultrasonic pulse remains noisy, UVP signal processor reduces the noise in the profile using repetition of ultrasonic pulses to take short time average during tens of pulse

repetition. In the experiments, the ultrasonic pulse emission was repeated 28 times for noise reduction, which results in the temporal resolution at 10 ms.

The Reynolds number of the flow is defined as

$$Re = \frac{U_{\text{bulk}} h}{\nu} = \frac{Q_{\text{liquid}}}{2W\nu}, \qquad \textbf{Equation 4.2}$$

where U_{bulk}, ν and Q_{liquid} are the bulk mean velocity, the kinematic viscosity and the volumetric flow rate of the liquid phase. The hydraulic equivalent diameter of the channel flow is calculated to be 4.5H, and the Reynolds number of a pipe-equivalent is therefore 4.5 times larger than the Re that was defined for the channel flow. In this chapter, the Re is defined under liquid single-phase conditions and is unmodified when considering the bubbles' contributions to the mean density, the effective viscosity, and the acceleration of the liquid flow velocity. According to the friction coefficient (C_f) data measured from the shear transducer, there is a transition regime from laminar to turbulent flows in the $800 \leq Re \leq 1200$ range, as shown in **Figure 4.3**. The experiments described in this chapter target flows where $Re > 1200$ to assess the effects of RBI in the turbulent flow regime.

4.2.2 Repetitive bubble injection (RBI)

The electromagnetic valve used to control the bubble injection has three different states, which are switched using control signals created by the function generator: these are the always closed state, the always open state and the periodically opened state. The definition of the temporal opening control of the valve is illustrated in **Figure 4.4**, where P, t_{open} and Q_{gas} are the valve operation period, the opening time of the valve and the instantaneous gas flow rate, respectively. When the valve opens, the injected bubbles have a local void fraction that is estimated using

$$\alpha_{\text{local}} = \frac{Q_{\text{gas}}}{Q_{\text{liquid}} + Q_{\text{gas}}}. \qquad \textbf{Equation 4.3}$$

Figure 4.5(a)–(d) shows photographs of bubble images taken at each phase Φ in a single injection, from the top of the channel at the downstream measurement location where the bubbles flow from left to right. The RBI conditions in this case are $\alpha_{\text{local}} \approx 1.50\%$, $P = 2.00$ s and $t_{\text{open}} = 1.00$ s. The streamwise length of the bubble swarm is much longer than the side of the square photograph under these conditions. Each part of the bubble swarm is composed of bubbles of different sizes, ranging from 1 mm up to 100 mm. The front region of the bubble swarm is led by some split air films. Because the initial state of the bubbles right after bubble injection is confirmed to be homogenous in terms of bubble size, the air film occupation at the front part of the swarm at the downstream location indicates that the air films migrate slightly more quickly than the other

bubbles. The evidence is shown in **Figure 4.6**, where the averaged streamwise velocities of bubbles are measured separately from the optical visualized images, i.e. **Figure 4.5**. This is consistently explained by the drag reduction effect of the air films, i.e., they accelerate the liquid flow for reduced friction. The central part of the bubble swarm is composed of bubbles of various sizes. In this region, the bubbles change their sizes because of fragmentation and coalescence. Finally, at the rear part of the swarm, only small bubbles remain but some intermediate sized bubbles, 1 mm < D_b ≤ 8 mm, form streamwise chains. This phenomenon is explained by bubble accumulation into low-speed streaks of the turbulent boundary layer, where the buoyancy of the bubbles also supports their accumulation (Harleman et al., 2011). However, bubbles of D_b ≤ 1 mm behave similarly to passive scalar along the wall, which is quasi-uniformly dispersed in the channel near the wall (Chouippe et al., 2014). **Figure 4.5**(e) shows a line-scanned image of the bubble swarm in two RBI cycles, where time progresses from left to right, and the spatial structure of the swarm is interpreted as the structure running from right to left. It has thus been confirmed that RBI produces the bubble swarms periodically and stably with good similarity.

Figure 4.7 shows a sample of the measurement results obtained by the shear transducer under the same conditions that were used for the previous visualization. The gray flat line in **Figure 4.7** indicates the averaged shear stress obtained under the same conditions but without bubble injection. The wall shear stress obtained from the shear transducer under the periodic passage of the bubble swarms also largely fluctuated as expected from the bubble swarm visualized in **Figure 4.5**. The graph shows the fluctuations in two cycles of RBI, where there is reduced shear stress for much of the time, but several moments show spiked increases in the stress above the average stress of the single-phase flow. In the next **Section 4.3**, we will present the statistical trends of the wall shear stress in detail.

4.2.3 Gas–liquid interface detection

The gas–liquid interface can be detected using the echo signal from pulsed ultrasound (Matikainen and Irons, 1986; Murakawa et al., 2008). Murai et al. (2010) also developed a combination of three different algorithms that enabled various types of gas–liquid interface to be detected using a single ultrasonic transducer. The echo amplitude of the ultrasonic pulse in the flow configuration presented here is shown in **Figure 4.8**(a). The data is obtained from synchronized measurements with the wall shear stress shown in **Figure 4.7**. In the graph, the values of y/h = 0 and 1 correspond to the upper wall surface and the center of the channel, respectively. The bubbles and the tracer particles reflect ultrasonic pulses with different reflection ratios, depending on their acoustic impedance relative to the surrounding liquid. The echo amplitude provided by the tracer particles distributed in the liquid phase has an almost equal value of approximately 250 ± 50 in an arbitrary digit code, which is expressed using white color. This level is unmodified over time. In contrast, the

ultrasound is unable to penetrate the gas phase and this leads to total reflection from the first gas–liquid interface along the path of the ultrasound pulse. The echo amplitude at the interface thus jumps up as it is reflected back to the ultrasonic transducer (see the red spots in **Figure 4.8**(a)). This point indicates that the gas–liquid interface is almost perpendicular to the ultrasonic path. An interface with a larger displacement angle to the ultrasonic path provides an oblique reflection of the ultrasound, which deflects the pulse away from the transducer. The echo amplitude is thus found to have a smaller value than that of the tracer particles that are dispersed in the surrounding liquid, which are identified by the blue spots in the figure. Consequently, both the red and blue spots in the figure form a profile of the location and the shape of the gas–liquid interface. Thus, detection of the variously-sized bubbles produced by RBI is possible if an adequate threshold is applied to the echo amplitude distribution that is measured in the two-dimensional space-time domain. The corresponding interface detection result is shown in **Figure 4.8**(b) where the regions above the first interface, i.e., the bottom surfaces of individual bubbles is colored black. The interface detection is performed by two-value thresholding; the echo intensity under 180 or over 290. When compared with the bubble distribution recorded by the camera (**Figure 4.5**(e)), it is confirmed that the technique presented here using the echo information works appropriately. However, it was noted that bubbles smaller than 2 mm will not always be detected because of weakened mirror reflection within the ultrasonic beam diameter of approximately 5 mm.

4.2.4 Velocity vector measurements

The UVP measurements provide a velocity component in the beam direction at all positions along the beam (Takeda 1991; 2012). Therefore, if two ultrasonic transducers are arranged in line symmetry as shown in **Figure 4.9**, a local velocity vector field is obtained near the beam crossing point. The velocity vector at the beam crossing point, **u**, is calculated as

$$\mathbf{u} = (u, v) = \left(\frac{\xi_1 - \xi_2}{2\sin\theta}, \frac{\xi_1 + \xi_2}{2\cos\theta} \right), \qquad \textbf{Equation 4.4}$$

where ξ_i is the velocity component along the ultrasonic beam direction, (u, v) are the streamwise and vertical velocity components of the liquid flows, respectively, and θ is the angle of the beam from the vertical axis. In this experiment, the transducers were arranged to measure the velocity vectors close to the upper wall: the beam-crossing point is located at $y/h \approx 0.22$. For measuring the velocity vectors at all the position in channel height, a frozen hypothesis is applied in the narrow region between two ultrasound beams; velocity vectors due to turbulence being invariant during the short horizontal advection between the beams. To perform this measurement with higher spatial resolution, the distance between the two ultrasonic transducers was set to be short enough at 10 mm, while θ was set to be small enough at ±8°. Reynolds shear stress from the velocity vector measured

in the beam crossing volume is always underestimated due to lack of spatial resolution. The underestimation expands as separating from the beam cross point as reported by Taishi et al. (2002). In our approach, the bias error is reduced by setting the two transducers installed narrowly so that beam crossing volume is elongated in the vertical direction as shown in **Figure 4.9**. The beam crossing angle at $\theta = \pm 8°$ allows us to secure the beam crossing volume reaching entire range of the half height of the channel; $0<y/h \leq 1.11$. Below this angle hinders accuracy of streamwise velocity obtainable from the UVPs. When combining the detected gas–liquid interface and the velocity vector fields in the liquid phase, the characteristics of the RBI-originated flow structure of bubbly two-phase flows in the channel can be fully and consistently investigated using the UVPs.

4.2.5 Controllability of RBI

Figure 4.10 shows a probability distribution for bubble existence in a single period of RBI at the downstream measurement location. The data is calculated by phase averaging of 12 swarms taken from the ultrasonic echo information that was explained in the previous **Subsection 4.2.3**, where the valve settings for RBI are P = 2.00 s and t_{open} = 1.00 s. **Figure 4.11** shows the average duration of a bubble swarm, i.e., the swarm persistence length in the time dimension, which is computed from the phase-averaged data of the bubble probability by thresholding with a half value (0.5). The error bars in the figure represent the standard deviation that occurs out of phase in RBI, which means cycle-by-cycle fluctuations in the swarm length. The results show that the duration is longer than the corresponding injection time, t_{open}, under all valve conditions. This is explained by the streamwise diffusion of the bubbles, which is subject to a velocity gradient with turbulence. In particular, the tail of the swarm, which consists of small bubbles, tends to migrate more slowly than the head of the swarm, as mentioned earlier. This gradually expands the swarm in the streamwise direction to elongate it from 25% up to 100% at x/H = 20 from the injection point. However, the duration is controlled in accordance with the given injection time, and increases monotonically with that injection time. It is also important to note that the duration is unaffected by changes in the valve operation period, P. In addition, the standard deviation is restricted to remain sufficiently small in comparison to the mean value. Therefore, we are able to conclude that the bubble swarms generated by the RBI instruments presented here have sufficient controllability and reproducibility to allow us to commence the parametric study.

4.3 Results and discussions

4.3.1 Drag reduction by continuous bubble injection

To discuss the effects of RBI, it is necessary to understand the drag reduction enabled by the commonly used continuous injection style. **Figure 4.12** shows the envelopes of the bubble interfaces in continuously injected bubbles at α_{mean} = 1.50% in a turbulent channel flow of $Re \approx$ 2200, where α_{mean} is the time-mean void fraction, which is the same as the local void fraction (α_{local}). The upper wall is almost entirely covered with many bubbles under this condition. **Figure 4.13** shows velocity distributions in the single-phase flow and the two-phase flow. Relative gradual increase of the averaged velocity at the single-phase flow indicates that the flow is an undeveloped turbulent flow, which is intentionally targeted in the present study. There is a dip of velocity near the center of channel, $y/h \approx 1$, due to measurement error of UVP from multi-reflection of ultrasonic wave. This technical problem is known among UVP users; UVP inevitably produces erroneous velocity data in a limited range along the measurement line when applied to the acoustic environment causing multi-reflection of ultrasonic wave. Channel flow confined narrowly by two parallel plates is typical cases, and thus we encounter the difficulty to completely avoid the appearance of local inaccurate data points (Murai et al., 2006). The position of erroneous data appearance is adjustable by modifying ultrasonic pulse repetition intervals. Our solution employed is to shift the erroneous range to the channel center so that the velocity profile near the wall is measured properly.

Because a boundary of the turbulent buffer layer is estimated to lie around 40 wall units from the upper wall in the single-phase flow case, almost all of these bubbles exist inside the original turbulent boundary layer, as profiled in **Figure 4.13**. The projection void fraction ($\alpha_{proj.}$), which is scaled on the top of the graph, is defined as the time-mean ratio of the bubble segment at each depth from the wall to the total sampling time obtained from the UVP echo signal. From the measured liquid streamwise velocity profiles, it is clearly seen that the velocity with bubble injection is faster than that of the single-phase flow alone. There are two reasons for this fact. One is decrease in hydrodynamic effective area for liquid flow due to occupation of gas layer in the channel. This causes global velocity increment, being estimated by equation of continuity. Another is alternation of stress boundary condition at the top of liquid phase from solid wall to free surface. This provides asymmetric velocity profile with increasing of the velocity in the top half and decreasing in the bottom half of the channel. These two effects appear simultaneously to result in the measured liquid velocity profile that is largely accelerated in the upper half of the channel.

To obtain the basic drag reduction performance produced by continuous bubble injection, the wall shear stress of the upper wall is measured as a function of the bulk-mean void fractions in the 0% $\leq \alpha_{mean} \leq$ 1.50% range. The maximum value of α_{mean} =1.50% is set thus because the upper wall

is almost completely covered with bubbles at this value. **Figure 4.14** shows the time-averaged percentage of the drag reduction effect, *DR*, on the upper wall, where the error bars represent the standard deviation of the temporal fluctuation component. This effect is defined as

$$DR = 1 - \frac{\tau_{\mathrm{mean}}}{\tau_0}, \qquad \textbf{Equation 4.5}$$

where τ_{mean} and τ_0 are the time-mean shear stress of the bubbly flows and the single-phase flow, respectively. The frictional Reynolds number in the single-phase flow, which is defined by

$$Re_{\tau 0} = \frac{h u_{\tau 0}}{\nu} = \frac{h\sqrt{\tau_0}}{\nu\sqrt{\rho_0}}, \qquad \textbf{Equation 4.6}$$

is 160, where the frictional velocity, $u_{\tau 0}$, is determined using

$$u_{\tau 0} = \sqrt{\frac{\tau_0}{\rho_0}}, \qquad \textbf{Equation 4.7}$$

where ρ_0 is the density of the liquid and h is the channel half height. In the continuous injection case, drag reduction is observed at higher void fractions, while the drag actually increases with bubble injection at lower void fractions, i.e., where $\alpha_{\mathrm{mean}} \leq 0.50\%$. The same trend has been reported by a number of previous researchers (e.g. Murai et al., 2007; Ceccio, 2010). To estimate the drag reduction sensitivity, a gain factor is estimated from the measured wall shear stresses; this factor is simply defined as $G = DR/\alpha_{\mathrm{mean}}$. The gain indicates the magnitude of the drag reduction percentage per unit of the percentage void fraction. If G exceeds unity, then it implies that the drag reduction is effectively amplified by more than the density reduction of the fluid caused by the mixing of the bubbles. Further large positive values of G indicate higher bubbly drag reduction efficiencies. The gain factor of the continuous bubble injection as a function of the mean void fraction is shown in **Figure 4.15**, where the error bars indicate the standard deviations of the data. The results show that the gain factor has a high value of around 17 at $\alpha_{\mathrm{mean}} \approx 1.50\%$, and that it gradually descends with decreasing α_{mean}. The descent trend becomes steep at around $\alpha_{\mathrm{mean}} < 1.0\%$ and the gain factor falls to a negative value for $\alpha_{\mathrm{mean}} < 0.5\%$. From the data acquired, we require bubbles that are at least larger than 0.5% in terms of their mean void fraction to obtain acceptable drag reduction performance, as long as the bubbles are injected continuously over time.

4.3.2 Drag reduction with RBI

The time chart of RBI is defined by opening the electromagnetic valve for short times (t_{open}) during the RBI operation period (P) with a fixed local void fraction (α_{local}), as shown in **Figure 4.16**. The simplest expectation is that the local value of the gain factor (G) during the passage of the bubble

swarms would maintain the same value under continuous bubble injection conditions at the same α_{local}. In this case, the total drag reduction effect, *DR*, is estimated using the occupation rate of the gas–liquid two-phase condition in time as:

$$DR = t_{\mathrm{open}} P^{-1} \alpha_{\mathrm{local}} G \,. \qquad \textbf{Equation 4.8}$$

In comparison with this, various complex phenomena would have to be combined to produce extra drag reduction effects in reality, which can be expressed as deviations (DR_{+}) from the above formula as follows:

$$DR = t_{\mathrm{open}} P^{-1} \alpha_{\mathrm{local}} G + DR_{+} \,. \qquad \textbf{Equation 4.9}$$

To evaluate the sign and the magnitude of DR_{+} clearly, we set a sufficiently high local void fraction, where $\alpha_{\mathrm{local}} \approx 1.50\%$, in this series of RBI performance tests. This void fraction is set for two reasons. The first is scientific interest, i.e., the drag reduction retains large sensitivity around this void fraction, as we confirmed for continuous bubble injection (see **Figure 4.15**), and it is therefore interesting to see how the effect is amplified by RBI for the same local void fraction. Another reason is a technical restriction, i.e., the extra component DR_{+} may be buried within the standard deviations of the shear stress when a low local void fraction is used for the RBI. **Table 4.2** shows the experimental conditions used to estimate the drag reduction by RBI in the flow at the fixed Reynolds number of $Re \approx 2200$, which was also used in the previous **Subsection 4.3.1**.

Figure 4.17 shows the percentage of the time-averaged drag reduction (*DR*) during RBI as the mean void fraction α_{mean} increases. Here, α_{mean} is varied using a combination of two parameters, i.e., the valve operation period (*P*) and the valve opening time (t_{open}). The plots and the error bars denote the mean values and their standard deviations, respectively, which are statistics taken from 20 measurement cycles, each of which takes a sampling time of 20 s. It is confirmed that the *DR* always has positive values over the entire tested mean void fraction range from 0 to 1.50%. Thus, the increasing drag region has been completely eliminated by RBI. The dashed line in the figure indicates the expected value of *DR* that was calculated using **Equation 4.8**. When $\alpha_{\mathrm{mean}} \geq 0.30\%$, the *DR* curve shows a convex variation because the measured value is larger than the expected value. This new result means that RBI provides a positive extra effect in terms of promoting drag reduction, which is associated with more complex responses, and happened to a two-phase turbulent boundary layer when subjected to periodic passage of bubble swarms.

Figure 4.18 shows the extra component of the drag reduction percentage, DR_{+}, which was defined by and computed using **Equation 4.9**. Although the standard deviation cannot be ignored in any case, the extra effect obtained is approximately 2% for $\alpha_{\mathrm{mean}} < 0.3\%$. This value of 2% might be considered to be low in engineering applications, but we emphasize the fact that a positive value

is obtained, which infers that clarification of the internal two-phase flow structure could lead to further amplification of DR_+.

4.3.3 Modification of the velocity field by RBI

The RBI provides not only void fraction fluctuations, but also acceleration and pulsation of the liquid flow both in and out of the boundary layer. These influences on each phase interact to produce a new effect in the form of the extra drag reduction mentioned earlier. **Figure 4.19** and **Figure 4.20** show the time-averaged distributions of the projection void fraction under each RBI condition and the corresponding distributions of the mean streamwise velocity in the liquid phase, which is accelerated by the bubbles. The data for the single-phase flow and the continuous bubble injection regimes are attached to these graphs for comparison. From **Figure 4.19**, it is confirmed that the local void fraction increases monotonically with increasing valve-opening time in any valve operating period case. The void fraction profiles seem to be similar to each other among all cases, including that of continuous bubble injection. Thus, RBI does not lead to any special phenomenon occurring in the vertical profile of the time-averaged void fraction. In contrast, the data in **Figure 4.20** shows that the mean liquid velocity in the RBI case remains almost the same as that of the single-phase flow case, unlike the continuous bubble injection case. This is explained by the disappearance of the bubble blockage effect, which is significant only for continuous bubble injection. By considering the mean liquid velocity profiles near the upper wall, it is also found that the velocity is locally accelerated with RBI in comparison to the single-phase flow value. This fact is consistent with the interpretation that the liquid phase flows smoothly near the upper wall when RBI provides a high level of drag reduction. From these two findings, it can be concluded that RBI concentrates all the effects of the bubbles into the boundary layer structure without changing the mean flow field out from the boundary layer.

To clarify the scenario described above, the phase-averaged streamwise velocity of the liquid phase is calculated. Here, the existence of bubbles at each measurement point is distinguished by the echo intensity, and only the velocity data corresponding to the liquid phase is used to calculate the streamwise velocity. One of the sample results is shown in **Figure 4.21**, where points at which all of the velocity data are distinguished as being gas phase data are represented as a white area. The experimental conditions used for the sample were P = 2.00 s and t_{open} = 1.00 s, which are the same as those for **Figure 4.8**, **Figure 4.10** and **Figure 4.20**(d). The figure clearly indicates that the streamwise velocities of the liquid phase under the bubble swarm are faster than those before the passage of the swarm. This becomes so because hydrodynamic effective cross-sectional area of the liquid flow is narrowed due to occupation of gas layer near the upper wall. Also, the replacement of the upper boundary for liquid flow from solid wall to free surface induces asymmetric base flow, partly analogous to open channel flows. These two effects make the streamwise velocity larger in

the upper half of the channel. On the other hand, the velocity pulsation of the liquid phase is insignificant in far region from the bubble swarm, $y/h > 0.4$. It is because the liquid phase near the bubble swarm, $y/h < 0.3$, is accelerated enough to conserve volume flow rate of the liquid phase. In general, artificial pulsations into a wall-bounded flow increase the average wall shear stress in turbulent flow regimes (Scotti and Piomelli, 2001; Blel et al., 2009). However, RBI result does not belong to this category and behaves rather more like a shear-thinning fluid, which has lower flow resistance in pulsatile flows.

To discuss the pulsation effect that is caused in the liquid phase, we must consider the possibility that the pulsatile flow itself promotes drag reduction, regardless of the material used for repetitive injection. To evaluate this consideration experimentally, the drag reduction percentage (*DR*) is measured in the case where the same amount of liquid is injected instead of the air bubbles at the same local volume fraction, $\alpha_{\mathrm{local}} \approx 1.50\%$, from the injector. The results are shown in **Figure 4.22**, where the repetitive injection conditions are $t_{\mathrm{open}} = 1.00$ s, $P = 2.00$ s and $\alpha_{\mathrm{mean}} \approx 0.76\%$. In both the cases of continuous and repetitive injections, the injection of the liquid causes large increases in the frictional drag, which results in negative *DR* values. Moreover, the repetitive injection makes the drag increment more than that with the continuous injection although amount of injected liquid is sufficiently low. In contrast, air bubble injection maintains positive *DR* values. Thus, the pulsatile effect contributes to the drag reduction only in the air bubbles case. When we consider the regeneration of the vortices by the pulsatile flow (Sykes et al., 1986) and the increase in the mean velocity caused by the liquid injection, the increasing percentage of drag caused by the liquid injection is understood to be reasonable. If the pulsations on the main flow promote drag reduction with RBI, then the wall shear stress should be lower than that in the continuous injection case, even with liquid injection. However, with repetitive liquid injection, the shear stress becomes higher than that in the continuous injection case. Kim and Sung (2003) simulated the effects of periodic blowing in a wind cross-flow and concluded that the turbulence intensities and the Reynolds shear stress are enhanced by injection in the downstream regions. Their conclusions agree with the presented experimental indications under the liquid injection conditions.

Based on these facts, we reach an understanding that the pulsatile flows of the liquid phase that are caused by RBI will enhance the wall shear stress, but this is not the case when the high-speed flow region coincides with a region that has a gas–liquid interface as a near-wall side boundary. In parallel, the local drag reduction caused by the bubble swarm allows the liquid beneath the swarm to flow more quickly. These two phenomena, which happen naturally at the boundary layer during RBI, provide stable and extra drag reduction.

For a deeper understanding of what occurs during RBI in the turbulent channel flows, the Reynolds shear stress profiles are calculated as averages of $u'v'$, where u' and v' are the time fluctuation components of the velocity vector field in the liquid phase that were measured using the

pair of ultrasound transducers. The profiles, which were normalized with reference to $u_{\tau 0}$, are shown in **Figure 4.23**. It should be reminded that the Reynolds shear stress profiles obtained using the two synchronized UVPs are generally underestimated as explained before. The profiles presented here therefore show the Reynolds shear stress components organized by large eddies resolvable by the UVPs. The profile for the single-phase condition at least agrees with a previous report measured at a similar *Re* (Wei and Willmarth, 1989), although it causes 11% underestimation in the case of UVP. Furthermore, let us reconsider that the flow targeted here is not fully developed turbulent channel flow, but is in development at low *Re* numbers. In the developing state, local laminar velocity profiles passes occasionally so that the near wall region has a velocity gradient calmer than fully turbulent flows as we already mentioned previously. This is why the time-average Reynolds shear stress is earlier grown in the channel center so that it is reversely measured lower near the wall. Consistently, the local inclination of the Reynolds shear stress at the channel center for the single-phase flow is almost the same as that estimated from the wall shear stress indicated by the grey diagonal line shown in the figure. Although the underestimation in Reynolds shear stress occurs, they do represent the same tendencies as the real values if we assess only the relative change. When compared with the single-phase condition profile, all profiles in the bubbly flows vary authentically. In the bubbly flow, the Reynolds shear stress has higher values than that in the single-phase flow at the far-wall region, where $y/h > 0.4$. There are two reasons for this behavior: the downward displacement of the shear layer caused by the intrusion of the bubbly two-phase layer near the upper wall, and the accelerated liquid flow in the central part of the channel for a certain blockage effect. The increase in the peak value explains that the momentum-transferring eddies are activated at the position, being consistent to our previous work of flow visualization (in the **Chapter 3**) which found that turbulent eddies are survived and conveyed below split air-films. However the peak does not directly affect the wall shear stress due to shielding effect of void layer near the wall. The shielding effect means a phenomenon that turbulence cannot migrate beyond the air-films as the films are longer than the turbulent eddies. This is consistently explained by the relaxation of Reynolds shear stress gradient roughly identified in the graphs. The Reynolds shear stress gradients become about 0.3–0.4 times smaller than those of the single-phase flow, and this tendency is qualitatively analogous to the data of Kitagawa et al. (2005). Since the Reynolds shear stress gradient is proportional to the wall shear stress in fully developed turbulent flows, the relaxation of the gradient in bubbly flow explains delay of turbulent momentum transfer in the wall-perpendicular direction. Therefore, RBI provides turbulence–modification type of drag reduction due to intermittent shielding effect of the air films which intensifies the local peak below the air films but calms down the gradient of Reynolds shear stress far from the wall.

Here we need to clearly distinguish the terminology on the effect of void layer; “blockage effect” and “shielding effect” which have different meaning. Blockage effect induces liquid

velocity increment entirely in the channel as liquid volume flow rate is fixed during bubbles occupy the near wall layer. Shielding effect is cut-off of turbulence momentum diffusion beyond the layer of individual air-films. In RBI operation, a point of study is the fact that these two effects are mixed and interacted unsteadily as being paid attention in the next **Subsection 4.3.4**.

4.3.4 RBI sensitivity to different Reynolds numbers

In this subsection, the sensitivity of RBI to the Reynolds number (*Re*) is investigated to evaluate applicability of RBI to higher *Re* conditions. Until here, the single-phase flow case, the continuous bubble injection case and two different cases of RBI were examined. The gas flow rate is fixed as a constant in all cases, while the liquid flow rate is increased to realize high *Re* flows so that the time-mean void fraction α_{mean} decreases for higher *Re* conditions. The experimental conditions are summarized in **Table 4.3**.

The drag reduction obtained for each *Re* is shown in **Figure 4.24**. Because the mean void fraction is set to be low (α_{mean} < 0.55%; see **Figure 4.13** and **Figure 4.14**), continuous bubble injection does not significantly modify the frictional drag under all *Re* conditions (see the dark gray boxes). The drag actually increases under lower *Re* conditions, which means that the drag reduction produced by bubble injection is advantageous for higher *Re* conditions. This trend has already been reported in many types of flow facility (van den Berg et al., 2007; Murai, 2014). In contrast, RBI produces a different drag reduction tendency (see the light gray and white boxes). At *Re* = 1700, the drag is increased by RBI to about 13%, which is 10% higher than that for continuous bubble injection. However, RBI does not change the drag so greatly at *Re* = 2300. At the highest condition of *Re* = 2700, RBI clearly starts to reduce the drag, particularly under the gently injected bubble conditions, where t_{open} = 1.00 s. If the bubbly drag reduction occurs due to the modified viscosity, percentage of drag reduction would be decreased as the Reynolds number increases. However, the data shows that drag reduction is rather promoted. This implies that there is insignificant role in the modified viscosity in present operation of RBI.

The modification of the Reynolds shear stress events has already been shown and discussed. However, the Reynolds shear stress is a time statistic-based value, and it is therefore difficult to discuss its relationship to the internal unsteady flow structure of the liquid caused by RBI. Here, we visualize time-dependent profiles of the Reynolds shear stress that is modified by the bubble swarms. Based on the reproducibility of both the bubble swarms and the corresponding flow field, the time-dependent shear stress field is computed as the phase-average distribution. **Figure 4.25** shows the result for t_{open} = 0.50 s for three different *Re*, for which the color bar is normalized relative to the squared friction velocity of the single-phase condition, $u_{\tau 0}$. The data in the figure indicate the differential component of the local value of $u'v'$ from the time-average distribution of the single-phase flow. Thus, the red and blue regions in the figure indicate increasing and

decreasing local Reynolds shear stress, respectively. The bubble swarm is painted black in each figure, where the front of each swarm is set at the initial phase angle, $\Phi = 0$ rad. The bubble swarms depicted are defined by their phase-averaged structures, which are distinguished as areas that have gas-existence probabilities that are higher than 0.50.

At low *Re*, the bubble swarm accompanies an area of high local Reynolds stress underneath the swarm (**Figure 4.25**(a)). This means that the bubble swarm produces velocity fluctuations to its ambience because the flow field remains in a nearly laminar state at this *Re*. With increasing *Re* (**Figure 4.25**(b)), the velocity fluctuations can be transported downstream and can survive against viscous dissipation, and this promotes the flow transition to a turbulent flow as a trigger of the disturbance. At even higher *Re*, the high Reynolds shear stress is no longer produced beneath the bubble swarm (**Figure 4.25**(c)), and in contrast, the region turns towards reduction of the shear stress. This local shear stress reduction is explained by the relaxation of the turbulence in the vicinity of the gas–liquid interface, i.e. the free-slip stress condition halts the growth of the turbulence eddies. In addition, the bubble swarm in the drag reduction state can flow downstream slightly more quickly than the liquid flow velocity. With this relative motion, the bubble swarm sweeps the fluid containing the vortical structures of the turbulence ahead of the swarm. This phenomenon was visualized in the **Chapter 3**, and we succeeded in obtaining consistent data for the Reynolds shear stress distribution here. In the previous paper, it was confirmed that the streamwise vortices in the buffer layer are swept under the bubble swarm and restore themselves after passing the swarm. It is generally known that these streamwise vortices and their bursting promote momentum transfer that results in the Reynolds shear stress. Therefore, a combination of the observed behavior of the streamwise vortices and the measured Reynolds shear stress reduction under the bubble swarm indicates that the swept streamwise vortices play a major role in lowering the momentum transfer. **Figure 4.26** shows the quadrant expression for the velocity fluctuations in the same layer, where $y/h \approx 0.25$, in the single-phase flow and under the bubble swarm, in the 0 rad $< \Phi < 2\pi/3$ rad range, generated by RBI with $t_{\mathrm{open}} = 0.50$ s at $Re \approx 3000$. **Figure 4.26**(a) and (b) show values calculated from the instantaneous velocity vectors obtained by the UVPs. Under the bubble swarm, the scattering of the velocity fluctuation shrinks in the vertical direction and lies more in the streamwise direction. This means that the turbulent vortical structure only survives in the tangential direction to the bottom surface of the bubble swarm, and loses the momentum transfer action.

4.4 Conclusions

We proposed the RBI technique to promote frictional drag reduction. RBI is proposed specifically to improve the drag reduction performance at low mean void fractions. The performance of RBI is

investigated comprehensively by measurement of the temporal variation of the local wall shear stress, the velocity vector field of the liquid phase, and the gas–liquid interface in turbulent horizontal channel flows. The flow conditions examined for the present RBI performance test are Reynolds number (Re) of $1700 \leq Re \leq 3000$, mean void fraction (α_{mean}) of$\alpha_{mean} \leq 1.5\%$, and bubble size (D_b) of $D_b \leq 100$ mm, respectively. RBI successfully generates bubble swarms periodically with suitably high reproducibility; these swarms have split air films on their front and small bubbles on their tails. These bubbles flow near the upper wall of the channel, which affect the upper boundary layer structure. This induces liquid flow velocity increment due to blockage effect for void occupation near the wall, and provides asymmetric mean velocity profile respect to the centerline of the channel. Another impact is alternation of upper stress boundary condition for liquid phase, which produces shielding effect of turbulence, i.e. presence of free surface near the solid wall. In RBI operation, these two effects take place unsteadily and interact to each other so that a new phenomenon comes up. As we expected prior to the experiments, the bubble swarms maintain a high gain factor for drag reduction because they provide locally high void fractions intermittently at low mean void fractions, which means that strong two-way interactions between two phases occur inside the turbulent boundary layer. When compared with continuous bubble injection, it is confirmed that RBI eliminates the drag increment region that previously occurred at low mean void fractions, and also produces an extra drag reduction component in addition to the void concentration effect. This extra effect is assessed via measurement of RBI's pulsatory effects on the liquid flow field. It is found that the mean liquid velocity at the far-wall region is not modified by RBI, while it is accelerated in the continuous bubble injection case. Instead, the near-wall structure of the turbulence is effectively altered by RBI. Evaluation of the wall shear stress for different Reynolds numbers indicated that RBI has advantages for application to the higher Re turbulent flows in the tested range. The Reynolds shear stress measured beneath the bubble swarm is obviously reduced for higher Re, which indicates relaxation of the turbulence because of the gas–liquid interface that lies close to the upper wall. When we consider these facts along with the results in the **Chapter 3**, it is suggested that the vortical structures that were swept by the local air films that lead the bubble swarm are reduced by these bubble swarms. In summary, the promotion of bubbly drag reduction by RBI is found to be provided by the following two major effects: i) isolation of the wall surface from the liquid flow by the reproducible intrusion of air films that naturally emerge in front of the bubble swarms during their advection; and ii) relaxation of the Reynolds shear stress events beneath the bubble swarm through sweeping of the vortical structures. Concerning the application of RBI to small bubbles comparable to turbulent eddy scales, we could expect different mechanism of drag reduction in which certain relaxation time outstands to sway the time-average drag. This is regarded as a separate topic, and set as our future work.

• Nomenclature and units

C	cycle of ultrasonic pulse, dimensionless
C_f	friction coefficient, dimensionless
c	speed of sound, m/s
D_b	bubble size, m
D_p	average diameter of tracer particles, m
DR	time-mean drag reduction, dimensionless
DR_+	extra drag reduction, dimensionless
G	gain factor, dimensionless
H	channel height, m
h	half channel height, m
P	valve operation period, s
Q_{gas}	gas flow rate at valve opening, m^3/s
Q_{liquid}	volumetric flow rate of test fluid, m^3/s
Re	Reynolds number, dimensionless
$Re_{\tau 0}$	frictional Reynolds number in single-phase flow, dimensionless
St	Stokes number, dimensionless
t	time, s
t_{open}	valve opening time, s
t_p	relaxation time of tracer particles in the liquid phase, s
t_η	Kolmogorov time scale, s
U_{bulk}	bulk mean velocity of test fluid, m/s
$\mathbf{u}$	velocity vector of test fluid, m/s
u_b	streamwise velocity of bubbles, m/s
u, v	streamwise and vertical velocity components of test flow, m/s
$u_{\tau 0}$	friction velocity in single-phase flow, m/s
W	channel width, m
x, y, z	x, y, z coordinates in channel, m
y^+	wall unit, dimensionless
α	void fraction, dimensionless
α_c	critical void fraction, dimensionless
α_{local}	void fraction during bubble injection, dimensionless
α_{mean}	time-mean void fraction, dimensionless
$\alpha_{proj.}$	projection void fraction, dimensionless
δ	turbulent boundary layer thickness, m
η	Kolmogorov length scale, m

θ	ultrasonic beam angle relative to vertical direction, degree
ν	kinematic viscosity of test fluid, m^2/s
ξ_i	velocity component along ultrasonic beam direction, m/s
ρ_0	density of test fluid in single-phase flow, kg/m^3
ρ_p	density of tracer particles, kg/m^3
τ	shear stress at upper wall, Pa
τ_{mean}	time-mean shear stress at upper wall, Pa
τ_0	time-mean shear stress at upper wall in single-phase flow, Pa
Φ	phase of bubble injection, rad
$< >$	phase-average
$\bar{}$	time-average

• References

van den Berg T.H., van Gils D.P.M., Lathrop D.P. and Lohse D., 2007. Bubbly turbulent drag reduction is a boundary layer effect, *Phys. Rev. Lett.* **98**, 084501.

Blel W., Le Gentil-Lelièvre C., Bénézech T., Legrand J. and Legentilhomme P., 2009. Application of turbulent pulsating flows to the bacterial removal during a cleaning in place procedure. Part 1: Experimental analysis of wall shear stress in a cylindrical pipe, *J. Food Eng.* **90**, 422–432.

Ceccio S.L., 2010. Frictional drag reduction of external flow with bubble and gas injection, *Annu. Rev. Fluid Mech.* **42**, 183–203.

Chouippe A., Climent E., Legendre D. and Gabillet C., 2014. Numerical simulation of bubble dispersion in turbulent Taylor–Couette flow, *Phys. Fluids* **26**, 043304.

Dean R.B., 1978. Reynolds number dependence of skin friction and other bulk flow variables in two-dimensional rectangular duct flow, *Trans. ASME J. Fluids Eng.* **100**, 215–223.

Elbing B.R., Winkel E.S., Lay K.A., Ceccio S.L., Dowling D.R. and Perlin M., 2008. Bubble-induced skin-friction drag reduction and the abrupt transition to air-layer drag reduction, *J. Fluid Mech.* **612**, 201–236.

Guin M.M., Kato H., Yamaguchi H., Maeda M. and Miyanaga M., 1996. Reduction of skin friction by microbubbles and its relation with near-wall bubble concentration in a channel, *J. Mar. Sci. Technol.* **1**, 241–254.

Harleman M.J.W., Delfos R., Terwisga T.J.C.V. and Westerweel J., 2011. Dispersion of bubbles in fully developed channel flow, *J. Phys.: Conf. Ser.* **318**, 052007.

Hoang C., Toda Y. and Sanada Y., 2009. Full scale experiment for frictional resistance reduction using air lubrication method, *Int. Offshore Polar Eng. Conf.*, 812–817.

Jacob B., Olivieri A., Miozzi M., Campana E.F. and Piva R., 2010. Drag reduction by microbubbles in a turbulent boundary layer, *Phys. Fluids* **22**, 115104.

Kato H., Iwashina T., Miyanaga M. and Yamaguchi H., 1999. Effect of microbubbles on the structure of turbulence in a turbulent boundary layer, *J. Mar. Sci. Technol.* **4**, 155–162.

Kawamura T. and Kodama Y., 2002. Numerical simulation method to resolve interaction between bubbles and turbulence, *Int. J. Heat Fluid Flow* **26**, 627–638.

Kim K. and Sung H.J., 2003. Effects of periodic blowing from spanwise slot on a turbulent boundary layer, *AIAA J.* **41**, 1913–1921.

Kitagawa A., Hishida K. and Kodama Y., 2005. Flow structure of microbubble-laden turbulent channel flow measured by PIV combined with the shadow image technique, *Exp. Fluids* **38**, 466–475.

Kodama Y., Kakugawa A., Takahashi T. and Kawashima H., 2000. Experimental study on microbubbles and their applicability to ships for skin friction reduction, *Int. J. Heat and Fluid Flow* **21**, 582–588.

Kodama Y., Takahashi T., Makino M., Hori T., Ueda T., Kawamura N., Shibata M., Kato H., Inoue T., Suzuki T., Toda Y. and Yamashita K., 2005. Practical application of microbubbles to ships – large scale model experiments and a new full scale experiment, *Int. Sympos. Smart Contr. Turbul.*, 213–218.

Kodama Y., Hinatsu M., Hori T., Kawashima H., Takeshi H., Makino M., Ohnawa M., Sanada Y., Murai Y. and Ohta S., 2008. A full-Scale air lubrication experiment using a large cement carrier for energy saving (Result and analysis). *Jpn. Soc. Naval Architects Ocean Eng.*, 163–166, (in Japanese).

Matikainen L. and Irons G.A., 1986. Ultrasonic system for the detection of transient liquid/gas interfaces using the pulse-echo technique, *Rev. Sci. Instrum.* **57**, 1661–1666.

McCormick M.E. and Bhattacharyya R., 1973. Drag reduction of a submersible hull by electrolysis, *Naval Eng. J.* **85**, 11–16.

Meng J.C.S. and Uhlman J.S., Jr., 1989. Microbubble formulation and splitting in a turbulent boundary layer for turbulence reduction, In: *Advances in Fluid Dynamics*, Springer; New York, 168–217.

Moriguchi Y. and Kato H., 2002. Influence of microbubble diameter and distribution on frictional resistance reduction. *J. Mar. Sci. Technol.* **7**, 79–85.

Murai Y., Fujii H., Tasaka Y. and Takeda Y., 2006. Turbulent bubbly channel flow investigated by ultrasound velocity profiler. *J. Fluid Sci. Technol.* **1**, 12-23.

Murai Y., Fukuda H., Oishi Y., Kodama Y. and Yamamoto F., 2007. Skin friction reduction by large air bubbles in a horizontal channel flow. *Int. J. Multiphase Flow* **33**, 147–163.

Murai Y., Tasaka Y., Nambu Y., Tasaka Y. and Gonzalez S.R., 2010. Ultrasonic detection of moving interfaces in gas-liquid two-phase flow, *Flow Meas. Instrum.* **21**, 356–366.

Murai Y., 2014. Frictional drag reduction by bubble injection, *Exp. Fluids* **55**, 1733.

Murakawa H., Kikura H. and Aritomi M., 2008. Application of ultrasonic multi-wave method for two-phase bubbly and slug flows, *Flow Meas. Instrum.* **19**, 205–213.

Oishi, Y. and Murai Y., 2014. Horizontal turbulent channel flow interacted by a single large bubble, *Exp. Thermal Fluid Sci.* **55**, 128–139.

Scotti A. and Piomelli U., 2001. Numerical simulation of pulsating turbulent channel flow. *Phys. Fluids* **13**, 1367–1384.

Sykes R., Lewellen W. and Parker S., 1986. On the vorticity dynamics of a turbulent jet in a crossflow, *J. Fluid Mech.* **168**, 393–413.

Taishi T., Kikura H. and Aritomi M., 2002. Effect of the measurement volume in turbulent pipe flow measurement by the ultrasonic velocity profile method (mean velocity profile and Reynolds stress measurement), *Exp. Fluids* **32**, 188–196.

Takeda Y., 1991. Development of an ultrasonic velocity profile monitor, *Nucl. Eng. Des.* **126**, 277–284.

Takeda Y. (Ed.), 2012. *Ultrasonic Doppler velocity profiler for fluid flow*, Springer; Japan.

Wei T. and Willmarth W.W., 1989. Reynolds–number effects on the structure of a turbulent channel flow, *J. Fluid Mech.* **204**, 57–95.

Xu J., Maxey M.R. and Karniadakis G.E.M., 2002. Numerical simulation of turbulent drag reduction using micro-bubbles, *J. Fluid Mech.* **468**, 271–281.

• Tables

Table 4.1 Measurement conditions.

Conditions for tracer particles		
Particle relaxation time (t_p)	0.27	ms
Maximum Stokes number (St_{max})	0.07	-
Conditions for UVPs		
Ultrasonic frequency	4	MHz
Cycles of ultrasonic pulse	4	-
Pulse repetitions	28	-
Time resolution	10	ms
Velocity resolution in bream direction	2.37	mm/s
Spatial resolution in bream direction	0.5	mm
Ultrasonic beam diameter	5	mm
Conditions for shear transducer		
Measurement area	25π	$(mm)^2$
Shear stress resolution	0.05	Pa
Time resolution	50	ms

Table 4.2 Experimental conditions.

Reynolds number (Re)	2200	-
Frictional Reynolds number in single-phase flow ($Re_{\tau 0}$)	160	-
Local void fraction (α_{local})	1.5×10^{-2}	-
Averaged void fraction (α_{mean})	$0 – 1.5\times10^{-2}$	-
RBI period (P)	2.00, 3.00, 4.00 and 5.00	s
Injection time (t_{open})	0.50, 1.00 and 1.50	s

Table 4.3 Experimental conditions.

Reynolds number (Re)	1700	2300	3000
Frictional Reynolds number in single-phase flow ($Re_{\tau 0}$)	126	160	200
Mean void fraction (α_{mean})	0.44 %	0.33 %	0.26 %
Injection time (t_{open}) = 0 s	Single-phase flow ($\alpha_{local} = \alpha_{mean} = 0$)		
Injection time (t_{open}) = ∞ s	Continuous injection ($\alpha_{local} = \alpha_{mean}$)		
Injection time (t_{open}) = 1.0 s	RBI period (P) = 3.00 s ($\alpha_{local} = 3\alpha_{mean}$)		
Injection time (t_{open}) = 0.5 s	RBI period (P) = 3.00 s ($\alpha_{local} = 6\alpha_{mean}$)		

- **Figures**

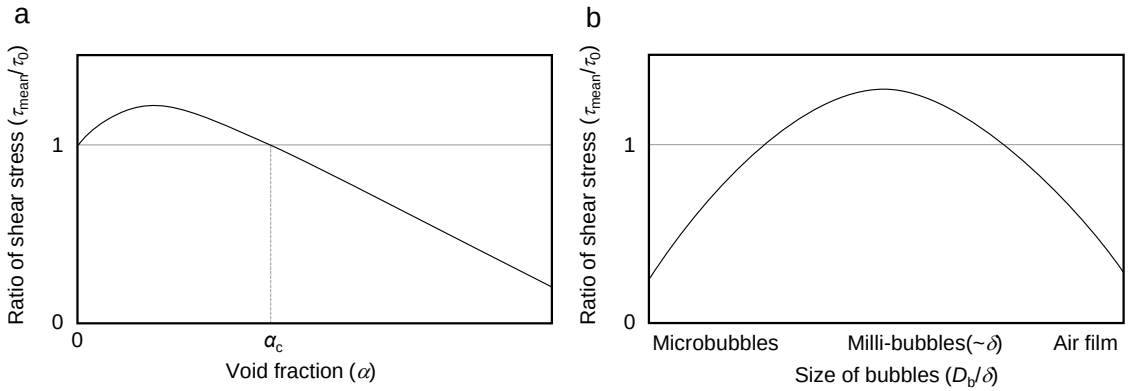

Figure 4.1 Schematic representations of wall shear stress modified by bubble injection parameterized in terms of (a) mean void fraction and (b) bubble size, where the flat lines represent the time-mean shear stress in the single-phase flow (τ_0), α_c is the critical void fraction required to obtain drag reduction, and δ is the turbulent boundary layer thickness.

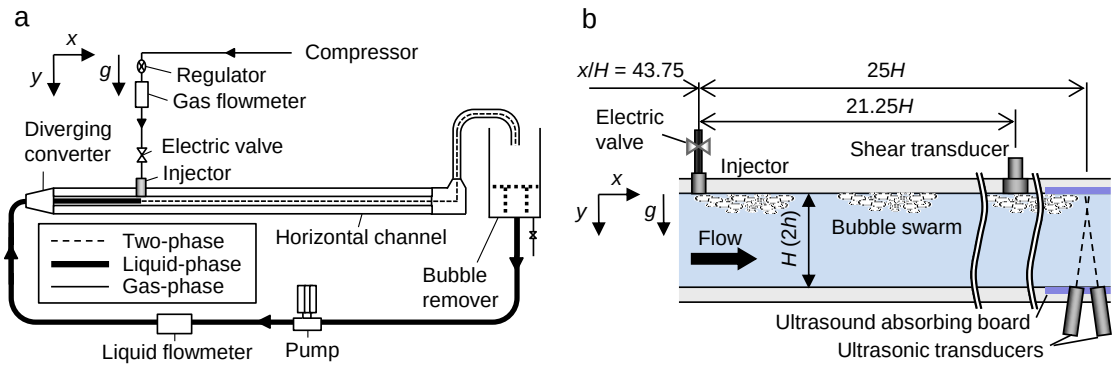

Figure 4.2 Schematic diagram of experimental setup: (a) overview and (b) details of the test section of the channel, where x and y are the distances from the channel inlet and from the upper wall, respectively, and the dashed lines indicate the ultrasonic beam paths from the ultrasonic transducer pair.

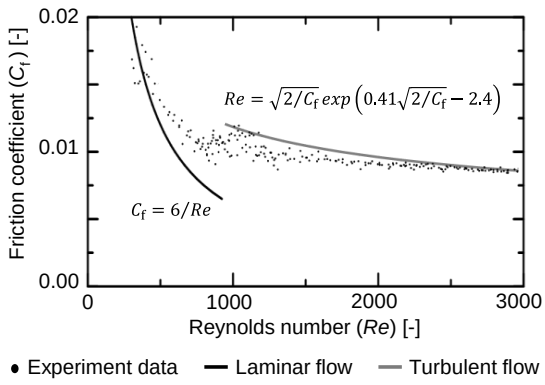

Figure 4.3 Relationship between the friction coefficient (C_f) and the Reynolds number (Re) under single-phase conditions for the experimental channel, where the solid lines indicate the variations in C_f reported by Dean (1978) and the dots are experimental data obtained using the present facility.

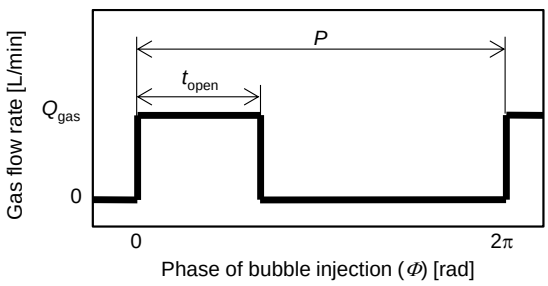

Figure 4.4 Time chart of the controlled gas flow rate for bubble swarm generation by the electromagnetic valve, where P, t_{open} and Q_{gas} are the valve operation period, the valve opening time and the instantaneous gas flow rate, respectively.

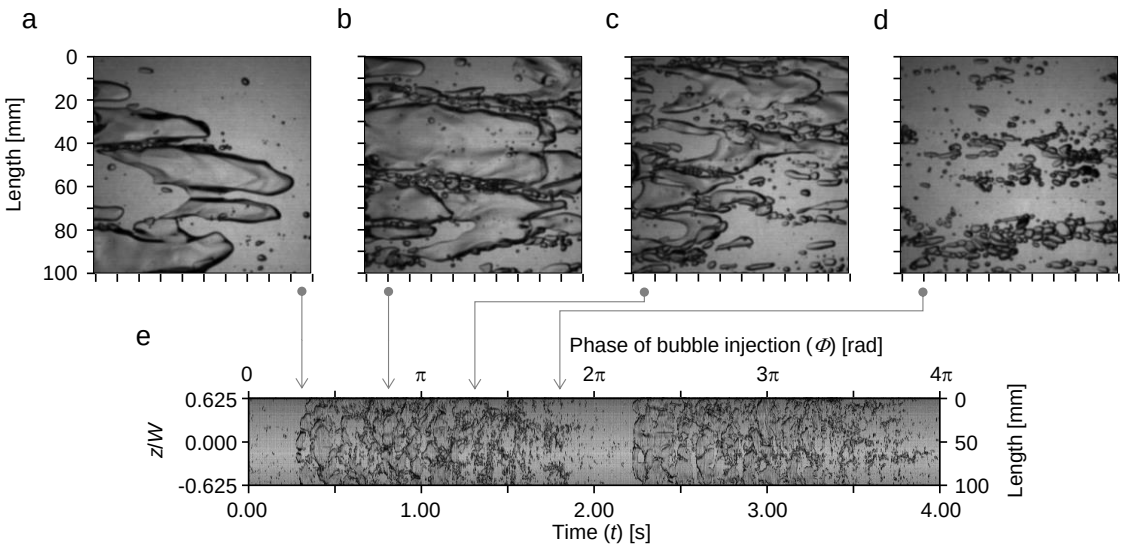

Figure 4.5 Photographs of bubble swarms generated by RBI that were taken by a camera located above the ultrasonic transducers; (a)–(d) show pictures at $\Phi = 0.3\pi$ rad, 0.8π rad, 1.3π rad and 1.8π rad, respectively, and (e) shows a line scanned image, where $Re \approx 2200$ in the horizontal channel flow and the RBI is controlled with $\alpha_{\mathrm{local}} \approx 1.50\%$, $P = 2.00$ s and $t_{\mathrm{open}} = 1.00$ s.

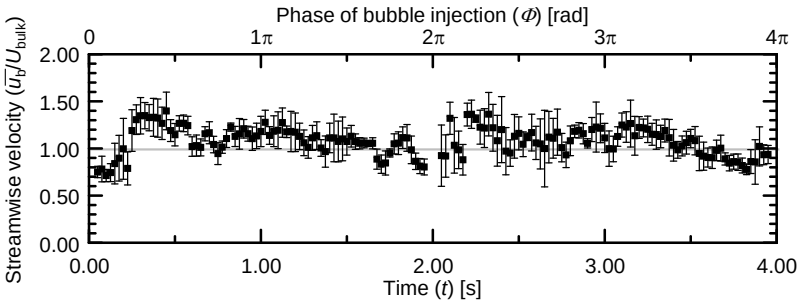

Figure 4.6 Averaged streamwise velocity of bubble swarms, which is shown in **Figure 4.5**, where the error bars and the gray line indicate the bulk velocity of test fluid and the standard deviation, respectively.

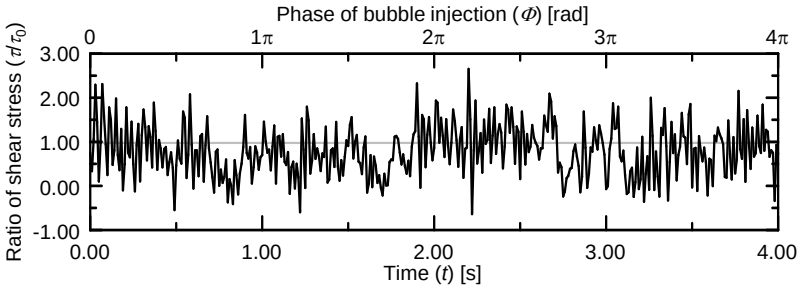

Figure 4.7 Sample of the wall shear stress with bubble swarms generated by RBI, which is controlled using $\alpha_{\mathrm{local}} \approx 1.50\%$, P = 2.00 s and t_{open} = 1.00 s, where $Re \approx 2200$ in the horizontal channel flow and the gray line indicates the average shear stress value without the bubbles.

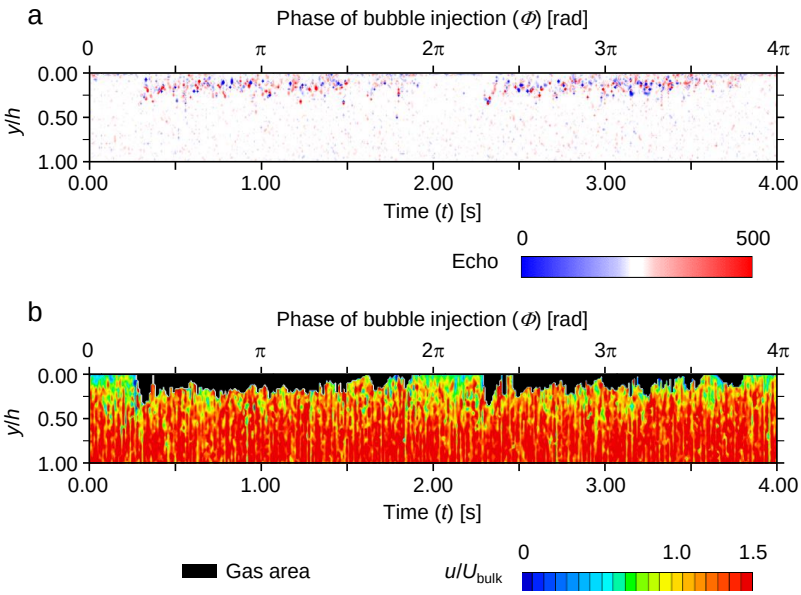

Figure 4.8 Sample of results obtained by the UVPs: (a) the original echo amplitude distribution and (b) the streamwise velocity distribution in the liquid phase with the detected gas–liquid interface, where the echo and the velocity are measured simultaneously with the wall shear stress shown in **Figure 4.7**.

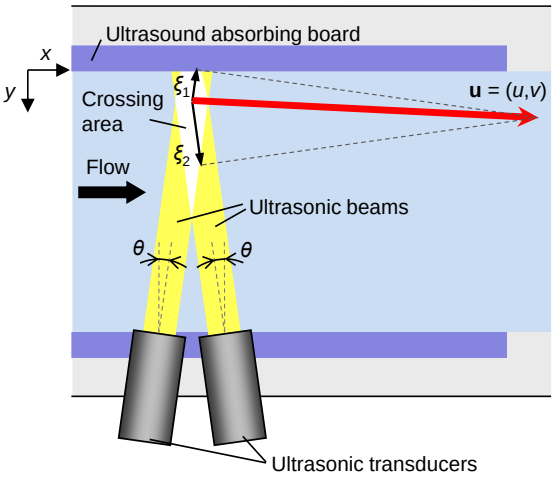

Figure 4.9 Relationships among the measured velocities and the flow velocity vector, where ξ_i is the velocity component measured by UVP and u = (u, v) is the flow velocity vector.

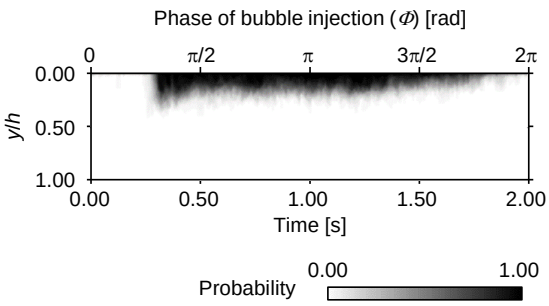

Figure 4.10 Probability distribution of bubble existence calculated based on the phase statistics of the gas phase position detected from the ultrasonic echo information, where the RBI setting values are P = 2.00 s and t_{open} = 1.00 s.

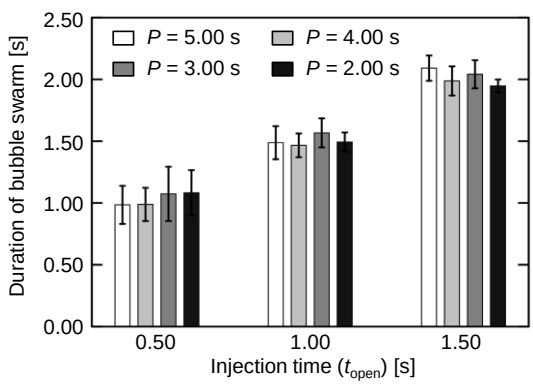

Figure 4.11 Durations of the bubble swarms recorded at the fixed point on the upper wall, where the error bars indicate the standard deviation.

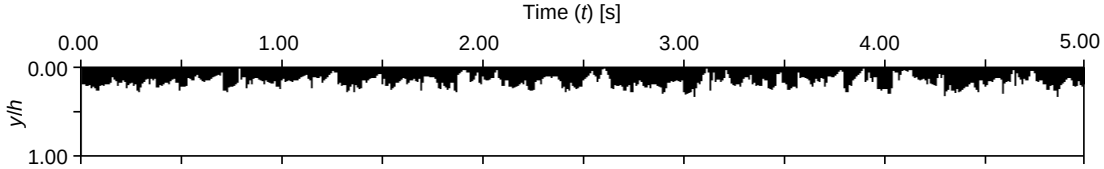

Figure 4.12 Envelope of bubble interfaces for continuously injected bubbles with $\alpha_{mean} \approx 1.50\%$ in turbulent flow with $Re \approx 2200$.

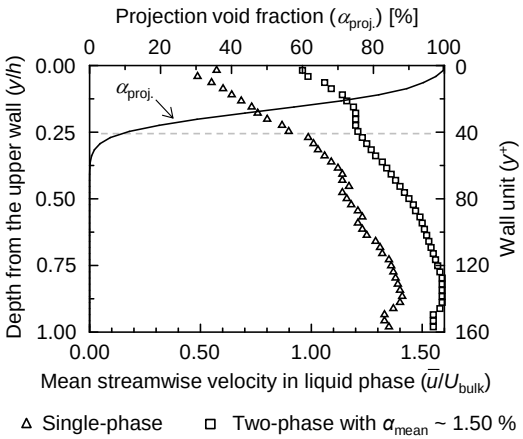

Figure 4.13 Mean streamwise velocity distribution in the liquid phase modified by continuous bubble injection (square symbol) and the distribution of the projection void fraction (solid line) obtained from the UVP echo signal, which was measured at the bulk mean void fraction of $\alpha_{mean} \approx 1.50\%$. The gray dashed line indicates the boundary between the buffer layer and the logarithmic layer in the single-phase flow that corresponds to 40 wall units.

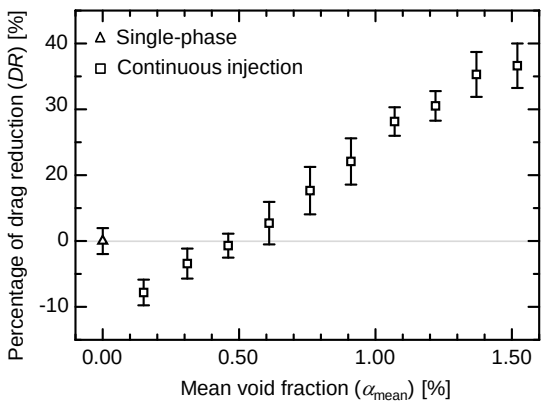

Figure 4.14 Drag reduction at the upper wall in continuous bubble injection regime, where the error bars indicate the standard deviations of the data.

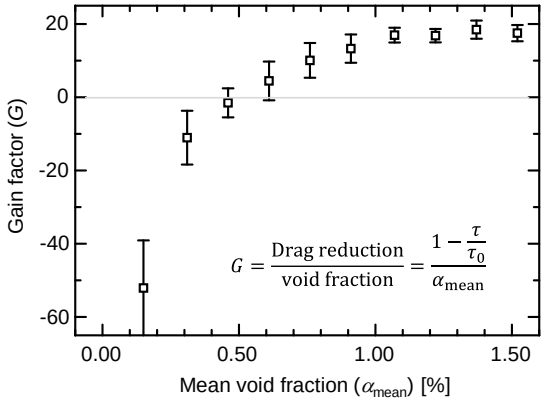

Figure 4.15 Gain factor of drag reduction in continuous bubble injection regime, where the error bars indicate the standard deviations of the data.

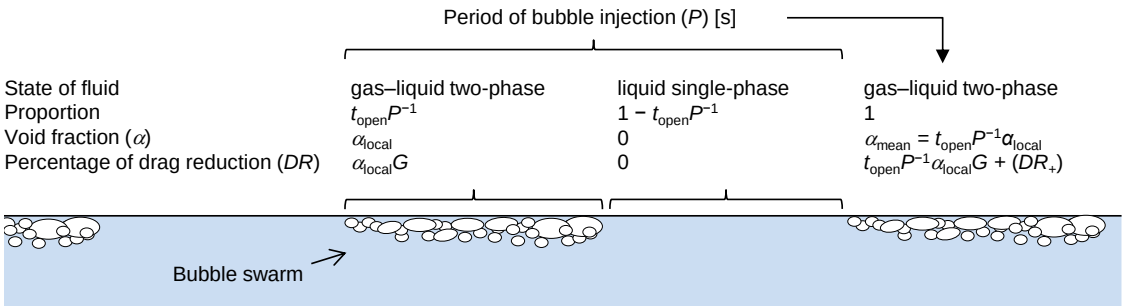

Figure 4.16 Concept of RBI, where DR_+ indicates extra drag reduction effects on the wall shear stress produced by RBI.

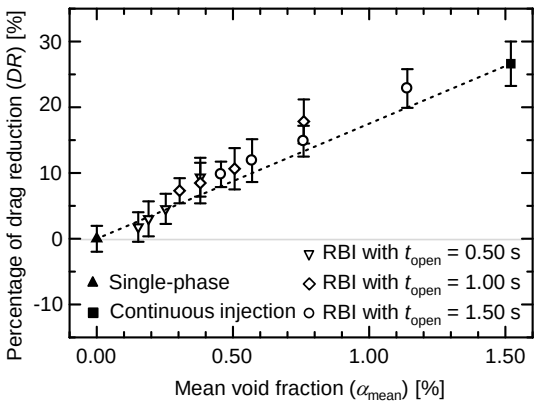

Figure 4.17 Time-averaged drag reduction for wall shear stress with RBI, where the dashed line indicates the drag reduction predicted from that of the continuous bubble injection regime, and the error bars denote the standard deviations of the data.

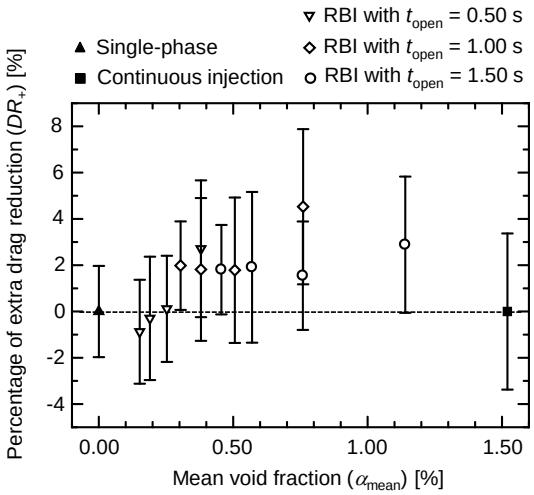

Figure 4.18 Extra drag reduction produced by RBI (DR_+), where the error bars indicate the standard deviations of the data.

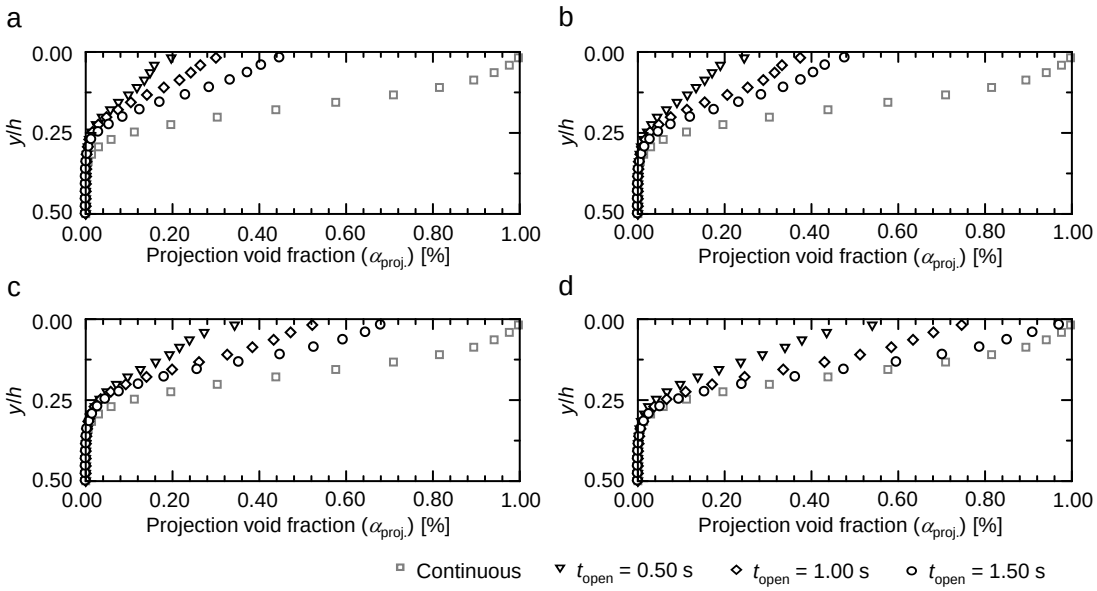

Figure 4.19 Projection void fraction distributions under each of the RBI conditions: (a) P = 5.00 s, (b) P = 4.00 s, (c) P = 3.00 s and (d) P = 2.00 s.

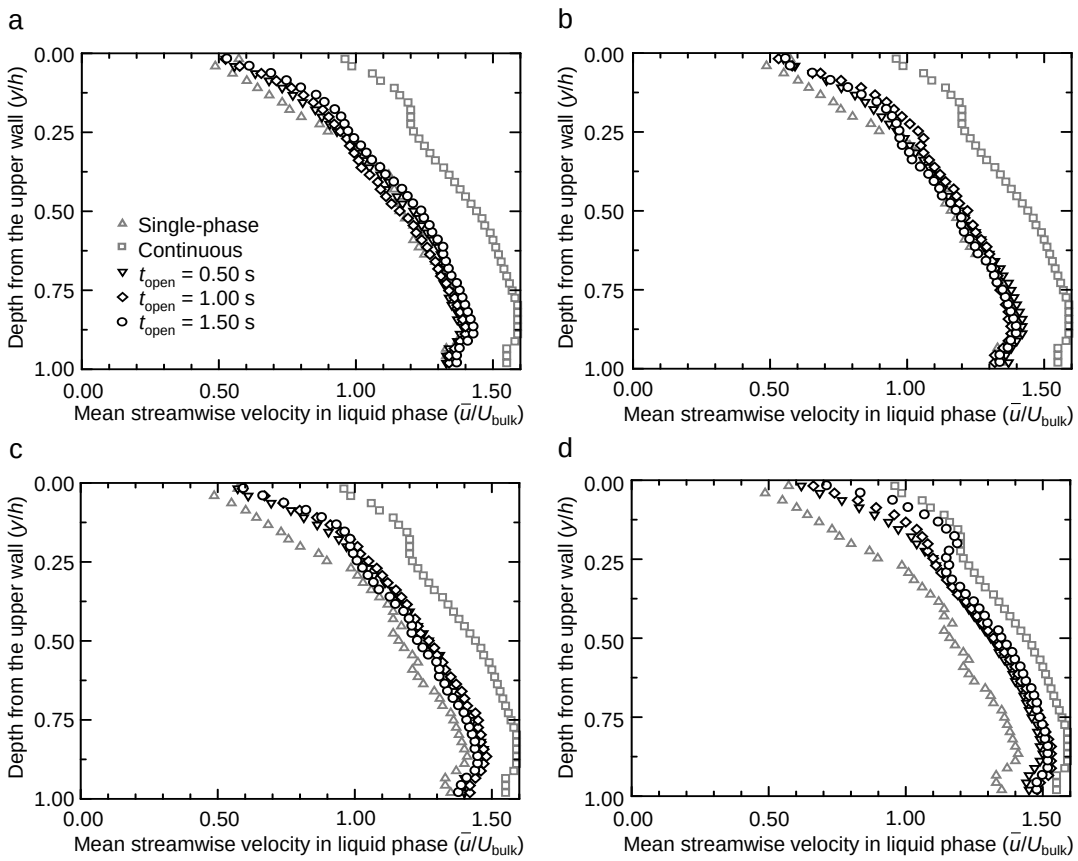

Figure 4.20 Mean streamwise velocity distributions in the liquid phase when accelerated by bubble injection: (a) P = 5.00 s, (b) P = 4.00 s, (c) P = 3.00 s and (d) P = 2.00 s.

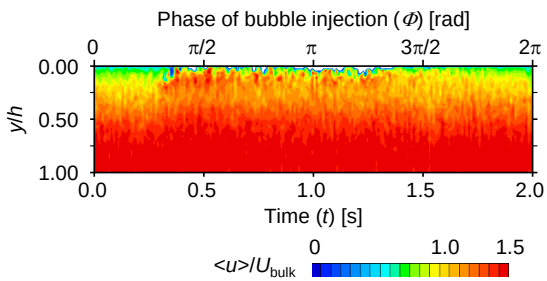

Figure 4.21 Phase-averaged streamwise velocity of the liquid phase flow when modified by controlled bubble injection under valve conditions of P = 2.00 s and t_{open} = 1.00 s, where the points at which all of the velocity data are distinguished as being gas phase are represented as white areas.

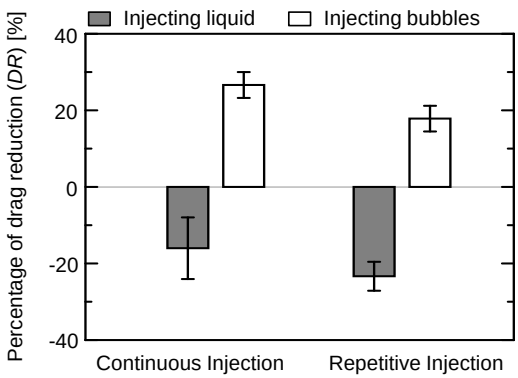

Figure 4.22 Modifications to the drag reduction caused by injection of bubbles or the same amount of liquid with $\alpha_{local} \approx 1.5\%$, where the gray line expresses each value for the single-phase flow and the repetitive injection conditions are P = 2.00 s, t_{open} = 1.00 s and $\alpha_{mean} \approx 0.76\%$, which is half of the value used for continuous injection.

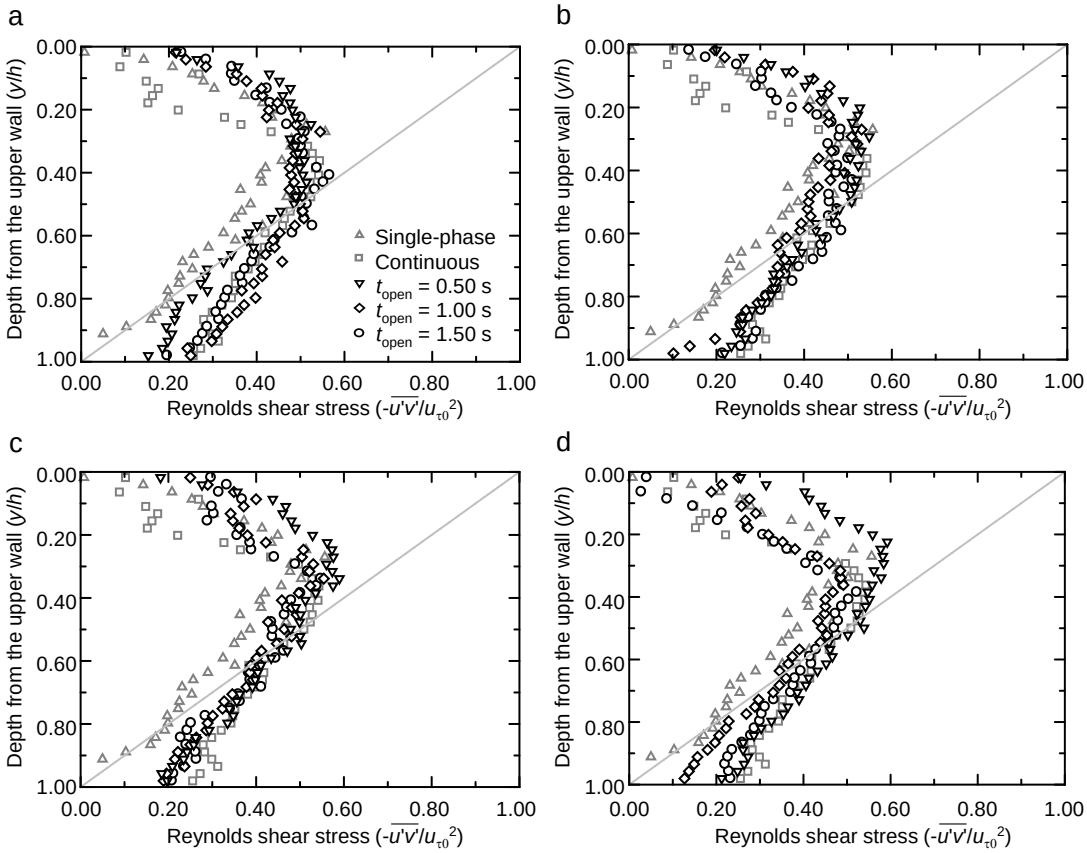

Figure 4.23 Reynolds shear stress profiles for different bubble injection periods: (a) P = 5.00 s, (b) P = 4.00 s, (c) P = 3.00 s and (d) P = 2.00 s, where the gray lines denote the wall shear stresses for single-phase flows obtained using a shear transducer.

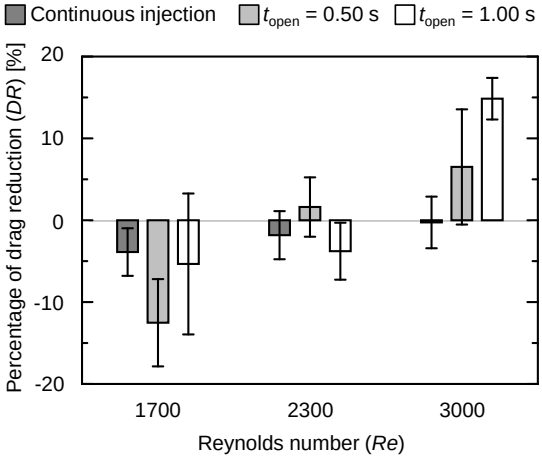

Figure 4.24 Drag reduction at each Reynolds number, where the mean void fraction is fixed to be the same at each Reynolds number.

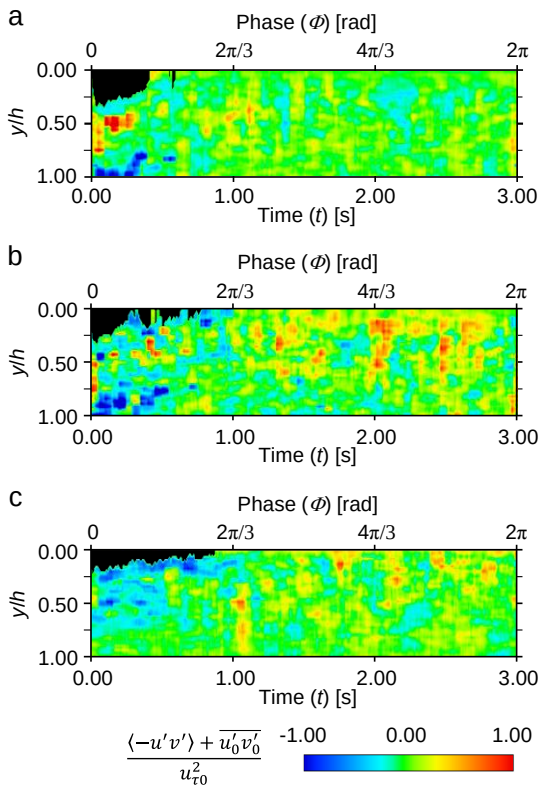

Figure 4.25 Phase-averaged Reynolds shear stress for RBI with t_{open} = 0.50 s: (a) $Re \approx 1700$, (b) $Re \approx 2300$ and (c) $Re \approx 3000$, where the black areas represent bubbles.

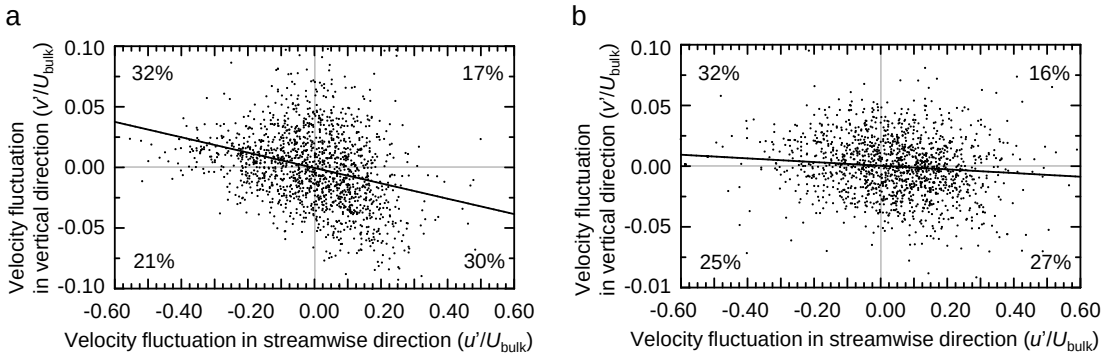

Figure 4.26 Velocity fluctuation distributions at $y/h \approx 0.25$ and $Re \approx 3000$: (a) single-phase and (b) under bubble swarms, in the 0 rad < Φ < $2\pi/3$ rad range, generated by RBI with t_{open} = 0.50 s, where the black lines are linearly fitted gradients of the plots and the values given at each corner denote the fraction of the plots that exist in each area.

5 Spatial transition of synthetic void waves in a horizontal bubbly channel flow

- **Preface**

Repetitive bubble injection (RBI) reduces drag by generating bubble swarms with a high local void fraction. For RBI to reduce drag in a system, such as in the cases of channels and ship hulls, it is necessary to know the variation of the void fraction across the system in order to control parameters and maintain a high void fraction. However, measuring the variation in a whole region is difficult in industrial fields. Therefore, in this chapter, we evaluate the transition of a voidage wave in a system and establish a simple model that expresses the transition. Finally, we estimate the transition using the established model and measurement data experimentally obtained from locations in the system.

5.1 Introduction

Gas–liquid two-phase flows that are often encountered in nature and in industry have long been studied because of the industrial needs for heat exchangers (Lee et al., 2002) and chemical reactors (Wilkinson et al., 1994). Despite the long history of study, we still do not fully comprehend bubbly flows because they have complex characteristics relating to the behaviors of bubbles such as deformation, coalescence and fragmentation. Many studies on bubbly flows have focused on the behaviors of bubbles in vertical systems (Hibiki and Ishii, 2002) because horizontal systems are unfavorable for industrial facilities. The behaviors of bubbles change dependency on the direction of buoyancy relative to the main flow direction (Troniewski and Ulbrich, 1984). In horizontal systems, bubbles float because of their buoyancy, and the void fraction is concentrated beneath the upper wall of a system. The concentrated void fraction disturbs the heat exchange between the liquid–phase and wall, and hardly contributes to mass transfer in the system. Therefore, until bubbly drag reduction was reported by McCormick and Bhattacharyya (1973), horizontal bubbly flows and the concentrated void fraction had been regarded as an unwanted obstruction in industrial fields. Bubbly drag reduction is expected to improve the performance of large vessels. Some shipbuilding companies have researched this technique of drag reduction for the reduction of energy consumption (Mizokami et al., 2013; Jang et al., 2014), but it has not yet been deployed on a commercial scale because of its low performance. According to a review written by Ceccio (2010), the performance basically increases with the void fraction. However so much energy is needed to inject air beneath the ship bottom; the amount of energy is proportional to the amount of air. As a result, the improvement in performance due to a large amount of injected air does not result in the low energy consumption of a vessel. In the **Chapter 4**, repetitive bubble injection (RBI) was proposed to improve the performance without increasing the total amount of injected air. RBI produces a locally high void fraction, namely a bubble swarm, through air injection within a short duration. The bubble swarm maintains a high drag reduction rate by keeping a high void fraction and promotes drag reduction through bubble–flow structure interactions (in the **Chapters 3** and **4**). To adopt and control RBI for a large ship, we need to know how the bubble swarms travel beneath the ship bottom. However, it is difficult to access information of bubbles at several locations on the ship bottom because of the high cost of maintenance of the measurement instrument under the severe conditions of actual situations. Furthermore, it is expected to be difficult to estimate the transition of the void fraction traveling beneath the ship bottom from results of laboratory–scale experiments because of the huge difference in scale with actual situations. We should therefore simulate and estimate the transition of the void fraction using only limited information of the bubbles.

Simulation codes that can be used to clarify behaviors of bubbly flow in vertical systems have been developed for the industrial needs of heat exchangers and chemical reactors (Lisseter and

Fowler, 1992; Murai and Matsumoto, 2000; Smolianski et al., 2008). Basically, determining the behaviors of bubbly flow is computationally expensive because of the complex mutual interactions of bubbles; e.g., bubble–bubble interactions (Kamp et al., 2001) and bubble–flow structure interactions (Fujiwara et al., 2004). The simulation of bubble behaviors in industrial fields requires a simple code with a low calculation load. Ito et al. (2004) suggested and demonstrated a simple one-dimensional void-propagation model based on a discrete bubble model. This simple model extends from vertical bubbly pipe flows to horizontal bubbly pipe flows (Ami et al., 2009). In the model for horizontal pipe flows, the void fraction in a unit calculation cell is assumed a single large bubble located in the cell. This assumption is reasonable for horizontal pipe flows because bubbles are concentrated at the top of the pipe and coalesce with each other. Unfortunately, this model is not suitable for flows beneath a horizontal flat plate because the assumption is inappropriate. For example, even if void fractions beneath the horizontal flat plate are the same, it is expected that bubble behaviors are affected by the bubble size, which depends on the bubble number density. It is therefore difficult to estimate the voidage wave beneath the horizontal flat plate from the initial condition of the voidage wave.

The present study constructs a simple one-dimensional model for voidage wave transition beneath a horizontal flat plate. As the first step, behaviors of bubble swarms in horizontal channel flows are estimated statistically, and a simple model based on experimental results is then suggested.

5.2 Experimental method

5.2.1 Experimental facility

Figure 5.1 shows schematic diagrams of the experimental facility. Experiments are performed using two kinds of working fluid and a horizontal rectangular channel, which is made of transparent acrylic resin boards with thickness of 10 mm and has a circulatory system for the working fluid. The working fluid is tap water or an aqueous solution of 1-pentanol, which is a surfactant that prevents the coalescence of bubbles (Winkel et al., 2004). The concentration (C) of 1-pentanol in the solution is 150 ppm. It is expected that we can estimate the effects on bubbles behavior under a limited bubble coalescence condition while ignoring bubble behavior caused by a difference in surface tension between the two working fluids. This is because the surface tension is hardly affected by the surfactant at this concentration. The surface tensions (σ_{Fluid}) are σ_{Water} =71.5 mN/m and $\sigma_{\text{1-pentanol}}$ = 69.5 mN/m, where $\sigma_{\text{1-pentanol}}$ is calculated as

$$\sigma_{\text{1-pentanol}} = \sigma_{\text{Water}} - 15.60893 \ln\left(1 + \frac{C}{0.1344}\right) \qquad \textbf{Equation 5.1}$$

following by Guitián and Joseph (1996). Experimental conditions of the fluid are summarized in **Table 5.1**.

The channel composes three main parts: a nozzle, test section and diffuser. The working fluid passes through the nozzle, which suppresses initial turbulence, before it is supplied to the test section. The nozzle is 1000 mm in length, 160 mm in width, 40 mm in inlet height and 20 mm in outlet height. The test section is 4000 mm in length, 160 mm in width (W) and 20 mm in height ($H = 2h$). An air injector is located on the upper wall of the test section at a distance of 1200 mm from the inlet of the test section; i.e., the outlet of the nozzle. Air is supplied by an air flow control system and injected into the working fluid through 103 holes that are 1 mm in diameter on the bottom of the air flow control system as shown in **Figure 5.1**(b), where the x, y, and z coordinates are defined as the streamwise distance from the injector, the vertical downward coordinate from the upper wall and the spanwise location from the center between the two side walls of the channel, respectively. The air flow control system comprises of a compressor, an isothermal chamber, a regulator, a thermometer, two pressure sensors, an electronic servo valve, a normal valve and an air flowmeter. Information of air temperature and pressure at the inlet and outlet of the servo valve is recorded to a personal computer, and the air flow rate is automatically controlled by the computer using the information. This system is designed as a small model of a system developed by Takeuchi and Kagawa (2013). Here, the experiments are designed to investigate the bubble swarm, which is generated by impulsively injecting air for a short opening duration of the servo valve. Unfortunately, air injection does not rapidly stop after the servo valve is closed because high air pressure is maintained in the cavity of the injector. A normal valve is mounted between the servo valve and the air flowmeter, and opened a little to release rapidly the high pressure to the atmosphere when the air supply is stopped. The air flowmeter monitors only air injected into the channel flows. To investigate passing of bubbles injected from the injector, a laser source, which emits two laser beams at angles ±6.4° from the vertical axis, is installed above the channel and two optical receivers that measure the intensity of each laser beam are installed under the channel. The diameter of the beams and the distance between the centers of the two beams are approximately 1.5 and 6.75 mm respectively at the interface between the fluid and upper wall. The location of the installation of the optical instrument is adjustable in the streamwise direction. In the experiments, the measuring position is limited to the range of 1000 mm < x < 2500 mm to ensure an entrance distance that maintains fully developed turbulent flows and to avoid effects of the outlet of the test section on the flows. To prevent a rapid decrease in pressure at the outlet of the test section, a diffuser designed as the mirror opposite of the nozzle is mounted between the end of the outlet and

the bubble removal tank. The working fluid without bubbles in the tank is circulated to the horizontal channel by a pump and the liquid flow rate (Q_l) is measured by a liquid flowmeter installed after the pump.

5.2.2 Experimental conditions

Experimental conditions are presented in **Table 5.2**. The Reynolds number (*Re*) of the channel flows is defined as

$$Re = \frac{hU_{\mathrm{bulk}}}{\nu} = \frac{hQ_{\mathrm{l}}}{\nu WH} \approx 17000, \qquad \textbf{Equation 5.2}$$

where U_{bulk} is the bulk velocity of the liquid flow and the kinematic viscosity of water (ν) is used, irrespective of the type of fluid. The servo valve is open for 0.1 s and the injection is repeated every 5 s in the period (*P*). This period is long enough for all bubbles to reach the removal tank. Therefore, when the next injection is performed, bubbles from the previous injection are not in the test section. Behaviors of bubbles have low reproducibility because the bubbles are affected by mutual interactions. Therefore, statistical analysis for bubbly flow is performed to estimate the behaviors 800 injections at each measurement location. **Figure 5.2** shows time variations of liquid and air flow rates. Standard deviations of the flow rates are small, approximately zero, compared with the average values. This suggests high reproducibility under the same conditions. The amount of air injected in *P* is

$$\int_0^P Q_{\mathrm{g}} dt \approx 89.5 \times 10^{-6}\ \mathrm{m}^3, \qquad \textbf{Equation 5.3}$$

where *t* is time from the start of air injection.

To estimate the effects of the surfactant (i.e., 1-pentanol) on the flow, streamwise velocity profiles for the liquid–phase in the turbulent channel flow at $Re \approx 19300$ are measured employing particle tracking velocimetry at x = 1000 mm, and the results are shown in **Figure 5.3**. The surfactant solution can reduce frictional drag (Ohlendorf et al., 1986; Kamada et al., 2011). If the frictional drag is reduced by 1-pentanol in the experiments, it is expected that the velocity profile is affected. However, there are no clear differences in the average or root-mean-square (RMS) of the streamwise velocity distribution between the two working fluids. Conditions of turbulent flows are therefore almost the same when 150 ppm 1-pentanol is added to water. However, the size of bubbles is clearly affected by 150 ppm 1-pentanol solution, and the bubbles are smaller than those in water as shown in **Figure 5.4**, because 150 ppm 1-pentanol prevents the coalescence of bubbles. We thus focus on the bubble behaviors affected by 150 ppm 1-pentanol and discuss them without considering the liquid–phase in the flows.

5.2.3 Signal processing

A method of detecting bubbles using two laser beams is explained in this subsection. **Figure 5.5**(a) shows the original signal transmitted from the optical receiver, when a bubble passes through the laser beam. The optical receiver used in the experiment observes variations in laser intensity. Therefore, when a bubble starts to interrupt the beam, the voltage of the signal rapidly decreases. The voltage then recovers slowly to zero, because of the bubble blocking the beam. The receiver cannot receive the beam by the bubble and the intensity does not changed. As the bubble escapes the beam, the opposite pattern of the signal is observed. By detecting a pair of negative and positive peaks, we can distinguish the bubble from the signal as shown in **Figure 5.5**(b). Samples of signals binarized as gas and liquid phases using the method mentioned above are shown in **Figure 5.6**, where top and bottom figures are obtained using the laser beams located in upstream and downstream regions of the channel, respectively. The bubble injection starts at $t = 0$ and is repeated every 5 s. **Figure 5.6**(a) confirms that a single bubble swarm exists in one period, periodically appearing approximately 0.8 s after air injection and having a concentrated density within a short time. **Figure 5.6**(b) presents sample signals for the magnified range 800 μs ≤ t ≤ 900 μs. In recognizing the velocity and size of bubbles, at the first, individual bubbles are recognized in one-to-one matching for gas–phases observed at each receiver. Next, we extract times (t_{H1}, t_{T1}, t_{H2} and t_{T2}) of the head and tail of a bubble observed by each receiver. The velocity (u_B), chord length (L_{CL}) and location of the chord center ($x_{c(t)}$) of a bubble are determined as

$$u_B = \frac{L_{LG}}{\frac{(t_{H2} - t_{H1}) + (t_{T2} - t_{T1})}{2}}, \qquad \textbf{Equation 5.4}$$

$$L_{CL} = u_B \frac{(t_{T1} - t_{H1}) + (t_{T2} - t_{H2})}{2}, \qquad \textbf{Equation 5.5}$$

and

$$x_{c(t)} = x + u_B\left(t - \frac{t_{H1} + t_{T1} + t_{H2} + t_{T2}}{4}\right), \qquad \textbf{Equation 5.6}$$

respectively, using the extracted times and L_{LG}. Employing this method, we can measure L_{CL} but cannot know the actual bubble diameter (D_B) because the bubble centers do not always pass through the laser beam as shown in **Figure 5.7**(a). Therefore, if the bubble size is estimated using L_{CL} and assuming $D_B = L_{CL}$, it is underestimated because $D_B \geq L_{CL}$.

The proper estimation of D_B using L_{CL} requires statistical analysis of L_{CL} (Clark and Turton, 1988; Ruf et al., 2000; Langston el al., 2001; Hukkanen and Braatz, 2003; Hoang et al., 2015).

Here, we consider the simplest case that all bubbles have a circular shape with the same D_B. **Figure 5.7**(b) shows five probability distributions of L_{CL} with circular bubbles ($F_{(L_{CL},D_B)}$), which is calculated as

$$F_{(L_{CL},D_B)} = \begin{cases} \dfrac{\left[1-\sqrt{1-\left(\dfrac{L_{CL}}{D_B}\right)^2}\right]_{L_{CL}-\Delta L}^{L_{CL}}}{\Delta L}, & L_{CL} \le D_B \\ 0, & L_{CL} > D_B \end{cases}. \qquad \textbf{Equation 5.7}$$

In the figure, the bin size of the length (ΔL) is 0.2 mm and D_B under different bubble conditions is fixed at 10, 20, 30, 40 and 50 mm. Bubbles in **Figure 5.4** have relatively circular shapes without deformations. Assuming that all bubbles in the experiments have circular shapes with different D_B, a probability distribution of D_B can be converted from a probability distribution of L_{CL} by multiplying with an inverse matrix ($\mathbf{M}^{-1}$), where $\mathbf{M}$ comprises $F_{(L_{CL},D_B)}$ with different D_B:

$$\mathbf{M} = \begin{pmatrix} F_{(L_{CL},D_B=\Delta L)} \\ F_{(L_{CL},D_B=2\Delta L)} \\ F_{(L_{CL},D_B=3\Delta L)} \\ \vdots \end{pmatrix}. \qquad \textbf{Equation 5.8}$$

Figure 5.8 shows a distribution of D_B converted from a distribution of L_{CL} obtained at x = 1000 mm for water, where ΔL = 0.2 mm. In the distribution of L_{CL}, the most common length is approximately 3 mm. However, the most probable length is approximately 4 mm in the converted distribution of D_B. Additionally, tiny bubbles smaller than 1 mm disappear in the conversion. These changes correspond with **Figure 5.4**(a), a snap picture taken at x = 1100 mm. The conversion is thus effective in the present research.

5.3 Results and discussions

5.3.1 Experimental estimation of voidage wave transition

5.3.1.1 Surfactant effects on bubble behaviors

We first estimate surfactant effects on bubble behaviors, such as the fragmentation and coalescence of bubbles, in horizontal turbulent channel flows. **Figure 5.9** and **Figure 5.10** show probability distributions of the size of bubbles passing at six measurement locations, from x = 1000 mm to x = 2500 mm at intervals of 300 mm, for water and 150 ppm 1-pentanol solution, respectively. The most probable D_B in the channel flows for water and 1-pentanol is approximately 4 and 3 mm,

respectively. In the water flows, the distribution of D_B is affected by bubble advection in the flow, and D_B becomes larger in the channel from x = 1000 mm to x = 1600 mm through bubble coalescences. At $x \geq 1900$ mm, the distribution starts to recover to the initial distribution seen at x = 1000 mm through the fragmentation of large bubbles due to turbulent shear. However, the most probable D_B remains high and does not recover. Meanwhile, although small bubbles somewhat increase in number in the distribution for the 1-pentanol solution, the overall shape of the distribution is hardly affected by advection when compared with the case for water because coalescence is prevented by the surfactant.

To estimate the fragmentation and the coalescence while considering measurement errors resulting from too many close-packed bubbles, we investigate conserved quantities obtained in the present measurement. When bubbles are adjacent to or in contact with each other, they are recognized as one large bubble in the present measurement. Bubbles beneath a horizontal wall have a height limit because of their buoyancy. The shape of the bubble thus depends on the size of the bubble and changes from being three dimensional to being two dimensional shape from the three dimensional shape when the size becomes large. **Figure 5.11** shows the regime classification of bubbles' behaviors and the changes in measured quantities, where we consider less than two bubbles to simplify the behaviors. In the figure, black and dashed gray circles respectively indicate the projection of existent bubbles and nonexistent large bubbles misrecognized when two small bubbles are in contact with each other. If fragmentation and coalescence do not occur in the flows (e.g., cases 1–3) it is possible that the number of bubbles (N) is affected by measurement error. In case 2, the measurement results reveal that N is halved and the sum of bubble lengths ($L_{total} = \sum D_B$) is conserved. Additionally, the sums of bubble projection areas ($A_{total} \propto \sum D_B^2$) and volumes ($V_{total} \propto \sum D_B^3$) dramatically increase because two small bubbles are misrecognized as a single large bubble. Case 3 presents the opposite situation of case 2. When fragmentation and coalescence occur in the flows, we have to consider eight more cases. Four bubble behaviors are added, and they are classified by the bubble shape. If the heights of bubbles are not affected by coalescence and fragmentation (i.e., bubbles change their shape two dimensionally), A_{total} is conserved. Meanwhile, V_{total} is conserved instead of A_{total} when the height changes in proportion to the diameter of the bubble projection (i.e., shape of the bubbles is changed three dimensionally). Variations in the measured values of N, L_{total}, A_{total}, and V_{total} in the channel flows are shown in **Figure 5.11**. The variations provide hints for understanding the behaviors. For example, cases 8 and 9 might frequently occur in the range $1600 \leq x \leq 2200$ for water flows because L_{total}, A_{total}, and V_{total} decrease independently for changes in N. However, we cannot estimate clearly the behaviors in the flows because the number of behaviors is more than the number of measured quantities. Furthermore, each quantity fluctuates for the channel flows and only N has a certain tendency for each working fluid, increasing for water flows and decreasing for 1-pentanol solution. This means

that several behaviors occur simultaneously in the flows and proportions of each behavior constantly change. We focus on measuring values at x = 1000 and 2500 mm because the variations between the two measurement points are larger than those between other measurement points. It is thus expected that it will be easier to suppose the most popular behavior than it is for the other shorter sections. All values for the water flows decrease with the advection of bubbles. This situation requires coalescence such as in cases 8–11. Meanwhile, N increases, L_{total} remains constant and other quantities decrease with advection in the 1-pentanol solution. This situation is similar to case 3. The values also confirm that bubble coalescence is prevented by adding 1-pentanol to water.

Figure 5.13 shows distributions of the gap (L_{BG}) between interfaces of two adjacent bubbles in the water flows, where gray lines indicate the distribution at x = 1000 mm. Bubble coalescence requires bubbles to approach other bubbles and make contact at their interfaces. Comparing the distributions at x = 1000 and 2500 mm, the most popular L_{BG} shifts from 1.4 to 0.6 mm with advection. Meanwhile, distributions of L_{BG} for 150 ppm 1-pentanol solution shown in **Figure 5.14** indicate changes different from those for water. While the propagation of L_{BG} with 1-pentanol decreases at L_{BG} < 7 mm, it increases at L_{BG} > 7 mm. L_{BG} thus becomes far away.

5.3.1.2 Advection of the projection void fraction

Ami et al. (2009) provided a one dimensional model of the traveling voidage wave in a horizontal pipe flows and simulated the voidage wave in a horizontal pipe flow through modeling, using mainly the void fraction in the unit area. Likewise, the transition of the voidage wave in a channel flow may be expressed using only the void fraction. To evaluate this possibility and to gain a hint for the one-dimensional advection modeling of the voidage wave, as the first step, the projection void fraction ($\alpha_{proj.}$) and the streamwise velocity (u_{void}) are investigated. **Figure 5.15** shows a schematic image of bubbles between two laser beams and indicates parameters used to calculate $\alpha_{proj.}$ and u_{void}. The parameters are L_{LG} and information (L_p and u_B) of each bubble between two laser beams, where L_p is the part of L_{LG}, located between the two beams and is calculated as

$$L_{\mathrm{p}} = \begin{cases} L_{\mathrm{CL}}, & x_{\mathrm{c}(x)} + \frac{L_{\mathrm{CL}}}{2} \le x + \frac{L_{\mathrm{LG}}}{2} \text{ and } x - \frac{L_{\mathrm{LG}}}{2} \le x_{\mathrm{c}(x)} - \frac{L_{\mathrm{CL}}}{2} \\ L_{\mathrm{CL}} - \left(\left(x_{\mathrm{c}(x)} + \frac{L_{\mathrm{CL}}}{2} \right) - \left(x + \frac{L_{\mathrm{LG}}}{2} \right) \right), & x_{\mathrm{c}(x)} + \frac{L_{\mathrm{CL}}}{2} > x + \frac{L_{\mathrm{LG}}}{2} \text{ and } x - \frac{L_{\mathrm{LG}}}{2} \le x_{\mathrm{c}(x)} - \frac{L_{\mathrm{CL}}}{2} \\ L_{\mathrm{CL}} - \left(\left(x - \frac{L_{\mathrm{LG}}}{2} \right) - \left(x_{\mathrm{c}(x)} - \frac{L_{\mathrm{CL}}}{2} \right) \right), & x_{\mathrm{c}(x)} + \frac{L_{\mathrm{CL}}}{2} \le x + \frac{L_{\mathrm{LG}}}{2} \text{ and } x - \frac{L_{\mathrm{LG}}}{2} > x_{\mathrm{c}(x)} - \frac{L_{\mathrm{CL}}}{2} \\ L_{\mathrm{LG}}, & x_{\mathrm{c}(x)} + \frac{L_{\mathrm{CL}}}{2} > x + \frac{L_{\mathrm{LG}}}{2} \text{ and } x - \frac{L_{\mathrm{LG}}}{2} > x_{\mathrm{c}(x)} - \frac{L_{\mathrm{CL}}}{2} \\ 0, & \text{other cases} \end{cases}.$$

Equation 5.9

In the present experiments, $\alpha_{\mathrm{proj.}}$ and u_{void} are defined as

$$\alpha_{\mathrm{proj.}} = \frac{\sum L_{\mathrm{p}}}{L_{\mathrm{LG}}}$$

Equation 5.10

and

$$u_{\mathrm{void}} = \frac{\sum L_{\mathrm{p}} u_{\mathrm{B}}}{\sum L_{\mathrm{p}}},$$

Equation 5.11

respectively. Phase-averaged distributions of $\alpha_{\mathrm{proj.}}$ obtained at each measurement location are summarized in **Figure 5.16**. The distributions at x = 1000 mm for water and 1-pentanol solution become concentrated within a short time, 0.8 s < t < 1.4 s, and the maximum value exceeds 60% although the shapes of the distributions are a little different. The distributions are diffused with the advection and the maximum value at x =1500 mm thus decreases to about 40%. Additionally, there is the tendency that $\alpha_{\mathrm{proj.}}$ located at the front of the bubble swarm diffuses more quickly than that at the rear of the swarm. **Figure 5.17** shows phase-averaged distributions of u_{void}, obtained at the same locations as the distributions of $\alpha_{\mathrm{proj.}}$. They shows that u_{void} at the front is higher than that at the rear and the gradient of the temporal variance of u_{void} decreases with advection.

If there is a direct and strong correlation between $\alpha_{\mathrm{proj.}}$ and u_{void} investigated in the channel flows, it is possible to express advection of the voidage wave using u_{void}. **Figure 5.18** shows scatter plots for estimating the relationship between $\alpha_{\mathrm{proj.}}$ and u_{void} of each fluid. They indicate that u_{void} is maintained and hardly depends on $\alpha_{\mathrm{proj.}}$. However, by tracking plots temporally, a weak non-linear relationship between them is confirmed from the figures, where the non-linearity is indicated by a clockwise rotation. The non-linearity appears notable for the 1-pentanol solution when compared with the case for water. Oishi et al. (2009) mentioned that there is a non-linear relationship between $\alpha_{\mathrm{proj.}}$ and the wall shear stress reduced by bubble passing and a fluctuation of void fraction promotes wall friction drag reduction by bubbles injected into a turbulent boundary layer.

Considering this and assuming that u_{void} increases as the wall shear stress decreases, the non-linearity in the present experimental results is explained by the promoted wall friction drag reduction.

5.3.1.3 Causes of non-linearity in the voidage wave transition

The previous subsubsection confirmed a weak non-linear relationship between $\alpha_{proj.}$ and u_{void}, but did not find a direct and strong correlation between them. We thus focus now on individual bubbles instead of the void fraction, and assume that the information of each bubble, such as L_{CL} and u_B, is condensed at $x_{c(t)}$ of each bubble. By making this assumption, we obtain one more piece of information about the bubbles; i.e., the number density (n) of bubbles whose $x_{c(t)}$ is located between the two laser beams (e.g., $n = 2/L_{LG}$ in the case of **Figure 5.15**). **Figure 5.19** shows phase-averaged distributions for n at the six values of x. In the distributions of $\alpha_{proj.}$, the maximum values at each value of x is not greatly affected by the type of working fluid. However, the maximum values of $<n>$ at each x for water are almost half those for the 1-pentanol solution. This is because the addition of 1-pentanol prevents bubble coalescence and the bubbles thus have smaller D_B (see **Figure 5.4**, **Figure 5.9** and **Figure 5.10**). A tendency similar to the variation in $\alpha_{proj.}$ is observed in the distributions of n. The front of the distributions of n diffuses more rapidly than the rear. This tendency is explained by the phase-averaged distributions of L_{CL} and u_B, shown in **Figure 5.20** and **Figure 5.21**, respectively. The distributions of L_{CL} at x = 1000 mm show that large bubbles having relatively long $<L_{CL}>$ are located at the front of the distributions, where n increases rapidly. When $<n>$ is high enough and is maintained, $<L_{CL}>$ is also maintained. $<L_{CL}>$ then starts to shorten as $<n>$ decreases. The distributions of u_B at x = 1000 mm are also classified into three parts although the duration of each part is different from that of other distributions. The bubble swarm has relatively high u_B at its front, a constant moderate u_B at its middle and relatively slow u_B at its rear. The distributions of L_{CL} and u_B are affected by advection through stretching in the temporal direction. In particular, durations of the middle and rear parts in the distributions of L_{CL} grow with the advection, and the front part in the distributions of u_B is connected smoothly to the rear part by the middle part that is extinguished with the advection. Considering changes in the distributions of n, L_{CL} and u_B, it is supposed that the fast diffusion of n at the front of the bubble swarm is due to that large bubbles located at the front of the bubble swarm being transported with high u_B, and being dissipated quickly by the channel flows when compared with bubbles of other size. To confirm this assumption, scatter plots for estimating the relationship between $<L_{CL}>$ and $<u_B>$ for each fluid are shown in **Figure 5.22**, where solid lines indicate linear trends. When $<L_{CL}>$ is shorter than approximately 2 mm, $<u_B>$ increaes with increasing $<L_{CL}>$. However, $<u_B>$ when $<L_{CL}>$ is longer than approximately 2 mm has a constant value and before increasing stepwise upon reaching a specific $<L_{CL}>$, approximately 5 mm for water and 4 mm for 1-pentanol solution.

Although u_{void} increases non-linearly with increasing of $<L_{CL}>$, large bubbles are transported more quickly than small bubbles in the channel flows. **Figure 5.23** shows two possible causes for the tendency. One is a non-linear relationship between the horizontal and vertical lengths of bubbles. Das et al. (2012) investigated the growth of a bubble beneath a horizontal wall by supplying air to a bubble. The bubble becomes larger in height and width, simultaneously, when the bubble is sufficiently small. However, when the bubble is large enough, the bubble stops growing in height. Here, it is assumed that bubbles are transported by drag induced by surrounding flows. Considering this assumption, the height of bubbles and the streamwise velocity profile in the liquid–phase shown in **Figure 5.3**, it is reasonable that $<u_B>$ for small $<L_{CL}>$ increases with increasing $<L_{CL}>$, and $<u_B>$ for sufficiently large $<L_{CL}>$ does not change. The increase in $<u_B>$ for the sufficiently long $<L_{CL}>$ is possibly due to the reduction of wall shear stress by large bubbles (Murai et al., 2007). When large bubbles pass through a horizontal turbulent channel flow, they reduce the frictional drag more so than small bubbles. As a result, u_B of the large bubbles is higher when the bubbles are large.

Figure 5.22 shows almost all plots obtained at x = 1600 mm for water and at x = 1900 mm for the 1-pentanol solution have higher bubble velocities than those that obtained under other conditions. For a clear estimation the probability distribution of u_B for all bubbles passing each measurement location is calculated. Results for water and 1-pentanol solution are shown in **Figure 5.24** and **Figure 5.25**, respectively, where the bin size of the velocity (Δu) is 0.08 m/s. These figures indicate that bubbles in the channel flows first accelerate first and then decelerate toward their initial streamwise velocity at x = 1000 mm. The reasons for the acceleration and deceleration are not yet known because there has been little previous research on bubble advection in horizontal flow systems. Two reasons for the phenomena are suggested. One is that the streamwise velocity of the bubble swarm in the channel flows fluctuates continuously because flow–bubbles interactions. The other is the outlet effects of the test section. To evaluate these suggestions, we need to measure bubble advection in a much longer channel. We leave this as future work.

5.3.2 Mathematical modeling of the voidage wave transition

We investigated the transition of voidage wave in channel flows by measuring information of bubbles at several locations. The investigation was easy to perform because it involved laboratory experiments using a transparent channel. In industrial fields, however, an investigation at several locations would require the expensive to installation of measurement windows. Furthermore, an immediate investigation at an exact location would be difficult to perform in the field. It is thus necessary to predict the voidage wave transition in a flow using limited information. Basically, it is necessary to solve the equation of bubble motion in expressing the voidage wave transition, and too much information is needed to solve the equation because of the complex motion of bubbles

resulting from their mutual interactions. As a result, the prediction is difficult to adopt in practice because it has a high cost, requires the collection of much information and has a high calculation cost. Here, we propose a mathematical model that is a simple one-dimensional model using $\alpha_{\text{proj.}}$ to represent the voidage wave transition and evaluate it using experimental results. Assuming that the transported value is conserved, transport phenomena have usually been described by an advection–diffusion equation, with $<\alpha_{\text{proj.}}>$ expressed as

$$\frac{\partial\langle\alpha_{\text{proj.}}\rangle}{\partial t}+U_{\text{m}}\frac{\partial\langle\alpha_{\text{proj.}}\rangle}{\partial x}+D_{\text{m}}\frac{\partial^2\langle\alpha_{\text{proj.}}\rangle}{\partial x^2}=0\,, \qquad \textbf{Equation 5.12}$$

where U_{m} and D_{m} are respectively linear advection and diffusion coefficients in the equation. The coefficients respectively relate to the pressure difference between a channel inlet and a channel outlet, and turbulent diffusion in a channel flow. Unfortunately, this equation does not express distortion of the waveform. To express the distortion, we propose using the Korteweg–de Vries–Burgers (KdV–B) equation, defined as

$$\frac{\partial\langle\alpha_{\text{proj.}}\rangle}{\partial t}+U_{\text{m}}\frac{\partial\langle\alpha_{\text{proj.}}\rangle}{\partial x}+B_{\text{m}}\langle\alpha_{\text{proj.}}\rangle\frac{\partial\langle\alpha_{\text{proj.}}\rangle}{\partial x}+D_{\text{m}}\frac{\partial^2\langle\alpha_{\text{proj.}}\rangle}{\partial x^2}+E_{\text{m}}\frac{\partial^3\langle\alpha_{\text{proj.}}\rangle}{\partial x^3}=0\,, \qquad \textbf{Equation 5.13}$$

where B_{m} and E_{m} are respectively non-linear advection and dispersion coefficients in the equation. The KdV–B equation has been introduced to describe a pressure wave in a bubbly flow (Wijngaarden, 1792) and a voidage wave in a fluidized bed using a two-fluid model (Harris and Crighton, 1994). Furthermore, Smereka and Banerjee (1988) estimated bubble clouds using a non-linear wave equation while considering a solitary wave solution. The newly added coefficients distort a waveform as shown in **Figure 5.26**. In the case that $B_{\text{m}} > 0$ and other quantities being zero, the waveform leans forward in space. Meanwhile, the waveform leans backward in space for $E_{\text{m}} > 0$ and the other quantities being zero. If the effects of these terms on the waveform maintain a balance, we see a soliton in the waveform. The prediction using the KdV–B equation is possible if we know appropriate coefficients in the equation that express the voidage wave transition. The appropriate coefficients will be found by substituting coefficients in the equation and performing an evaluation by comparing the voidage wave obtained at x = 2500 mm in the experiments and a numerical simulation. Initial conditions of the simulation at x = 1000 mm are the same as experiment results obtained at the same location and parameters for the simulation are given in **Table 5.3**. For the simulation, **Equation 5.13** is transformed to the conserved equation

$$\frac{\partial\langle\alpha_{\text{proj.}}\rangle}{\partial t}+U_{\text{m}}\frac{\partial\langle\alpha_{\text{proj.}}\rangle}{\partial x}+B_{\text{m}}\frac{\partial\langle\alpha_{\text{proj.}}\rangle^2}{2\partial x}+D_{\text{m}}\frac{\partial^2\langle\alpha_{\text{proj.}}\rangle}{\partial x^2}+E_{\text{m}}\frac{\partial^3\langle\alpha_{\text{proj.}}\rangle}{\partial x^3}=0\,. \qquad \textbf{Equation 5.14}$$

We adopt a cubic interpolated propagation scheme for the linear advection term to minimize the effect of numerical diffusion (Takewaki et al., 1985) because of the diffusion term in the equation. If the effect of numerical diffusion is strong, D_{m} is underestimated. To adopt a cubic interpolated propagation scheme, **Equation 5.14** is divided into two equations:

$$\begin{cases}\dfrac{\partial\langle\alpha_{\text{proj.}}\rangle}{\partial t}+U_{\text{m}}\dfrac{\partial\langle\alpha_{\text{proj.}}\rangle}{\partial x}=0, & \text{linearadvectior} \qquad \textbf{Equation 5.15}\\[2ex] \dfrac{\partial\langle\alpha_{\text{proj.}}\rangle}{\partial t}+B_{\text{m}}\dfrac{\partial\langle\alpha_{\text{proj.}}\rangle^2}{2\partial x}+D_{\text{m}}\dfrac{\partial^2\langle\alpha_{\text{proj.}}\rangle}{\partial x^2}+E_{\text{m}}\dfrac{\partial^3\langle\alpha_{\text{proj.}}\rangle}{\partial x^3}=0, & \text{theothers} \qquad \textbf{Equation 5.16}\end{cases}.$$

A forward time central space scheme with a fourth order Runge–Kutta scheme is adopted to simulate the other terms. The sequence of the simulation is (i) calculation of the linear advection term, (ii) simulation of the other terms for a voidage wave applied to the linear advection term, and (iii) the progression of one time step (Δt). The void fraction under any definition has to be in the range of 0–1. Therefore, when a value of $<\alpha_{\text{proj.}}>$ is larger than 1.1 or lower than –0.1 at any location when the simulation is performed, it is judged that the combination of coefficients used in the simulation is not appropriate.

Fifteen combinations of coefficients with the highest correlations for each working fluid are given in **Table 5.4**. Values of U_{m} and D_{m} for each fluid do not vary greatly in the table, but values of B_{m} and E_{m} are fluctuated because they take positive and negative values, respectively. **Table 5.5** gives correlations between two coefficients in **Table 5.4**. Correlations between U_{m} and B_{m} are stronger than other correlations. These coefficients between U_{m} and B_{m} are related to the average traveling velocity of the waveform. Hence, when a value of B_{m} decreases, a value of U_{m} has to increase to maintain the average traveling velocity. In the case of $B_{\text{m}} < 0$ and $E_{\text{m}} > 0$, the non-linear advection and dispersion terms have the same effect on the waveform. The waveform leans backward in space for combinations of a negative B_{m} and a positive E_{m}. Therefore, there is correlation between B_{m} and E_{m} in the table, and it is expected that the shape of the waveform is broken with the advection and finally becomes flat because $B_{\text{m}}E_{\text{m}} \leq 0$; i.e., solitary waves do not form in the wave. Values of B_{m} for water are lower than those for 1-pentanol solution; i.e,, the non-linearity is strengthened by adding 1-pentanol to water. This corresponds with the non-linear relationship between $<\alpha_{\text{proj.}}>$ and $<u_{\text{void}}>$ as shown in **Figure 5.18**.

The variation in $<\alpha_{\text{proj.}}>$ simulated using appropriate coefficients is shown in **Figure 5.27**, where solid lines indicate $<\alpha_{\text{proj.}}>$ obtained from the experiments and the simulated waveform is sampled at intervals of 0.02 s. A correlation used for evaluation is calculated using the variation of

$<\alpha_{\text{proj.}}>$ in P. Therefore, although the maximum correlation is high, exceeding 0.99, there is a difference between the two waveforms at x = 2500 obtained from experiments and simulation near the highest $<\alpha_{\text{proj.}}>$ in the waveforms. However, shapes near the front and rear of the waveform are successfully described by the KdV–B equation. Likewise, the predicted voidage waveforms at x = 1300, 1600, 1900 and 2200 mm correspond with the front and a rear regions of experimental results although fluctuation with a high frequency in the middle of the waveforms is smoothed in the simulation. These results indicate that the voidage wave transition gradually develops without a sudden change in the channel flows. Assuming that the transition is dominated by the coefficients, as found in the simulation, in a flow for the same type of channel but a longer distance, we can predict the voidage wave at any place in the channel using experimental results obtained for two locations. The predicted wave is shown in **Figure 5.28**. The waveform for water travels more quickly than that for 1-pentanol solution and diffuses more slowly than that for 1-pentanol solution.

5.4 Conclusions

We statistically estimated the transition of a bubble swarm, introduced by a short duration of air injection, in horizontal turbulent channel flows with different working fluids water and 150 ppm 1-pentanol solution, and proposed a simple one-dimensional mathematical model based on experimental results. A voidage wave (i.e., the bubble swarm) has the tendency that its waveform leans backward because of a non-linear relationship between the void fraction and void traveling speed. This non-linearly is due to large bubbles traveling more quickly than small bubbles. As a result, bubbles are classified according to size when the bubble swarm travels with a main flow, and large bubbles are located at the front of the swarm. When adding 150 ppm 1-pentanol to water, the bubbles become smaller. Additionally, the distance between bubbles in 1-pentanol solution increases with advection while bubbles in water come close together with advection and coalesce. The diffusion of the void fraction with advection is thus promoted by 1-pentanol solution.

To express the transition of the voidage wave as simple one-dimensional modeling, we proposed the use of the Korteweg–de Vries–Burgers equation, which includes non-linear advection and a dispersion terms. Voidage waves obtained from experiments are substituted into the Korteweg–de Vries–Burgers equation, and coefficients of each term in the equation are determined by changing the values of each coefficient and comparing voidage waves obtained from experiments and the equation. The non-linear advection and dispersion terms take negative and positive values, respectively. The voidage wave thus cannot maintain its waveform and the waveform collapses with advection. This is because these two terms lean the waveform in the same backward direction and a solitary wave does not exist in the voidage wave. Using the equation and

the determined coefficients, we can predict the voidage wave at any location in the channel using two voidage waves experimentally obtained at different locations.

• Nomenclature and units

A_{total}	total projection area of bubbles in the period, m^2
B_m	non-linear advection coefficient in mathematical modeling, m/s
C	concentration of 1-pentanol solution, dimensionless
D_B	diameter of a bubble, m
D_m	diffusion coefficient in mathematical modeling, m^2/s
E_m	dispersion coefficient in mathematical modeling, m^2/s
$F_{(L_{CL}, D_B)}$	probability distribution function of the chord length in a circular bubble with a fixed size, m^{-1}
H	height in the channel, m
h	half the height in the channel, m
L_{CL}	chord length of a bubble, m
L_{BG}	gap between gas–liquid interface of two bubbles, m
L_{LG}	gap between two laser beams, m
L_p	part of L_{LG} located between two laser beams, m
L_{total}	total sum of diameters of bubbles in the period, m
$\mathbf{M}$	matrix comprising $F_{(L_{CL}, D_B)}$ with different bubble sizes, dimensionless
N	number of bubbles passing a measurement point in an injection period, dimensionless
n	number density of bubbles, m^{-1}
P	period of repetitive bubble injection, s
Q_l	liquid flow rate, m^3/s
Q_g	gas flow rate, m^3/s
Re	Reynolds number, dimensionless
t	time since air injection, s
t_{H1}	time that a bubble head is detected from the signal of receiver 1, s
t_{H2}	time that a bubble head is detected from the signal of receiver 2, s
t_{T1}	time that a bubble tail is detected from the signal of receiver 1, s
t_{T2}	time that a bubble tail is detected from the signal of receiver 2, s
U_{bulk}	bulk velocity of the main flow, m/s
U_m	advection coefficient in mathematical modeling, m/s
u	streamwise velocity of the flow at each height, m/s
u_B	streamwise velocity of a bubble, m/s
u_{rms}	root mean square of the streamwise velocity of a flow at each height, m/s
u_{void}	streamwise velocity of the void fraction, m/s
V_{total}	total volume of bubbles in the period, m^3
W	width in the channel, m

x, y, z	x, y and z coordinates in the channel, m
$x_{c(t)}$	location of the center of a bubble's chord, m
$\alpha_{proj.}$	projection void fraction, dimensionless
ΔL	bin size of the length distribution, m
Δu	bin size of the velocity distribution, m/s
ν	kinematic viscosity of water, m^2/s
σ_{Fluid}	surface tension of fluid, N/m
$< >$	phase-average
$\bar{}$	time-average

• References

Ami T., Umekawa H., Ozawa M. and Shoji M., 2009. Traveling void wave in horizontal two-phase flow, *Int. J. Multiphase Flow* **52**, 5682–5690.

Ceccio S.L., 2010. Frictional drag reduction of external flow with bubble and gas injection, *Annu. Rev. Fluid Mech.* **42**, 183–203.

Chesters A.K. and Colin C., 2001. Bubble coalescence in turbulent flows: a mechanistic model for turbulence-induced coalescence applied to microgravity bubbly pipe flow, *Int. J. Multiphase Flow* **27**, 1363–1396.

Clark N.N. and Turton R., 1988. Chord length distributions related to bubble size distributions in multiphase flows, *Int. J. Multiphase Flow* **14**, 413–424.

Das S., Morsi Y.S., Brooks G., Chen J.J.J. and Yang W., 2012. Principal characteristics of a bubble formation on a horizontal downward facing surface, *Colloid Surf. A: Physicochem. Eng. Asp.* **411**, 94–104.

Fujiwara A., Danmoto Y., Hishida K. and Maeda M., 2004. Bubble deformation and flow structure measured by double shadow images and PIV/LIF, *Exp. Fluids* **36**, 157–165.

Guitián J. and Joseph D. 1996. Foaminess measurements using a shaker bottle, Department of Aerospace Engineering and Mechanics, University of Minnesota, Minneapolis, USA.

Harris S.E. and Crighton D.G., 1994. Solitons, solitary waves, and voidage disturbances in gas-fluidized beds, *J. Fluid Mech.* **266**, 243–276.

Hibiki T. and Ishii M., 2002. Interfacial area concentration of bubbly flow systems, *Chem. Eng. Sci.* **57**, 3967–3977.

Hoang N.H., Euh D.J., Yun B.J and Song C.-H., 2015. A new method of relating a chord length distribution to a bubble size distribution for vertical bubbly flows, *Int. J. Multiphase Flow* **71**, 23–31.

Hukkanen E.J. and Braatz R.D., 2003. Measurement of particle size distribution in suspension polymerization using in situ laser backscattering, *Sensors Actuators B* **96**, 451–459.

Ito K., Inoue M., Ozawa M. and Shoji M., 2004. A simplified model of gas–liquid two-phase flow pattern transition, *Heat Transfer-Asian Res.* **33**, 445–461.

Jang J., Choi S.H., Ahn S., Kim B. and Seo J.S., 2014. Experimental investigation of frictional resistance reduction with air layer on the hull bottom of a ship. *Int. J. Nav. Archit. Ocean Eng.* **6**, 363–379.

Kamada K., Furukawa H., Kurokawa T., Tada T., Tominaga T., Nakano Y. and Gong J.P., 2011. Surfactant-induced friction reduction for hydrogels in the boundary lubrication regime, *J. Phys.: Condens. Matter* **23**, 284107.

Kamp A.M., Chesters A.K. and Colin C., 2001. Bubble coalescence in turbulent flows: a mechanistic model for turbulence-induced coalescence applied to microgravity bubbly pipe flow, *Int. J. Multiphase Flow* **27**, 1363–1396.

Langston P.A., Burbidge A.S., Jones T.F. and Simmons M.J.H., 2001. Particle and droplet size analysis from chord measurements using Bayes' theorem, *Powder Techol.* **116**, 33–42.

Troniewski L. and Ulbrich R, 1984. Two-phase gas–liquid flow in rectangular channels, *Chem. Eng. Sci.* **39**, 751–765.

Lisseter P.E. and Fowler A.C., 1992. Bubbly Flow—II: Modelling void fraction waves, *Int. J. Multiphase flow* **18**, 205–215.

Lee T.H., Park G.C. and Lee D.J., 2002. Local flow characteristics of subcooled boiling flow of water in a vertical concentric annulus, *Int. J. Multiphase flow* **28**, 1351–1368.

McCormick M.E. and Bhattacharyya R., 1973. Drag reduction of a submersible hull by electrolysis, *Naval Eng. J.* **85**, 11–16.

Mizokami S., Kawakado M., Kawano M., Hasegawa T. and Hirakawa I., 2013. Implementation of ship energy-saving operations with Mitsubishi air lubrication system, *MHI. Technical Review* **50**, 44–49.

Murai Y. and Matsumoto Y., 2000. Numerical Study of the Three-Dimensional Structure of a Bubble Plume, *J. Fluids Eng.* **122**, 754–760.

Murai Y., Fukuda H., Oishi Y., Kodama Y. and Yamamoto F., 2007. Skin friction reduction by large air bubbles in a horizontal channel flow, *Int. J. Multiphase Flow* **33**, 147–163.

Ohlendorf D., Interthal W. and Hoffman H., 1986. Surfaetant systems for drag reduction: physico-chemical properties and rheological behavior, *Rheol. Acta* **25**, 468–486.

Oishi Y., Murai Y., Tasaka Y. and Takeda Y., 2009. Frictional drag reduction by wavy advection of deformable bubbles, *J. Phys.: Conf. Ser.* **147**, 012020.

Park K., 2013. Experimental study of bubble characteristics and heat transfer in subcooled flow boiling of R-134a, Master thesis, Department of Energy and Process Engineering, *Norwegian University of Science and Technology*, Trondheim, Norway.

Ruf A., Worlitschek J. and Mazzotti M., 2000. Modeling and experimental analysis of PSD measurements through FBRM, *Part. Part. Syst. Charact.* **17**, 167–179.

Smereka P. and Banerjee S., 1988. The dynamics of periodically driven bubble clouds, *Phys. Fluids* **31**, 3519–3531.

Smolianski A., Haario H. and Luukka P., 2008. Numerical study of dynamics of single bubbles and bubble swarms, *Appl. Math. Mod.* **32**, 641–659.

Takeuchi T. and Kagawa T., 2013. Applicability of frequency response test for stability evaluation of gas pressure regulator. *Trans. Soc. Instrum. Control Eng.*, 747–754, (in Japanese).

Takewaki H., Nishiguchi A. and Yabe T, 1985. Cubic interpolated pseudo-particle method (CIP) for solving hyperbolic-type equations, *J. Comput. phys.* **61**, 261–268.

van Wijngaarden L., 1972. One-Dimensional Flow of Liquids Containing Small Gas Bubbles, *Annu. Rev. Fluid Mech.* **4**, 369–396.

Wilkinson P.M., Haringa H. and Van Dierendonck L.L., 1994. Mass transfer and bubble size in a bubble column under pressure, *Chem. Eng.* **49**, 1417–1427.

Winkel E.S., Ceccio S.L. Dowling D.R. and Perlin M., 2004. Bubble-size distributions produced by wall injection of air into flowing freshwater, saltwater and surfactant solutions, *Exp. Fluid* **37**, 802–810.

• Tables

Table 5.1 Experimental conditions of working fluids.

Temperature of the test fluid	26	°C
Density of water	997	kg/m^3
Kinematic viscosity of water (ν)	0.88×10^{-6}	m^2/s
Surface tension of water (σ_{water})	71.5×10^{-3}	N/m
Surface tension of 150 ppm 1-pentanol solution ($\sigma_{\mathrm{1\text{-}pentanol}}$)	69.5×10^{-3}	N/m

Table 5.2 Setting for experimental facilities.

Bulk velocity of the flow (U_{bulk})	1.5	m/s
Reynolds number (Re)	17000	-
Opening duration of the servo valve	0.1	s
Amount of injected air in a period	89.5×10^{-6}	m^3
Period of the air injection event (P)	5	s
Number of air injections	800	-
Sampling frequency of the data logger	5	kHz
Measurement location from the injector	1000–2500	mm

Table 5.3 Calculation parameters for the mathematical modeling.

Calculation region in time (t)	$0\ \mathrm{s} \le t \le P = 5\ \mathrm{s}$	
Calculation region in space (x)	$1000\ \mathrm{mm} \le x \le 2600\ \mathrm{mm}$	
Range of the linear advection term coefficient (U_{n})	$0.5\ \mathrm{m/s} \le U_{\mathrm{n}} \le 1.5\ \mathrm{m/s}$	
Range of the diffusion term coefficient (D_{n})	$-0.01\ \mathrm{m^2/s} \le D_{\mathrm{n}} \le 0.01\ \mathrm{m^2/s}$	
Range of the dispersion term coefficient (E_{n})	$-0.0005\ \mathrm{m^3/s} \le E_{\mathrm{n}} \le 0.0005\ \mathrm{m^3/s}$	
Range of the non-linear advection term coefficient (B_{n})	$-0.5\ \mathrm{m/s} \le B_{\mathrm{n}} \le 0.5\ \mathrm{m/s}$	
Calculating scheme for the advection term	cubic interpolated propagation scheme	
Calculating scheme for the other terms	forward time central space scheme with a fourth order Runge–Kutta	
Time step	1	ms
Space step	5	mm
Step of the linear advection term coefficient	0.02	m/s
Step of the diffusion term coefficient	0.0004	m^2/s
Step of the dispersion term coefficient	0.00002	m^3/s
Step of the non-linear advection term coefficient	0.02	m/s

Table 5.4 Fifteen combinations of coefficients with the highest correlations.

With water				
U_m [m/s]	B_m [m/s]	D_m [m^2/s]	E_m [m^3/s]	Correlation at x = 2500 mm
1.30	–0.10	0.0036	0.00008	0.9972214
1.30	–0.10	0.0040	0.00006	0.9971907
1.30	–0.10	0.0036	0.00006	0.9971509
1.30	–0.12	0.0040	0.00006	0.9971240
1.30	–0.10	0.0044	0.00008	0.9970917
1.30	–0.12	0.0036	0.00006	0.9970531
1.30	–0.12	0.0040	0.00002	0.9970381
1.30	–0.12	0.0044	0.00006	0.9970375
1.30	–0.12	0.0036	0.00002	0.9969698
1.30	–0.12	0.0044	0.00002	0.9969515
1.28	–0.02	0.0040	0.00006	0.9969475
1.30	–0.10	0.0036	0.00004	0.9969437
1.30	–0.08	0.0040	0.00008	0.9969423
1.30	–0.14	0.0040	0.00002	0.9969149
1.30	–0.12	0.0040	0.00008	0.9969068
With 150 ppm 1-pentanol solution				
U_m [m/s]	B_m [m/s]	D_m [m^2/s]	E_m [m^3/s]	Correlation at x = 2500 mm
1.24	–0.22	0.0080	0.00000	0.9988188
1.22	–0.12	0.0080	0.00004	0.9987926
1.24	–0.24	0.0084	–0.00004	0.9987926
1.24	–0.22	0.0080	0.00002	0.9987892
1.24	–0.24	0.0080	–0.00006	0.9987864
1.22	–0.12	0.0080	0.00006	0.9987854
1.24	–0.24	0.0084	–0.00006	0.9987767
1.24	–0.20	0.0084	0.00006	0.9987756
1.24	–0.22	0.0080	–0.00002	0.9987719
1.22	–0.10	0.0076	0.00010	0.998769
1.22	–0.10	0.0084	0.00012	0.9987614
1.24	–0.26	0.0084	–0.00010	0.9987574
1.24	–0.20	0.0080	0.00008	0.9987535
1.22	–0.12	0.0084	0.00004	0.9987486
1.24	–0.26	0.0080	–0.00010	0.9987477

Table 5.5 Correlations between two coefficients in **Table 5.4**.

With water				
	U_m [m/s]	B_m [m/s]	D_m [m^2/s]	E_m [m^3/s]
U_m [m/s]	-	–0.851	–0.050	–0.078
B_m [m/s]	–0.851	-	–0.037	0.380
D_m [m^2/s]	–0.050	–0.037	-	0.027
E_m [m^3/s]	–0.078	0.380	0.027	-
With 150 ppm 1-Pentanol solution				
	U_m [m/s]	B_m [m/s]	D_m [m^2/s]	E_m [m^3/s]
U_m [m/s]	-	–0.953	0.158	–0.651
B_m [m/s]	–0.953	-	–0.204	0.884
D_m [m^2/s]	–0.158	–0.204	-	–0.208
E_m [m^3/s]	–0.651	0.884	–0.208	-

- **Figures**

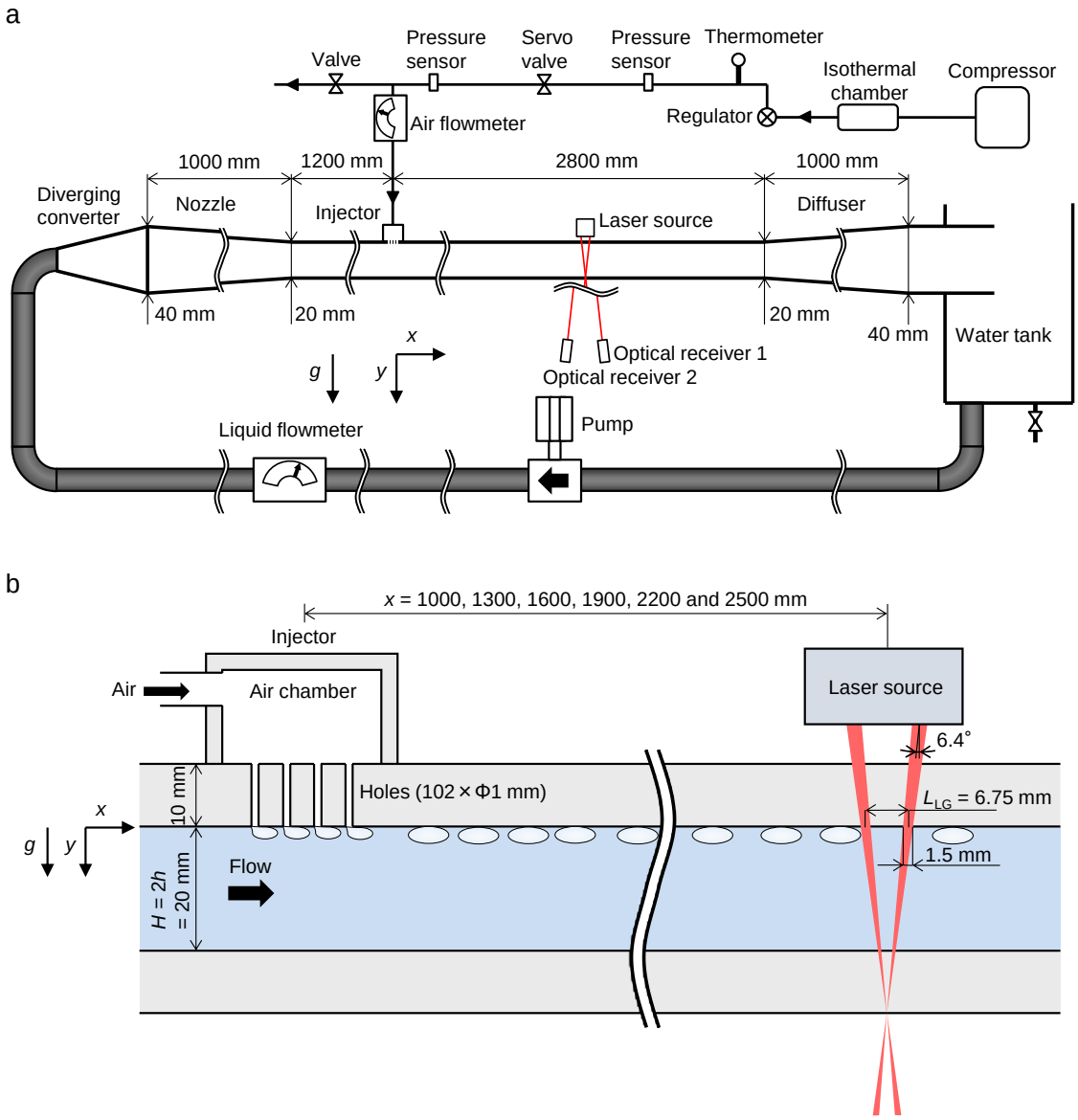

Figure 5.1 Schematic diagram of the experimental facility; (a) overview and (b) details of the test section of the channel, where x and y are the distances from the injector and the upper wall, respectively, and the red lines indicate the laser paths from the laser source.

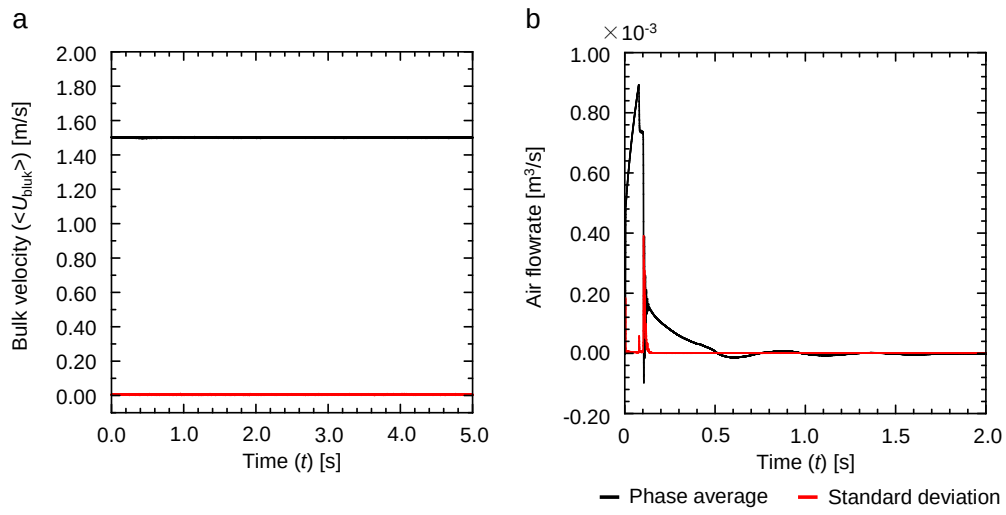

Figure 5.2 Reproducibility of flow control in repeated experiments; (a) liquid pump and (b) air injection.

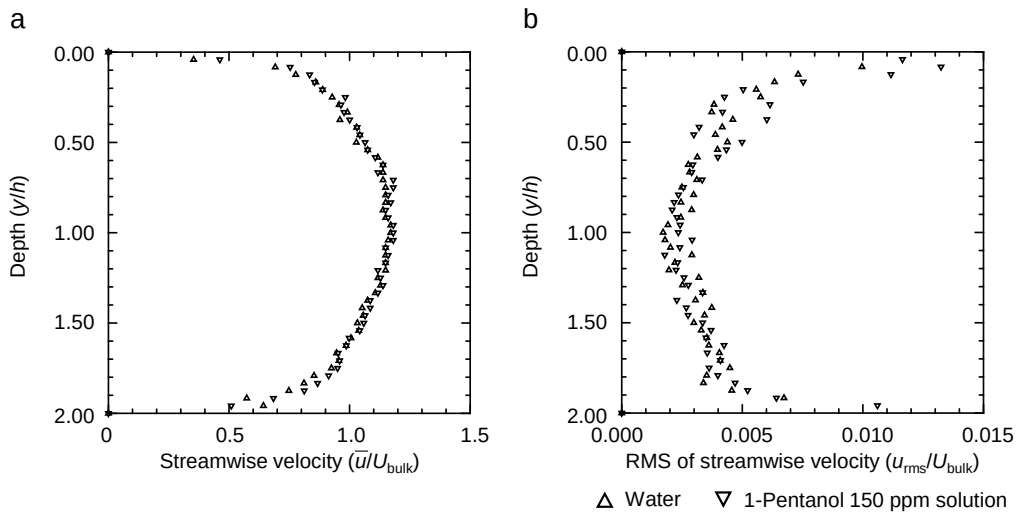

Figure 5.3 Effect of 150 ppm 1-pentanol on streamwise velocity profiles in the liquid–phase of the turbulent channel flow at $Re \approx 19300$, where the velocities are obtained by particle tracking velocimetry measurement at x = 1000 mm; (a) averaged streamwise velocity distribution and (b) RMS of the streamwise velocity distribution.

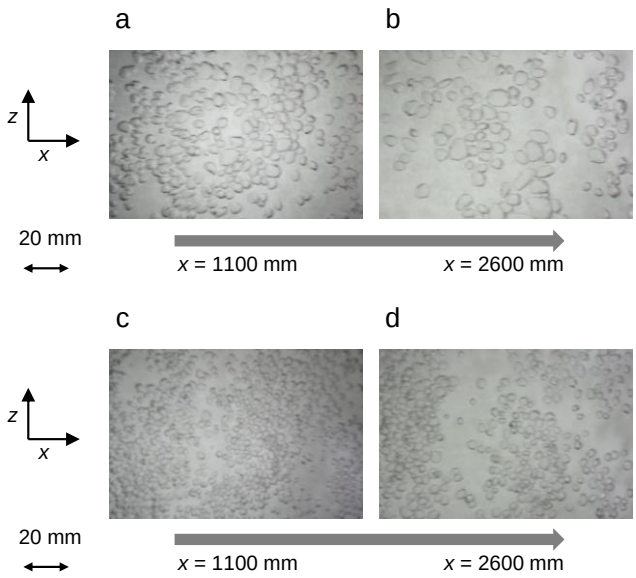

Figure 5.4 Snap pictures of bubbles taken by a camera installed above the channel at *x*' = 1100 mm and 2600 mm; (a), (b) for the water and (c), (d) for 1-pentanol solution.

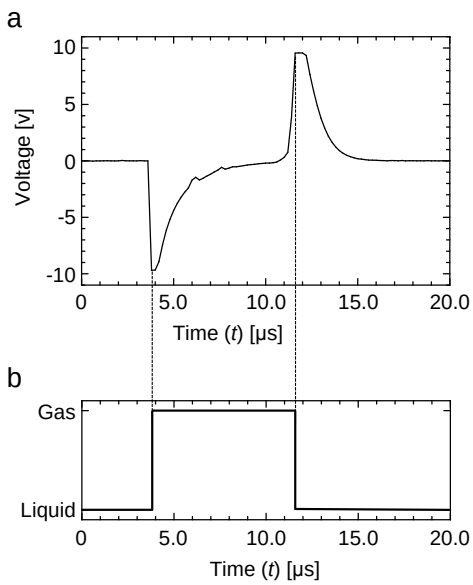

Figure 5.5 Signal obtained by an optical receiver when a bubble passes at a measurement line; (a) original signal, and (b) gas–phase detected from a pair of positive and negative peaks in the original signal.

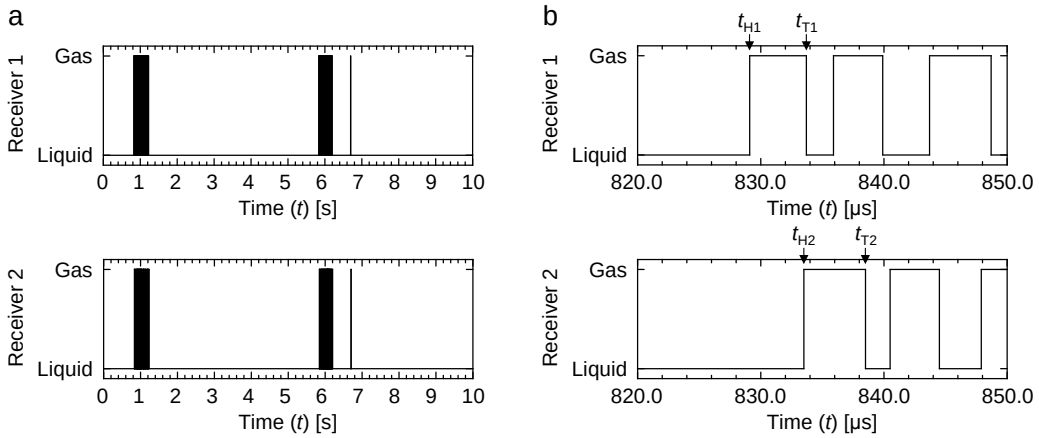

Figure 5.6 Samples of binary signals obtained from optical receivers; (a) overall views and (b) magnified views of 820 μs ≤ t ≤ 850 μs, where the bubble injection starts at t = 0 s and is repeated every 5 s, and t_{H1}, t_{T1}, t_{H2} and t_{T2} are times of the head and tail of a bubble observed by each receiver.

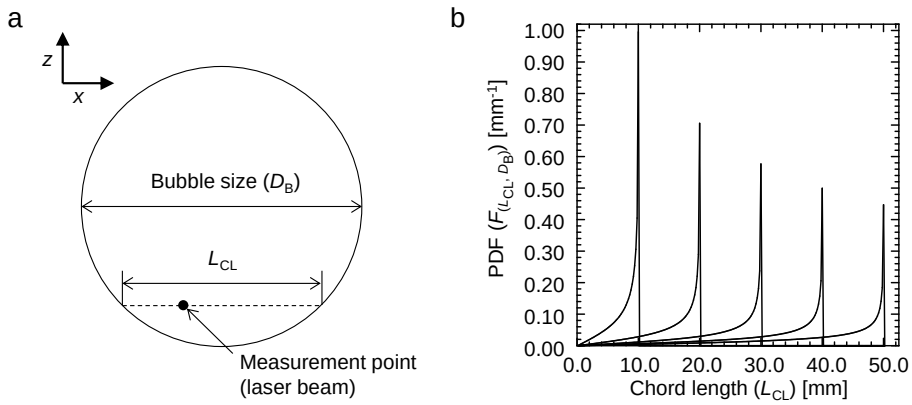

Figure 5.7 Relationship between the size and chord length of a bubble: (a) definition of chord length and (b) the chord length probability distribution of a circular bubble in five cases, where the bubble size in each case is D_B = 10, 20, 30, 40 and 50 mm, and bin size of the length (ΔL) is 0.2mm.

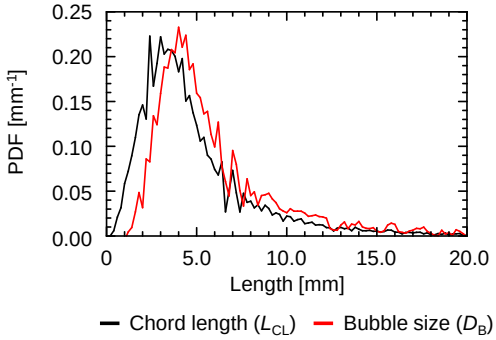

Figure 5.8 Bubble size distribution converted from a chord length distribution measured at x = 1000 mm for water, where ΔL = 0.2mm.

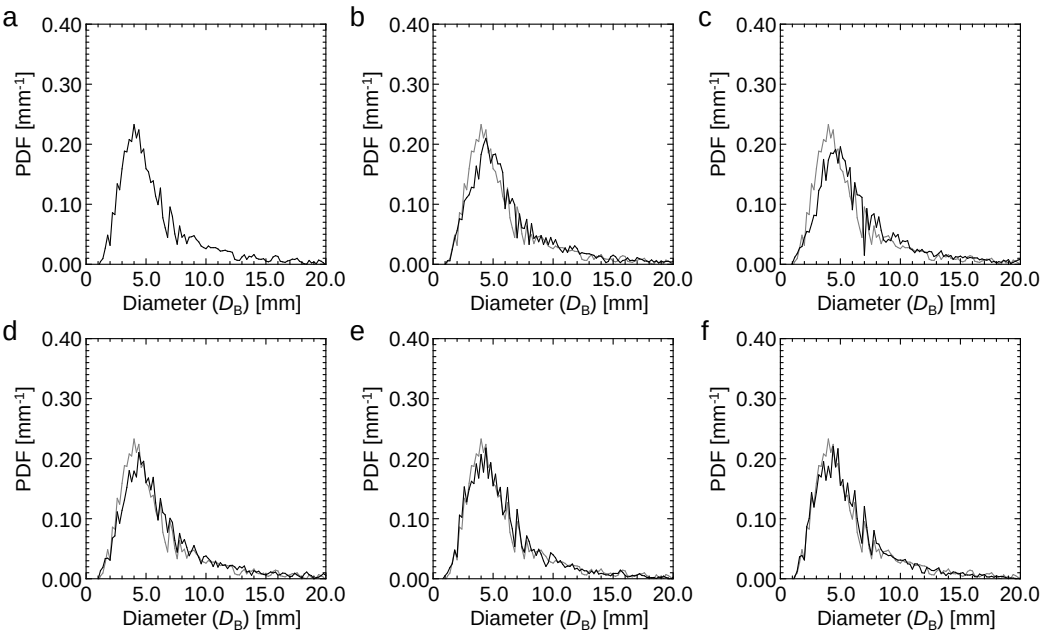

Figure 5.9 Probability distributions of size of bubbles passing at each measurement location for water; (a) x = 1000 mm, (b) 1300 mm, (c) 1600 mm, (d) 1900 mm, (e) 2200 mm and (f) 2500 mm, where gray lines indicate the distribution of (a) and ΔL = 0.2mm.

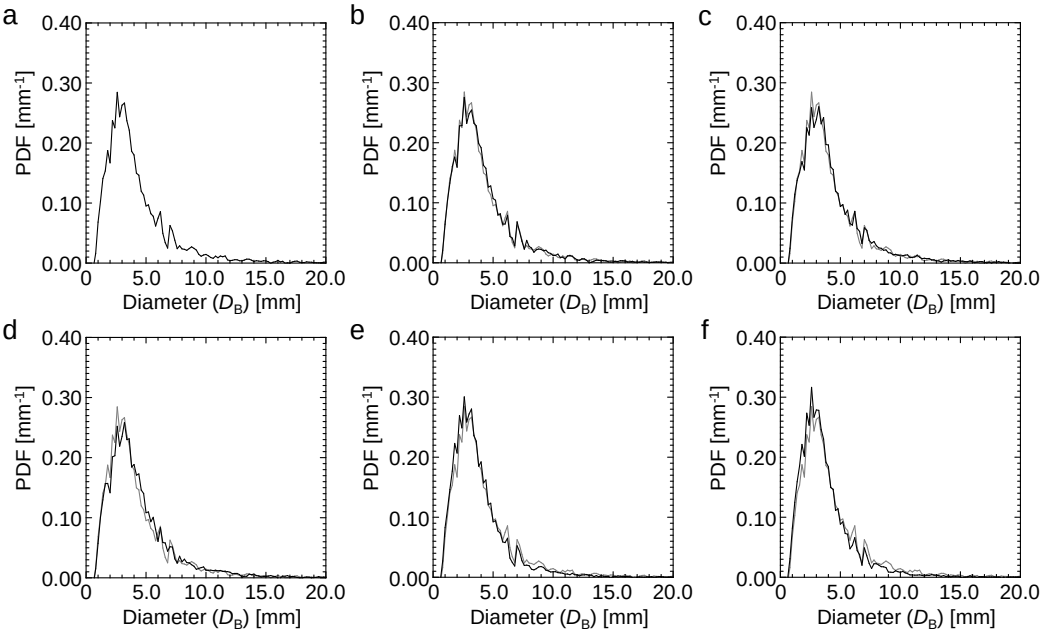

Figure 5.10 Probability distributions of size of bubbles passing at each measurement location for 1-pentanol solution; (a) x = 1000 mm, (b) 1300 mm, (c) 1600 mm, (d) 1900 mm, (e) 2200 mm and (f) 2500 mm, where gray lines indicate the distribution of (a) and ΔL = 0.2mm.

	Case 1:	Case 2:	Case 3:
Bubble behavior	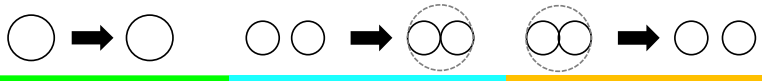		
Number (N)	N	$N/2$	$2N$
Length ($L_{total} = \sum D_B$)	L_{total}	L_{total}	L_{total}
Area ($A_{total} \propto \sum D_B^2$)	A_{total}	$2A_{total}$	$A_{total}/2$
Volume ($V_{total} \propto \sum D_B^3$)	V_{total}	$4V_{total}$	$V_{total}/4$

	Case 4 and 5:		Case 6 and 7:	
Bubble behavior				
Conserved quantity	Projection area	Volume	Projection area	Volume
Number (N)	$2N$	$2N$	N	N
Length ($L_{total} = \sum D_B$)	$2^{1/2}L_{total}$	$2^{2/3}L_{total}$	$2^{1/2}L_{total}$	$2^{2/3}L_{total}$
Area ($A_{total} \propto \sum D_B^2$)	A_{total}	$2^{1/3}A_{total}$	$2A_{total}$	$2^{4/3}A_{total}$
Volume ($V_{total} \propto \sum D_B^3$)	$V_{total}/2^{1/2}$	V_{total}	$2^{3/2}V_{total}$	$4V_{total}$

	Case 8 and 9:		Case 10 and 11:	
Bubble behavior				
Conserved quantity	Projection area	Volume	Projection area	Volume
Number (N)	$N/2$	$N/2$	N	N
Length ($L_{total} = \sum D_B$)	$L_{total}/2^{1/2}$	$L_{total}/2^{2/3}$	$L_{total}/2^{1/2}$	$L_{total}/2^{2/3}$
Area ($A_{total} \propto \sum D_B^2$)	A_{total}	$A_{total}/2^{1/3}$	$A_{total}/2$	$A_{total}/2^{4/3}$
Volume ($V_{total} \propto \sum D_B^3$)	$2^{1/2}V_{total}$	V_{total}	$V_{total}/2^{3/2}$	$V_{total}/4$
	Meaning of color	Decreased value	Maintained value	Increased value

Figure 5.11 Measured quantities affected by bubble behaviors, where black and dashed gray circles indicate the projection of real bubbles and the illusion of large bubbles when two small bubbles are in contact with each other, respectively.

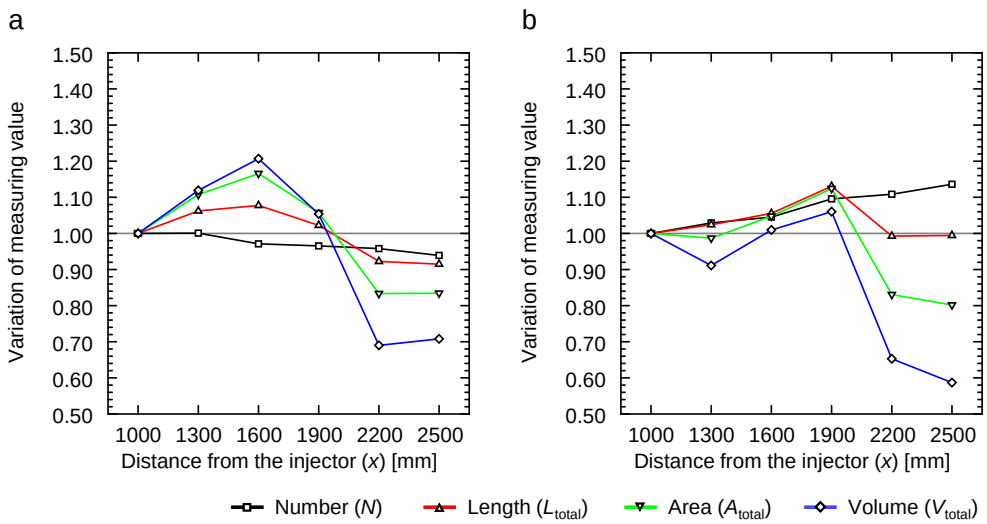

Figure 5.12 Variation of measured quantities for a bubble swarm traveling in the flow; (a) for water and (b) for 1-pentanol solution, where all values are compared with the values at x = 1000 mm.

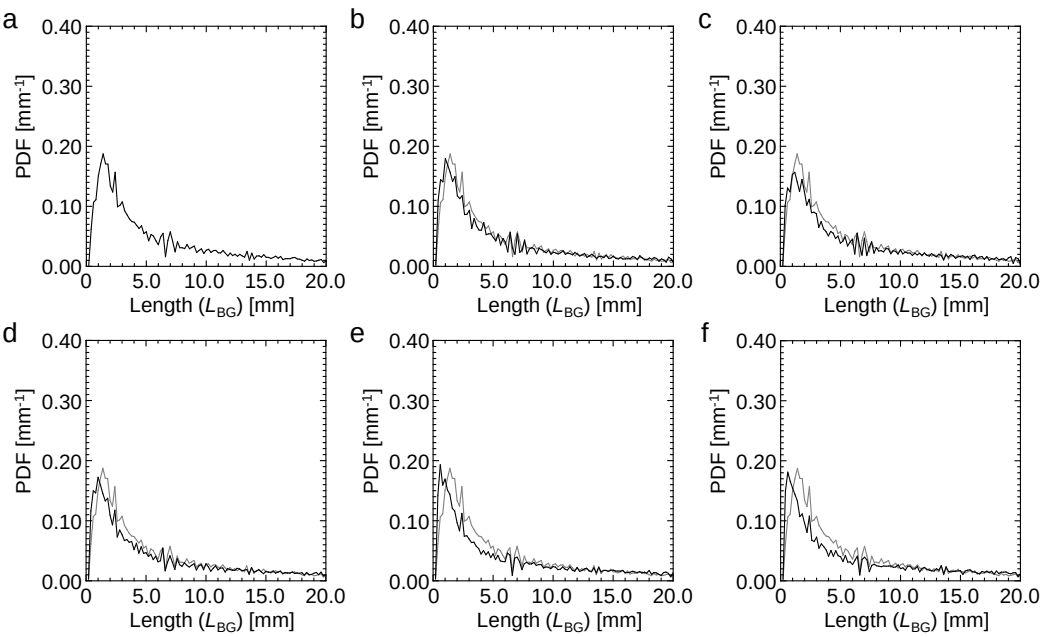

Figure 5.13 Distribution of the gap between bubbles for water; (a) x = 1000 mm, (b) 1300 mm, (c) 1600 mm, (d) 1900 mm, (e) 2200 mm and (f) 2500 mm, where gray lines indicate the distribution of (a) and ΔL = 0.2mm.

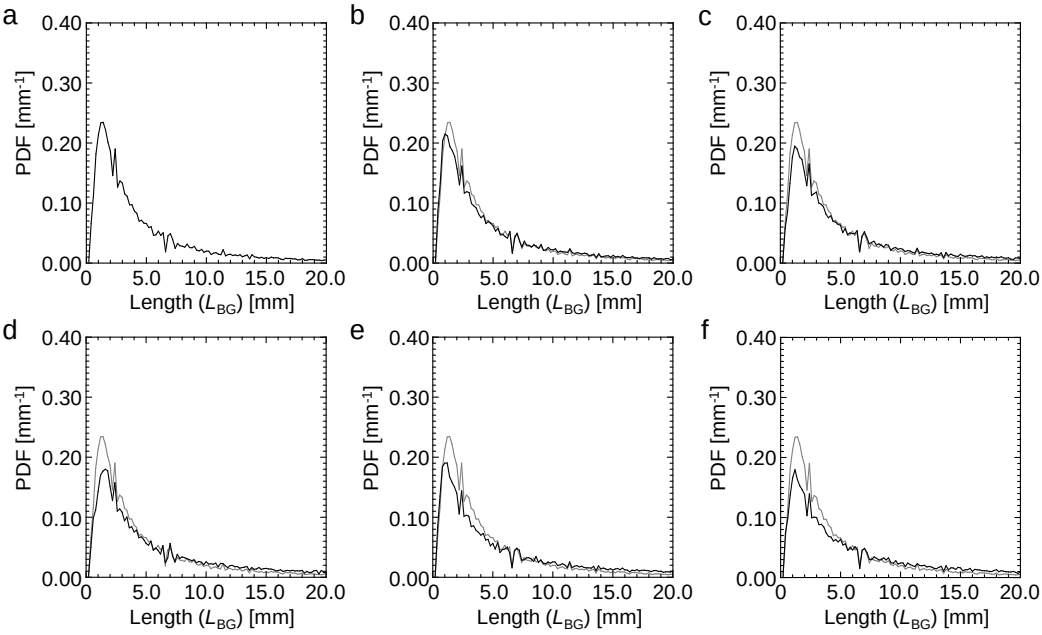

Figure 5.14 Distribution of the gap between bubbles for 1-pentanol; (a) x = 1000 mm, (b) 1300 mm, (c) 1600 mm, (d) 1900 mm, (e) 2200 mm and (f) 2500 mm, where gray lines indicate the distribution of (a) and ΔL = 0.2mm.

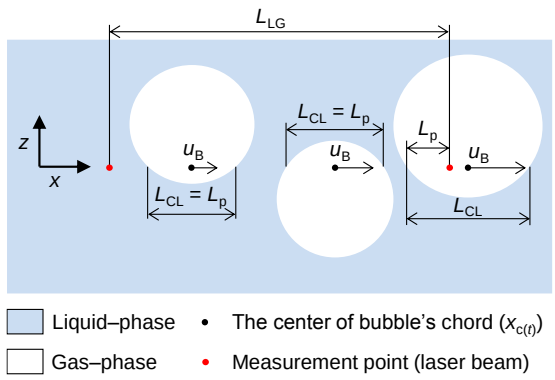

Figure 5.15 Schematic image of bubbles between two laser beams, where L_p and u_B are the part of L_{LG} located between two measurement points and the streamwise velocity of each bubble.

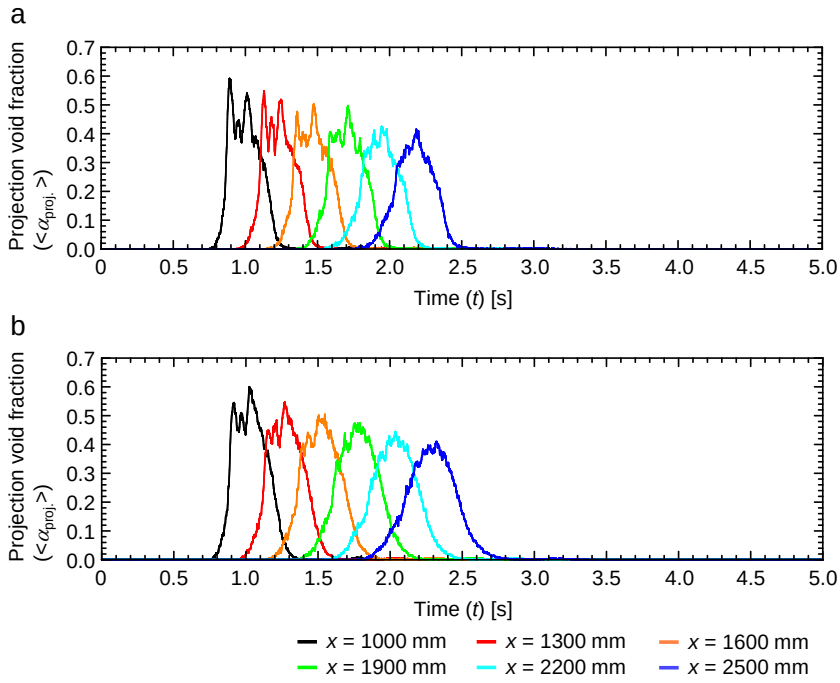

Figure 5.16 Projection void fraction between two laser beams; (a) for water and (b) for 1-pentanol solution.

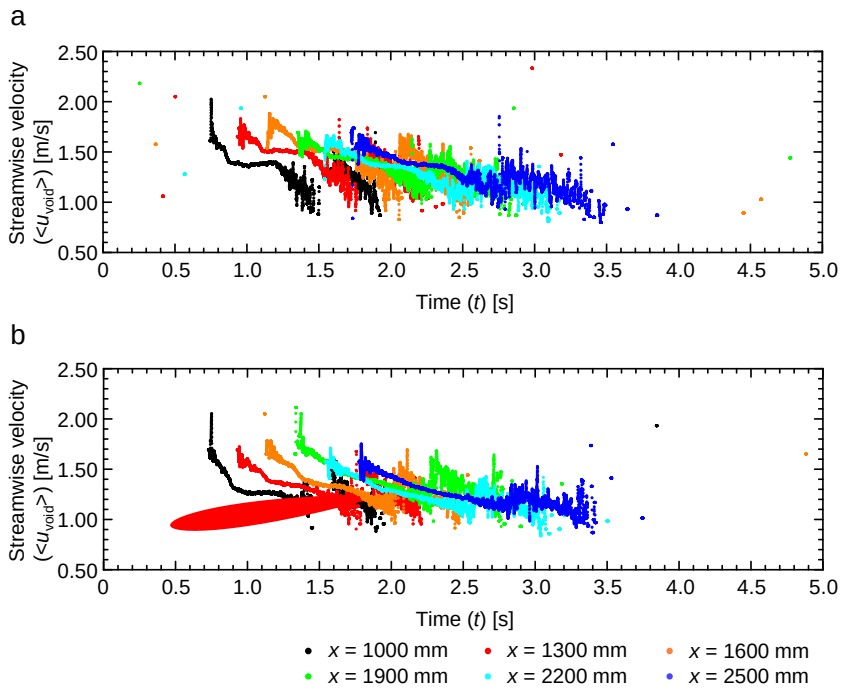

Figure 5.17 Streamwise velocity distribution for $<\alpha_{proj.}>$ between two laser beams; (a) for water and (b) for 1-pentanol solution.

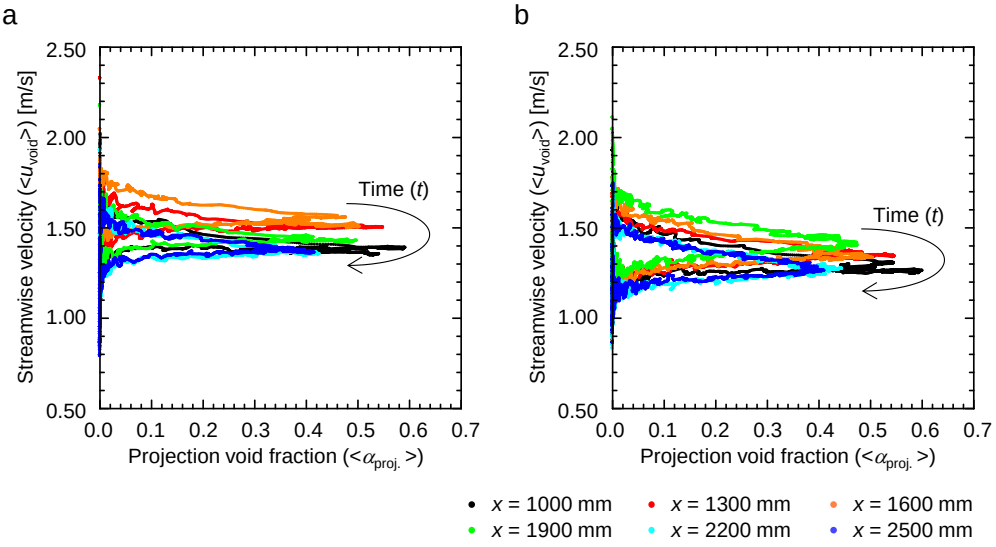

Figure 5.18 Relationship between $<\alpha_{\text{proj.}}>$ and $<u_{\text{void}}>$; (a) for water and (b) for 1-pentanol solution.

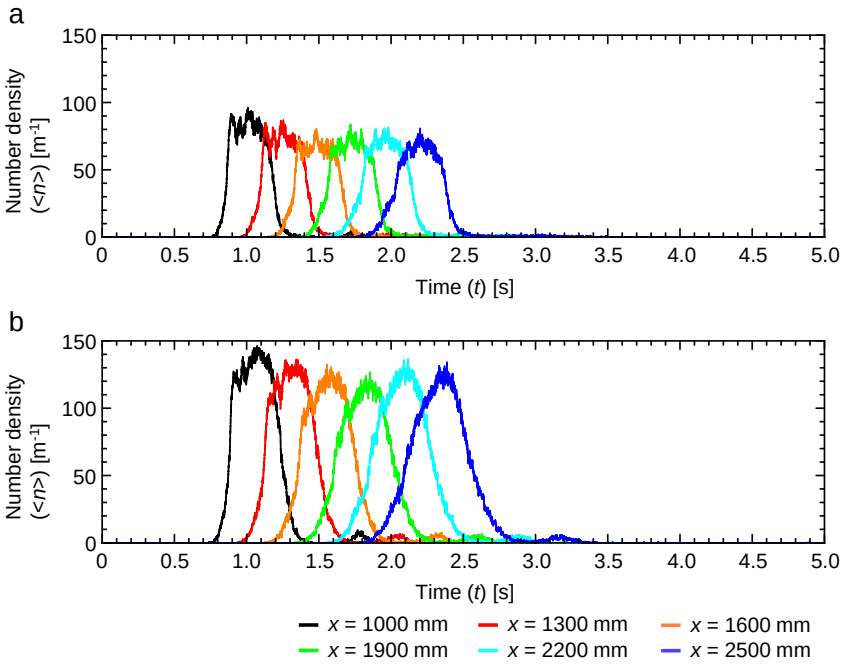

Figure 5.19 Number density distribution of the bubbles having $x_{c(t)}$ between two laser beams; (a) for water and (b) for 1-pentanol solution.

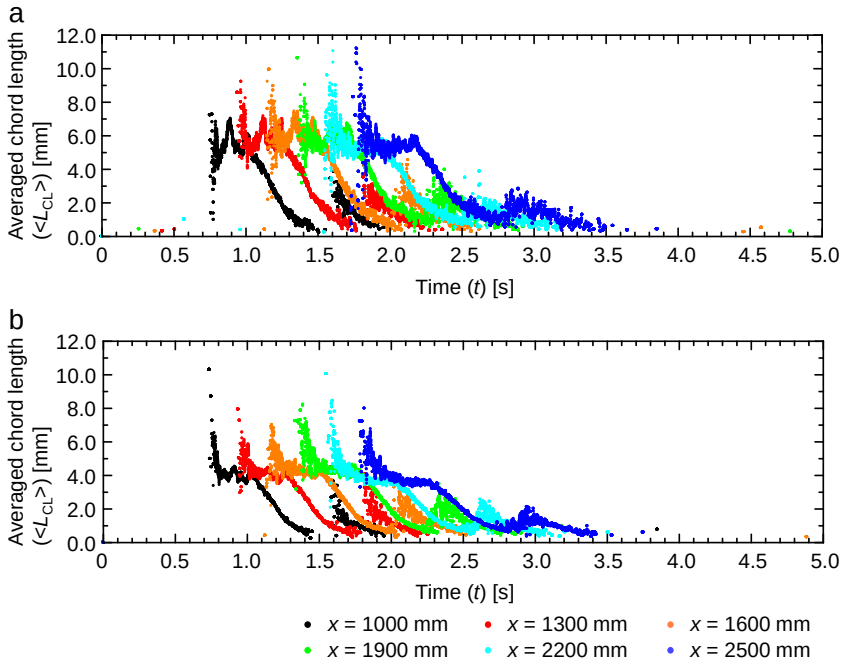

Figure 5.20 Distributions of the averaged chord length of bubbles having $x_{c(t)}$ between laser beams; (a) for water and (b) for 1-pentanol solution.

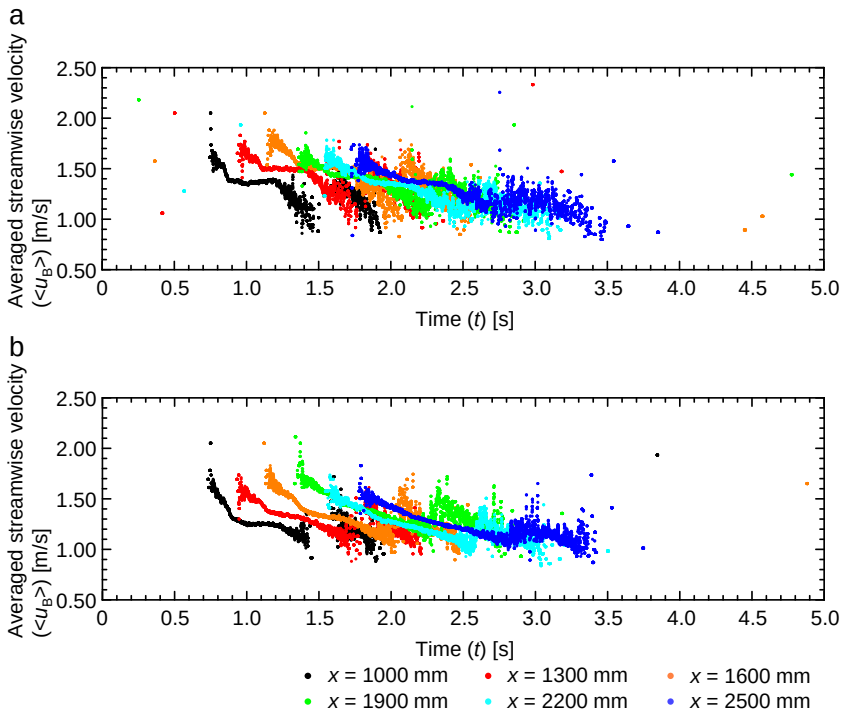

Figure 5.21 Distributions of the averaged streamwise velocity for the bubbles having $x_{c(t)}$ between laser beams; (a) for water and (b) for 1-pentanol solution.

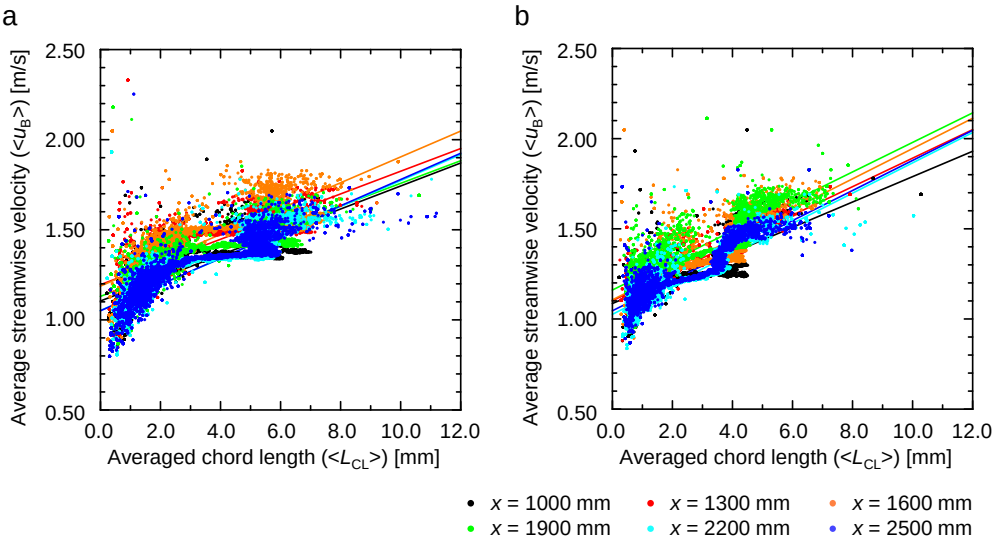

Figure 5.22 Relationship between <L_{CL}> and <u_B>; (a) for water and (b) for 1-pentanol solution, where solid lines indicate linear trends.

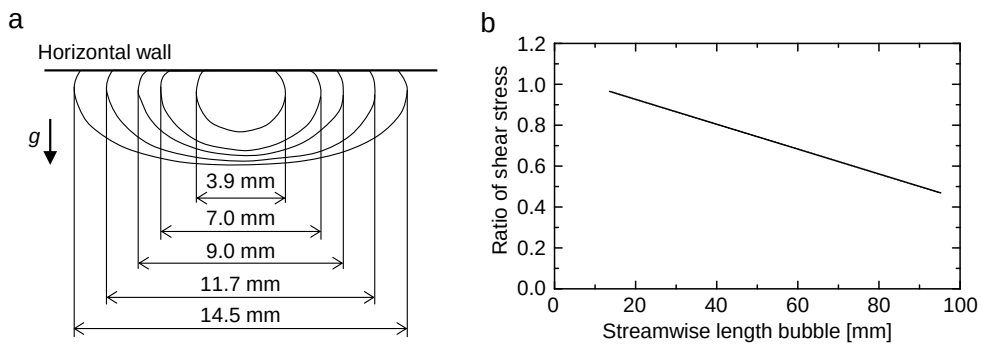

Figure 5.23 Possible causes as different streamwise velocities of bubbles when the bubble sizes are different; (a) a non-linear relationship between horizontal and vertical lengths, where shapes of bubbles beneath a horizontal wall are investigated in still water (Das et al., 2012), and (b) reduction of wall shear stress by large bubbles, where this tendency is observed in an experiment using a horizontal turbulent channel flow (Murai et al., 2007).

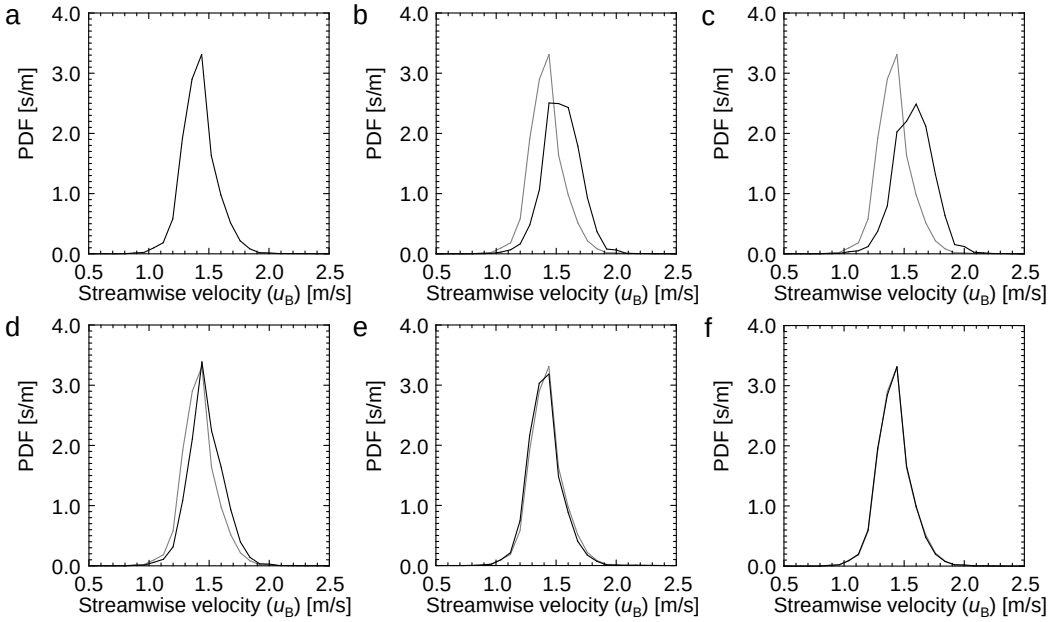

Figure 5.24 Probability distributions of the streamwise velocity of bubbles passing each measurement location for water; (a) x = 1000 mm, (b) 1300 mm, (c) 1600 mm, (d) 1900 mm, (e) 2200 mm and (f) 2500 mm, where gray lines indicate the distribution of (a) and the bin size of the velocity (Δu) is 0.08 m/s.

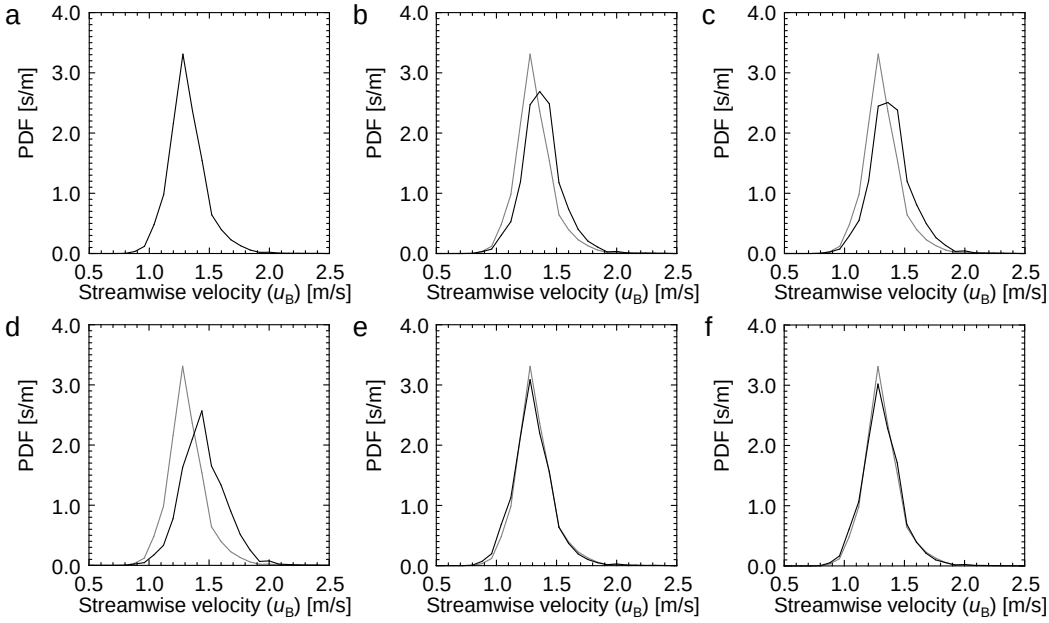

Figure 5.25 Probability distributions of the streamwise velocity of bubbles passing each measurement location for 1-pentanol solution; (a) x = 1000 mm, (b) 1300 mm, (c) 1600 mm, (d) 1900 mm, (e) 2200 mm and (f) 2500 mm, where gray lines indicate the distribution of (a) and Δu = 0.08 m/s.

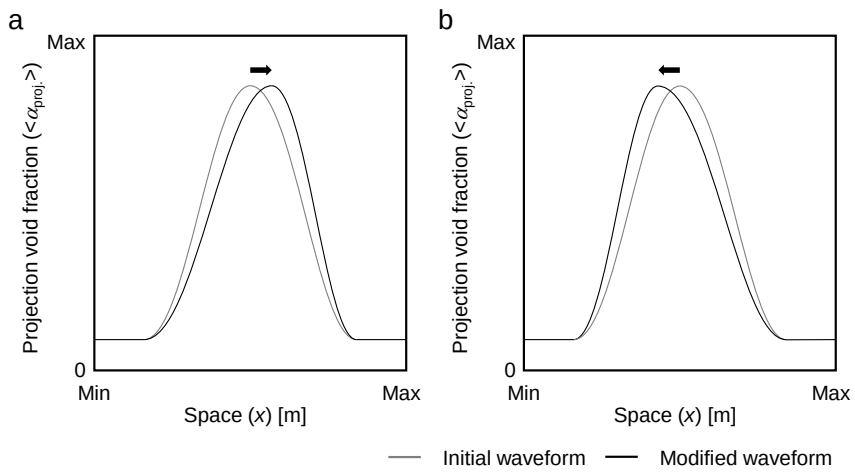

Figure 5.26 Schematic diagram of waveforms modified by (a) non-linear advection (B_m) and (b) dispersion (E_m) coefficients in **Equation 5.13**, a KdV–B equation, where coefficients in the equation are such that $B_m > 0$ and the others are zero in (a), and $E_m > 0$ and the others are zero in (b).

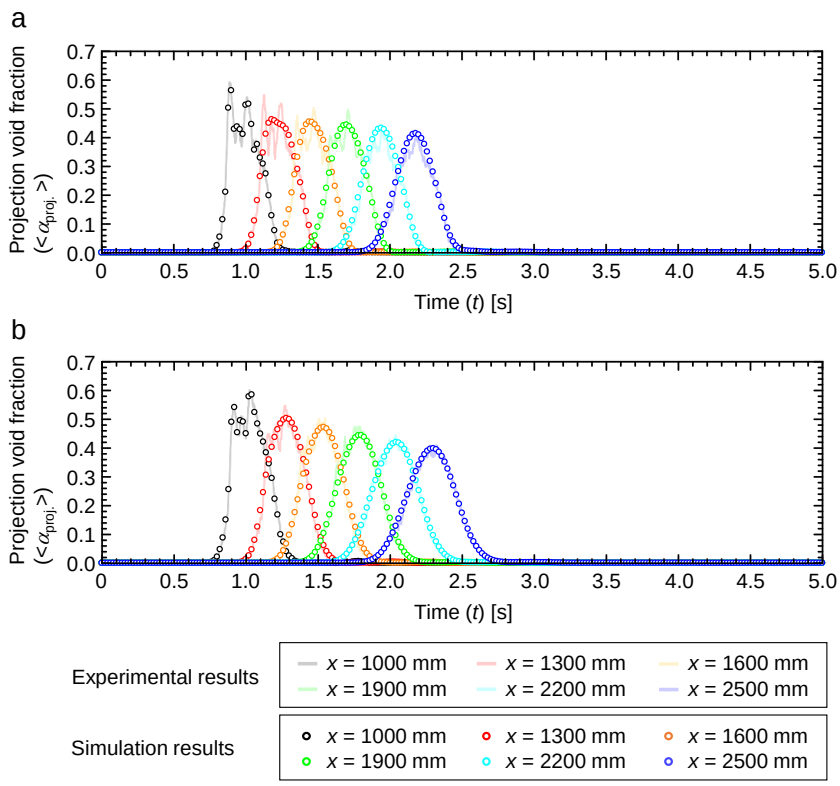

Figure 5.27 Voidage wave transitions simulated by mathematical modeling whose coefficients are selected as simulated waveforms x = 2500 mm become similar to experimental results; (a) for water and (b) for 1-pentanol solution.

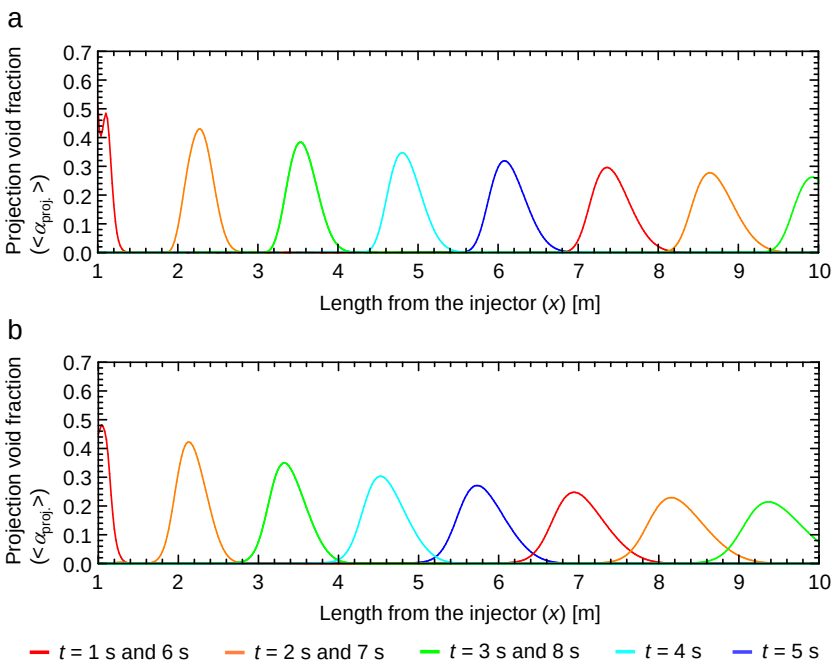

Figure 5.28 Voidage wave transitions predicted by the mathematical modeling whose coefficients are the same as those used in **Figure 5.27**, (a) for water and (b) for 1-pentanol solution.

6 Ultrasonic pulse echography for bubbles traveling in the proximity of a wall

• Preface

To predict transition of voidage wave in a system using a model established in the **Chapter 5**, void fractions experimentally obtained from some places at the system are required. In almost cases, a measurement window is needed to measure the void fraction at the system. However, in industrial fields, installing the window is hard or impossible because of mechanical or chemical durability. Furthermore, methodology for the measurement is restricted for the same reasons. In this chapter, we try to develop a novel methodology for the measurement of without any changing on the system using ultrasonic pulse generated from an ultrasonic velocimetry profiler (UVP). If we success the development, we can obtain information of voidage wave and velocity profile in liquid–phase, simultaneously.

6.1 Introduction

How do bubbles move within the boundary layer near a wall? This question has been considered for a long time and is a critical issue in fluid, thermal, and chemical engineering applications where boundary layer control is required. Bubbly drag reduction is an effective approach to control turbulent momentum transfer along a wall, and is applicable to large vessels (McCormick and Bhattacharyya, 1973; Ceccio, 2010). This technique is currently applied for cruising vessels (Kodama et al., 2008; Mizokami et al., 2010; 2013; Kumagai et al., 2015); however, the internal structure of bubbly turbulent shear flow remains unknown owing to the complex behavior of deformable bubbles. Murai (2014) recently summarized the 40-year history of drag reduction by bubble injection, and called for advanced measurement techniques that can quantitatively monitor two-phase flow structures appearing in practical applications. For instance, two-phase flows show large spatio-temporal variations in void fraction in high-Reynolds-number applications as observed by voidage waves. Moreover, the mean bubble size and bubble depth from the wall remain immeasurable in high-speed, two-phase flows, such as those present in sea trials. Oishi et al. (2009) noted the importance of naturally induced spatio-temporal fluctuations of the void fraction along the boundary layer, which improves the average drag reduction compared with the case of a uniform bubble flow. We have previously developed a repetitive bubble injection technique to artificially provide void waves and have succeeded in enhancing drag reduction using this technique (in the **Chapter 4**). Local bubble advection is believed to affect heat and mass transfer in the proximity of a wall. This is a motivation to develop a new method to monitor bubbles traveling inside boundary layers. Furthermore, such a measurement should be resistant to the high-speed flow environment and turbulent shear, and should be easily maintained for use in natural environments such as sea water.

Table 6.1 summarizes the currently available techniques for bubble detection in two-phase flows. The sensing principles are classified according to the signal used for measurement, regardless of the intrusiveness to the flow, as electric wire mesh sensors (Prasser et al., 2001), optical fibers (Saito et al., 2009), optical shadowgraphy (Kitagawa et al., 2005; Sathe et al., 2010), radiography (Mäkiharju et al., 2013), ray-attenuation-based computed tomography (CT) (Kumar et al., 1997; Prasser et al., 2005; Olerni et al., 2013), and the ultrasonic pulse method (Murai et al., 2010). Although all techniques have inherent advantages and drawbacks, the ultrasonic pulse method stands out because it permits non-invasive time-resolved bubble sensing as long as the flow speed is lower than 10 m/s (i.e., slower than the bulk speed of sound in a bubbly mixture). Here ultrasonic echography is adopted because it allows visualization of bubbles in the 2D space–time domain. Ultrasonic echography is further classified as either transmitted-wave or reflection-wave echography, as listed in **Table 6.2**. The former provides the spatial constitution of materials based on the principle of tomography using differences in the speed of sound (Glover and Sharp, 1977) or

attenuation (Dines and Kak, 1979); however, this has only rarely been applied to bubbly flows because of the non-penetrative nature beyond gas–liquid interfaces that are longer than the ultrasound beam diameter. In ultrasonic bubble identification, the amplitude of the ultrasonic echo scattered from individual bubbles can be the primary measurement. An alternative method is to use information from the null Doppler shift, because a local standing wave emerges close to the bubble surface (Murai et al., 2009). Murakawa et al. (2008) designed an ultrasound transducer embedding two piezo-electric elements for emitting and receiving ultrasonic waves of two different frequencies to distinguish bubbles from solid particles significantly smaller than the bubbles. We previously identified the surfaces of bubbles using differences in echo intensity between tracer particles and bubbles in bubbly flows (in the **Chapters 2** and **4**). Already we succeeded the bubble surface detection by ultrasonic pulse in these previous chapters, but it requires acoustic refractive index matching board embedded in wall to avoid echo from the wall. Therefore, installing locations for echography techniques already introduced in the thesis are constrained because the acoustic refractive index matching board has a low durability. Recently, an ultrasonic detector of the air layer on a ship's hull was commercially developed (Yamashita et al., 2012); however, this detector is unable to resolve individual bubbles and remains a qualitative tool for macroscopic void passages because of its low sampling frequency. Because the velocity and size of bubbles around the surface of a ship's hull are quite fast and small (ca. 3–8 m/s and 0.2–3.0 mm, respectively) (Johansen et al., 2010), only time-resolved echography over O(kHz) can provide information relating to modification of the boundary layer for turbulent boundary layer control.

In this chapter, we develop an ultrasonic echography system with high spatial and temporal resolution to obtain detailed information about advective bubbles, such as their shape and the thickness of the liquid film between the wall and the bubbles. Furthermore, to allow future application to real vessels, an ultrasonic velocity profiler (UVP) is used so that velocity profiling for the turbulent boundary layer is realized simultaneously during measurement. A representative configuration of the measurement system is schematically shown in **Figure 6.1**. An ultrasound transducer is separated from a bubbly flow by a wall to protect the transducer from physical damage. The echo signals from the bubbles and the wall are superimposed; therefore, it is necessary to distinguish the signal from the bubbles from combined signal. The objective of this chapter is to address this point, which we approach theoretically and experimentally by investigating the ultrasonic pulse behavior beyond the solid–liquid and gas–liquid interfaces in three dimensions. In particular, we try to measure the thickness of the liquid film flowing between the solid wall and moving bubbles with time-resolved echography because the presence of the film sensitively influences the macroscopic structure of the bubbly shear flow along the wall (Tisné et al., 2003). Although many techniques for measuring film thickness have been developed (Lu et al., 1993; Kamei and Serizawa, 1998; Pedersen et al., 2000; Fiedler et al., 2003; Reddyhoff et al., 2006), they

use single-cycle ultrasonic pulses to achieve a short spatial pulse length (i.e., a high spatial resolution) by avoiding echo signals from the wall and the bubbles. To enable the simultaneous measurement of the Doppler velocimetry for liquid flow monitoring, the ultrasound pulse needs to contain several cycles to provide sufficient information to analyze the frequency shift. This generally leads to a situation where the liquid film is thinner than the spatial ultrasonic pulse length. Therefore, it is challenging to identify bubbles from echo signals, which are composed of multiple reflections from many cycles propagating in the film. A technique for such an acoustic environment was proposed by Hunter et al. (2012) who succeeded in the ultrasound-based measurement of a liquid film flow bound by two solid walls. They adopted a calibration-based approach and successfully detected films thinner than 100 μm as functions of time. In this chapter, we investigate the local liquid films formed between the wall and moving deformable bubbles as a function of time. Thus, their technique cannot be applied. To establish a methodology to investigate bubbly boundary layers, experimental and numerical analyses are undertaken. We demonstrate the application of this method in a horizontal bubbly channel flow and in a towing tank facility with a model ship. Through this study, it is possible to suppose effective monitoring of bubbles injected beneath the ship bottom for the drag reduction assessment as an important application of the present echography technique. Application area is, however, not restricted, and all of demands for monitoring of bubbles traveling in a pipe or a duct, made by an opaque material will be satisfied by the present technique.

6.2 Experimental and simulation details

6.2.1 Experimental analysis

6.2.1.1 Experimental setup

As shown in **Figure 6.1**, the experimental setup is composed of four components: an ultrasound transducer, a wall separating the transducer and the water, a UVP, and a data logger. The ultrasound transducer with a resonance frequency (f_U) of 8 MHz is mounted on the outer surface of the wall and connected to the UVP (UVP-DUO MX, MET-FLOW) to generate the ultrasonic emission and echo signals. The ultrasonic beam diameter (D_U) is 2.5 mm and the divergence half-angle is 2.2°. The frequency and diameter affect various aspects of bubble detection, such as the spatial resolution, accuracy, and the range of measuring distances. In general, it is possible to distinguish small bubbles using a thin ultrasonic beam with a high frequency because it has a high spatial resolution owing to its short wavelength. Moreover, at high ultrasonic frequency, it is easier to achieve a fine beam diameter with sufficiently large acoustic pressure intensity. However, high-frequency ultrasonic waves experience significant attenuation, which restricts the range of

distances over which the velocity can be measured in the beam direction by the UVP. The echo signal received by the UVP to obtain the velocity profiles is transmitted to the data logger (DIG-100M1002-PCI, CONTEC) with a sampling frequency (f_s) of 100 MHz. This sampling frequency is 12.5 times higher than the ultrasonic frequency, which makes it possible to resolve the echo signal. The measurement parameters for the UVP and the data logger are summarized in **Table 6.3**. The wall between the transducer and the water is made of a transparent acrylic board with 10-mm thickness and is used for three purposes: (i) to optically inspect the conditions of bubbles beneath the wall, (ii) to protect the transducer from physical damage such as that incurred under high shear stress, and (iii) to avoid jamming of the echo signal by ultrasonic emission noise. It is expected that the noise will be attenuated by the transducer upon receiving the first echo signal from the liquid–solid interface because the wall is sufficiently thick.

6.2.1.2 Detection of bubbles in contact with the wall from the echo intensity

When an ultrasonic beam propagating in a material reaches the surface of another material with a different acoustic impedance, a reflection echo is generated at the interface of the two materials. The echo amplitude from a bubble in a liquid medium is large compared with that from solid materials in liquid because the acoustic impedance of air is considerably lower than that of liquids and solids. For example, the acoustic impedances ($Z_{material}$) of air, water, and an acrylic plate are approximately 428, 1.5×10^6, and 3.2×10^6 kg/m^{2}s, respectively. Thus, the presence of bubbles is generally identified from a large echo amplitude (Matikainen et al., 1986; Wada et al., 2006; Karpiouk et al., 2008). First, the echo amplitude from bubbles beneath the wall in still water was investigated. **Figure 6.2**(a) shows the emission and echo signals from the liquid–solid interface recorded by the data logger in the absence of bubbles. The emission signal from the 4-cycle UVP pulse can be seen at $t < 0.50$ μs. After the initial four cycles, a noisy signal emerges, which is also generated by the UVP upon termination of the pulse. The echo signal from the wall appears at $t \approx 8.00$ μs; at this time, the noise is attenuated owing to the sufficiently thick wall. When a single bubble that is larger than the beam diameter is present beneath the upper wall under the transducer (see **Figure 6.1**), propagation of the ultrasonic beam is blocked. The amplitude of the echo signal at $t \approx 8.00$ increases in this case, as can be seen in **Figure 6.2**(b), although this signal is composed of two echo signals from the liquid–solid and gas–liquid interfaces because the distance between the two interfaces is too small. These results suggest that the presence of a large bubble can be identified by analysis of the echo amplitudes.

To determine the extent to which the amplitude is increased by the presence of bubbles, the maximum echo amplitudes with bubbles of different sizes ($0.8 < D_B/D_U < 6.4$) was investigated as shown in **Figure 6.3**, where D_B/D_U is the bubble size normalized with respect to the ultrasonic beam diameter. The bubbles do not move and are in contact with the upper wall in still water. The

upper surfaces on the bubbles flattens because the buoyancy force exceeds the surface tension. Although a higher echo amplitude is expected from a flat surface, the sides of the bubbles are still round. Thus, an investigation of the maximum echo amplitude is required that considers the whole shape of the bubble surface. **Figure 6.4** shows the maximum echo amplitudes from bubbles at various distances (L_d) from the center of the bubble to the center of the beam. The maximum echo amplitude (V_M) from the echo signal is normalized with respect to the amplitude of the signal measured from the upper wall (V_W). In the region above the bubble, the echo amplitude is approximately 1.5 times larger than that from the upper wall. Therefore, if we know the maximum echo amplitude from the wall, it is possible to detect the surfaces of bubbles near the wall by comparing the maximum echo amplitudes. Beyond a certain distance from the upper wall, it is not possible to detect bubbles using the peak in the echo signal. In this case, two peaks appear in the signal, the second of which originates from the bubble surface instead of from the bottom wall. The depth of the surface below the upper wall is obtained from the time delay between the upper wall and the surface.

6.2.2 Numerical simulation

6.2.2.1 Conditions

In the previous **Subsection 6.2.1**, it was confirmed that stationary bubbles that have a relatively flat shape beneath the wall are detectable based on the echo amplitude. However, advective bubbles have different shapes to stationary bubbles and cannot be detected accurately using the same procedure. It is supposed that the maximum echo amplitude from advective bubbles is weaker as a result their round shapes. If the maximum echo amplitude from bubbles beneath the wall is similar to that from the wall, they are difficult to detect. To evaluate the extent to which the amplitude is reduced by the rounder surface, numerical simulations of an ultrasonic wave reflected by a spherical bubble were performed. Before the numerical simulations, the waveform of the ultrasonic pulse emitted from the transducer investigated for use in the simulations. To avoid noise from the UVP, the ultrasonic pulse was measured by another ultrasound transducer, which was positioned collinearly and was movable, as shown in **Figure 6.5**(a). **Figure 6.5**(b) shows four sample waveforms measured at different distances from the emitter. These results demonstrate that although the ultrasonic pulse exponentially decays with distance, the waveform is maintained. The experimentally obtained waveform in **Figure 6.5**(c) is modeled, and the modeled waveform is used as the emission signal in the simulation. The simulation is performed in a 3D domain, which is an authentic model of the area near the upper wall, as schematically shown in **Figure 6.6**; the conditions of the domain are summarized in **Table 6.4**. The finite-difference time-domain algorithm adopted in the present simulation is useful for solving elastic and acoustic waves at an interface

(Schroder and Scott, 2002). In the simulation, Higdon's absorbing boundary condition is applied to prevent reflection of the ultrasonic wave at the boundaries of the calculated region (Higdon, 1992). It is assumed that the acoustic impedance of air (Z_{air}) is zero, such that the ultrasonic wave is perfectly reflected at the gas–liquid interface. A 2.5-mm-diameter transducer located at the boundary of the *z*–*x* section of the elastic field emits an ultrasonic pulse with the same parameters as in the experiment and receives the echo signal. The physical properties of the acrylic resin used are representative values generally used in simulations because the properties of commercially available resins change over time and between manufacturers.

6.2.2.2 Echo intensity from a bubble in contact with the wall

The two conditions shown in **Figure 6.7** (i.e., no bubble and a small spherical bubble with D_B/D_U = 0.8 at the liquid–solid interface) are numerically calculated, where the light gray, dark gray, and white represent acrylic resin, water, and air, respectively. **Figure 6.8** shows the acoustic pressure of the echo averaged over the surface of the transducer (P_r) normalized with respect to the maximum acoustic pressure for ultrasonic emission (P_0). In the experiment with stagnant bubbles, the maximum echo amplitude was almost 1.5 times larger than that from the liquid–solid interface (i.e., the upper wall) in the absence of bubbles. It is supposed that even if a bubble has a round shape, it will produce a discriminable echo from the upper wall because the acoustic pressure is proportionally converted to a voltage by the ultrasound transducer. However, the results of the simulation indicate that the echo amplitude is almost the same with and without a bubble present. This is because the ultrasonic pulse is scattered by the round surface of the bubble, as seen in **Figure 6.9**. The simulated results for bubbles of different size (D_B) and oblateness (Γ) are summarized in **Figure 6.10**, where P_M and P_W are the maximum echo amplitude with and without a bubble, respectively: Γ is defined as

$$\Gamma = 1 - \frac{a}{b}, \qquad \textbf{Equation 6.1}$$

where *a* and *b* are the major and the minor length of the bubbles, respectively. Even for a large spherical bubble (D_B/D_U = 0.8 and Γ = 0) beneath the wall, P_M increased by only 17% compared to the case without a bubble present because of the round bubble surface. However, for bubbles with flatter surfaces (i.e., with higher Γ), P_M significantly increased. When $\Gamma \geq 0.9$, P_M was approximately 50% higher compared to the case without a bubble present, which is in good agreement with the experimental results shown in **Figure 6.4**. This means that the increased echo amplitude observed in the experiment is caused by the flatter bubble surface. To detect bubbles of the dimensions considered in the simulation based on the echo amplitude, we have to be able to

detect small variations in the echo signal. For instance, the minimum increase in echo amplitude in the simulations was just 3.8% for a bubble with D_B/D_U = 0.6 and Γ = 0.25.

6.2.2.3 Calculation of liquid film thickness

Although detection of a bubble beneath the wall is possible by comparing P_M with P_W, this does not provide information about the thickness of the liquid film between the bubble and the wall. In cases where the liquid film thickness is measured by an ultrasonic pulse with a spatial pulse length longer than the film thickness, general measurement techniques cannot be used because the echo signals from the liquid–solid interface (i.e., the wall surface) and the gas–liquid interface (i.e., the. bubble surface) are superimposed. Therefore, to measure the liquid film thickness, it is necessary that the echo signal from the bubble is extracted from the combined signal. The black and gray lines in **Figure 6.11**(a) show the waveform of the echo from the wall, $W_{(t)}$, and the waveform of the combined echo signal, $S_{(t)}$. To extract the echo waveform, $S_{(t)}$ is subtracted from $W_{(t)}$; the differential between the two signals, $B_{(t)}$, is shown in **Figure 6.11**(b). An increase of the maximum amplitude of $B_{(t)}$, P_B, with higher Γ is expected from the change in P_M. **Figure 6.12** shows samples of $B_{(t)}$ with a fixed bubble size (D_B/D_U = 0.6) and three different values of Γ (0, 0.5, and 1.0). An increase in Γ results not only in a higher P_B as expected, but also a phase shift of the echo waveform. In the simulations, the average locations of the bubbles' upper surfaces are lifted when the bubbles have different values of Γ because they are in contact with the wall. The phase shift makes bubble detection much easier, using P_B instead of P_M. For example, if $P_M = P_W$ and only the echo phase is shifted by the bubble, the bubble is detectable by evaluation of P_B; this is not possible based on an evaluation of P_M. We evaluate P_B for several different bubbles in contact with the wall and the results are summarized in **Figure 6.13**, where the echo from the wall is measured at P_B/P_W = 0. Even for a tiny bubble (D_B/D_U = 0.4), the calculated value of P_B is more that 5% greater than P_W. As previously discussed, the minimum increase in P_M was 3.8%. Therefore, it is possible that bubbles near the wall are more easily detected by comparing P_B and P_W instead of P_M and P_W.

$B_{(t)}$ provides information for measuring the liquid film thickness. When a bubble is located away from the wall, $B_{(t)}$ appears with a certain delay. **Figure 6.12** shows the delayed echo waveform from a bubble located 0.2 mm from the wall. Apart from the location, the conditions of the bubble are the same as that in **Figure 6.11**, which is a simulation of a bubble in contact with the wall. The echo waveform of $B_{(t)}$ in **Figure 6.14**(b) appears with a delay of 0.27 μs relative to that in **Figure 6.11**. This delay corresponds to the time required for the ultrasonic wave to complete a round trip between the wall and the bubble. Under the idealized conditions of the simulation, it is possible to accurately determine the delay and the distance. However, under experimental conditions, the accuracy of the waveform depends on the voltage resolution of the data logger. If P_B is lower than the voltage resolution, the bubble is not detected. Furthermore, the properties of the

wall material are unknown in many cases and it is difficult to know when an echo from the wall will appear even if the wall thickness is known. Therefore, it is necessary that the wall thickness and bubble location are determined from the echo waveforms. As seen in **Figure 6.14**, the wall and the bubble can be detected when the echo amplitude exceeds a threshold. The exact distance is defined as the shortest distance between the bubble and the wall, and the distance between the wall and the bubble (d_B) is calculated using the time delay (t_{delay}) and the speed of sound in water (c_w):

$$d_B = \frac{c_w t_{delay}}{2}. \qquad \textbf{Equation 6.2}$$

To evaluate the accuracy of this method, d_B of six different bubbles (using three different values of D_B and two different values of Γ) were investigated for four thresholds; the results are shown in **Figure 6.15**. When the threshold was set at 0.2% of P_M, the accuracy was within 0.1 mm although the bubble is small and spherical. Furthermore, d_B increased linearly in all cases. However, the accuracy for the small spherical bubble fluctuated at large thresholds (e.g., at 5% of P_M) and this bubble became undetectable when the threshold was set above P_B. The resolution of the data logger used corresponds to 1.3% of P_M. Although the accuracy is poor compared with that at 1.3% of P_M, the linearity of d_B is still maintained. From these results, it is concluded that this method is applicable for practical use if the bubbles' shapes are maintained while they traverses the ultrasonic beam.

6.3 Application in real situations

6.3.1 Horizontal channel flow

To confirm the applicability of the present technique in real situations, the surfaces of advective bubbles were detected in a turbulent channel flow. **Figure 6.16** is a schematic diagram of the experimental setup. The test section is a horizontal, rectangular channel composed of transparent acrylic boards, 40-mm high ($2h$), 160-mm wide, 6000-mm long, and with a wall thickness of 10 mm. The x, y, and z coordinates are defined as the streamwise distance from the channel inlet, vertical distance from the upper wall, and the spanwise distance from the inner wall of the channel, respectively. Tap water at 21 °C is used as the working fluid with a kinematic viscosity (ν) of 9.8×10^{-7} m^2/s and speed of sound (c_w) of 1486 m/s. To generate bubbles in the test section, ambient air is injected by a compressor through an injector comprising many tiny holes mounted on the upper wall in the upstream region of the channel at x = 1.5 m. A water tank is installed at the end of the channel to remove bubbles in the flow; the water is circulated using a pump. The ultrasound transducer for echography is located on the outer surface of the upper wall, 2.0 m from the injector.

The echography settings are listed in **Table 6.3**; the pulse repetition frequency (f_r) was fixed at 15 kHz.

Figure 6.17 shows traveling bubbles beneath the wall at $Re_h \approx 30000$ with $\alpha_{channel} \approx 0.17\%$, where the Reynolds number (Re_h) and void fraction ($\alpha_{channel}$) are defined as

$$Re_h = \frac{hU_{bulk}}{\nu} \qquad \textbf{Equation 6.3}$$

and

$$\alpha_{channel} = \frac{Q_{gas}}{Q_{liquid} + Q_{gas}}; \qquad \textbf{Equation 6.4}$$

U_{bulk}, Q_{gas}, and Q_{liquid} are the bulk mean velocity of the flow, gas flow rate, and liquid flow rate, respectively. The bubble sizes in the flow are distributed in the range of 3 mm < D_B < 20 mm. The echo amplitude with advective bubbles in the turbulent channel flow is shown in **Figure 6.18**(a). The length scales, streamwise length (x') and depth (y) are converted from the time-domain data. The spatial resolution in each direction, $\Delta x'$ and Δy, are evaluated using Taylor's hypothesis on frozen turbulence and from c_w, respectively:

$$\Delta x' = \frac{u_B}{f_r} \qquad \textbf{Equation 6.5}$$

and

$$\Delta y = \frac{c_W}{2 f_s}, \qquad \textbf{Equation 6.6}$$

where the average value of u_B is obtained using a camera. A large echo amplitude exists under the upper wall and an echo signal modified by the surfaces of the bubbles also appears. The modified echo signal nearest to the top wall at each value of x' is plotted in **Figure 6.18**(b). These plots represent the upper surfaces of the bubbles. There sizes of the two bubbles in **Figure 6.18** were measured from the camera images. The bubbles have a flat upper surface because of the upper wall and their buoyancy. Moreover, the top of each bubble experiences a lift force because bubbles have higher advection velocities than the streamwise velocity of the ambient water flow near the wall and move to a downstream region. Depending on their shape and the lift force, the advective bubbles may have a liquid film above them. This shape-dependent behavior was previously studied by optical visualization and the results are shown in **Figure 6.19** (Oishi and Murai, 2014). In summary, we have demonstrated the successful application of this bubble detection system with high temporal resolution.

6.3.2 Model ship experiment

Experiments using a model ship were designed to evaluate the ultrasonic bubble measurement system. The experiments were performed in a towing tank at Hiroshima University. The experimental parameters are listed in **Table 6.5**. The water temperature in the tank was 24°C and the viscosity and speed of sound were ν = 9.2×10^{-7} m^2/s and c = 1494 m/s, respectively. A photograph and schematic diagrams of the model ship are shown in **Figure 6.20**. The model ship was made of transparent acrylic resin with dimensions of 4000 mm in overall length (L), 600 mm in width (W) and 500 mm in height (H). The x, y, and z coordinates are defined as the streamwise distance from the leading edge, vertical position from the bottom plate, and spanwise position from the center of the ship, respectively. To avoid the effects of the wave generated by the prow, two side walls were installed at y = 20 mm, as shown in **Figure 6.20**(d). To simulate a boundary layer on a flat plate, the ship bottom was constructed using a flat plate, and the leading edges of the bottom plate and two side walls were machined at 45°. Bubbles were injected by an air injector located at x = 0.7 m. Air was introduced to a buffer chamber with a total volume of 5.0×10^{-3} m^3 by a compressor, and injected into the boundary layer through a 100-μm-diameter porous plate, as shown in **Figure 6.20**(e). An ultrasound transducer for bubble detection was placed on the upper surface of the bottom wall at x = 2.2 m. The echography settings are listed in **Table 6.3**; f_r was fixed at 20 kHz.

Figure 6.21 is a snapshot picture of bubbles traveling beneath the ship bottom taken by a camera located above the ultrasound transducer at a towing speed (U_{ship}) of 2.0 m/s and Q_{gas} of 100 L/min. The Reynolds number on the flat plate (Re_x) without bubbles and the void fraction on the boundary layer estimated from its thickness (α_δ) are 4.8×10^6 and 4.2%, respectively. They are defined as

$$Re_x = \frac{xU_{\mathrm{ship}}}{\nu} \qquad \textbf{Equation 6.7}$$

and

$$\alpha_\delta = \frac{Q_{\mathrm{gas}}}{Q_{\mathrm{liquid}} + Q_{\mathrm{gas}}} \approx \frac{Q_{\mathrm{gas}}}{W\int_0^{\delta_x} u_y dy}, \qquad \textbf{Equation 6.8}$$

where the 99% turbulent boundary layer thickness (δ_x) and streamwise velocity distribution (u_y) in the layer are assumed as

$$\delta_x = \frac{0.37x}{Re_x^{\frac{1}{5}}} \qquad \textbf{Equation 6.9}$$

and

$$u_y = U_{\text{ship}} \left(\frac{y}{\delta_x} \right)^{\frac{1}{7}}, \qquad \textbf{Equation 6.10}$$

respectively. Bubbles with a broad size distribution ($D_B \approx$ 1–20 mm) have the interfacial wave as indicated by the shadows on their upper surfaces in the figure. Capillary waves on the bubbles' surfaces indicate that a liquid film exists between the wall and the bubbles. Although the visualization confirms the presence of the liquid film, it cannot be used to estimate its thickness. **Figure 6.22**(a) shows an original echo distribution under the bottom of the ship used to measure the film thickness. The echo distribution is modified when bubbles pass under the ultrasound transducer. The upper surfaces of the bubbles detected using the modified echo are shown in **Figure 6.22**(b). The thickness of the liquid film is determined to be approximately 0.1–1 mm from the gas–liquid interface.

6.4 Conclusions

Heat, mass, and momentum transfer in a turbulent boundary layer in the vicinity of a wall are affected by the behavior of bubbles in the layer. In particular, the thickness of the liquid film between the wall and the traveling bubbles is important. We designed an ultrasonic echography system that can be applied under the typical flow conditions of ships. A relatively long spatial pulse length (0.76 mm) was used to ensure deep propagation of the pulse and to allow it to be coupled with ultrasonic velocity profiling (UVP). Bubbles larger than 1 mm were easily detected with the present echography system because they migrate at speeds between 0 and 37 m/s. The measurable range depends on the diameter of the ultrasonic beam and the pulse repetition rate as long as the signal-to-noise ratio of the echo intensity is kept high. 3D numerical analysis of the wave equation for bubbles of different sizes and shapes, and at different locations confirmed that the measurement principle is valid if the echo waveform from the wall in the absence of bubbles is determined. The best spatial resolution of the bubble surface was 0.5λ (where λ is the fundamental ultrasonic frequency) and the poorest resolution was 1.5λ for spherical bubbles smaller than the diameter of the ultrasonic beam. After optimization of the experimental parameters, the technique was applied for bubble monitoring for two different experimental configurations: a horizontal channel and a model ship subjected to bubbly turbulent flow in the boundary layer. In both configurations, the streamwise length of bubbles and the shape of the bubbles' upper surfaces, obtained from liquid film thickness located on the ultrasound beam, agreed quantitatively with optical visualizations. Furthermore, bubbles accompanying liquid films that fluctuate rapidly were successfully measured although their characteristic thickness was approximately 0.1–1.0 mm (i.e., shorter than λ). Various

extensions of this technique may follow in the future. For example, the ultrasound transducers may be positioned at different locations in spanwise and streamwise directions, which would result in spanwise bubble oblateness and improve the migration velocity, respectively (e.g. the **Chapter 5**).

• Nomenclature and units

a, b	long and short lengths of a spherical bubble, m
$B_{(t)}$	echo signal from the bubble surface, Pa
c_w	speed of sound in water, m/s
D_U	diameter of the ultrasonic beam, m
D_B	size of the bubble, m
d_B	distance between the wall and bubble surface, m
f_r	pulse repetition frequency, Hz
f_s	sampling frequency, Hz
f_U	ultrasonic frequency, Hz
H	height of the model ship, m
h	half height of the channel, m
L	length of the model ship, m
L_d	distance from the center of the bubble to the center of the ultrasonic beam, m
L_p	pass length of the ultrasonic beam, m
L_x, L_y, L_z	distance in each direction for a region of the numerical simulation, m
n	number of cycles in the ultrasound pulse, dimensionless
P	acoustic pressure, Pa
P_0	maximum emitted acoustic pressure, Pa
P_B	maximum echo amplitude from the bubble surface, Pa
P_M	maximum echo amplitude, Pa
P_r	acoustic pressure received by the receiving ultrasound transducer, Pa
P_W	maximum echo from the upper wall, Pa
Re_h	Reynolds number defined by the half height of the channel, dimensionless
Re_x	Reynolds number on the flat plate, dimensionless
$S_{(t)}$	echo signal from the wall and bubble surface, Pa
t_{delay}	time for a round trip of ultrasonic pulses in the liquid film, s
t	time, s
U_{bulk}	bulk mean velocity of the test flow, m/s
U_{ship}	main flow velocity under the ship (equivalent to towing speed), m/s
u_B	advection velocity of the bubble surface, m/s
u_y	streamwise velocity distribution in the turbulent boundary layer, m/s
V	echo amplitude, V
V_M	maximum echo amplitude near the upper wall, V
V_W	maximum echo amplitude from the upper wall, V
W	width of the model ship, m

$W_{(t)}$	echo signal from the wall, Pa
x, y, z	x, y, z coordinates in the experimental setup, m
x'	streamwise length from the measurement point, m
$\Delta x', \Delta y$	spatial resolution in the x and y directions of the ultrasonic measurement, m
Z_{material}	acoustic impedance of the material, kg/m^{2}s
$\alpha_{\mathrm{channel}}$	void fraction in the channel flow, dimensionless
α_{δ}	void fraction in the turbulent boundary layer on the flat plate, dimensionless
Γ	oblateness of a spheroidal bubble, dimensionless
δ_x	99% turbulent boundary layer thickness, m
λ	wavelength of the ultrasound, m
ν	kinematic viscosity of the test fluid, m^2/s

• References

Ceccio S.L., 2010. Frictional drag reduction of external flow with bubble and gas injection, *Annu. Rev. Fluid Mech.* **42**, 183–203.

Dines D.A. and Kak A.C., 1979. Ultrasonic attenuation tomography of soft tissues, *Ultrasonic imaging* **1**, 16–33.

Fiedler S., Yildiz S. and Auracher H., 2003. Determination of film thickness and flooding during reflux condensation in a small, inclined tube with an ultrasonic transducer, *int. j. Energy Res.* **27**, 315–325.

Glover G. and Sharp H., 1977, Reconstruction of ultrasound propagation speed distributions in soft tissue: time-of-flight tomography, *IEEE Trans. Sonics Ultrason.* **Su-24**, 229–234.

Higdon R.L., 1992. Absorbing boundary conditions for acoustic and elastic waves in stratified media, *J. Comput. Phys.* **101**, 386–418.

Hunter A., Dwyer-Joyce R. and Harper P., 2012. Calibration and validation of ultrasonic reflection methods for thin-film measurement in tribology, *Meas. Sci. Technol.* **23**, 105605.

Johansen J., Castro A.M. and Carrica P., 2010. Full-scale two-phase flow measurements on Athena research vessel, *Int. J. Multiphase Flow* **36**, 720–737.

Kamei T. and Serizawa A., 1998. Measurement of 2-dimensional local instantaneous liquid film thickness around simulated nuclear fuel rod by ultrasonic transmission technique, *Nucl. Eng. Des.* **184**, 349–362.

Karpiouk A.B., Aglyamov S.R., Bourgeois F., Ben-Yakar A. and Emelianov S.Y., 2008. Quantitative ultrasound method to detect and monitor laser-induced cavitation bubbles, *J. Biomed. Opt.* **13**, 034011.

Kitagawa A., Hishida K. and Kodama Y., 2005. Flow structure of microbubble-laden turbulent channel flow measured by PIV combined with the shadow image technique, *Exp. Fluid* **38**, 466–475.

Kodama Y., Hinatsu M., Hori T., Kawashima H., Takeshi H., Makino M., Ohnawa M., Sanada Y., Murai Y. and Ohta S., 2008. A full-scale air lubrication experiment using a large cement carrier for energy saving (result and analysis), *The Japan Society Naval Architects and Ocean Engineers*, 163–166 (in Japanese).

Kumagai I., Takahashi Y. and Murai Y., 2015. A new power-saving device for air bubble generation using a hydrofoil for reducing ship drag: theory, experiments, and applications to ships, *Ocean Eng.* **95**, 183–194.

Kumar S.B., Moslemian D. and Duduković M.P., 1997. Gas-holdup measurements in bubble columns using computed tomography, *AIChE J.* **43**, 1414–1425.

Lu Q., Suryanrayana N.V. and Christododoulu C., 1993. Film thickness measurement with an ultrasonic transducer, *Exp. Thermal Fluid Sci.* **7**, 354–361.

Mäkiharju S.A., Gabillet C., Paik B.G., Chang N.A., Perlin M. and Ceccio S.L., 2013, Time-resolved two-dimensional X-ray densitometry of a two-phase flow downstream of a ventilated cavity, *Exp. Fluid* **54**, 1561.

Matikainen L., Irons G.A., Morala E.C. and Chang J.S., 1986. Ultrasonic system for the detection of transient liquid/gas interfaces using the pulse–echo technique, *Rev. Sci. Instrum.* **57**, 1661–1666.

McCormick M.E. and Bhattacharyya R., 1973. Drag reduction of a submersible hull by electrolysis, *Naval Engineers J.* **85**, 11–16.

Mizokami S., Kawakita C., Kodan Y., Takano S., Higasa S. and Shignaga R., 2010. Experimental study of air lubrication method and verification of effects on actual hull by means of sea trial, *MHI. Technical Review* **47**, 41–47.

Mizokami S., Kawakado M., Kawano M., Hasegawa T. and Hirakawa I., 2013. Implementation of ship energy-saving operations with Mitsubishi air lubrication system, *MHI. Technical Review* **50**, 44–49.

Murai Y., Ohta S., Shigetomi A., Tasaka Y. and Takeda Y., 2009. Development of an ultrasonic void fraction profiler, *Meas. Sci. Technol.* **20**, 114003.

Murai Y., Tasaka Y., Nambu Y., Takeda Y. and Gonzalez S.R.A., 2010. Ultrasonic detection of moving interfaces in gas–liquid two-phase flow, *Flow Meas. Instrum.* **21**, 356–366.

Murai Y., 2014. Frictional drag reduction by bubble injection, *Exp. Fluids* **55**, 1773.

Murakawa H., Kukura H. and Aritomi M., 2008. Application of ultrasonic multi-wave method for two-phase bubbly and slug flows, *Flow Meas. Instrum.* **19**, 205–213.

Oishi Y., Murai Y., Tasaka Y. and Takeda Y., 2009. Frictional drag reduction by wavy advection of deformable bubbles, *J. Phys.: Conf. Ser.* **147**, 012020.

Oishi Y. and Murai Y., 2014. Horizontal turbulent channel flow interacted by a single large bubble, *Exp. Thermal Fluid Sci.* **55**, 128–139.

Olerni C., Jia J. and Wang M., 2013. Measurement of air distribution and void fraction of an upwards air–water flow using electrical resistance tomography and a wire-mesh sensor, *Meas. Sci. Technol.* **24**, 035403.

Pedersen P.C., Cakareski Z. and Hermanson J.C., 2000. Ultrasonic monitoring of film condensation for applications in reduced gravity, *Ultrasonics* **38**, 486–490.

Prasser H.M., Scholz D. and Zippe C., 2001. Bubble size measurement using wire-mesh sensors, *Flow Meas. Instrum.* **12**, 299–312.

Prasser H.M., Misawa M. and Tiseanu I., 2005. Comparison between wire-mesh sensor and ultra-fast X-ray tomograph for an air–water flow in a vertical pipe, *Flow Meas. Instrum.* **16**, 73–83.

Reddyhoff R., Dwyer-Joyce P. and Harper P., 2006. Ultrasonic measurement of film thickness in mechanical seals, *Sealing Technol.* **2006**, 7–11.

Saito T., Matsuda K., Ozawa Y., Oishi S. and Aoshima S., 2009. Measurement of tiny droplets using a newly developed optical fibre probe micro-fabricated by a femtosecond pulse laser, *Meas. Sci. Technol.* **20**, 114002.

Sathe M.J., Thaker I.H., Strand T.E. and Joshi J.B., 2010. Advanced PIV/LIF and shadowgraphy system to visualize flow structure in two-phase bubbly flows, *Chem. Eng. Sci.* **65**, 2431–2442.

Schroder C.T. and Scott W.R.Jr., 2002. On the stability of the FDTD algorithm for elastic media at a material interface, *IEEE Trans. Geo. Rem. Sens.* **40**, 474–481.

Tisné P., Aloui F. and Doubliez L., 2003. Analysis of wall shear stress in wet foam flows using the electrochemical method, *Int. J. Multiphase Flow* **29**, 841–854.

Wada S., Kikura H. and Aritomi M., 2006. Pattern recognition and signal processing of ultrasonic echo signal on two-phase flow, *Flow Meas. Instrum.* **17**, 207–224.

Yamashita T., Horiuchi H. and Yoshida R., 2012. Development of bubble sensor system *JRC. Review* **63**, 34–37 (in Japanese), http://www.jrc.co.jp/eng/company/html/review63/08.html (in English).

• Tables

Table 6.1 Characteristics of techniques used to measure bubbles.

Equipment	Wire sensor	Optical fiber	Camera	Radiation	CT scanner	Ultrasound transducer
Principle	Electric conductivity	Refractive index	Projection of image	Transmissivity	CT	Acoustic impedance
Interference of the flow	Invasive	Invasive	Non-invasive	Non-invasive	Non-invasive	Non-invasive
Spatial dimensions	1	0 (point-wise)	2	2	3	1
Load of data processing	Low	Low	High	High	High	Low

Table 6.2 Classification of ultrasonic echography techniques.

Received wave	Transmitted	Transmitted	Reflected	Reflected	Reflected
Principle	Attenuation	Speed of sound	Speed of sound	Doppler shift	Echo intensity
Measured value	Amplitude	Time of flight	Time of flight	Frequency	Amplitude
Converted value	Volume fraction of material	Volume fraction of material	Length	Velocity	Type of material

Table 6.3 Instrument settings.

UVP (ultrasonic velocity profiler)		
Ultrasonic frequency (f_U)	8	MHz
Number of cycles (n)	4	-
Wavelength (λ)	0.19	mm
Spatial pulse length	0.76	mm
Pulse repetition frequency (f_r)	15–20	kHz
Voltage of ultrasonic pulse emission signal	150	V
Diameter of ultrasonic beam (D_U)	2.5	mm
Divergence half-angle	2.2	degrees
Data logger		
Sampling frequency (f_s)	100	MHz
Range of voltage	±2	V
Resolution of voltage	4	mV

Table 6.4 Parameters for the numerical simulation.

Algorithm	finite-difference time-domain	
Calculating region ($L_x \times L_y \times L_z$)	5×15×5	mm^3
Space step	20	μm
Time step	2.5	ns
Absorbing boundary condition	Higdon second order	
Acoustic impedance of air (Z_{air})	0	kg/m^2s
Speed of sound in water (c_w)	1480	m/s
Density of water	980	kg/m^3
Attenuation rate in water	0.2	dB/m/MHz
Density of acrylic resin	1190	kg/m^3
Young's modulus of acrylic resin	3.14	GPa
Poisson ratio of acrylic resin	0.35	-
Attenuation rate in acrylic resin	42	dB/m/MHz

Table 6.5 Parameters of the model ship experiment.

Towing tank		
Length	80	m
Depth	3.5	m
Width	8	m
Towing train		
Acceleration	±0.1	m/s^2
Maximum speed	3.00	m/s
Model ship		
Material	acrylic resin	
Length (L)	4000	mm
Height (H)	500	mm
Width (W)	600	mm
Weight (empty load)	149.2	kg
Draft (empty load)	68	mm

- **Figures**

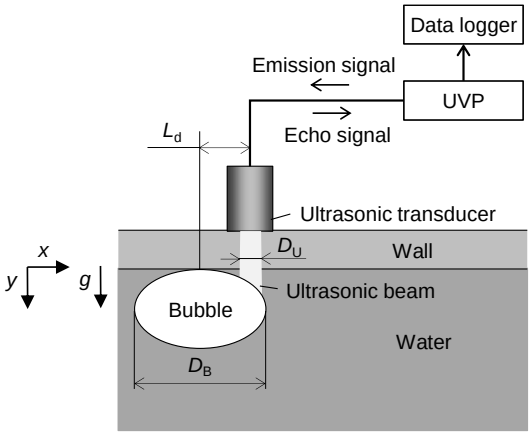

Figure 6.1 Schematic diagram of the experimental setup, where D_B, D_U, and L_d are the bubble size, diameter of the ultrasonic beam, and horizontal displacement from the center of the bubble to the center of the ultrasonic beam, respectively.

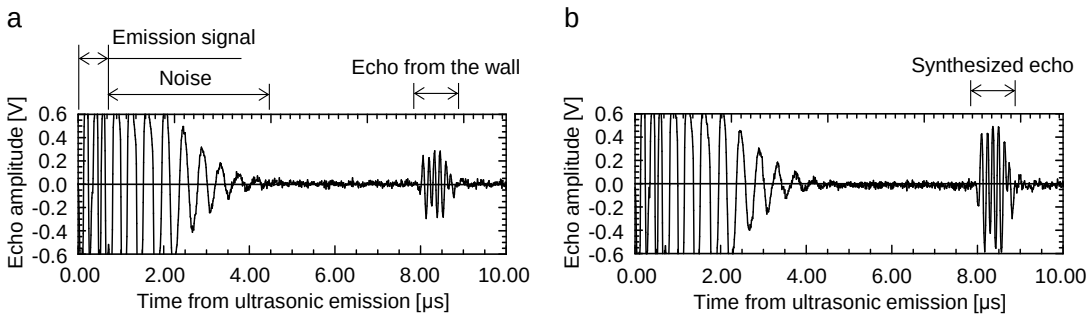

Figure 6.2 Echo amplitude recorded by the data logger: (a) without a bubble and (b) with a bubble, where the signal is composed of the echo signals from the wall and from the bubble.

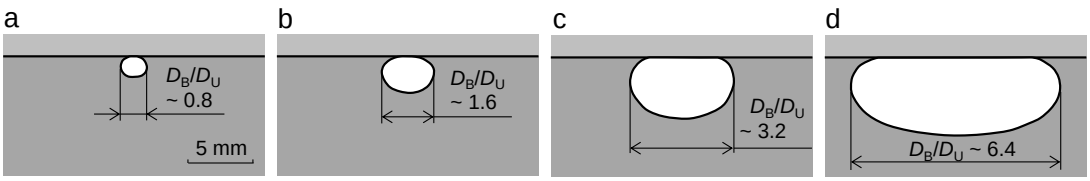

Figure 6.3 Illustrations of bubbles of different sizes beneath the wall in still water: (a) $D_B/D_U \approx 0.8$, (b) $D_B/D_U \approx 1.6$, (c) $D_B/D_U \approx 3.2$, and (d) $D_B/D_U \approx 6.4$.

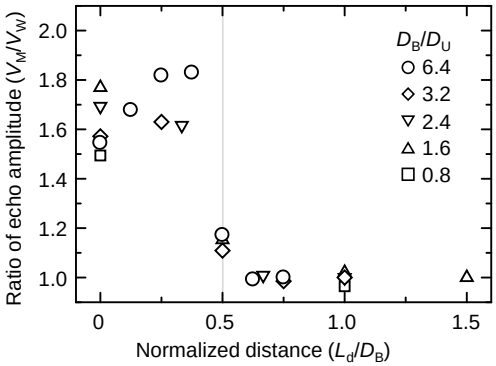

Figure 6.4 Maximum echo amplitude from bubble surface normalized with respect to that measured from the upper wall; the gray line represents the bubble surface.

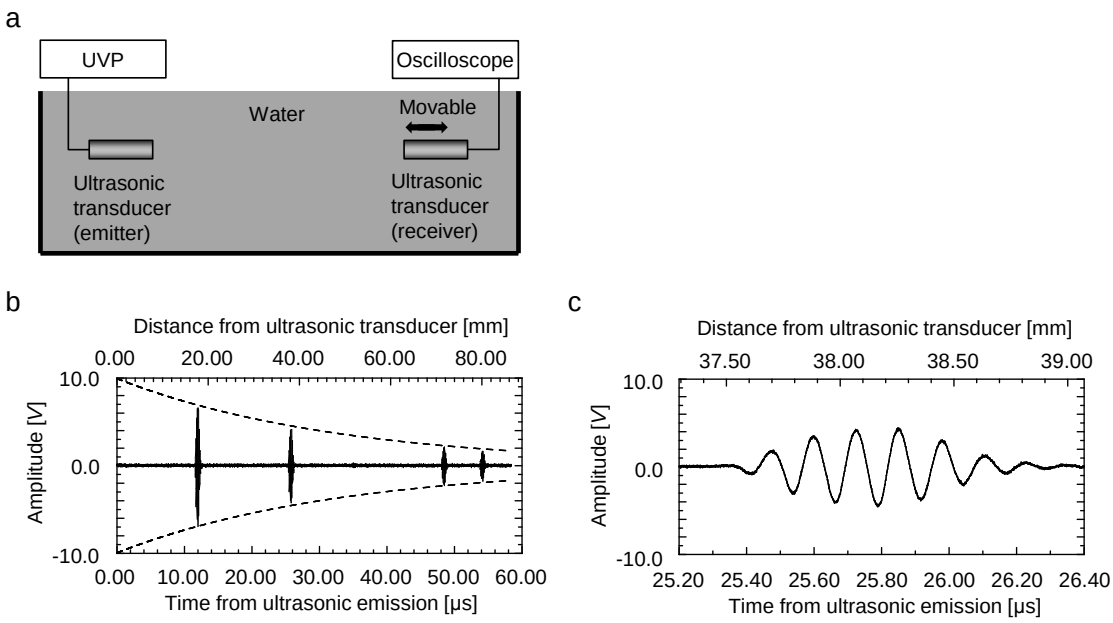

Figure 6.5 Ultrasonic pulse emitted from the ultrasound transducer: (a) schematic diagram of the experimental setup used to measure the pulse, (b) sample signals received at four different distances from the emitter, and (c) detailed pulse waveform.

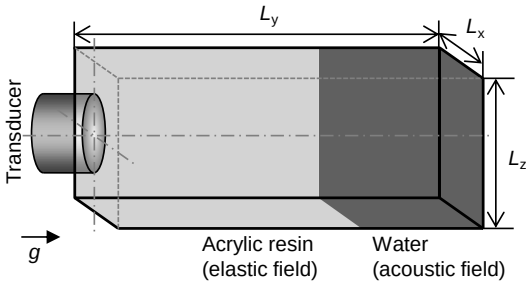

Figure 6.6 Schematic diagram of the 3D domain for numerical simulation of the elastic and acoustic waves, where L_x, L_y, and L_z are the distances in each direction, which are set at 5, 15, and 5 mm, respectively, contacting surface of the transducer is set on acrylic resin and located at the center of domain.

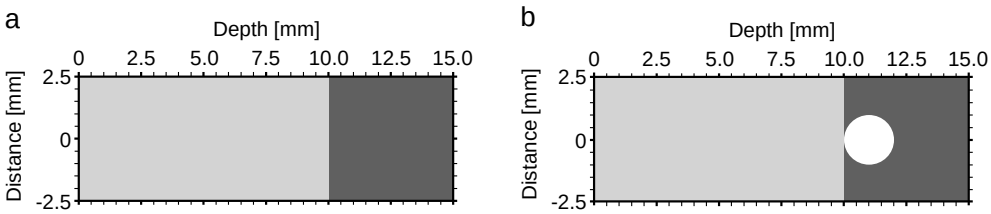

Figure 6.7 Conditions for the numerical simulation, where light gray, dark gray, and white represent acrylic resin, water, and air: (a) without a bubble and (b) for a small spherical bubble with D_B/D_U = 0.8.

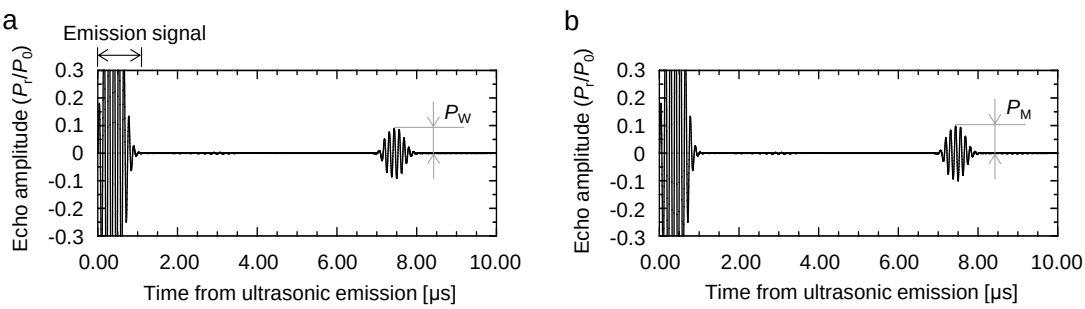

Figure 6.8 Echo amplitude received by the ultrasound transducer: (a) without a bubble and (b) with a small spherical bubble with D_B/D_U = 0.8, where signals in $t \leq 1.00$are the emission signal, the amplitude (P_r) is determined as the average of all received acoustic pressures at the surface of the transducer, P_0 is the maximum acoustic pressure for ultrasonic emission, and P_W and P_M are the maximum echo amplitude in the absence and presence of the bubble.

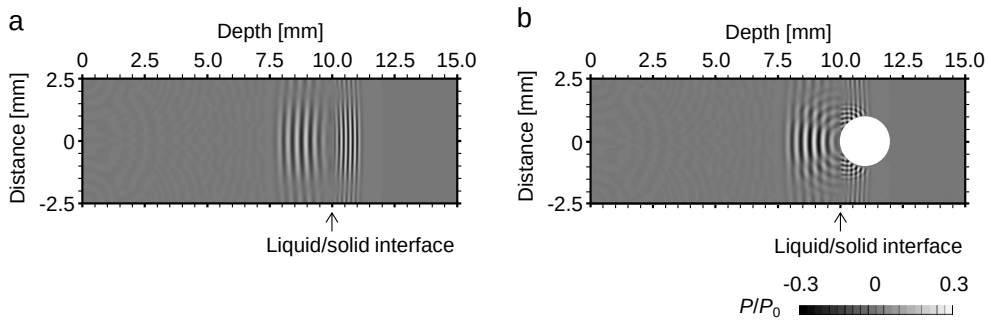

Figure 6.9 Ultrasonic pulse reflected from the wall: (a) without a bubble and (b) with a small spherical bubble with D_B/D_U = 0.8 indicated by the white circle.

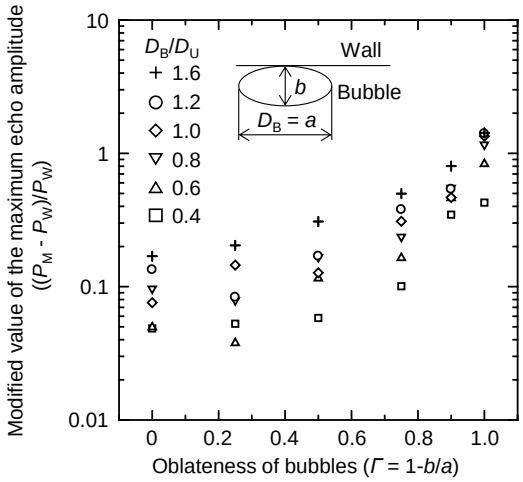

Figure 6.10 Ratio of the maximum echo amplitude from the surfaces of bubbles of different shapes, where the gray line indicates the maximum echo amplitude from the upper wall and D_B/D_U is the relative size of the bubble compared to the ultrasonic beam diameter.

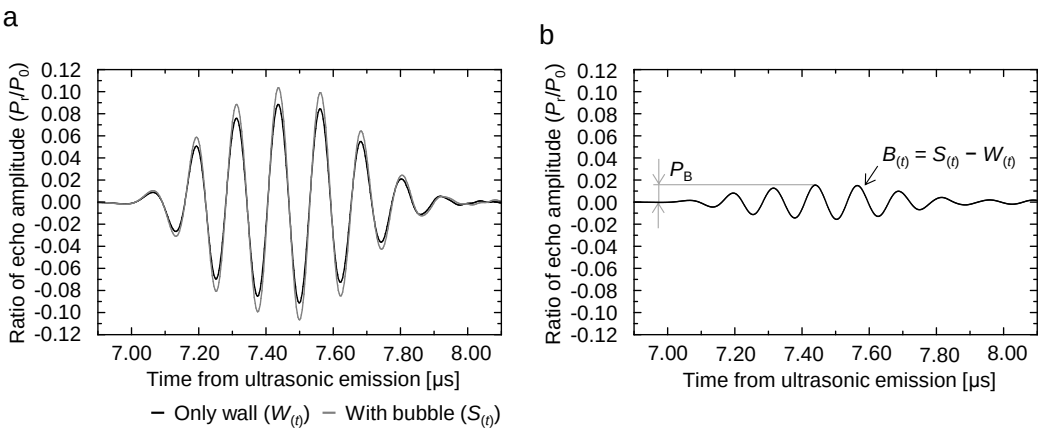

Figure 6.11 (a) Echo waveform without and with a bubble with D_B/D_U = 1.6 and Γ = 0; and (b) echo waveform from the bubble surface calculated from the two waveforms in (a).

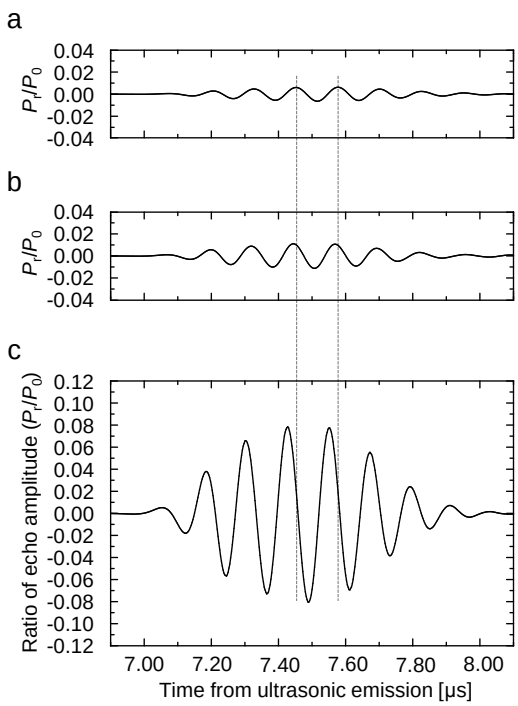

Figure 6.12 Changes of phase and amplitude of the echo waveforms of bubbles with D_B/D_U = 0.6 for different values of Γ: (a) Γ = 0.0, (b) Γ = 0.5, and (c) Γ = 1.0.

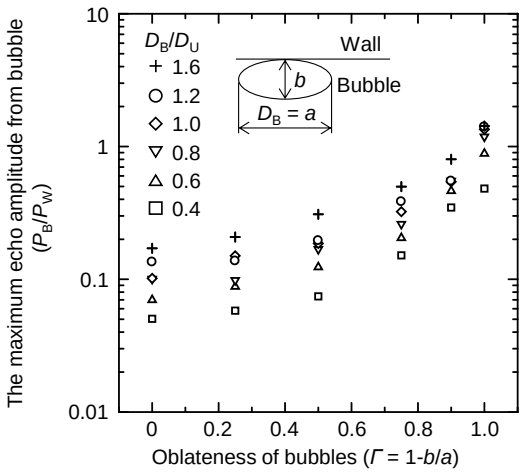

Figure 6.13 Maximum difference in the echo amplitudes from the upper wall and the bubble surface for different bubble oblatenesses (Γ) and relative bubble sizes (D_B/D_U), where P_W is the maximum echo amplitude from the wall and P_B = 0 means that the echo signals with and without the bubble are the same.

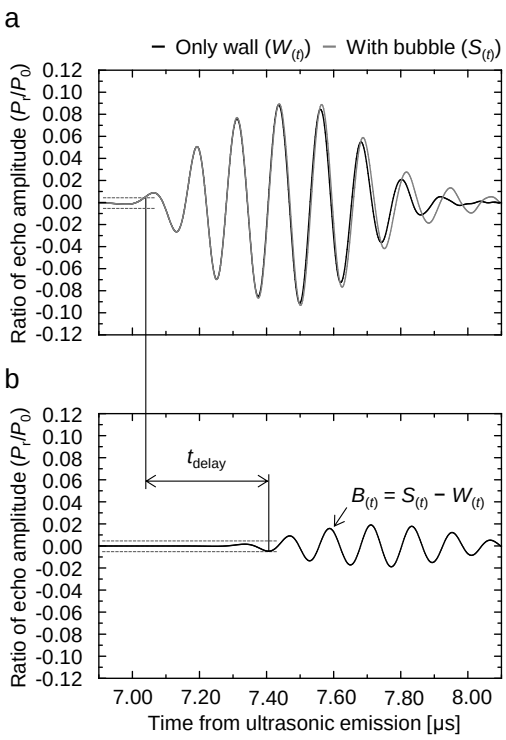

Figure 6.14 (a) Echo waveforms without a bubble and with a bubble with D_B/D_U = 1.6 and Γ = 0 that is 0.2 mm from the wall; (b) echo waveform from the bubble surface calculated from the two waveforms in (a), where the dashed lines indicate a threshold and t_{delay} is the delay between the two waveforms.

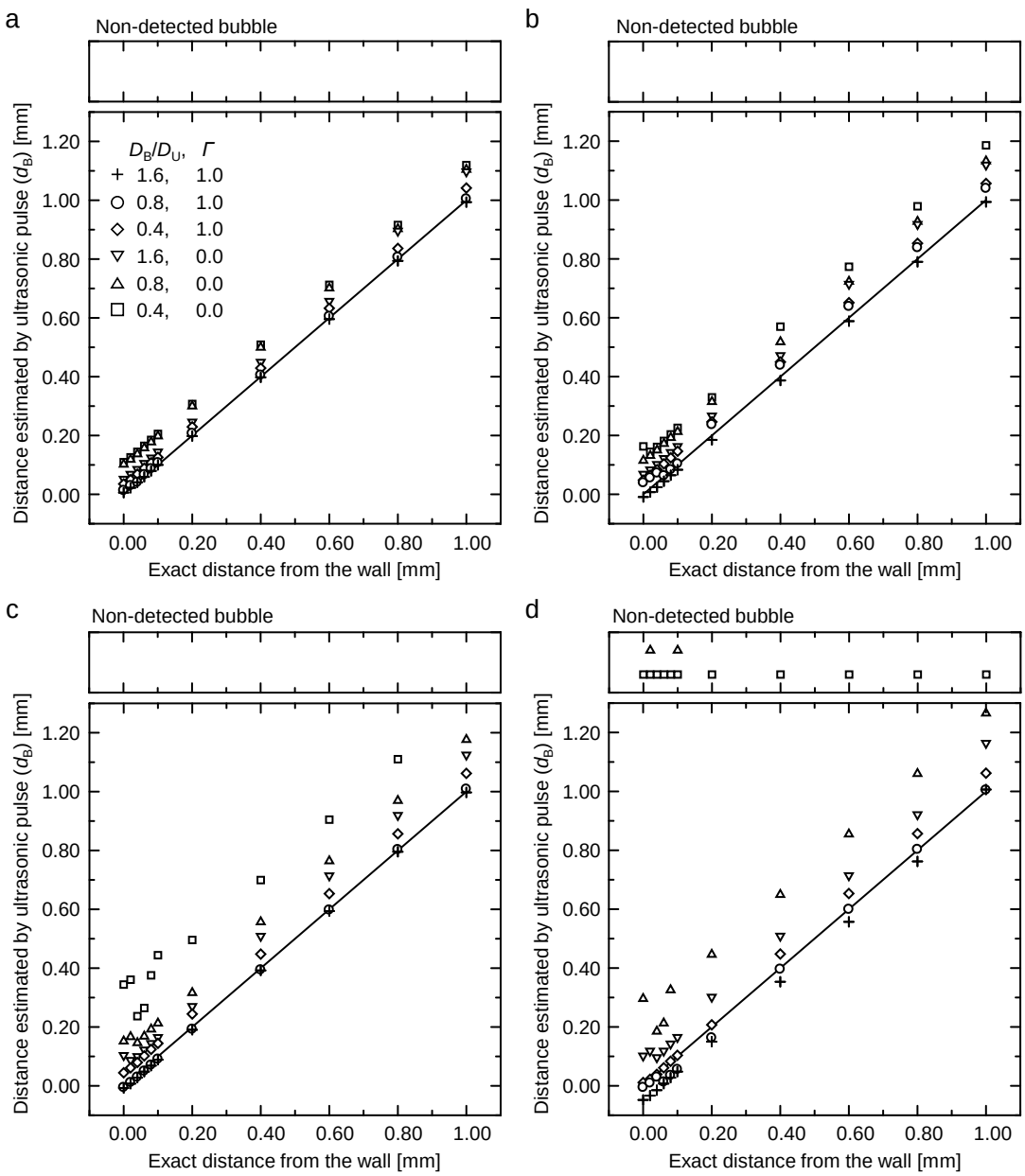

Figure 6.15 Accuracy of the bubble locations determined under the wall for various threshold voltages: (a) 0.2%, (b) 1.3%, (c) 5%, and (d) 10% of P_M.

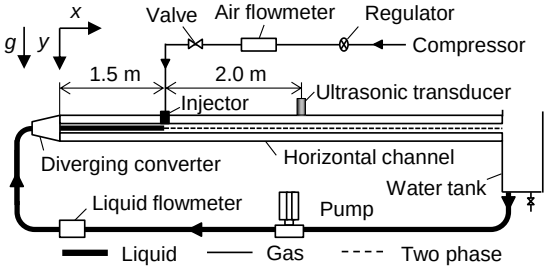

Figure 6.16 Schematic diagram of the horizontal channel.

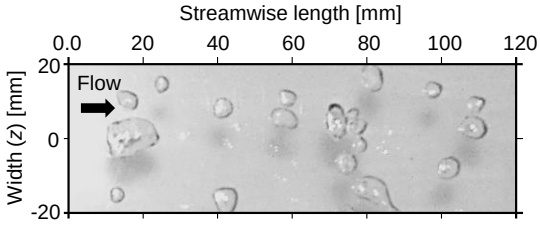

Figure 6.17 Snapshot picture of advective bubbles in the channel flow taken from above in the test section.

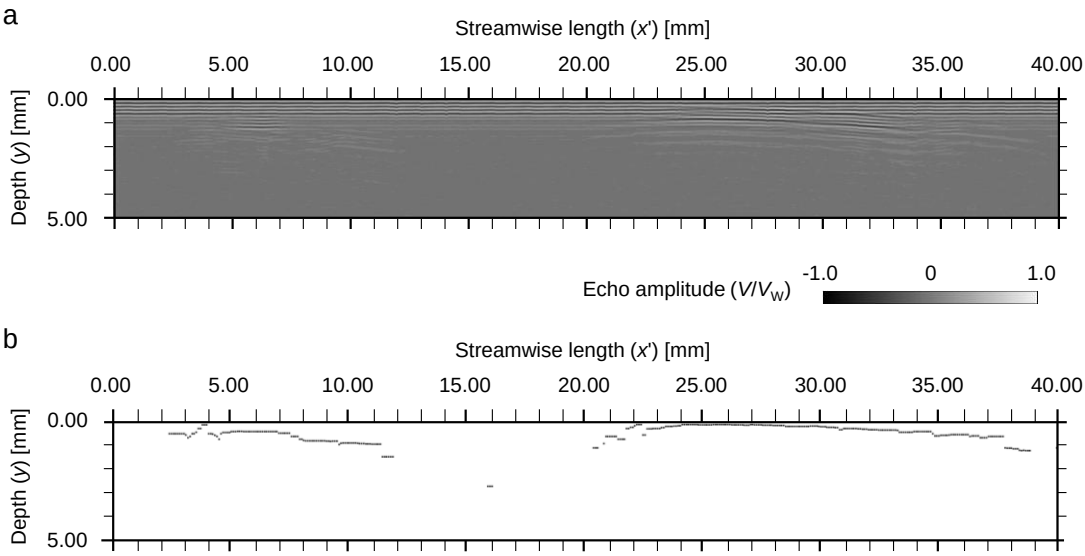

Figure 6.18 Advective bubbles in a turbulent channel flow with Re_h = 30000: (a) original echo amplitude distribution and (b) detected upper surfaces of bubbles.

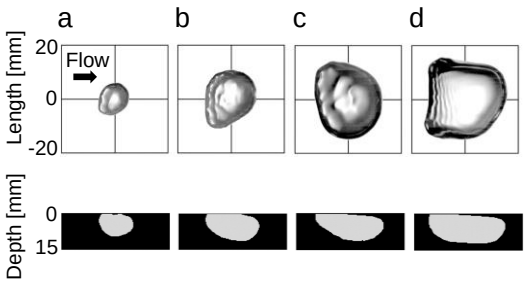

Figure 6.19 Shapes of bubbles in a channel flow with Re_h = 18520 obtained by optical visualization: (a) $D_B \approx 10$ mm, (b) $D_B \approx 20$ mm, (c) $D_B \approx 26$ mm, and (d) $D_B \approx 28$ mm, where the upper and lower panels are the top and side views, respectively. The figure taken from Oishi and Murai (2014), courtesy of Y. Murai.

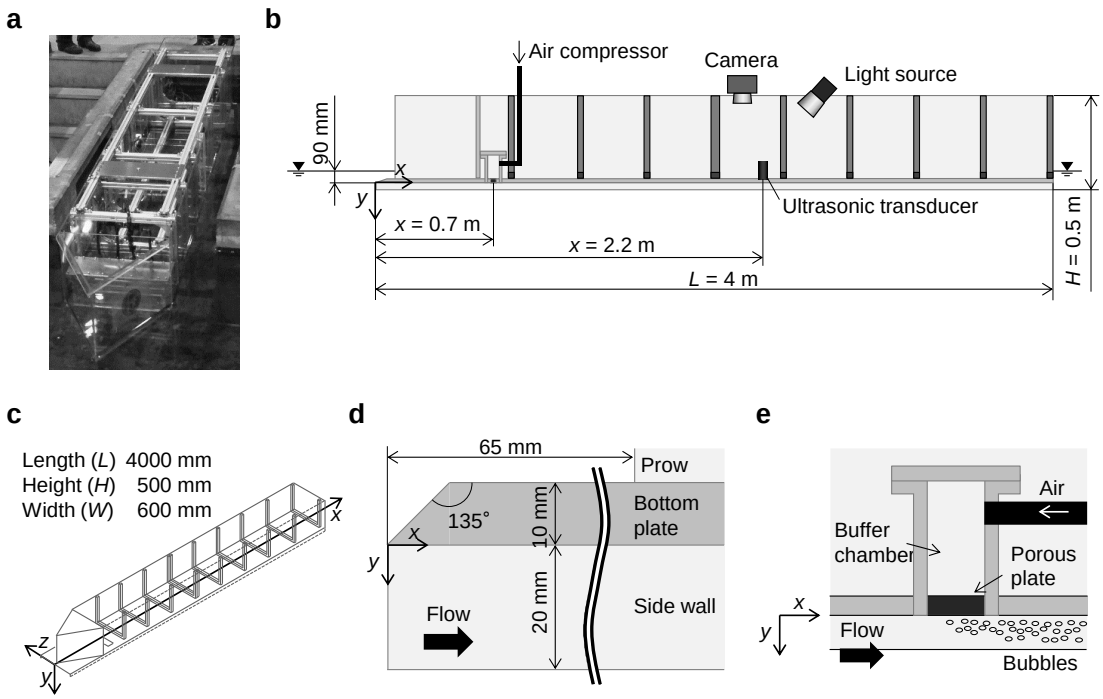

Figure 6.20 (a) Overview photograph of the ship, and (b)–(e) schematic diagrams of the side view of the ship, overview of the ship, leading edge, and injector, respectively.

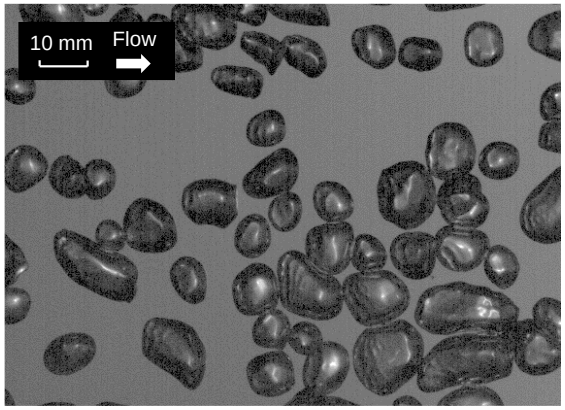

Figure 6.21 Snapshot picture of bubbles traveling beneath the bottom of the ship taken by a camera placed above the ultrasound transducer.

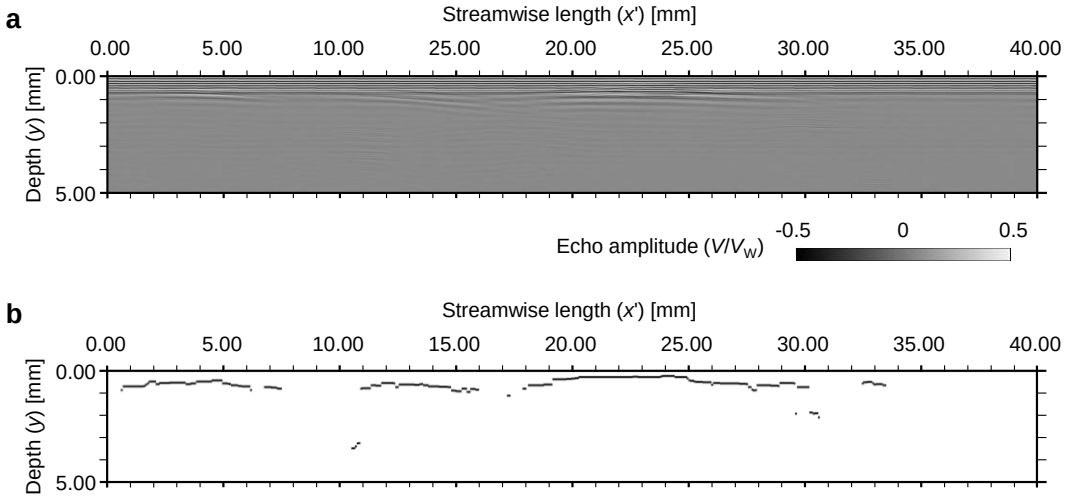

Figure 6.22 Result of the ultrasonic measurement performed on the model ship: (a) original echo amplitude distribution and (b) detected upper surfaces of bubbles.

7 Conclusions

7.1 Summaries of each chapter

We proposed repetitive bubble injection (RBI) for promoting drag reduction by bubble injection into a turbulent boundary layer and reproducibility of voidage wave transition. Some experiments were performed using a model ship with a towing tank and using horizontal rectangular channels to evaluate a possibility of adopting RBI at external and inner flows, and a mechanism of promoted drag reduction by RBI. Furthermore, methodologies for measuring bubbly flow and predicting voidage wave in the whole region using measurement results obtained at some places were developed. Details were reported in chapters 2–5. Summaries of Contents in each chapter are as described below.

In the **Chapter 2**, information of bubbles traveling in a boundary layer beneath a horizontal flat plate were investigated using the model ship, installing bubble injection system utilizing an air compressor. From variations of wall shear stress and liquid film thickness obtained by echography, it is confirmed that shear stress is decreased when the film thickness is thin. And from motion analysis of the bubbles, even relatively smaller bubbles with a few millimeter size are hard to change fluid properties such as effective viscosity. In case of continuous bubble injection used ordinarily, it is confirmed that voidage wave is generated naturally in the boundary layer by forming bubble cluster. In summary, the bubbles affect the boundary layer by interaction with flow structures in the layer and it is expected that the natural voidage wave helps to maintain the fluctuation of void fraction generated by RBI in a downstream region when artificial voidage wave resonates with the natural one.

In the **Chapters 3** and **4**, effects of bubble swarms, i.e. the artificial voidage wave, generated by the RBI on horizontal flows and its controllability were estimated using a 6 m rectangular channel. At first, in the **Chapter 3**, interaction between vortical flow structures near the wall and the bubble swarm in the channel flow was visualized by means of two-color laser-sheet illumination of the wall turbulence with a dilute suspension of flakes. By statistical analysis of visualized images, it is suggested that a possibility that streamwise vortices in the buffer layer are swept by the bubble swarm and survive until the swarm is passing above them. Next, in the **Chapter 4**, reproducibility of the bubble swarm, wall shear stress and the velocity vector field in the liquid phase were investigated by a simultaneous measurement system composed by a shear sensor and two ultrasonic velocity profiler (UVP) for estimating effects of the RBI in channel flows. Considering the suggestion in the **Chapter 3** and results in this chapter, drag reduction effect enhanced by the RBI is caused by air lubrication and by suppression of Reynolds shear stress

events in the turbulent vortical structures beneath the bubble swarm. In the final analysis, the RBI is a useful technique to improve efficiency of the boundary layer control and provide the reproducibility of the control.

In the **Chapter 5**, distributions of bubbles in the bubble swarm were investigated statistically at several downstream locations on the channel flows. From the variations of the distributions for size and number density of bubbles in each the location, a tendency is confirmed that large bubbles are traveling with a faster velocity than that of small bubbles. As a result, bubbles are classified according to size when the bubble swarm is traveling with a main flow and large bubbles are located in a front region of the swarm. From the experimental results, a one-dimensional mathematical model, i.e. the Korteweg–de Vries–Burgers equation, for transition of void fraction of the bubble swarm is established. In industrial fields, it is required to estimate the void fraction distribution in all locations. Therefore, this model is expected to help to predict it.

In the **Chapter 6**, a new echography was introduced for measuring bubble information such as shape of the bubble and liquid film thickness above the bubble, in the boundary layer using ultrasonic pulse emitted from the UVP. Although it is hard to adopt optical visualizations in industrial systems to measure flow velocity fields and bubbles because of many environmental limits of the systems, ultrasonic echography techniques are still adoptable in many cases. This new echography can obtain location of gas–liquid interface and velocity distribution in liquid–phase, simultaneously, because it uses an echo signal which is a concomitant when the UVP measures velocity profiles of liquid–phase in a flow. Therefore it is suitable for the industrial systems. Methodology was examined experimentally and numerically, and then demonstrations of the echography were performed at experimental facilities. We confirmed that the new echography was successfully developed.

7.2 Prospect of repetitive bubble injection

From several experiments performed in the thesis, we confirmed a possibility that RBI is possible to be employed at a vessel, which is an open flow system, and reduce efficiently frictional drag on ship bottom. Also, methodologies for measuring voidage wave transition beneath the ship bottom and predicting voidage wave transition using measuring results were developed. **Figure 7.1** shows an expected illustration of a container ship adopting RBI and ultrasonic echography systems, where ultrasonic transducers mounted at front and rear regions on the ship bottom monitor a velocity vector fields and transition of voidage wave, simultaneously. In the figure, bubble swarms are injected at head of the ship bottom into beneath the ship bottom and two echography systems are installed at a front and a rear, respectively, on the ship bottom. We can obtain velocity vector field in liquid–phase beneath each system because each echography system is consisted of two ultrasonic

transducers having different angle to the vertical direction and located on the streamwise direction (see the **Chapter 4**). Furthermore, information of individual bubbles, e.g. streamwise velocity, size and distance from the ship bottom, and projection void fraction are monitored by processing echo signals obtained from each transducer (see the **Chapters 5** and **6**). They allow that we control parameters of RBI for more effective drag reduction by a feedback of measured data.

- **Figures**

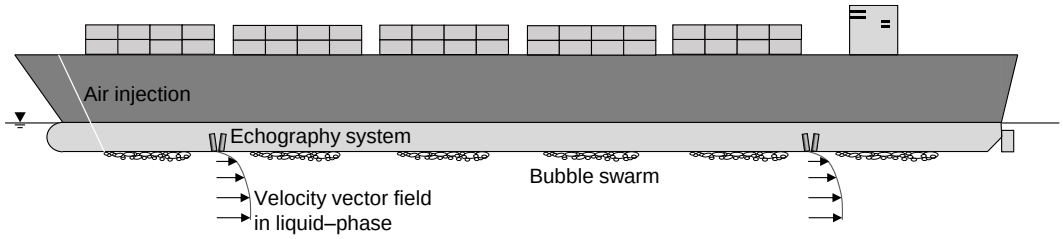

Figure 7.1 Expected illustration of a container ship adopting RBI and ultrasonic echography systems, where ultrasonic transducers mounted at front and rear regions on the ship bottom monitor a velocity vector fields, transition of voidage wave and depth of individual bubbles, simultaneously.

List of publications

• Journals

1. Junpei Ohkubo, Yuji Tasaka, **Hyun Jin Park** and Yuichi Murai, 2016. Extraction of 3D vortex structures from a turbulent puff in a pipe using two-color illumination and flakes, *Journal of Visualization*, (accepted).
2. **Hyun Jin Park**, Yuji Tasaka and Yuichi Murai, 2015. Ultrasonic pulse echography for bubbles traveling in the proximity of a wall, *Measurement Science and Technology*, Vol. 26, 125301.
3. **Hyun Jin Park**, Yuji Tasaka, Yoshihiko Oishi and Yuichi Murai, 2015. Drag reduction promoted by repetitive bubble injection in turbulent channel flows, *International Journal Multiphase Flow*, Vol. 75, pp. 12–25.
4. **Hyun Jin Park**, Yuji Tasaka, Yuichi Murai and Yoshihiko Oishi, 2014. Vortical structures swept by a bubble swarm in turbulent boundary layers, *Chemical Engineering Science*, Vol. 116, pp. 486–496.
5. **Hyun Jin Park**, Yoshihiko Oishi, Yuji Tasaka, Yuichi Murai and Takeda Yasushi, 2009. Turbulent shear control with oscillatory bubble injection, *Journal of Physics: Conference Series*, Vol. 147, 012037.

• International conference papers

– Proceedings with review

1. **Hyun Jin Park**, Yuji Tasaka, Yoshihiko Oishi and Yuichi Murai, 2015. Ultrasonic measurement of bubble motions in a wall boundary layer, *ASME-JSME-KSME Joint Fluids Engineering Conference 2015*, AJK2015-20242, Seoul, Korea.
2. **Hyun Jin Park**, Hirohide Kayukawa, Yuji Tasaka, Yoshihiko Oishi and Yuichi Murai, 2014. Ultrasound detection of wall-travelling bubbles for diagnosis of drag reduction, *9th International Symposium on Ultrasonic Doppler Methods for Fluid Mechanical and Fluid Engineering*, pp. 53–56, Strasburg, France.
3. **Hyun Jin Park**, Yoshihiko Oishi, Yuji Tasaka, Yuichi Murai and Takeda Yasushi, 2008. Turbulent shear control with oscillatory bubble injection, *6th International Symposium on Measurement Techniques for Multiphase Flows*, 41, Naha, Japan.

- **Proceedings without review**

1. Yuichi Murai, Yuji Tasaka and **Hyun Jin Park**, 2016. Frictional drag reduction by small bubbles versus large bubbles, *Proceedings Workshop on Transition Control in Dispersed Flows, Brest Seminar for French-Japanese Research Collaboration*, pp.11, Brest, France.
2. Kensuke Toda, **Hyun Jin Park**, Yoshihiko Oishi, Yuji Tasaka and Yuichi Murai, 2015. Time-Resolved LDV for bubble-laden turbulent boundary layers, *9th International Symposium on Measurement Techniques for Multiphase Flows*, D115, Sapporo, Japan.
3. Yuichi Murai, **Hyun Jin Park**, Yoshihiko Oishi and Yuji Tasaka, 2014. Drag reduction by repetitive bubble injection, *5th Symposium of AECoR between ETH and HU in Zurich*, 50, Zurich, Switzarland.
4. Yuji Tasaka, Yuichi Murai, **Hyun Jin Park** and Yukihiro Tohge, 2011. Improvement of efficiency for frictional drag reduction by repetitive bubble injection, *Bulletin of 64th Annual Meeting of the Division of Fluid Dynamics*, Vol. 56, No. 18, pp. 267, Baltimore, USA.
5. **Hyun Jin Park**, Yuji Tasaka, Yuichi Murai and Takeda Yasushi, 2009. Drag reduction by active control of bubble injection, *8th International Symposium on Marine Engineering*, 87, Pusan, Korea.
6. **Hyun Jin Park**, Yuji Tasaka, Yuichi Murai and Takeda Yasushi, 2008. Optimization of bubble injection for frictional drag reduction, *7th JSME-KSME Thermal and Fluids Engineering Conference*, E133, Sapporo, Japan.
7. **Hyun Jin Park**, Yuji Tasaka, Yuichi Murai, Yoshihiko Oishi and Takeda Yasushi, 2008. Frictional drag reduction promoted by intermittent bubble injection, *European Drag Reduction and Flow Control Meeting 2008*, ADD4, Ostritz, Germany.

- **Posters**

1. **Hyun Jin Park**, Yuji Tasaka and Yuichi Murai, 2015. Sweeping and redevelopment of longitudinal vortices in a turbulent boundary layer by injecting bubble swarms, *American Physical Society 68th Annual Meeting of the Division of Fluid Dynamics*, KP1.84, Boston, USA.
2. **Hyun Jin Park**, Yoshihiko Oishi, Yuji Tasaka and Yuichi Murai, 2014. Ultrasonic measurement of bubble motions in a wall boundary layer, *2014 HU-SNU Symposium on Mechanical and Aerospace Engineering*, HU-4, Sapporo, Japan.
3. **Hyun Jin Park**, Yoshihiko Oishi, Yuji Tasaka and Yuichi Murai, 2013. Promoted frictional drag reduction by repetitive bubble injection in turbulent flow, *2013 SNU-HU Joint Symposium on Mechanical and Aerospace Engineering*, 8, Seoul, Korea.

• Preprints of domestic conferences

1. Yoshihiko Oishi, **Hyun Jin Park**, Yuji Tasaka and Yuichi Murai, 2015. Visualization of bubble behavior beneath a model ship in large towing tank experiments, *The Japanese Society of Mechanical Engineering Division of Fluid Dynamics 93th Conference*, 0601, Tokyo, Japan.
2. Kensuke Toda, **Hyun Jin Park**, Yoshihiko Oishi, Yuji Tasaka and Yuichi Murai, 2015. Flow modifications in a viscous sublayer by advective bubbles in a turbulent channel flow, *Multiphase flow symposium 2015*, E153, Kochi, Japan.
3. Kensuke Toda, Ozaki T., **Hyun Jin Park**, Yoshihiko Oishi, Yuji Tasaka and Yuichi Murai, 2014. LDV measurement of turbulent boundary layer in a channel flow, *43th The Japanese Society of Mechanical Engineering Hokkaido Branch Students Meeting*, S2-1-05, Sapporo, Japan.
4. **Hyun Jin Park**, Yuji Tasaka, Yoshihiko Oishi and Yuichi Murai, 2014. Time-resolved measurement of advective bubbles in turbulent channel flow by ultrasound, *Multiphase flow symposium 2014*, A113, Sapporo, Japan.
5. Kayukawa H., **Hyun Jin Park**, Yoshihiko Oishi, Yuji Tasaka and Yuichi Murai, 2013. Monitoring of gas-liquid two-phase flows in a horizontal channel with ultrasonic velocity profiler, *The Japanese Society of Mechanical Engineering Division of Fluid Dynamics 91th Conference*, 0214, Fukuoka, Japan.
6. **Hyun Jin Park**, Yoshihiko Oishi, Yuji Tasaka and Yuichi Murai, 2013. Maintained void rate fluctuation by periodic bubble injection, *The Japanese Society of Mechanical Engineering Division of Fluid Dynamics 91th Conference*, 0312, Fukuoka, Japan.
7. Yuichi Murai, **Hyun Jin Park**, Yoshihiko Oishi and Yuji Tasaka, 2013. Two-color visualization of vortical structures with flake type tracer (viewing in multiphase flow), *Visualization Society of Japan Symposium 2013*, P05-004, Tokyo, Japan.
8. Yuji Tasaka, **Hyun Jin Park**, Yuichi Murai and Takeda Yasushi, 2010. Improvement for efficiency of frictional drag reduction by repetitive bubble injection, *The Japanese Society of Multiphase Flow Annual Conference 2010*, pp. 290–291, Hamamatsu, Japan.
9. **Hyun Jin Park**, Yuji Tasaka, Yuichi Murai and Takeda Yasushi, 2009. Frictional drag reduction with bubbles by periodic injection, *The Japanese Society of Multiphase Flow Annual Conference 2009*, pp. 50–51, Kumamoto, Japan.
10. **Hyun Jin Park**, Yuji Tasaka, Yuichi Murai, Yoshihiko Oishi and Takeda Yasushi, 2008. Persistency of bubble-affected area in horizontal channel flow, *The Japanese Society of Multiphase Flow Annual Conference 2008*, pp. 296–297, Aizu, Japan.

• Technical reports & exhibitions

1. Yuji Tasaka, Watamura Tomoaki, **Hyun Jin Park**, Yuichi Murai and Yoshihiko Oishi, 2014. Approaches for flow control and ship drag reduction using micorobubble, *Chemical Engineering*, Vol. 78, No. 9, pp. 593–596.
2. **Hyun Jin Park**, Yuji Tasaka, Yuichi Murai and Takeda Yasushi, 2009. Bubbles on twin-colored turbulence carpet, *Gallery of Fluid Motion – Poster, 62th Annual Meeting of the APS DFD*, Minneapolis, USA.

Curriculum vitae

Park, Hyun Jin (朴 炫珍)

- **Educations**

Apr. 2013 – Mar. 2016	Ph.D. of Engineering, Division of Energy and Environmental Systems, Graduate School of Engineering, Hokkaido University, Japan.
Apr. 2008 – Mar. 2010	Master of Engineering, Division of Energy and Environmental Systems, Graduate School of Engineering, Hokkaido University, Japan.
Apr. 2004 – Mar. 2008	Bachelor of Engineering, Department of Mechanical Engineering, School of Engineering, Hokkaido University, Japan
Oct. 2003 – Mar. 2003	International Student Center, Hokkaido University, Japan.
Mar. 2003 – Aug. 2003	Institute of International Education, Kyung Hee University, Korea.
Mar. 2000 – Feb. 2003	Gwangju Science High School, Korea.

- **Research experiences**

Apr. 2013 – Mar. 2016	Ph.D. thesis: Repetitive Bubble Injection for Control of Turbulent Boundary Layers, Laboratory for Flow Control, Division of Energy and Environmental Systems, Graduate School of Engineering, Hokkaido University, Japan.
Mar. 2010 – May. 2013	Researches on Air flow Control for Temperature Equalization and Defrost Techniques in a Refrigerator, Refrigerator R&D Laboratory, Refrigerator Division, Home Appliance Company, LG electronics Inc., Korea.
Apr. 2008 – Mar. 2010	Master's thesis: Promoting Frictional Drag Reduction by Repetitive Bubble Injection, Laboratory for Flow Control, Division of Energy and Environmental Systems, Graduate School of Engineering, Hokkaido University, Japan.
Apr. 2007 – Mar. 2008	Bachelor's thesis: Optimization of Bubble Injection for Frictional Drag Reduction, Laboratory for Flow Control, Department of Mechanical Engineering, School of Engineering, Hokkaido University, Japan.

• Professional experiences

Apr. 2015 – Mar. 2016	Japan Society for the Promotion of Science research fellow (DC2), Graduate School of Engineering, Hokkaido University, Japan.
Mar. 2012 – May. 2013	Assistant Research Engineer, Home Appliance Company, LG Electronics Inc., Korea.
Apr. 2010 – Feb. 2012	Research Engineer, Home Appliance Company, LG Electronics Inc., Korea.

• Teaching experiences

30th Apr. 2015	Teaching, Fluid Power Systems, Division of Energy and Environmental Systems, Graduate School of Engineering, Hokkaido University, Japan. Content: Basics of Fan
Apr. 2014 – Jul. 2014	Teaching Assistant, Laboratory seminar, Department of Mechanical and Intelligent System Engineering, School of Engineering, Hokkaido University, Japan.

• Honors & awards

– Grants

Apr. 2015 – Present	Grant no. 15J00147, Japan Society for the Promotion of Science research fellow.
Apr. 2014 – Mar. 2016	Research Grant from the Fundamental Research Developing Association for Shipbuilding and Offshore.

– Scholarships

Apr. 2014 – Mar. 2015	Rotary Yoneyama Memorial Foundation Scholarship.
Apr. 2008 – Mar. 2010	LG Electronics Scholarship.
Mar. 2003 – Mar. 2008	Korea–Japan Joint Government Scholarship Program for Students in Departments of Science and Engineering.

– Memberships

Jul. 2014 – Present	Member, the American Physical Society.
Sep. 2014 – Present	Member, the Japan Society for Multiphase Flow.